UCLA
UCLA Electronic Theses and Dissertations

Title

Search for New Heavy Resonances Decaying to W, Z, or Higgs Bosons and Upgrade of the Compact Muon Solenoid Level-1 Muon Trigger for the High Luminosity Large Hadron Collider

Permalink

https://escholarship.org/uc/item/9wp0g3pw

Author

Hamilton, David Warren

Publication Date

2021

Peer reviewed|Thesis/dissertation

UNIVERSITY OF CALIFORNIA

Los Angeles

Search for New Heavy Resonances Decaying to W, Z, or Higgs Bosons and Upgrade of the
Compact Muon Solenoid Level-1 Muon Trigger for the High Luminosity Large Hadron
Collider

A dissertation submitted in partial satisfaction

of the requirements for the degree

Doctor of Philosophy in Physics

by

David Warren Hamilton

2021

ABSTRACT OF THE DISSERTATION

Search for New Heavy Resonances Decaying to W, Z, or Higgs Bosons and Upgrade of the Compact Muon Solenoid Level-1 Muon Trigger for the High Luminosity Large Hadron Collider

by

David Warren Hamilton

Doctor of Philosophy in Physics

University of California, Los Angeles, 2021

Professor Michail Bachtis, Chair

This thesis describes the search for a new heavy boson decaying to a pair of heavy electroweak bosons (WW, WZ, or WH) in the semileptonic final state (electron or muon, missing transverse momentum, and jet), using the data obtained from proton collisions in the Compact Muon Solenoid detector at the Large Hadron Collider. The data used, collected during the second run of the Large Hadron Collider, has integrated luminosities of 35.9 fb^{-1}, 41.5 fb^{-1}, and 59.7 fb^{-1} recorded for the years of 2016, 2017, and 2018, respectively. The analysis performed makes use of a novel two-dimensional signal extraction technique performed in the plane of the diboson invariant mass and jet mass, with the search performed in the resonance mass range from 1.0 to 4.5 TeV. Results are obtained in terms of asymptotic exclusion limits, with no significant deviation from Standard Model predictions observed. We also present studies towards a novel muon tracking algorithm for the Level-1 Trigger of the Compact Muon Solenoid detector at the future High Luminosity Large Hadron Collider.

The dissertation of David Warren Hamilton is approved.

Thomas Dumitrescu

Jay Hauser

David Saltzberg

Michail Bachtis, Committee Chair

University of California, Los Angeles

2021

To my parents, Gary and Elaine, for their endless love and support

TABLE OF CONTENTS

x

LIST OF TABLES

ACKNOWLEDGMENTS

Beyond the friends I made here at UCLA, there are still many from my undergraduate experience at UT Austin that have supported me during their own graduate studies. In particular, I would like to thank Ruy Ibanez Amador, Paul Campbell, Alex Wilhelm, and Thanh Ha, for all the time spent together whenever I'd visit home, and for all our late night gaming sessions. I would also like to thank my childhood friend, Scott Wold, for keeping up with me all these years and being another reason to look forward to visiting Austin. Finally, I would like to thank my parents, Gary and Elaine, and my siblings, Laura and Matthew, for their love and support throughout my time in graduate school.

VITA

2013-2015	Undergraduate Tutor, University of Texas, Austin, Texas
2013-2015	Undergraduate Research Assistant, University of Texas
2014	Undergraduate Research Intern, Brookhaven National Laboratory
2015	B.S. (Physics) and B.S. (Mathematics), University of Texas
2015-2017, 2020	Teaching Assistant, Department of Physics and Astronomy, UCLA, Los Angeles, California
2017	M.S. (Physics), UCLA
2017-2021	Graduate Research Assistant, Department of Physics and Astronomy, UCLA

CHAPTER 1

Introduction

Questions surrounding the nature of matter and its interactions go as far back as at least the 6th century BC in ancient Greece and India [1, 2], but the modern study of particle physics and its experimental techniques did not arise until the turn of the 20th century. Some argue that the study of particle physics began in 1897 when J. J. Thomson discovered the electron through his experiments on cathode rays, in which it was discovered that the rays emitted by a heated filament were, in fact, not rays at all, but were actually streams of small charged particles [3]. This led Thomson to the conclusion that atoms must be composite, and that electrons were one of the main components. Later, the Rutherford scattering experiment demonstrated that the bulk of the mass and charge of an atom is concentrated in a small core we now know as the nucleus [4], which led to the discovery of the proton. Then, in 1932, James Chadwick discovered the neutron and completed the atomic picture of matter [5].

Meanwhile, in 1900, Max Planck proposed a solution to the ultraviolet catastrophe, which was a prediction from classical physics that the total power emitted by an ideal black body at thermal equilibrium should be infinite [6]. Planck resolved the problem by assuming that electromagnetic radiation emitted by a black body can only come in discrete energy packets, which resulted in a power spectrum that matched with experiments at the time. While Planck had no explanation for why the energy came in discrete packets, Einstein took this notion a step further in 1905 by instead insisting that the electromagnetic field itself was quantized, and that the discrete packets were actually particles [7], which we now know as photons (denoted by the symbol γ). In addition to explaining the observed behavior

of the black body power spectrum, Einstein's theory also provided an explanation for the photoelectric effect, for which he eventually received the 1921 Nobel Prize in Physics [8].

Despite the success of the Rutherford scattering experiment and the subsequent discovery of the proton, the question of how protons—which are positively charged and should repel each other via the electromagnetic force—could be bound together was a lingering issue. Later in the 1930's and 40's, experiments with cosmic rays led to the discovery of the μ lepton and the π meson [9]. Initial experiments did not distinguish between the two particles, and it was thought that the π meson was the mediator of a new force that binds the protons in the nucleus of an atom together. This force came to be known as the strong force, although neither the μ lepton nor the π meson turned out to be the true mediators of this force. Later experiments involving deep scattering to probe atomic nuclei would give indirect evidence for the existence of the gluon (g)—the true mediator of the strong force.

Just prior to the discovery of the π meson, the positron was discovered in 1931 [10], which was the first example of an antiparticle—an oppositely charged twin to a particle. Another landmark discovery around the same time was the discovery of neutrinos, which were postulated in 1930 by Wolfgang Pauli to explain beta decays in atomic nuclei [11]. Their existence was deduced in order to reconcile the observed energy spectrum of the electron emitted during the decay process $n \rightarrow p^+ + e^- + \bar{\nu}_e$, as the results were kinematically inconsistent with a two-body decay. It was also later experimentally verified in 1962 that there was more than one neutrino, and each is associated to a corresponding lepton [12].

By the 1950's, more particles were discovered through cosmic ray experiments, and the first particle accelerators started to come online. At this point, the field of particle physics was mired with the problem of finding structure to all of the new particles that were being discovered. Many new mesons were discovered during this period and into the 1960's, such as kaons, η's, and Λ's [13,14]. Eventually this issue of categorizing the new particles was resolved in 1964 with the development of the quark model by Murray Gell-Mann and George Zweig, who both independently proposed that hadrons (baryons and mesons) are all composite and

made up of elementary particles called quarks [15, 16]. The original quark model only had three quarks: the up quark (u), the down quark (d), and the strange quark (s). The model also proposed that every baryon is made of three quarks, and every meson is made of a quark and an antiquark. This elegantly explained the properties of all as of yet observed baryons and mesons, and it superseded the original classification scheme known as the Eightfold Way. However, this model was initially met with skepticism, but deep inelastic scattering experiments in the 1960's and 1970's would confirm that the proton indeed has substructure consistent with the quark model [17, 18].

Then in 1974, the simultaneous discovery of the J/ψ meson at Brookhaven National Lab and the Stanford Linear Accelerator Facility would give further evidence for the quark model, as it turned out to be a bound state of a new quark—called the charm quark (c)—and its antiquark [19, 20]. Later experiments in the following years would also produce baryons with this new quark, along with a new lepton called the τ lepton, a neutrino associated with the τ called the ν_τ [21], and a new quark called the bottom quark (b) after discovering the upsilon meson [22]. By this point, there were six leptons (e, μ, τ, ν_e, ν_μ, ν_τ), and five quarks (u, d, c, s, b). It seemed reasonable to think that there would perhaps be a sixth quark, bringing the number of quarks in line with the number of leptons. While this turned out to be true, the discovery of the sixth quark, known as the top quark (t), would not come until much later in 1995 at the Tevatron [23].

Another remaining issue was the lack of experimental evidence for a mediator of the weak nuclear force, which is responsible for radioactive decay of atoms. In 1967, Steven Weinberg's work on electroweak unification predicted the existence and the masses of the mediators of the weak force, known as the $W^\pm$ and Z bosons [24]. His work, along with Sheldon Glashow and Abdus Salam, would lead to the three being awarded the 1979 Nobel Prize in Physics [25]. The discovery of the $W^\pm$ and Z bosons would then occur at the European Organization for Nuclear Research (CERN) in 1983, with the observed masses falling well within the predicted ranges given by electroweak theory [26, 27]. These crucial

developments helped lead to widespread acceptance of the Standard Model (SM) of particle physics, and with the discovery of the top quark in 1995, the sub-atomic picture of matter was in a much tidier state than compared to the beginning of the 20th century: there are six quarks, six leptons, and four gauge bosons (g, γ, $W^{\pm}$, Z) that mediate the strong, weak, and electromagnetic interactions.

One particle predicted by the Standard Model still eluded experiments up to this point. A key prediction of the Standard Model is that of the Higgs mechanism, through which the gauge bosons for the weak interaction have their masses imparted onto them via the mechanism of spontaneous symmetry breaking. This required the existence of a new particle known as the Higgs boson, and despite the fact that the Higgs mechanism was developed during the formulation of the Standard Model in the 1960's [28], it would not be until much later that the particle itself was discovered. After the discovery of the top quark, the Higgs boson would elude physicists for almost two decades before being discovered at the Large Hadron Collider (LHC) at CERN in 2012 [29, 30].

The discovery of the Higgs boson marked another triumph for the predictive power of the Standard Model. But despite all of its success over the last few decades, there are still longstanding issues that the Standard Model is currently incapable of addressing. While it describes the strong, weak, and electromagnetic interactions very well at the energy scales present experiments have access to, one major shortcoming of the Standard Model is that it does not include gravitational interactions. In fact, the Standard Model is incompatible with general relativity [31]. Efforts to formulate a quantum theory of gravity are still ongoing, and the effects of gravitational interactions at such small scales would be extremely difficult to observe in an experimental setting. Another issue is that the baryonic matter that the Standard Model describes only makes up about 5% of the observed universe, while another 27% is dark matter, and the remaining 68% is dark energy [32]—neither of which the Standard Model accounts for. Finally, the Standard Model does not account for the observed matter-antimatter asymmetry, as it predicts that matter and antimatter should have been

created in equal amounts at the beginning of the universe [33].

Efforts to search for new physics beyond the Standard Model (BSM) are ongoing, and many theories such as supersymmetric models (SUSY) or Grand Unified Theories (GUTs) predict exotic new particles that may be produced in particle accelerators. In addition to verifying the existence of the Higgs boson, an equally important goal of the LHC at CERN is to search for evidence of such exotic particles, or to find any observations that deviate from the predictions of the Standard Model [34, 35].

This work describes the search for a new fundamental particle using data obtained by the LHC during Run 2 between 2016 and 2018. Chapter 2 describes the theoretical background and motivation for searching for a new particle, and begins with a brief overview of the Standard Model of particle physics, later going over theoretical models beyond the Standard Model relevant for the search. In chapter 3, we go over the LHC and the Compact Muon Solenoid (CMS) detector from which the data for the search was obtained, with descriptions of the core components of the detector. Afterwards in chapter 4, the analysis portion of the search is described, with a complete explanation of how the process was performed and what results were obtained. Finally, in chapter 5, additional work that was performed towards a novel algorithm for detecting muons in the CMS detector is presented.

CHAPTER 2

Theory and Motivation for Searching for a Heavy New Resonance

2.1 Introduction

Prior to the development of the Standard Model, attempts to reconcile quantum mechanics with special relativity resulted in the foundations of quantum field theory. The first example of a successful quantum field theory is quantum electrodynamics (QED), which was principally developed by Richard Feynman and Julian Schwinger. For their work in QED, they shared the 1965 Nobel Prize along with Sin-Itiro Tomonaga [36]. To this day, it stands as one of the most precisely tested theories of physics, with quantities such as the anomalous magnetic dipole moment of the electron a_e as predicted by QED agreeing with experiment by more than 10 significant digits [37].

However, while QED on its own is successful within its domain of modeling electromagnetic interactions, it does not concern itself with the other two interactions of the Standard Model: the strong and weak nuclear forces. The description of these two forces proved to be more mathematically complicated than QED, and the development of the quantum field theories that describe them did not come about until the 1960's and 1970's with the electroweak (EW) theory of Weinberg, Glashow, and Salam, and the theory of quantum chromodynamics (QCD) of Gell-Mann and Zweig. EW theory and QCD also have their roots in Yang-Mills theory developed by Chen Ning Yang and Robert Mills in the 1950's [38], as they are both examples of non-abelian gauge theories. The Standard Model is the resulting theory that

came about by combining EW theory with QCD[1].

Today, the Standard Model remains as the dominant theory describing three of the four known forces, with gravity excluded due to its inability to be renormalized when approached as a quantum field theory. The theory itself stands as one of the most well-tested models of physics in history, and all elementary particles predicted by the theory have been found, with the Higgs boson completing the family after being discovered in the summer of 2012. However, despite the success of this theory, many fundamental questions of physics still remain unanswered. As previously mentioned in chapter 1, the theory does not include gravity, as it only accounts for the electromagnetic, strong, and weak nuclear forces. It also does not account for the existence of Dark Matter or Dark Energy, and there are long-standing issues that the theory is currently incapable of addressing, such as the hierarchy problem [40]. The theory is therefore regarded as incomplete, and efforts to find physics beyond the Standard Model are ongoing.

In this chapter, we briefly explore the main aspects of the Standard Model in section 2.2, looking at the fundamental particles that it describes, and some of its mathematical foundations. Later, in section 2.3, we describe the theoretical background relevant to the search for a new fundamental particle beyond the Standard Model that this work presents.

2.2   The Standard Model of Particle Physics

The Standard Model is the prevailing theory in particle physics that classifies all known elementary particles, and describes how they interact with each other via the electromagnetic, weak, and strong forces. Mathematically, the Standard Model is a gauge quantum field theory resulting from the combination of both EW theory and QCD. Attempts at simply quantizing relativistic particles in the same way that nonrelativistic particles were quantized

---

[1]While the theory itself began development in the 1960's, the term "Standard Model" was coined by Pais and Treiman in 1975 [39].

gives rise to problems such as negative-energy states and violations of causality [41]. The need for the field description therefore arises from requiring that our theory obeys causality in the context of special relativity, and that our theory allows for the creation and annihilation of particles. Each elementary particle and antiparticle is associated with a field, individual particles are treated as excitations of the field, and the interactions between each of the different fields allow for the creation and annihilation of particles.

2.2.1 The Elementary Particles

The Standard Model describes the interactions between the elementary particles, which are classified as quarks, leptons, gauge bosons, and scalar bosons. Quarks and leptons are classified as fermions since they have half-integer values for their spin, while the scalar and gauge bosons are eponymously named for the fact that they are bosons and therefore have integer values for their spin. A table of all particles described by the theory can be seen in figure 2.1, labeled with their masses, charges, and spins, with the fermions grouped by generation.

2.2.1.1 Quarks

Quarks are spin-1/2 particles that interact via the strong and weak nuclear forces, as well as the electromagnetic force. The up and down quarks make up the protons and neutrons of everyday matter that we see and interact with. For example, a proton is made up of two u's and one d (uud), while a neutron is made of two d's and one u (ddu). These are just two of the many different combinations of composite particles that can be formed by quarks.

There are two main combinations of quarks to consider: mesons and baryons. Mesons are composed of one quark and an antiquark, and baryons are composed of three quarks or three antiquarks. For example, pions ($\pi^0/\pi^\pm$) were the first mesons to be observed, and they can be electrically charged when comprised only of up or down quark-antiquark pairs (i.e., a

Figure 2.1: Table of all Standard Model particles grouped by generation and type, labeled with mass, charge, and spin [42]. Particle types are colored green for quarks, red for leptons, blue for gauge bosons, and orange for scalar bosons.

π^+ is made from the combination $u\bar{d}$, and a π^- is made from $d\bar{u}$), or they can be electrically neutral (i.e., a π^0 is made from $u\bar{u}$ or $d\bar{d}$). On the other hand, protons and neutrons are examples of baryons, as they are each made of three quarks. Both baryons and mesons are examples of hadrons: bound states of quarks.

One unique aspect of quarks is that they carry color charge, and all hadrons are considered 'colorless' states. The three quarks in a baryon have red, green, and blue (or antired, antigreen, and antiblue) charge to form a colorless combination, and mesons can come in pairs of red and antired, green and antigreen, and blue and antiblue. This phenomenon is known as color confinement, and while there is currently no analytic proof of color confinement in QCD, no colorless configuration of quarks has been observed [43].

2.2.1.2 Leptons

Leptons, like quarks, are also spin-1/2 particles that can be electrically charged. Unlike quarks, they only interact via the electromagnetic and weak nuclear forces. The electron is the most familiar lepton, as it is a component of the atoms that are found in everyday interactions. However, it also has two heavier cousins: the muon and the tau. Both of these particles have the same charge as the electron, but their masses are much larger. Finally, leptons also include neutrinos, which are extremely light particles that have no electric charge, and therefore only interact via the weak force.

2.2.1.3 Gauge Bosons

The gauge bosons include the gluon, the photon, and the $W^\pm$ and Z bosons. Each gauge boson is a spin-1 particle that mediates the three fundamental interactions that the Standard Model describes. Gluons are massless particles that mediate the strong nuclear force, and they only interact with quarks since they are the only particles to carry color charge. Photons are the most familiar example of the gauge bosons, as we can quite literally see them since

light is made of photons. They are massless particles that mediate the electromagnetic force, and they interact with any particle that is electrically charged. Finally, the Z and $W^\pm$ bosons are massive particles that mediate the weak nuclear force, which is responsible for radioactive decay.

2.2.1.4 Scalar Bosons

The last category of bosons to consider is the scalar bosons, which are spin-0 particles. This family contains only one member: the Higgs boson. The need for the Higgs boson arises due to the fact the previously mentioned massive gauge bosons ($W^\pm$ and Z) do not have intrinsic masses. Rather, the Higgs boson is responsible for giving the massive gauge bosons their masses. This occurs through the Higgs mechanism, in which spontaneous symmetry breaking and gauge invariance cause the Higgs field to interact with the $W^\pm$ and Z fields in the Standard model, thereby imparting the observed masses onto the particles.

2.2.2 Mathematical Structure of the Standard Model

As the Standard Model is a quantum field theory, it has a Lagrangian density[2] $\mathcal{L}_{\mathrm{SM}}$ that contains all the information about the fields corresponding to each particle and how they interact with each other. The terms present in $\mathcal{L}_{\mathrm{SM}}$ allow us to compute probability amplitudes for particle production and decay processes through the method of Feynman diagrams. The Standard Model is also a non-abelian gauge theory, in which the internal symmetry group is $SU(3)_C \times SU(2)_L \times U(1)_Y$ [44]. The $SU(3)_C$ symmetry group corresponds to the QCD interactions of the quarks and gluons, while the $SU(2)_L \times U(1)_Y$ group corresponds to the electroweak interactions. The symmetries of these groups lead to conservation of color charge C, weak isospin T_3, and weak hypercharge[3] Y_W.

---

[2]It is typical in particle physics to simply refer to a Lagrangian density as a Lagrangian.

[3]Electric charge Q arises as a linear combination of T_3 and Y_W given by $Q = T_3 + \frac{1}{2}Y_W$.

2.2.2.1 Lagrangian Formalism

A simple yet illustrative example of a Lagrangian for a quantum field theory is that of QED for a spin-1/2 field [45]:

$$\mathcal{L}_{\text{QED}} = -\frac{1}{4}F_{\mu\nu}F^{\mu\nu} + \bar{\psi}(i\gamma^{\mu}D_{\mu} - m)\psi. \tag{2.1}$$

Here, ψ is a spin-1/2 field, $\bar{\psi} \equiv \psi^{\dagger}\gamma^{0}$ is the Dirac adjoint for ψ, $F^{\mu\nu} \equiv \partial^{\mu}A^{\nu} - \partial^{\nu}A^{\mu}$ is the electromagnetic field strength tensor, $D_{\mu} \equiv \partial_{\mu} + ieA_{\mu}$ is the gauge covariant derivative, γ^{μ} is the set of Dirac matrices, and m is the mass of the particle corresponding to the field ψ.

The classical equations of motion for the fields can be obtained through the Euler-Lagrange equation for a field ϕ, which is given by

$$\frac{\partial \mathcal{L}}{\partial \phi} - \partial_{\mu}\left[\frac{\partial \mathcal{L}}{\partial(\partial_{\mu}\phi)}\right] = 0. \tag{2.2}$$

Applying equation 2.2 to the spin-1/2 field ψ yields

$$(i\gamma^{\mu}D_{\mu} - m)\psi = 0, \tag{2.3}$$

which is the Dirac equation with the gauge covariant derivative in place of the usual partial derivative. On the other hand, for A^{μ}, using equation 2.2 gives us

$$\partial_{\mu}F^{\mu\nu} = e\bar{\psi}\gamma^{\nu}\psi = J^{\nu}, \tag{2.4}$$

which are the inhomogeneous Maxwell equations for the electromagnetic field, with four-vector current $J^{\nu} \equiv e\bar{\psi}\gamma^{\nu}\psi$.

2.2.2.2 Gauge Theory

One of the most foundational aspects of the Standard Model is the notion of gauge invariance, which means that the Lagrangian $\mathcal{L}$ remains invariant under a set of transformations. The invariance of the Lagrangian under these transformations leads to conservation laws as a consequence of Noether's theorem. This is at the heart of the Standard Model and why it is an $SU(3)_C \times SU(2)_L \times U(1)_Y$ gauge theory.

To see this, consider the Dirac Lagrangian for a spin-1/2 field given by

$$\mathcal{L}_{\mathrm{Dirac}} = \bar{\psi}(i\gamma^\mu \partial_\mu - m)\psi. \tag{2.5}$$

This Lagrangian is invariant under the global $U(1)$ transformation $\psi \to e^{i\alpha}\psi$, as $\bar{\psi} \to e^{-i\alpha}\bar{\psi}$ and the product $\bar{\psi}\psi$ remains the same. However, if we insist on a local $U(1)$ transformation such that $\psi \to e^{i\alpha(x)}\psi$, then the invariance is broken since the transformed Lagrangian obtains an additional term:

$$\mathcal{L} \to \mathcal{L} - \bar{\psi}\gamma^\mu[\partial_\mu \alpha(x)]\psi. \tag{2.6}$$

The symmetry can be restored by adding an interaction term with a gauge field A_μ in the Lagrangian and demanding that it transform along with ψ, and by adding an interaction term $\mathcal{L}_{\mathrm{int}}$:

$$A_\mu \to A_\mu - \frac{1}{e}\partial_\mu \alpha(x), \qquad \mathcal{L}_{\mathrm{int}} = -e\bar{\psi}\gamma^\mu A_\mu \psi. \tag{2.7}$$

But introducing the gauge field requires that we also add a kinetic term $-\frac{1}{4}F_{\mu\nu}F^{\mu\nu}$ for A_μ, with $F^{\mu\nu} = \partial^\mu A^\nu - \partial^\nu A^\mu$. Then the full Lagrangian is now

$$\mathcal{L} = -\frac{1}{4}F_{\mu\nu}F^{\mu\nu} + \bar{\psi}(i\gamma^\mu \partial_\mu - m)\psi - e\bar{\psi}\gamma^\mu A_\mu \psi = -\frac{1}{4}F_{\mu\nu}F^{\mu\nu} + \bar{\psi}(i\gamma^\mu D_\mu - m)\psi, \tag{2.8}$$

where $D_\mu = \partial_\mu + ieA_\mu$ is the gauge covariant derivative. This is in fact the QED Lagrangian of equation 2.1. Thus, $\mathcal{L}_{\mathrm{QED}}$ is exhibits a local $U(1)$ symmetry, and applying Noether's

theorem to the $U(1)$ gauge transformations reveals that the conserved quantity under this symmetry is electric charge Q.

This same process can be applied to the overall $SU(3)_C \times SU(2)_L \times U(1)_Y$ gauge group to obtain conservation of color charge C, weak isospin T_3, and weak hypercharge Y_W. The method of introducing a gauge field and replacing ordinary derivatives with gauge covariant derivatives to obtain local gauge symmetry is known as the minimal coupling rule [46]. While the example of local $U(1)$ symmetry with the QED Lagrangian is simpler due to the fact that $U(1)$ is an abelian group, the process is similar for the non-abelian groups such as $SU(3)$ and $SU(2)$. Thus, the gauge bosons are named for the fact that their fields naturally arise from demanding local gauge symmetry for the SM Lagrangian.

2.2.2.3 The Higgs Mechanism

One lingering issue arising from introducing the gauge fields is that the fields are required to be massless, otherwise the mass terms arising from the fields would spoil the gauge invariance. For QCD this is not an issue since gluons are massless. However, for EW theory this is a problem since the photon is massless, but the $W^\pm$ and Z bosons are not.

The Higgs mechanism solves this through spontaneous symmetry breaking by introducing a scalar field that interacts with the gauge fields in such a way that the masses are imparted onto them. To see this mechanism in action, we may consider a simple model with a complex scalar field $\phi = \phi_1 + i\phi_2$ with the following Lagrangian [47]:

$$\mathcal{L} = \frac{1}{2}(\partial_\mu \phi)^*(\partial^\mu \phi) + \frac{1}{2}\mu^2(\phi^*\phi) - \frac{1}{4}\lambda^2(\phi^*\phi)^2. \tag{2.9}$$

By inspection, this Lagrangian has a $U(1)$ global symmetry under the transformation $\phi \rightarrow e^{i\theta}\phi$. However, in order to apply perturbation theory so that we may use Feynman diagrams to compute scattering amplitudes, the Lagrangian must be defined so that the fields are shifted to the global minimum of the potential. We may do so by noticing that the minimum

of the potential lies on a circle of radius μ/λ in (ϕ_1, ϕ_2) space, and by rewriting $\mathcal{L}$ in terms of new fields $\eta \equiv \phi_1 - \mu/\lambda$ and $\xi \equiv \phi_2$, the Lagrangian is now

$$
\begin{aligned}
\mathcal{L} = {} & \frac{1}{2}(\partial_\mu \xi)(\partial^\mu \xi) + \frac{1}{2}(\partial_\mu \eta)(\partial^\mu \eta) - \mu^2 \eta^2 \\
& - \left[\mu\lambda(\eta^3 + \eta\xi^2) + \frac{\lambda^2}{4}(\eta^4 + \xi^4 + 2\eta^2\xi^2) \right] + \frac{\mu^2}{4\lambda^2}.
\end{aligned}
\tag{2.10}
$$

Reading off the quadradic terms in $\mathcal{L}$ reveals that the fields have acquired masses $m_\eta = \sqrt{2}\mu$ and $m_\xi = 0$.

However, the Lagrangian no longer exhibits the global $U(1)$ symmetry that was present when written in terms of ϕ and ϕ^*, and there is now a massless field ξ present. This phenomenon in which the original symmetry is no longer present is known as spontaneous symmetry breaking, and the introduction of a massless scalar field is a consequence of Goldstone's theorem, which states that the spontaneous breaking of a continuous global symmetry is accompanied by the presence of a massless Goldstone boson [48]. Evidently, ξ is the Goldstone boson present in the theory.

We may repeat this process but instead promote the original global $U(1)$ symmetry to a local symmetry and take the usual approach of introducing a gauge field A^μ and gauge covariant derivative $D_\mu = \partial_\mu + ieA_\mu$. After applying the shift in the fields η and ξ so that the potential is instead written about the minimum, the new Lagrangian with the gauge field is

$$
\begin{aligned}
\mathcal{L} = {} & \frac{1}{2}(\partial_\mu \xi)(\partial^\mu \xi) + \frac{1}{2}(\partial_\mu \eta)(\partial^\mu \eta) - \mu^2 \eta^2 - \frac{1}{4}F_{\mu\nu}F^{\mu\nu} + \frac{1}{2}\frac{e^2\mu^2}{\lambda^2}A_\mu A^\mu \\
& + e[\eta(\partial_\mu \xi) - \xi(\partial_\mu \eta)]A^\mu + \frac{e^2\mu}{\lambda}\eta A_\mu A^\mu + \frac{1}{2}e^2(\xi^2 + \eta^2)A_\mu A^\mu \\
& - \lambda\mu(\eta^3 + \eta\xi^2) - \frac{1}{4}\lambda^2(\eta^4 + 2\eta^2\xi^2 + \xi^4) + \frac{e\mu}{\lambda}(\partial_\mu \xi)A^\mu + \frac{\mu^4}{4\lambda^2}.
\end{aligned}
\tag{2.11}
$$

Again we have a massive η field, and now the gauge field A^μ has acquired a mass $m_A = e\mu/\lambda$. But there are two problems: the Goldstone boson ξ is still present, and there is now a term in $\mathcal{L}$ of the form $(\partial_\mu \xi)A^\mu$. Any term in the Lagrangian that is bilinear in two different fields

indicates that $\mathcal{L}$ is not written in terms of fields corresponding to physical particles.

Both issues are resolved by applying a gauge transformation to the original fields ϕ and ϕ^* so that $\phi \rightarrow e^{i\theta}\phi$ and $\phi^* \rightarrow e^{-i\theta}\phi^*$, with $\theta = -\arctan(\phi_2/\phi_1)$. This is equivalent to setting $\phi_2 = 0$, which means that $\xi = 0$ as well. Since the Lagrangian is invariant under the $U(1)$ gauge transformation, we are left with all terms that do not contain ξ, and hence

$$
\begin{aligned}
\mathcal{L} = {} & \frac{1}{2}(\partial_\mu \eta)(\partial^\mu \eta) - \mu^2 \eta^2 - \frac{1}{4}F_{\mu\nu}F^{\mu\nu} + \frac{1}{2}\frac{e^2\mu^2}{\lambda^2}A_\mu A^\mu + \frac{e^2\mu}{\lambda}\eta A_\mu A^\mu \\
& + \frac{1}{2}e^2\eta^2 A_\mu A^\mu - \lambda\mu\eta^3 - \frac{1}{4}\lambda^2\eta^4 + \frac{\mu^4}{4\lambda^2}.
\end{aligned}
\tag{2.12}
$$

Thus, the Goldstone boson is eliminated, we are left with the massive scalar field η and the massive gauge field A^μ, and the gauge field has also acquired a longitudinal polarization state in the process.

The Higgs mechanism is ultimately the result of combining spontaneous symmetry breaking and local gauge invariance [49], and applying this process to the $SU(2)_L \times U(1)_Y$ EW theory accounts for the masses of the electroweak $W^\pm$ and Z bosons, while also introducing the Higgs field itself. It is for this reason that discovering the Higgs boson was of the utmost importance in verifying the Standard Model's description of the electroweak sector. Meanwhile, the fermions gain their masses through a Yukawa interaction with the Higgs field.

2.2.3   Beyond the Standard Model

The incompleteness of the Standard Model has driven theoretical developments of alternative models that resolve its shortcomings [50]. A few examples are Grand Unified Theories, supersymmetry, and models based on extra spatial dimensions. While such theories are currently of high interest due to the prospect of superseding the Standard Model, some are based on developments that predate the Standard Model itself.

2.2.3.1   The Hierarchy Problem

One major outstanding issue relevant to this work is the inability of the Standard Model to deal with the hierarchy problem. Using three fundamental constants, one may define the Planck mass as

$$m_P = \sqrt{\frac{\hbar c}{G}} \approx 1.22 \times 10^{19} \text{ MeV}/c^2, \qquad (2.13)$$

where $\hbar$ is the reduced Planck constant, c is the speed of light, and G is Newton's gravitational constant. This defines an energy scale at which effects due to gravity would become apparent in particle physics experiments [51]. However, this energy scale is vastly larger than what can be obtained in contemporary accelerators. Figure 2.2 shows the comparison between the Planck scale, the electroweak symmetry breaking scale, and the current center-of-mass energy $\sqrt{s}$ at the Large Hadron Collider.
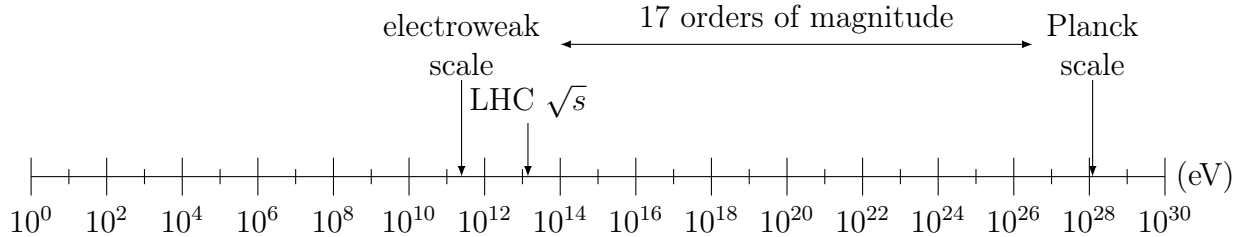
Figure 2.2: Comparison between the electroweak scale, LHC center-of-mass energy $\sqrt{s}$, and Planck scale in eV. The hierarchy problem arises due to the unexplained difference between the Planck scale at which gravitational effects become apparent and the energy scale at which electroweak symmetry breaking occurs, which are 17 orders of magnitude apart.

The issues caused by the hierarchy problem are more apparent when considering the mass corrections to the Higgs boson. The Higgs boson mass m_H is corrected through one-loop Feynman diagrams that are proportional to m_H^2 [52], two examples of which can be seen in figure 2.3. Such corrections require a momentum cutoff Λ when evaluating the loop integrals obtained from the diagrams, and if the cutoff is on the same order as m_P, the correction to

m_H^2 ends up being far larger than the required value. While this effect only directly applies to m_H^2, the rest of the massive SM particles are indirectly sensitive to the cutoff Λ due to the fact that they gain their masses through the vacuum expectation value of the Higgs field $\langle H \rangle$. This means that the mass spectrum of the SM is sensitive to Λ. It also does not suffice to simply pick a sufficiently small cutoff, as this requires new physics at the energy scale of Λ to change the behavior of the propagators in the one-loop mass correction terms.
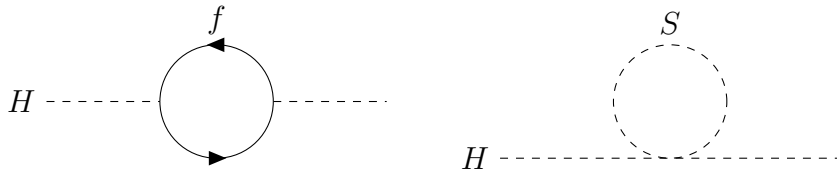
Figure 2.3: One-loop Feynman diagrams with a Higgs boson coupling to a fermion f (left), and a scalar S (right). Such diagrams contribute quadratic corrections m_H^2 to the Higgs boson mass.

In the absence of some mechanism that resolves this issue, we are left with having to fine-tune parameters of the Standard Model in order to address the hierarchy problem. On the other hand, some BSM theories seek to address this problem in a more natural manner that does not require such fine-tuning. Such theories result in new physics that may be experimentally verified, with some predicting the existence of new heavy particles that could be detected in collision events at the LHC.

2.2.3.2 Supersymmetric Theories

Supersymmetry extends the notion of local symmetry to fermionic and bosonic fields, suggesting that there are symmetry transformations that mix the fields into each other [53]. SUSY theories suggest that every known fermion has a corresponding bosonic partner, and every known boson has a corresponding fermionic partner. For example, the electron would have a spin-0 supersymmetric partner known as the 'selectron', and there would be other

supersymmetric partners such as 'squarks' and 'sneutrinos'. Bosonic particles would have partners such as the 'photoino', 'gluino', 'wino', and 'zino'. However, one main issue is that no such supersymmetric partners have been identified, and the simplest models predict that they should have the same mass as their SM partners. This suggests that if there is a supersymmetric theory that turns out to be correct, there must be a spontaneously broken symmetry mechanism that causes supersymmetric partners to differ in mass from their SM partners [54].

2.2.3.3 Grand Unified Theories

Grand Unified Theories are largely inspired by the success of the electroweak unification. In the same way that the electromagnetic and weak forces become a single interaction at a particular energy scale, GUTs aim to unify the strong force with the other two forces of the Standard Model. This requires a symmetry group that contains the $SU(3)_C \times SU(2)_L \times U(1)_Y$ group as a subgroup. The first example of a GUT was the Georgi-Glashow model that was based on the $SU(5)$ group [55]. A unique aspect of such theories is that they often predict that the proton is unstable and can decay due to new gauge bosons that couple quarks to leptons[4]. However, proton decay has not been observed [57], and the current lower bound for the lifetime of the proton is inconsistent with the Georgi-Glashow model. Despite this, there are still other models based on more complex groups, such as E_6 [58] or $SO(10)$ [59], that are candidates for further investigation.

2.2.3.4 Warped Extra Dimensions

There are many BSM theories that suggest that there are extra spatial dimensions, some of which are based on work done well before the formulation of the Standard Model. Classical Kaluza-Klein theory has its roots in the early 20th century, and its main feature is

---

[4]Such bosons are often called 'leptoquarks' [56].

the addition of a fourth spatial dimension [60]. It is a unified field theory that combines gravity and electromagnetism, and it rests on the idea that the extra spatial dimension is compactified in such a way that makes it experimentally difficult to observe. The integration of electromagnetism into the theory neatly follows from symmetry considerations due to the extra spatial dimension.

Such work involving extra dimensions has paved the way for later theoretical developments in the field. Randall-Sundrum (RS) models are examples of this, which propose that there is an extra fourth spatial dimension that has a strongly warped geometry [61]. These models are based on the idea that the spatial dimensions of the universe are restricted to a brane embedded within a higher-dimensional space known as the "bulk." In such a framework, the elementary particles—except for the graviton—are localized in (3+1)-dimensional branes, while the graviton is able to propagate in the bulk. The warped geometry is such that there are two branes in these models: the Tevbrane where the SM particles are localized, and the Planckbrane where the gravitational force becomes much stronger.

2.3   Search for a Heavy Diboson Resonance

This thesis presents results on the search for a new heavy X resonance decaying into a pair of bosons as part of efforts to explore BSM physics at the LHC. The decays of interest are $X \to WV$ and $X \to WH$, where $V = W^{\pm}, Z$ is any of the three massive electroweak vector bosons and H is the Higgs boson discovered at the LHC in 2012. We consider semileptonic final event states in which the $W^{\pm}$ decays leptonically via $W \to \ell\nu$, where ℓ is either an electron or a muon, as this provides a clean experimental signature and an efficient online event selection. The other V/H boson decays hadronically through the process $V \to q\bar{q}^{(\prime)}$ or $H \to b\bar{b}$ and is reconstructed as a single massive jet. Three production modes are considered based on the benchmark models used: vector boson fusion (VBF), gluon-gluon fusion (ggF), and Drell-Yan (DY) production. For ggF and DY processes there are no additional objects

produced in the event, but for VBF processes there are two forward-facing jets, which are narrow cones of hadrons and other particles produced by the hadronization of a quark.

This work is motivated in part by models such as those mentioned in subsection 2.2.3, and is a continuation of a previous search using the 2016 data collected by the LHC during Run 2 [62]. The previous analysis was conducted using only two benchmark signal models, and it was agnostic to the method of production for an X resonance. This work instead uses multiple benchmark signal models and considers three production methods.

2.3.1 Narrow Resonance Models

The search conducted in this work is model independent—it is not specific to a signal model and can cover many possibilities for an X resonance. However, benchmark models based on the BSM theories described in subsection 2.2.3 are used in order to model hypothetical collision events in the LHC that result in the final event states of interest. The structure of these events then informs us about making our selection cuts for our search, as will be discussed in chapter 4. This search covers spin-0, spin-1, and spin-2 bosonic resonances, and is based on the following benchmark models:

1. **Spin-0 Bulk Radion:** A neutral scalar boson appearing in RS models that can decay to the vector bosons $W^{\pm}$ and Z via $\phi \rightarrow WW$ and $\phi \rightarrow ZZ$ [63, 64].

2. **Spin-1 W'/Z' Boson:** Heavier versions of the spin-1 $W^{\pm}$ and Z bosons that can decay via $W' \rightarrow WZ$, $W' \rightarrow WH$, $Z' \rightarrow WW$, and $Z' \rightarrow ZH$ [65].

3. **Spin-2 Bulk Graviton:** A spin-2 resonance from a bulk RS model that decays via $G_{\mathrm{bulk}} \rightarrow WW$ and $G_{\mathrm{bulk}} \rightarrow ZZ$ [66, 67].

These benchmarks cover a wide range of possibilities for candidate BSM bosonic resonances to be discovered. The models used also assume a narrow resonance, which means that the internal width of the resonance is smaller than the resolution of the experiment.

Despite the variety in signal models, they may all result in similar semileptonic final states, thereby allowing the analysis to be model independent. Furthermore, based on previous searches that have been conducted, they are all expected to be in the TeV mass range.

2.3.1.1 Model Parameters

The Bulk Radion and Bulk Graviton benchmark models make use of common parameters because they are both based on RS theories. In particular, the metric considered with the extra spatial dimension φ is given by [68]

$$\mathrm{d}s^2 = e^{-2kr_c\varphi}\eta_{\mu\nu}\,\mathrm{d}x^\mu\,\mathrm{d}x^\nu + r_c^2\,\mathrm{d}\varphi^2 , \tag{2.14}$$

where $0 \leq \varphi \leq \pi$, r_c is the finite size of the φ dimension, x^μ are the familiar 4D spacetime coordinates, $\eta_{\mu\nu}$ is the Minkowski metric, and k is the curvature factor given by

$$k \equiv \sqrt{\frac{-\Lambda}{24M_5^2}}. \tag{2.15}$$

Here, Λ is the vacuum energy density on the branes/bulk, and M_5 is the 5D Planck mass. The Bulk Graviton model used for this analysis is parameterized in terms of the dimensionless curvature given by $\tilde{k} \equiv k/\overline{M}_P$, where $\overline{M}_P^2 = \frac{M_5^3}{k}\left(1 - e^{2\pi kr_c}\right)$ is the 4D Planck mass obtained by integrating out the extra dimension φ.

For the Radion model, there are two parameters that are considered. The first is the dimensionless combination kr_c, given by

$$kr_c = \frac{1}{\pi}\ln\left(3.83\tilde{k}\frac{\overline{M}_P}{M_G}\right), \tag{2.16}$$

where M_G is the graviton mass. The second parameter $\Lambda_R \equiv e^{-\pi kr_c}\sqrt{\frac{6M_5^3}{k}}$ determines the

strength of the coupling of the Radion with matter in the interaction Lagrangian

$$\mathcal{L}_\phi = -\frac{1}{\Lambda_R}\phi a_i T^{\mu(i)}{}_\mu, \tag{2.17}$$

where the $a_i T^{\mu(i)}{}_\mu$ are interaction terms obtained from taking the trace of the energy-momentum tensor $T^{\mu\nu}$, with i denoting the type of matter field in the interaction (i.e., massive gauge bosons or fermions).

Meanwhile, the W'/Z' model considered for ggF and DY processes is the Heavy Vector Triplet (HVT) model B, and model C for VBF processes, as described in reference [65]. The model introduces a spin-1 field ρ_μ that transforms under the $SO(4)$ group, with a Lagrangian

$$\mathcal{L}_\rho = -\frac{1}{4\hat{g}'^2}(B_{\mu\nu})^2 - \frac{1}{4\hat{g}^2}(W^a_{\mu\nu})^2 + \frac{f^2}{4}d^i_\mu d^{\mu i} - \frac{1}{4g^2_\rho}(\rho^a_{\mu\nu})^2 + \frac{m^2_\rho}{2g^2_\rho}(p^a_\mu - e^a_\mu)^2. \tag{2.18}$$

The field strength tensor for ρ is $\rho^a_{\mu\nu} = D_{[\mu}V^a_{\nu]} - \epsilon^{abc}V^b_\mu V^c_\nu - W^a_{\mu\nu}$, where $V^a_\mu \equiv \rho^a_\mu + W^a_\mu$ is the vector triplet for which the model is named. Meanwhile, the d^i_μ and e^a_μ terms contain interactions between the Higgs field and other fields, f is the Goldstone-Boson-Higgs decay constant, and g_ρ, $\hat{g}$, and $\hat{g}'$ are coupling constants. For the parameters of the models, it is convenient to instead rewrite the coupling constants as

$$g_V = g_\rho, \qquad \frac{1}{g^2} = \frac{1}{\hat{g}^2} + \frac{1}{\hat{g}^2_\rho}, \qquad g' = \hat{g}'. \tag{2.19}$$

There are several parameters that describe the three variants of the HVT models, but for this analysis we are interested only in three: g_V, c_H, and c_F, which describe the interaction strength of the new vector bosons, Higgs boson coupling, and fermion coupling, respectively. In terms of other model parameters, the two couplings are

$$c_H = \frac{g_V}{\sqrt{g^2_V - \tilde{c}^2_{VW}g^2}}\left(\tilde{c}_H + \frac{g^2}{g^2_V}\tilde{c}_{VW}\right), \qquad c_F = \frac{g_V}{\sqrt{g^2_V - \tilde{c}^2_{VW}g^2}}(\tilde{c}_F + \tilde{c}_{VW}), \tag{2.20}$$

23

where the $\tilde{c}$ quantities are transformed versions of the original c couplings and the subscripts denote the interaction terms they couple to. For model B, $g_V \leq 4\pi$, $c_H \approx 1$, and $c_F \approx 1$, while for model C the fermionic couplings are zero, with $g_V \approx 1$ and $c_F = 0$.

2.3.2 Expected Event Structure

The decay processes $X \to WV \to \ell\nu q\bar{q}^{(\prime)}$ and $X \to WH \to \ell\nu b\bar{b}$ were chosen due to the fact that one-lepton events are ideal for such an analysis, as the final states that are generated provide a clean signal that suppresses background. Furthermore, the semileptonic final state is also a good compromise for search sensitivity since it is cleaner than an all-hadronic final state, and it produces more expected signal than an all-leptonic state. The ggF and DY production modes produce only the $\ell\nu q\bar{q}^{(\prime)}$ and $\ell\nu b\bar{b}$ semileptonic final states resulting from the decay of the X resonance. Meanwhile, although the VBF production channel is rarer than the ggF and DY production modes by a factor of 10 to 100, its particular event signature further suppresses background events and uniquely results in forward-facing jets [69]. All benchmark models used in this analysis are capable of this production mechanism. Such a process has been used in the past as one of the discovery channels for the Higgs boson, and it remains an important class of events at the LHC. The spin-0 Bulk Radion and spin-2 Bulk Graviton models both have ggF production modes, while the spin-1 W' and Z' models can be produced via a DY process. Examples of Feynman diagrams for all three production processes of an X resonance with the resulting final states can be seen in figure 2.4.

Because the expected mass of the bosonic resonance lies in the TeV range, the final event state has a highly boosted topology, which is illustrated in figure 2.5. The two initial state quarks from the VBF process in the diagram of figure 2.4 result in two forward-facing jets in the final state that are highly energetic and collimated. Meanwhile, the lepton-neutrino pair from the $W \to \ell\nu$ decay will have momenta opposite to that of the jet that results from the hadronic decay of the V/H boson. The jet from the $V \to q\bar{q}^{(\prime)}$ or $H \to b\bar{b}$ decay will also have two-pronged substructure since the decay results in a quark-antiquark pair. Lastly,
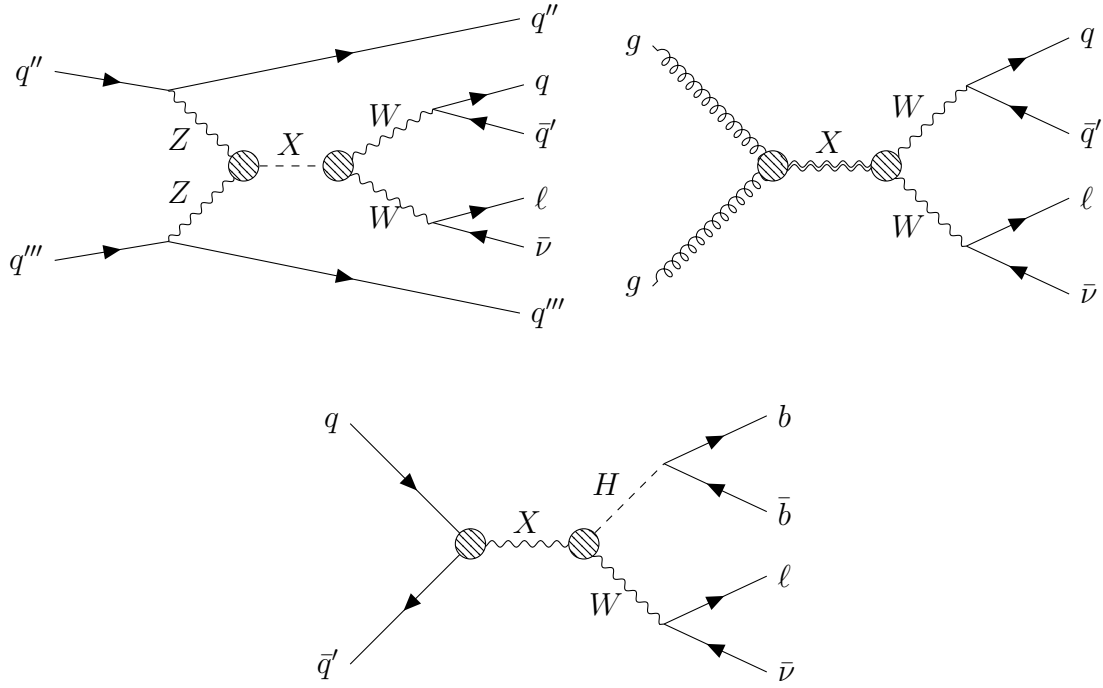
Figure 2.4: Feynman diagrams for production via vector boson fusion of a neutral spin-0 resonance X decaying to the final state $\ell\nu q\bar{q}'$ (top left), gluon-gluon fusion for a spin-2 resonance X decaying to the final state $\ell\nu q\bar{q}'$ (top right), and a Drell-Yan process for a charged spin-1 resonance X decaying to the final state $\ell\nu b\bar{b}$ (bottom). The search for an X boson will involve looking for a final state in which there is a single merged jet from the V/H boson, a lepton ℓ with its corresponding neutrino produced from the $W^{\pm}$ decay, and in the case of VBF production, two forward-facing jets.

both the lepton-neutrino pair and the jet will be highly collimated since the $W^{\pm}$ and V/H bosons that produced them will have momenta of several hundred GeV or above.
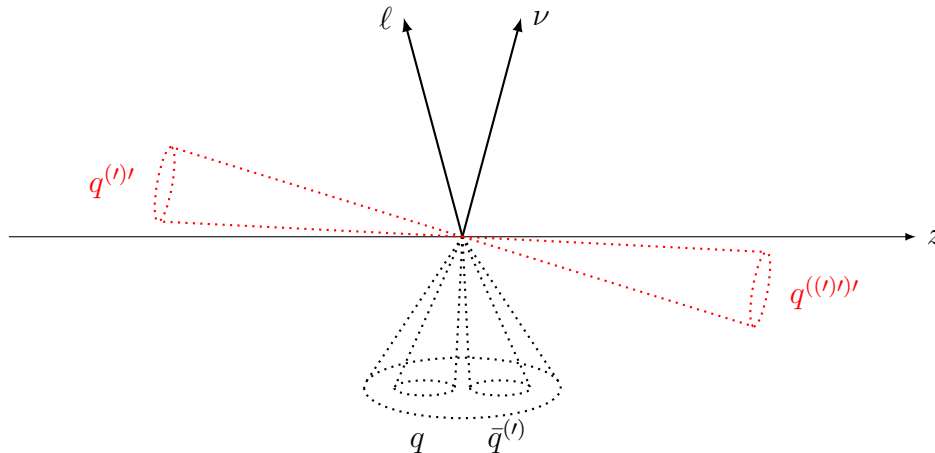
Figure 2.5: Illustration of event topology for collision events of interest in the CMS detector. The semi-leptonic final state produces a $W^{\pm}$ boson that decays via $W \to \ell\nu$ and produces the lepton-neutrino pair. Opposite to that is a single massive jet with two-pronged substructure that is produced via $V \to q\bar{q}^{(\prime)}$ or $H \to b\bar{b}$. Finally, the VBF production process results in two forward-facing jets, labeled by $q^{(\prime)\prime}$ and $q^{((\prime)\prime)\prime}$, which are colored red.

2.4   Conclusion

A brief overview of the Standard Model of particle physics is presented, with an outline of the mathematical details underlying the theory. We explore unsolved problems related to the SM and some Beyond Standard Model theories that potentially address these issues, with relevant models discussed to motivate the search for a heavy diboson resonance. The expected event structure for the decay of the bosonic resonance is described, which lays the foundation for the analysis strategy in chapter 4.

CHAPTER 3

Experimental Setup

3.1 Introduction

Accelerators have been at the heart of particle and nuclear physics since they first came online in the mid-20th century. Initial experiments that established the existence of familiar particles such as muons and pions utilized cosmic rays, and cosmic rays are still used today for various projects such as the IceCube Neutrino Observatory [70]. However, accelerator facilities offer numerous advantages over using cosmic rays. One is that the energies of the beams may be controlled by experimenters, which allows for studying the energy dependence of interactions. Another is that the projectile type in the beam may be chosen in order to select for certain interactions. Finally, the interactions take place at a specified location where detectors may be installed.

The center-of-mass energy[1] E_{CM} is a defining feature of an accelerator, as it is a measure of the energy available to produce particles in collision events [72]. There are two types of accelerators to consider in this respect: fixed-target and colliders. A key distinction between them is how they differ in their center-of-mass energies based on the parameters of the accelerator. Fixed-target accelerators involve a single beam that is directed to a stationary target in the lab frame, with a center-of-mass energy given by

$$E_{\mathrm{CM}} = \sqrt{m_b^2 c^4 + m_t^2 c^4 + 2 m_t c^2 E_L},\tag{3.1}$$

---

[1]Sometimes instead written in terms of the Mandelstam variable s as $\sqrt{s} = E_{\mathrm{CM}}$ [71].

where m_b is the mass of the particles in the beam, m_t is the mass of the particles in the stationary target, and E_L is the energy of the beam as measured in the lab frame. While the beam energy can be calibrated, this form of $E_{\rm CM}$ goes as $\sqrt{E_L}$ for high beam energies.

On the other hand, colliders involve two beams of particles that are directed to cross into each other and collide at a fixed position where the detectors are located. In this case, given two beams with energies $E_{L,1}$ and $E_{L,2}$ as measured in the lab frame, the center-of-mass energy is simply

$$E_{\rm CM} = E_{L,1} + E_{L,2}, \tag{3.2}$$

and if $E_{L,1} = E_{L,2} = E_L$, this reduces to $E_{\rm CM} = 2E_L$. Thus, colliders have the advantage that they depend linearly on beam energy and therefore have higher gains in $E_{\rm CM}$ compared to fixed-target accelerators.

There are also two different types of accelerator geometries: linear and circular. Linear accelerators have charged particles pass in a straight line through a series of metal pipes known as drift tubes, with the tubes connected to a radio frequency oscillator that generates the accelerating electric field in the tubes. While linear accelerators operate on simpler design principles compared to circular accelerators, they have to be very long in order to reach high center-of-mass energies. On the other hand, circular colliders accelerate particles along a circular trajectory using electromagnets, which allows for continuously accelerating particles along the beamline to achieve similar collision energies despite being smaller than linear accelerators. However, circular accelerators are more difficult to operate because of the need to maintain the circular orbit of the particles. They are also limited by the amount of power needed to compensate for the energy losses of the particles due to synchrotron radiation.

Another consideration is the type of particle used in collisions, as accelerators may be made to collide either leptons or hadrons. Leptonic colliders make use of electrons or positrons, while hadronic colliders use protons, antiprotons, or even ions. Because collisions

in leptonic colliders only involve electroweak interactions in the initial state, there are no sources of QCD background and the resulting final states are relatively clean and easier to analyze. Leptonic collisions also allow for more precise measurements because the initial state and collision energy of the particles is well-defined, while hadron colliders require sophisticated techniques to reconstruct the initial state due to the fact that hadrons are composite. However, hadronic collisions involve both electroweak and QCD interactions in the initial state because of the quark content of the hadrons, and this allows for more production methods of exotic particles, and hence more final states. Furthermore, because the collision energy of constituent quarks varies, this allows for a wide range of collision energies, making hadronic colliders well-suited for discovering new particles. Hadronic colliders are also more ideal for circular accelerators due to the fact that protons, antiprotons, and ions do not lose as much energy to synchrotron radiation compared to electrons and positrons.

A key parameter of an accelerator is the luminosity $\mathcal{L}$. Given a cross section σ for a process, and a rate at which events occur R, the luminosity is the constant of proportionality such that

$$R = \mathcal{L}\sigma, \tag{3.3}$$

where $\mathcal{L}$ has units of $\mathrm{cm}^{-2}\mathrm{s}^{-1}$. In some cases it is useful to instead consider the time integral of the luminosity $\mathcal{L}_{\mathrm{int}}$, which is given by

$$\mathcal{L}_{\mathrm{int}} = \int \mathcal{L}\,\mathrm{d}t\,. \tag{3.4}$$

This can then be used with equation 3.3 to obtain the number of collision events N_{event} for a process:

$$N_{\mathrm{event}} = \mathcal{L}_{\mathrm{int}}\sigma. \tag{3.5}$$

Thus, by increasing the luminosity (and hence the integrated luminosity), we may increase the number of expected collision events of interest for a given process. The luminosity may also be expressed in terms of parameters relevant to the beam, as it is essentially an

instantaneous measure of particle flux. For example, given the number of particles per bunch for two Gaussian beams N_1 and N_2, revolution frequency f, and number of bunches N_b, the luminosity is

$$\mathcal{L} = f \frac{N_1 N_2 N_b}{4\pi \sigma_x \sigma_y}, \tag{3.6}$$

where σ_x and σ_y are the standard deviations in the x and y directions for the beam distributions [73].

The search for new physics has driven advances in accelerator center-of-mass energies and luminosities that allow for discovering exotic collision events. Figure 3.1 shows the constituent center-of-mass energies for various accelerator facilities as a function of the year in which they came online. These advances have resulted in the discovery of massive particles that the first accelerators in the 1960's were not capable of producing, such as the $W^{\pm}$ and Z bosons, and the top quark. Even following the success of the Higgs boson discovery in 2012 and the ongoing search for new particles at the LHC, there are still upgrades being installed on the LHC to increase its luminosity, and there are proposals for new accelerator facilities with higher center-of-mass energies [74].

This chapter explores the main features of the Large Hadron Collider facility at CERN in section 3.2, where the collision events used in the search were obtained. A complete documentation of the LHC machine can be found in reference [76]. We then turn our attention to the Compact Muon Solenoid detector in section 3.3 and briefly go over the main components of the device, which was used to record the collision events at the LHC. This overview is based on documents concerning CMS in references [77, 78].

3.2 The Large Hadron Collider

The Large Hadron Collider is a circular collider accelerator facility with two superconducting rings that are capable of accelerating protons or heavy ions to relativistic speeds, and it is located just outside of Geneva on the French-Swiss border. It is the largest and most powerful

Figure 3.1: Plot of the constituent center-of-mass energies for hadronic and e^+e^- colliders since 1960 [75]. The discoveries of massive particles such as the $W^\pm$ and Z bosons and the top quark were made possible thanks to advances in accelerator technology that allowed for higher center-of-mass energies and luminosities.
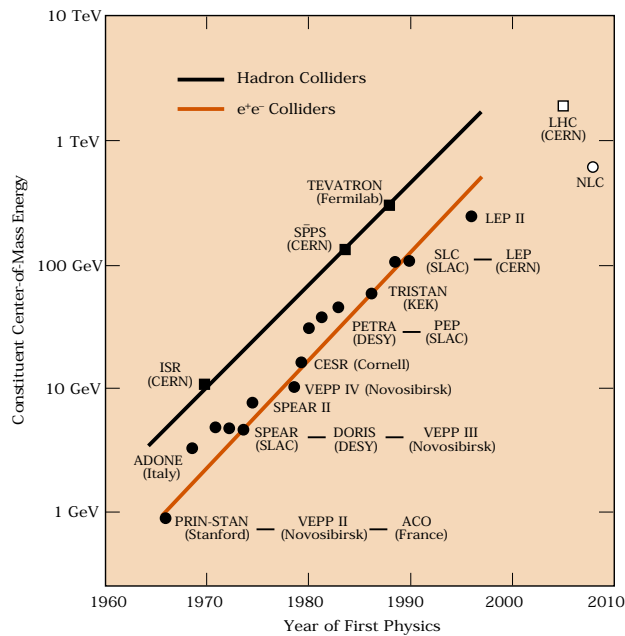
collider in the world, with plans to extend its service life into the 2030's and 2040's. It has a circumference of 26.7 km and was built into an existing tunnel that was used for the Large Electron-Positron (LEP) collider, which was used from 1989 to 2000. Four main detectors are used to study collision events and are placed along the beamline, consisting of the ALICE, ATLAS, CMS, and LHCb experiments. Figure 3.2 shows the complete CERN accelerator complex with all of its components. The ATLAS and CMS facilities are general-purpose detectors designed for a large physics program, which includes studying the Higgs boson and searching new physics arising from proton collisions, while ALICE is optimized for studying heavy-ion collisions with stripped lead ions (e.g., $^{208}\text{Pb}^{82+}$) to investigate the properties of quark-gluon plasma, and LHCb is designed to study the physics of bottom quarks and CP violation in b-hadron interactions.

The LHC beam is fed through a multi-stage process in which protons are stripped from hydrogen atoms and are first accelerated through a series of preaccelerators before being injected into the LHC beam. Protons start at the Linac2 facility, where they are initially accelerated to 50 MeV before being transferred to the Proton Synchrotron Booster (PSB), where they reach 1.4 GeV. They are then sent to the Proton Synchrotron (PS) and reach energies of 25 GeV, after which they are accelerated further to 450 GeV at the Super Proton Synchrotron (SPS). The protons then reach the LHC where they are accelerated to 6.5 TeV each. The process is similar for lead ions, where they instead start at Linac3 with 4.2 MeV/n, then move through the Low Energy Ion Ring (LEIR) before being transferred to the PS, then the SPS, and then injected into the LHC.

While the LHC was built with the intent of achieving center-of-mass energies of $\sqrt{s} = 14$ TeV in proton collisions, the data collected for this work was recorded over a period in which the center-of-mass energy was $\sqrt{s} = 13$ TeV. It also has a specific expression for the luminosity given by

$$\mathcal{L}_{\text{LHC}} = \frac{N_b^2 n_b f_{\text{rev}} \gamma_r}{4\pi \epsilon_n \beta^*} F, \tag{3.7}$$

where N_b is the number of particles per bunch, n_b is the number of bunches per beam, f_{rev}
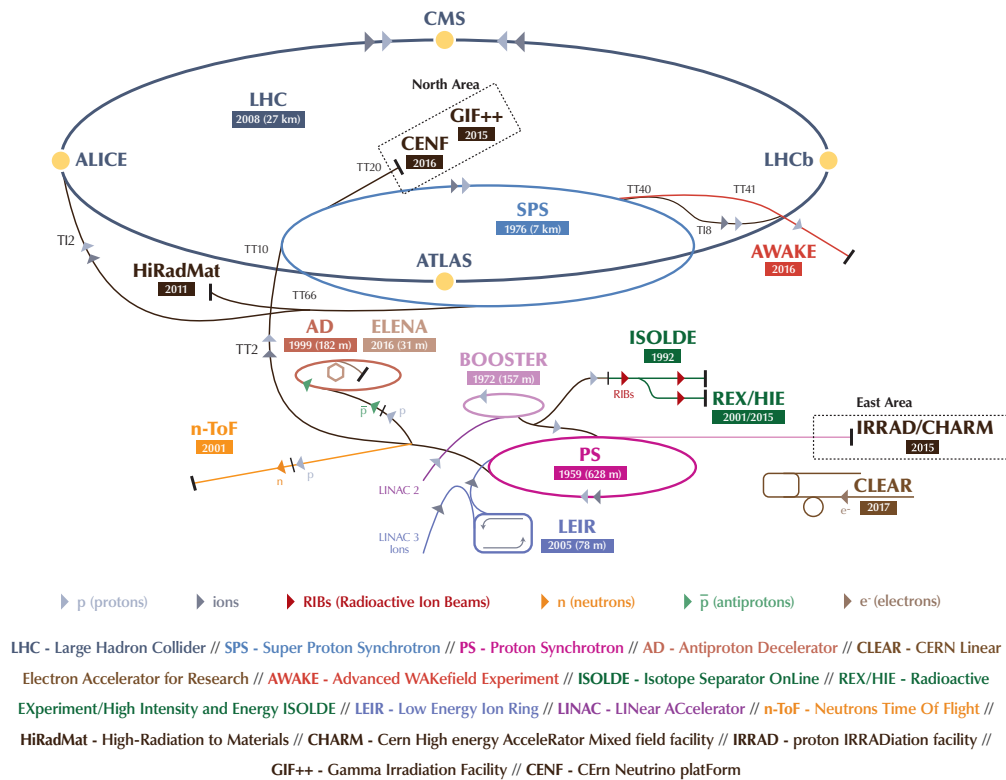
Figure 3.2: Layout of the CERN accelerator complex [79]. The LHC is one of several accelerators present at the facility, with multiple detectors along the beamline such as ATLAS, CMS, ALICE, and LHCb.

is the revolution frequency, γ_r is the Lorentz factor, ϵ_n is the normalized transverse beam emittance, β^* is the beta function at the collision point, and F is the geometric luminosity reduction factor. The LHC is designed to reach a luminosity of 10^{34} cm^{-2}s^{-1}, but surpassed this value in June 2016 [80]. Figure 3.3 shows the integrated luminosities as a function of time delivered to the CMS detector during Run 2, which ran during the years 2015-2018. Both ATLAS and CMS are the main high luminosity experiments, with integrated luminosities of 41.0 fb^{-1}, 49.8 fb^{-1}, and 67.9 fb^{-1} delivered[2] to CMS over the Run 2 years of 2016, 2017, and 2018 respectively. This corresponds to a total integrated luminosity of 158.7 fb^{-1} at CMS over Run 2.
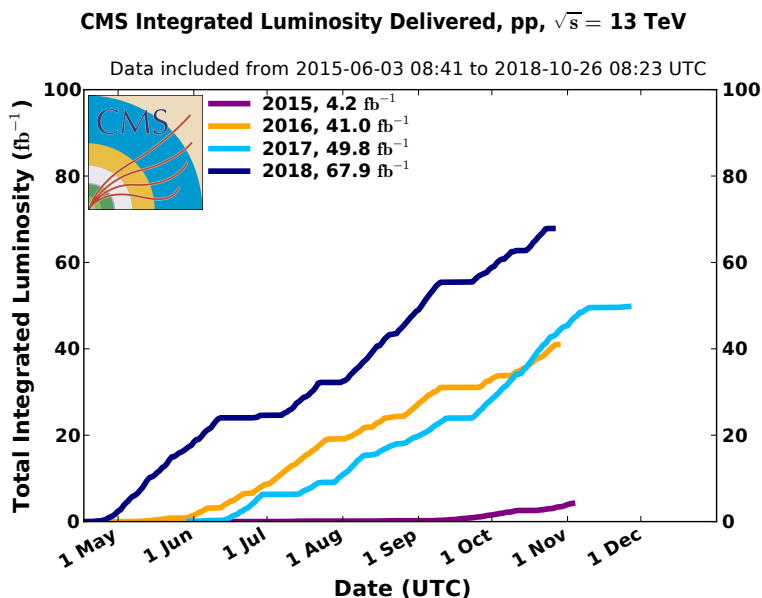
Figure 3.3: Integrated luminosities delivered to CMS as a function of time for the years 2015-2018 [81]. This corresponds to a total integrated luminosity of 158.7 fb^{-1} delivered to CMS during the Run 2 years of 2016-2018.

---

[2]These numbers differ from the *recorded* values obtained from CMS that are used in the analysis for chapter 4.

3.3 The Compact Muon Solenoid

The Compact Muon Solenoid is one of the main general-purpose detectors at the LHC, and it along with ATLAS independently discovered of the Higgs boson in 2012 [29,30]. The CMS detector is located 100 meters underground on the French side of the border near the village of Cessy. It is a cylindrical apparatus with a solenoidal magnet that is coaxial with the beamline of the LHC, with the entire CMS detector having a 14.6 m diameter and a length of 21.6 m, and it is composed of several subdetector systems. The coordinate system used by CMS is defined such that z-axis is lies along the LHC beam, with the y-axis pointing vertically upward and the x-axis pointing radially inward. This leads to the azimuthal angle ϕ being measured from the x-axis in the x-y plane, with the radial coordinate denoted by r. The polar angle θ is defined with respect to the z-axis, but in practice one typically uses pseudorapidity defined by $\eta = -\ln\tan(\theta/2)$.

One of its primary functions is to accurately identify the charge and momentum of muons emerging from collision events as their trajectories are bent through the magnetic field. Muons are ideal for reconstructing collisions due to their relatively long lifetime ($\tau_\mu = 2.2$ μs), large mass ($m_\mu = 105.7$ MeV/c^2), and low radiation losses when propagating through matter [82]. This makes muons the most penetrative and easily identifiable charged particles that can be found in collision events. In addition to identifying muons, the CMS detector also has other subdetectors for identifying electrons, photons, and hadrons. These detection systems are designed in order to meet the demands that come with the LHC's high luminosity, as there are more than 50 proton interactions every 25 ns, which results in around 1,000 particles emerging for each bunch crossing. A cut-away diagram of the detector with various components labeled may be seen in figure 3.4.

The silicon tracker is used to measure the initial trajectories of charged particles emerging from collisions. The electromagnetic calorimeter (ECAL) is encased by the hadronic calorimeter (HCAL), which detects hadron jets and neutrinos or exotic particles through

missing transverse momentum. Both calorimeters are surrounded by the muon detection chambers embedded within the return yoke that are used to identify muon charges and momenta. Finally, the Cherenkov-based forward calorimeter has both an electromagnetic and hadronic section, lying just outside of the endcaps for the muon chambers.

CMS DETECTOR

Total weight : 14,000 tonnes
Overall diameter : 15.0 m
Overall length : 28.7 m
Magnetic field : 3.8 T

STEEL RETURN YOKE
12,500 tonnes

SILICON TRACKERS
Pixel (100x150 μm²) ~1.9 m² ~124M channels
Microstrips (80–180 μm) ~200 m² ~9.6M channels

SUPERCONDUCTING SOLENOID
Niobium titanium coil carrying ~18,000 A

MUON CHAMBERS
Barrel: 250 Drift Tube, 480 Resistive Plate Chambers
Endcaps: 540 Cathode Strip, 576 Resistive Plate Chambers

PRESHOWER
Silicon strips ~16 m² ~137,000 channels

FORWARD CALORIMETER
Steel + Quartz fibres ~2,000 Channels

CRYSTAL ELECTROMAGNETIC CALORIMETER (ECAL)
~76,000 scintillating PbWO₄ crystals

HADRON CALORIMETER (HCAL)
Brass + Plastic scintillator ~7,000 channels

Figure 3.4: Cut-away diagram of the CMS detector with components labeled as configured in 2018 for Run 2 [83]. The detector and its components are coaxial with the LHC beam and give wide geometric coverage over the interaction point where the collisions are produced.

One of the central components of the detector is the superconducting solenoid, a 13 m long and 6 m inner diameter magnet that provides a 4 T magnetic field for bending charged particles while operating at a temperature of 4.45 K. The field generated by the solenoid has a nominal current of 19.14 kA, an inductance of 14.2 H, and a stored energy of 2.6 GJ. The solenoid is supplemented by a 12,500 t flux return yoke that pulls the magnetic field lines back into the muon chambers to allow for high resolution detection of muons produced

in collision events. There are five wheels and two endcaps that comprise this return yoke, with four layers of detection chambers in both the wheels and the endcaps.

3.3.1 Inner Tracking System

The inner tracking system measures the momenta of charged particles emerging from collisions and is used to reconstruct secondary vertices for events. One of the key aspects of the tracking system is the need to choose a design that results in minimal energy loss in charged particles passing through the detector, as this is needed to retain an accurate measurement of their trajectories. Additionally, in order to meet the demands that come with the severe radiation damage that occurs from the large particle flux, the need for efficient cooling, and the level of granularity necessary to measure the tracks of charged particles, the tracking system is based entirely on silicon detectors. The tracker is 5.8 m long and has a diameter of 2.5 m, surrounding the interaction point where collisions occur. It has a pixel detector with three barrel layers that span radii from 4.4 cm to 10.2 cm, as well as a silicon strip tracker with ten layers that extends to a radius of about 1.1 m. Both the pixel detector and silicon strip tracker have endcaps that allow for an acceptance of $|\eta| < 2.5$.

3.3.1.1 The Pixel Detector

The pixel detector allows for precise tracking and small impact parameter resolution, which is crucial for secondary vertex reconstruction. It covers a total area of around 1 m^2 and is comprised of 66 million pixels. The detector has very high efficiency in the barrel region, with losses in efficiency starting around $|\eta| > 2.1$. Each pixel cell occupies an area of 100×150 µm^2, which allows for high track resolution in the r-ϕ plane and in the z direction. Figure 3.5 shows an illustration of the pixel detector. As charged particles pass through a silicon pixel, they impart energy onto the electrons in the silicon atoms, which ejects the electrons and generates a current that goes into a readout chip attached to the pixel. Each pixel consumes

about 55 µW of power, which results in 3.6 kW of power for the entirety of the pixel detector. To avoid overheating from the power consumption, the pixels are mounted on cooling tubes, with 10 for the barrel and 4 for the two end disks.
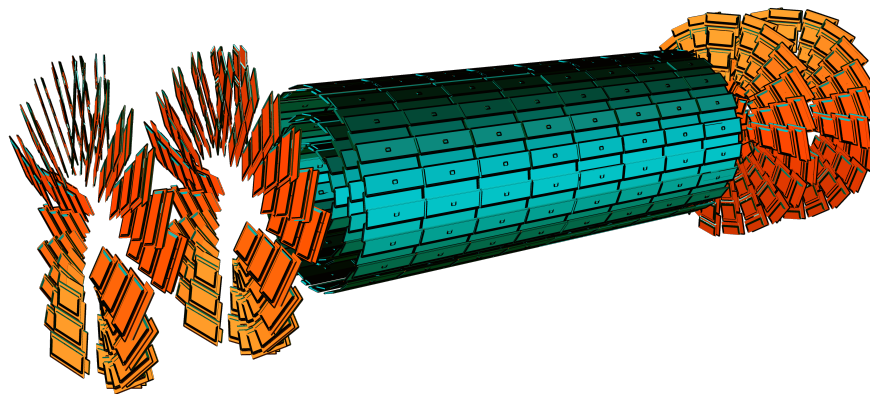
Figure 3.5: Illustration of the CMS pixel detector, with the barrel region colored in blue, and the endcap regions colored in orange [84]. A current is generated as charged particles pass through the pixel cells and eject electrons, which is read by a readout chip attached to each pixel.

3.3.1.2   The Silicon Strip Tracker

Once particles pass through the three layers of the pixel detector, they then go through the silicon strip tracker. The strip tracker has 15,148 detector modules in total, spread out among several layers, with each module containing 24,244 silicon sensors along with electronic readouts supported by a carbon fiber or graphite frame [85,86]. These strips consist of p-on-n type silicon sensors, which operate with reverse bias to minimize leakage current across the p-n junction. As charged particles pass through the sensors, electron-hole pairs are created along the particle's trajectory, which generates a drift current that is amplified and read as signal. Figure 3.6 shows the layout of the strip tracker. The Tracker Inner Barrel (TIB) has four inner barrel layers of silicon strips placed between radii of 255.0 mm and 498.0 mm, and has a length of 1.4 m along the LHC beamline centered at the interaction point. The TIB

is closed off by the Tracker Inner Disks (TID), with the two endcaps containing three disks each placed along the z axis between ± 800 mm and ± 900 mm from the interaction point. The Tracker Outer Barrel (TOB) consists of two double-sided layers of silicon strips just outside the TIB, followed by four single-sided layers, with the layers having radii between 608 mm and 1080 mm. The TOB is closed off by the Tracker End Caps (TEC) which extend radially from 220 mm to 1135 mm and from ± 1240 mm to ± 2800 mm along the beamline.

Figure 3.6: Layout of the CMS silicon strip tracker as seen in the r-z plane [87]. The Tracker Inner Barrel (TIB) has four inner barrel layers of silicon strips, which is closed off by the Tracker Inner Disks (TID) containing three disks in both of the endcaps. The Tracker Outer Barrel (TOB) has two double-sided layers of silicon strips outside of the TIB and is closed off by the Tracker End Caps (TEC).

3.3.2 Calorimeters

The CMS detector is equipped with various calorimeters that are designed to measure the energies of particles emerging from the collision events. Unlike the inner tracking system, the calorimeters are designed to abruptly halt any particles passing through them and record the energies of the stopped particles. The electromagnetic calorimeter (ECAL) and preshower

detector lie just outside of the silicon tracker and are designed to detect photons and electrons. These are both encased by the hadron calorimeter (HCAL), which is used to measure hadron jets. Because of the good hermiticity of the HCAL, it is also capable of measuring missing transverse momentum resulting from neutrinos or exotic particles. Both the ECAL and HCAL are supplemented by the forward calorimeter, which is a Cherenkov-based detector that has electromagnetic and hadronic sections.

3.3.2.1 Electromagnetic Calorimeter

The ECAL consists of 61,200 lead tungstate ($PbWO_4$) crystal scintillators in the barrel region covering the pesudorapidity range $|\eta| < 1.479$, with an additional 7,324 crystals in each of the two endcaps to close off the calorimeter. Figure 3.7 shows an illustration of a module of the ECAL in the barrel region. Scintillators are materials that emit light after absorbing ionizing radiation, which are attached to a photodetector and generate a current via the photoelectric effect. These crystals were selected due to their density (8.28 g/cm^3), radiation length (0.89 cm), and Molière radius (2.2 cm), all of which allow for high resolution measurement of electron and photon energies while withstanding the harsh radiation levels of the LHC. The photodetectors attached to the scintillators are also specially designed to operate in the 4 T magnetic field generated by the solenoid. Additionally, around 80% of the light from the scintillation effect is emitted in the LHC bunch crossing time of 25 ns, which reduces the energy contributions from previous or later collision events. The crystals measure 22×22 mm^2 at the front face and 26×26 mm^2 at the rear face, corresponding to 0.0174×0.0174 in the η-ϕ plane, and have a length of 230 mm.

The ECAL also encloses a preshower detector that is designed to screen out neutral pions, as they can decay into two closely-spaced high-energy photons. It also helps with identifying electrons against minimum ionizing particles and improves the position resolution for electrons and photons. The preshower operates in the region $1.653 < |\eta| < 2.6$, and is closed off by two endcaps. It is made of two layers, with lead radiators that generate
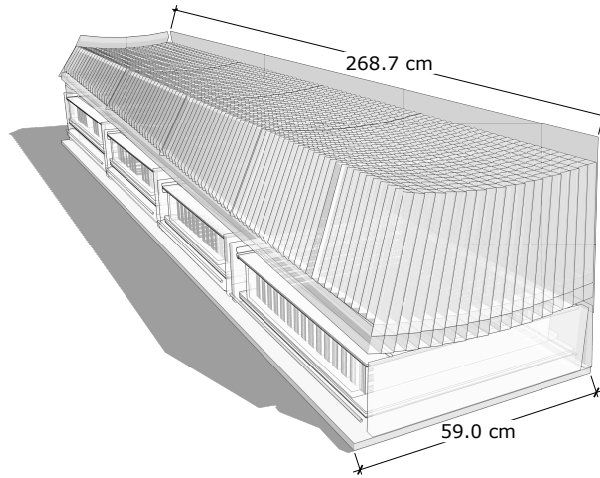
Figure 3.7: Illustration of a module of the CMS ECAL in the barrel showing the layout of the lead tungstate scintillators [88]. The scintillators emit light after absorbing ionizing radiation, each of which are attached to photodetectors and generate a current from the scintillation light.

electromagnetic showers when penetrated by incoming photons and electrons, and silicon strip sensors placed after each radiator to measure the deposited energies from the showers. The detector strips are much finer than that of the ECAL crystals and are 2 mm wide, which allows for distinguishing individual photons from pion decays.

3.3.2.2 Hadron Calorimeter

Outside of the ECAL lies the various layers of the HCAL, which is divided into four sections. Figure 3.8 shows the layout of the HCAL. The first of these is the barrel (HB), which covers the pseudorapidity range $|\eta| < 1.3$. The HB has 36 azimuthal wedges that are constructed out of brass absorber plates bolted together in a staggered geometry. Between the layers of brass are tiles of plastic scintillators that cover an area of 0.087×0.087 in the η-ϕ plane. To maximize the coverage of the HCAL and obtain an accurate reading of the deposited energies, the wedges are bolted together so as to allow for no more of a gap than 2 mm between the

wedges. The endcaps (HE) cover the HB section and extend over the pseudorapidity range $1.3 < |\eta| < 3$. Scintillators in this region have a granularity of $\Delta\eta \times \Delta\phi = 0.087 \times 0.087$ in the region $|\eta| < 1.6$, and $\Delta\eta \times \Delta\phi \approx 0.017 \times 0.017$ for $|\eta| \geq 1.6$. The outer calorimeter (HO) sits just outside of the vacuum tank of the solenoid, divided into five rings aligned along the axis of the LHC beam. The central ring of the HO has two layers of scintillators at radii of 3.82 m and 4.07 m, while the other rings only have a single scintillator layer at 4.07 m. Finally, the forward calorimeter (HF) consists of two detectors that are 11.2 m away from the interaction point on both sides of CMS. The HF faces the unique challenge of dealing with intense radiation, as most of the energy from the collisions is directed into the forward regions of the detector. For this reason, quartz fibers were used as the scintillation material, and the signal is generated when charged shower particles above the Cherenkov threshold generate Cherenkov light.
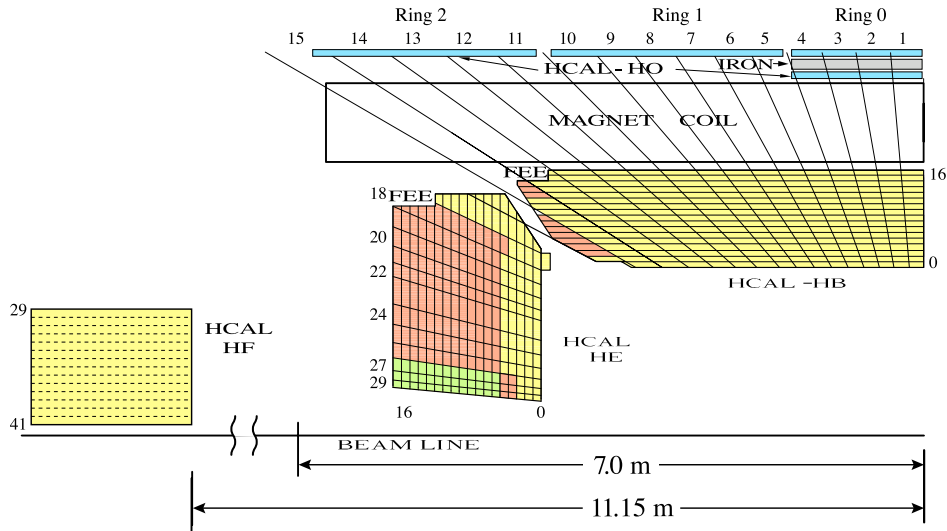
Figure 3.8: Layout of the HCAL in the r-z plane [89]. The HCAL surrounds the ECAL and has four sections denoted by the barrel (HB), endcaps (HE), outer calorimeter (HO), and forward calorimeter (HF). The scintillation material in the HB, HE, and HO sections is made of plastic, while the HF section uses quartz fibers in order to withstand the intense radiation in the forward region of the detector.

3.3.3 Muon Tracking System

The muon system is of central importance to the CMS detector. From its inception as a detector, it was recognized that muons would be one of the primary tools for reconstructing collision events. One reason for this is the fact that final states with muons present offer some of the best results for mass resolution, thereby increasing the discovery potential for new physics. This was one of the considerations taken into account when designing the CMS detector to optimize for the observation of the Higgs boson before it was discovered. The so-called $H \rightarrow ZZ^{(*)} \rightarrow 4\ell$ "golden channel" has the cleanest signal when all four of the leptons in the final state are muons [90]. Moreover, muons are expected to be produced in many decay events for exotic particles from BSM theories. As such, the muon system is designed to provide robust and accurate muon identification, momentum measurement, and triggering for events. This is achieved thanks to the combination of the strong solenoidal magnetic field and the flux return yoke. The return yoke allows for pulling the magnetic field lines from the solenoid to the outer region where the muon detection chambers are located, and it also screens out hadrons by absorbing them. The detection hits in the layers of the muon chambers then allow for reconstructing the charge and momentum of the muons.

There are three kinds of gaseous detection chambers that are used to identify and measure muons: drift tubes (DTs), cathode strip chambers (CSCs), and resistive plate chambers (RPCs). The outer region of CMS has 250 DTs in the barrel region covering pseudorapidities of $|\eta| < 1.2$, while the endcaps on both ends of CMS have 540 CSCs covering the region $0.9 < |\eta| < 2.4$. The RPCs are distributed throughout both regions of CMS, with 480 in the barrel and 576 in the endcaps. In total, there are 1,846 muon chambers present on the detector, with the chambers distributed among four layers in both the barrel and endcap regions to allow for track reconstruction. The barrel region is split up into five concentric wheels that are numbered from -2 to $+2$, with wheel 0 centered at the interaction point. Figure 3.9 shows a cross section of the CMS detector in the r-z plane as configured during Run 2, with DTs, CSCs, and RPCs labeled.
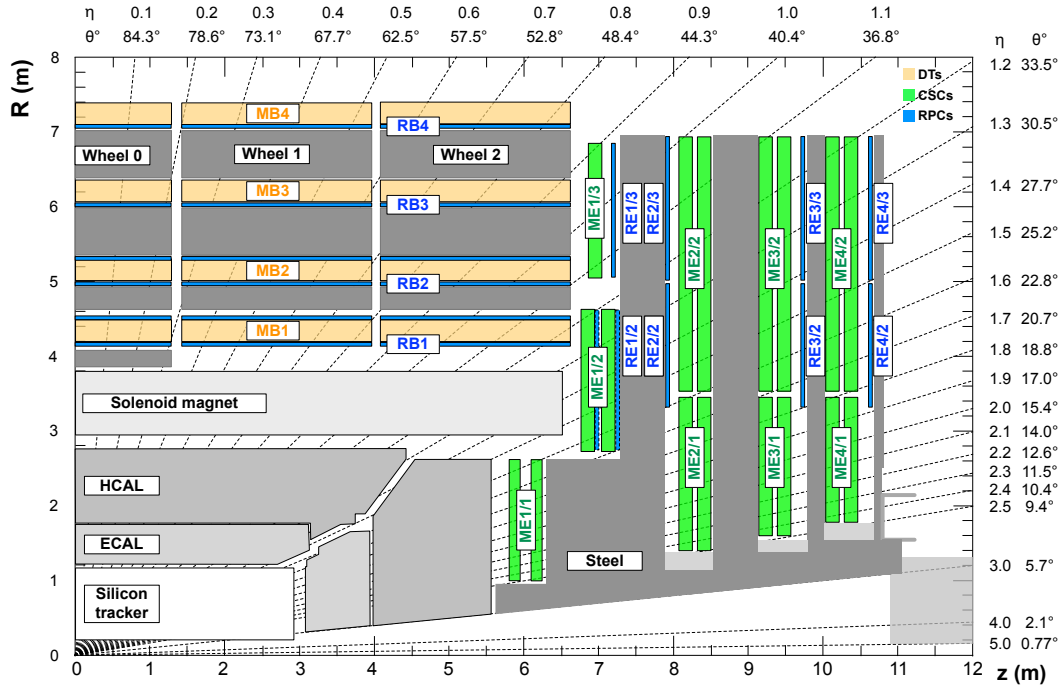
Figure 3.9: Cross section of the CMS detector in the *r*-*z* plane as configured during Run 2 [91]. The barrel region contains a combination of drift tubes and resistive plate chambers distributed among five concentric wheels surrounding the detector, covering a pseudorapidity range of $|\eta| < 1.2$. The endcaps on either side cover the range $0.9 < |\eta| < 2.4$, and have combinations of cathode strip chambers and resistive plate chambers present. There are 250 drift tubes and 480 resistive plate chambers in the barrel, and 540 cathode strip chambers and 576 resistive plate chambers in the endcaps, making a total of 1,846 muon chambers distributed throughout CMS. Both the barrel and endcaps have four layers of muon chambers to allow for track reconstruction.

3.3.3.1 Drift Tubes

The DT system in the barrel region is distributed among the four layers present in each wheel surrounding the interaction point, with the layers referred to as stations. The stations are numbered according to how close they are to the interaction point, with station 1 being the innermost layer and station 4 being the outermost. Each drift tube contains a gaseous mix of Ar (85%) and CO_2 (15%), with sensitive wires inside of the tubes held at a specified potential. An illustration of an individual drift tube cell can be seen in figure 3.10. As muons pass through the gas, they impart enough ionization energy to knock off electrons from the atoms of the argon gas, which are then attracted to the wire and cause a cascade of additional electrons from the gas to be deposited onto the wire and generate a current. Meanwhile, the carbon dioxide acts as a quenching gas by absorbing photons that are released from de-exciting electrons in the argon atoms, thereby preventing any further cascades resulting from the release of electrons by the emitted photons. The muon's position can then be inferred from where the electrons hit the wire, and how far the muon was from the wire. Additionally, the muon track and momentum can be reconstructed by using multiple detection hits from different stations in the barrel. Each DT allows for a position resolution of 0.25 mm.

3.3.3.2 Cathode Strip Chambers

The CSCs in the endcaps operate under a similar principle to that of the DTs in the barrel region. They are made of trapezoidal panels and have a gas mix of Ar (40%), CO_2 (50%), and CF_4 (10%). Figure 3.11 shows a cut-away diagram of a CSC chamber. Inside of the CSCs are arrays of positively-charged anode wires and negatively-charged cathode copper strips that are perpendicular to each other. When muons ionize the gas after passing through the chamber, they cause an avalanche of electrons to deposit onto the wire and generate a current, but they also cause an induced charge on the copper strips. This allows for a precise measurement of ϕ for the passing muons and a coarse measurement of r from the anode wires,
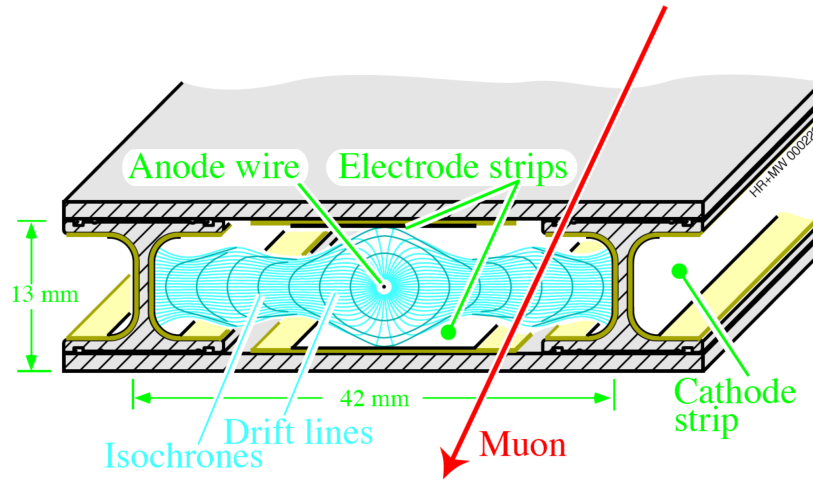
Figure 3.10: Illustration of a drift tube cell [92]. As muons pass through the cell, they ionize the gas and cause a cascade of electrons that deposit onto the anode wire and generate a current. The current is readout by the detector and allows for measuring muon momentum.

resulting in a 0.2 mm resolution position measurement, as well as a fast time measurement.

3.3.3.3   Resistive Plate Chambers

RPCs are used to supplement the DTs in the barrel and the CSCs in the endcaps. They are gaseous detectors that consist of two parallel plastic plates with high resistivity, one being a positively-charged anode and the other a negatively-charged cathode. Figure 3.12 shows an example of a double gap RPC design. The gaseous mix in the RPCs is $C_2H_2F_4$ (95.2%), isoC$_4$H$_{10}$ (4.5%), and SF_6 (0.3%). The electron cascade caused by the ionization of a passing muon generates a signal on external detecting strips, which allows for a coarse spatial measurement, but a very fast time measurement (1 ns) that is shorter than the 25 ns between each bunch crossing. Their fast response time is used in the trigger system in order to determine whether or not event data should be saved based on the measured muon momentum.

46
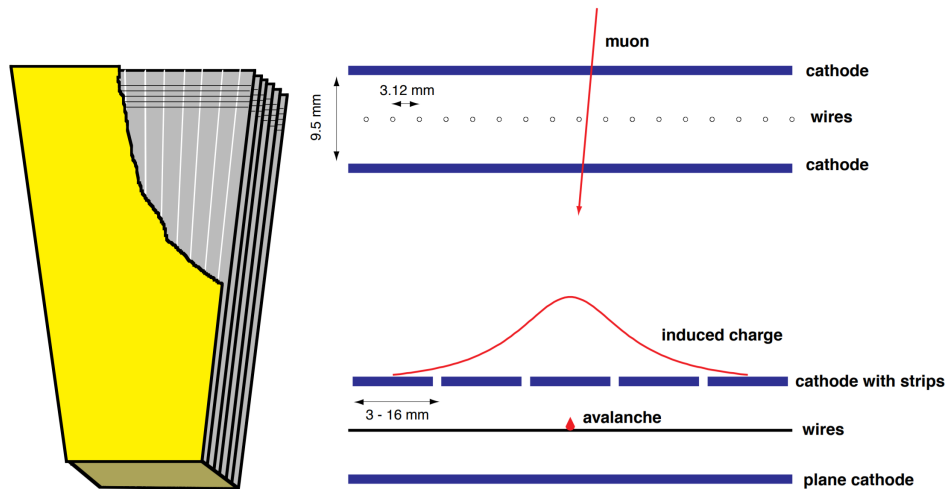
Figure 3.11: Cut-away diagram of a CSC (left) with an illustration of the ionization mechanism (right) [93]. As muons ionize the gas, the resulting electron avalanche deposits onto the wires and generate a current, while also inducing a charge onto the cathode strips. This gives a measurement of the muon position for both ϕ and r.
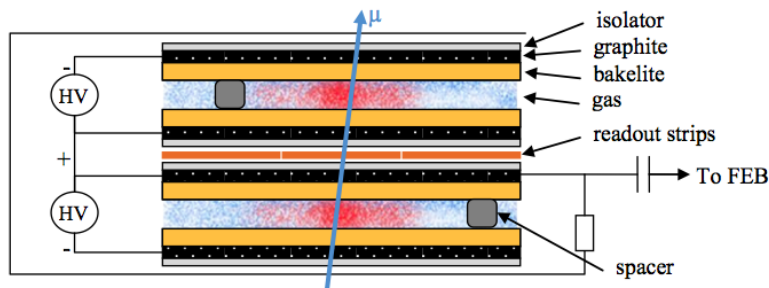
Figure 3.12: Illustration of a double gap RPC design [94]. The electron cascade generated by the ionization process induces a signal on the readout strips, which gives a coarse spatial measurement. DTs and CSCs are supplemented by RPCs that are used by the trigger system due to their fast response time.

3.3.4 Trigger System

One of the unique challenges facing detectors at the LHC is the large amount of collision events that occur at the interaction points. Proton collisions occur every 25 ns, corresponding to a rate of 40 MHz. With 50 simultaneous pp collisions for every bunch crossing, this corresponds to 2×10^9 interactions every second. It is not possible to meet the hardware demands for recording every single collision event, nor would it be prudent to do so since most events are soft collisions between protons that do not reveal any new physics. Furthermore, it would be too computationally expensive to reconstruct every collision event even if the previously mentioned limitations were not an issue. Thus, the trigger system is needed in order to select for high-energy events of interest, while also recording them at a reasonable rate that allows for long-term storage.

The trigger system has two levels, consisting of a Level-1 (L1) Trigger, and a High-Level Trigger (HLT) [95]. The L1 Trigger is hardware-based and is comprised of custom-designed processors, featuring large Field Programmable Gate Arrays (FPGAs) that use data from the calorimeters and muon system. The HLT is software-based and consists of a conventional CPU farm, which has access to a complete readout from the L1 Trigger and is able to perform more advanced calculations with the data. The trigger system as whole reduces the rate by a factor of 10^6, with the L1 Trigger designed to have an output rate of 100 kHz. In practice, the L1 Trigger is not operated at its maximum output and instead runs at 30 kHz as a safety measure, and the L1 trigger output is further reduced by the HLT to around 1 kHz.

3.3.4.1 Level-1 Trigger

The architecture of the L1 trigger can be seen in figure 3.13. At the local level, the L1 Trigger consists of Trigger Primitive Generators (TPGs) that are activated by track segments or hit patterns in muon chambers, and energy deposits in the calorimeters. The trigger primitives are then used by the Regional Triggers to form trigger objects for candidate particles, such

as electrons, photons, and muons. These objects have to be ranked and sorted based on their energy, momenta, and quality. The highest rank objects are then transferred to the Global Trigger and are evaluated to determine whether or not they will be passed onto the HLT. This is determined by the Trigger Control System (TCS), which will then pass a Level-1 Accept (L1A) decision back to the Global Trigger. The allowed latency between the a single bunch crossing and the L1A decision in the L1 Trigger is 3.2 µs, which requires the entire process to be pipelined so that the L1 Trigger may operate continuously.
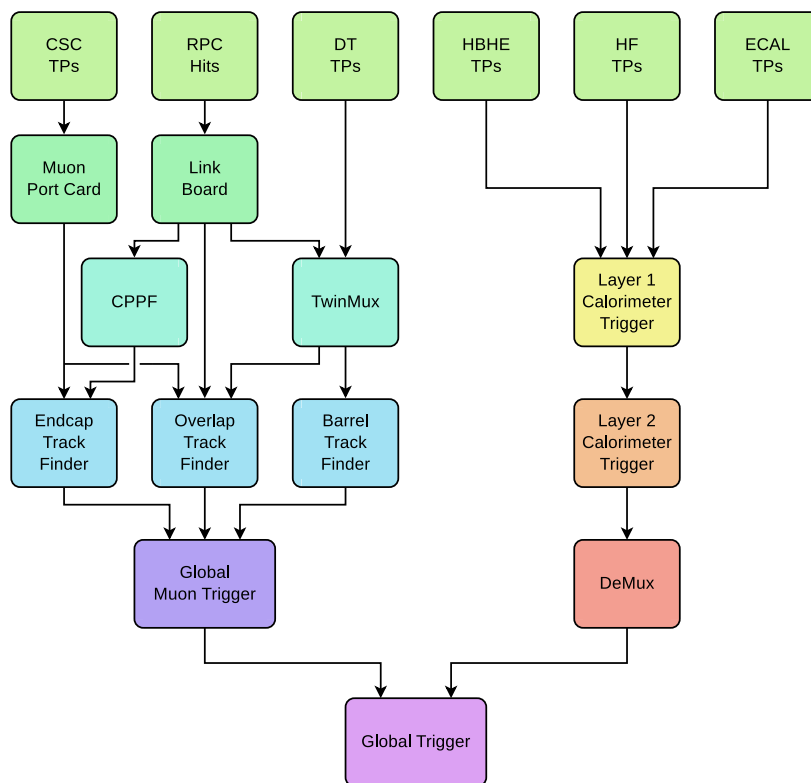
Figure 3.13: Illustration of the L1 Trigger architecture as configured during Run 2 [96]. The Trigger Primitives (TPs) are generated by track segments or hit patterns in muon chambers, and energy deposits in calorimeters. These objects are ranked and sorted by energy, momenta, and quality, which are then passed onto the Global Trigger to determine whether or not the events will be kept and passed to the HLT.

3.3.4.2 High Level Trigger

After receiving the L1A signal, the complete readout data from the rest of the detector is sent to the HLT to be further analyzed. The HLT is entirely software-based, and it is run on a farm of commercial computers, using various algorithms to reconstruct the full event and performs tasks such as matching tracks from the inner tracker to muon detection hits in the chambers, or identifying high-energy photons. Since the HLT is software, the algorithms used to reconstruct the events have changed over the operational history of the CMS detector [97]. The data is processed through the HLT in a modular manner using trigger paths, which are sequences of reconstruction and filtering blocks of increasing complexity that reconstruct physics objects and apply selection cuts to them. Faster algorithms run first in a path, and then the remaining products are filtered. After passing through the HLT, the events are then recorded for offline analysis, and the rate of recorded events after passing through the trigger system as a whole is cut down to be on the order of only a few 10^2 Hz. The recorded events are then passed onto the Data Acquisition (DAQ) system [98].

3.3.5 Event Reconstruction

Once the data for an event is processed through the HLT, the event reconstruction process uses the resulting objects from the HLT, such as energy clusters and tracks, to identify particles and jets. Event reconstruction at CMS is handled through the Particle-Flow (PF) algorithm [99, 100], which uses a combination of objects from each sub-detector system to identify candidate particles. In particular, the principal objects identified are electrons, muons, photons, charged hadrons, and neutral hadrons, along with their directions, energies, and types. These objects can then be used to reconstruct jets to determine quark and gluon energies, determine missing transverse momentum $p_\mathrm{T}^\mathrm{miss}$ resulting from neutrinos and other undetectable particles, reconstruct tau leptons from their decay products, and tag b jets.

Accurately reconstructing the constituents of an event is a challenging task due to the

fact that most stable particles that are produced in collisions tend to have low p_T. For example, in a quark or gluon jet with a p_T of 500 GeV, the average p_T carried by its stable constituent particles is on the order of 10 GeV, and for jets with a total p_T below 100 GeV this reduces to only a few GeV per stable constituent. In order to discriminate between jets that are produced by heavy exotic particles and those that originate from SM background processes, it is crucial to accurately reconstruct as many final stable particles in the event as possible, many of which will have low p_T and energy.

3.3.5.1 The Particle-Flow Algorithm

The basic elements of PF inputs are objects that come from the CMS sub-detectors: charged particle tracks from the inner tracker, energy clusters reconstructed in the ECAL and HCAL, and muon tracks from the muon chambers. These inputs can be grouped together into objects known as PF blocks through a link algorithm, which are topologically linked together to identify each particle while also avoiding double counting from different detectors. A block typically contains only one, two, or three of the aforementioned elements from the CMS sub-detectors. Once the blocks in the event are identified, the Particle-Flow algorithm receives them as input and begins reconstructing individual particles.

The PF algorithm proceeds in the following steps for each block:

1. Create PF muons from inner tracker tracks and muon stubs, then remove the corresponding tracks.

2. Create PF electrons from tracks and ECAL PF clusters if they pass identification criteria, then remove the corresponding tracks.

3. Tighter quality criteria on the transverse momenta are applied to the remaining tracks to remove fake tracks.

4. Energies of the remaining ECAL and HCAL PF clusters are calibrated and have the

expected energies of the muons from the corresponding clusters subtracted.

5. Links between ECAL/HCAL clusters and tracks are sorted and either kept or discarded in order to determine which clusters resulted from which tracks.

6. If the total calibrated calorimetric energy is smaller than the total track momentum by more than three standard deviations, a search for muons and fake tracks is performed with looser criteria.

7. The remaining tracks result in PF charged hadrons, with the momentum taken from the track momentum if it is not consistent with the calorimetric energy, or obtained from a fit of the measurements in the tracker and the calorimeters.

8. Neutral particles are identified if the total calibrated cluster energy is larger than the total associated track momentum, with PF photons being created if the calorimetric energy excess is larger than the total ECAL energy, and PF neutral hadrons being created with the remaining part of the excess calibrated ECAL and HCAL energies.

9. The remaining ECAL and HCAL clusters without links to tracks produce PF photons and PF neutral hadrons, respectively.

After the PF candidates are obtained, they are then used for various tasks in analyses, such as reconstructing jets and determining $p_\mathrm{T}^\mathrm{miss}$ for the event.

3.3.5.2   Jet Clustering

In hadronic collisions, the scattering of partons (the quarks and gluons that make up hadrons) gives rise to collimated showers of particles known as jets. These showers arise due to the fact that quarks and gluons do not exist in isolation long enough to be observed, as they immediately hadronize into other particles that have no QCD flavor charge. It is therefore not possible to directly observe the quarks and gluons that give rise to jets, and their presence

must instead be inferred from reconstructing jets and determining the total jet momentum. Once PF objects are identified, jets may be reconstructed by using a clustering algorithm that groups together particles from a candidate jet.

One of the most commonly used jet clustering algorithm is the anti-k_{T} algorithm. The algorithm reconstructs jets by introducing distances d_{ij} between objects i and j, and $d_{i,B}$ between object i and the beam B [101]. The algorithm starts by assigning values for d_{ij} and $d_{i,B}$ for all objects in the final state, and finds the minimum value among the distances. If the minimum value is a $d_{i,B}$ value, then object i is declared to be a jet and removed from the list, and the algorithm starts over from the first step. If instead it is a d_{ij} value, then objects i and j are combined and the algorithm goes back to the first step. This process is repeated until all particles have been declared jets, with d_{ij} and $d_{i,B}$ defined by

$$d_{ij} = \min\left(k_{\mathrm{T},i}^{2p}, k_{\mathrm{T},j}^{2p}\right)\frac{\Delta_{ij}^2}{R^2}, \tag{3.8}$$

$$d_{i,B} = k_{\mathrm{T},i}^{2p}, \tag{3.9}$$

where $\Delta_{ij}^2 = (y_i - y_j)^2 + (\phi_i - \phi_j)^2$, with $k_{T,i}$ as the transverse momentum for object i, y_i the rapidity for object i, ϕ_i the azimuthual angle for object i, R the distance parameter for the algorithm, and p a parameter determined by the jet clustering algorithm. For the anti-k_{T} algorithm, $p = -1$, with other algorithms taking on different values, such as $p = 1$ for the k_{T} algorithm [102].

3.4 Conclusion

The LHC facility and CMS detector are discussed, which were used to obtain the data for the search that this work describes in chapter 4, and which also concern the novel muon tracking algorithm covered in chapter 5. An overview of the subdetector systems of the CMS experiment is presented, which includes the inner tracking system, calorimeters, muon

tracking, and trigger system. We also present a brief description of the event reconstruction process, which outlines the main steps of the particle flow algorithm, as well as the anti-k_T algorithm for clustering jets.

CHAPTER 4

Search for a Heavy Diboson Resonance

4.1 Introduction

In chapter 2, we explored some of the motivation behind BSM searches and examples of BSM theories that predict exotic new particles that may be found in collision events at accelerator facilities. We also enumerated some of the benchmark models from BSM theories, which were the spin-0 Bulk Radion, spin-1 W' and Z' bosons, and the spin-2 Bulk Graviton. Additionally, we discussed the three production modes that this work focuses on (VBF, ggF, and DY), and the final state that is produced.

Previous searches have been conducted for dibosonic resonances at both CMS and AT-LAS, although none have found evidence of such a resonance being observed at the LHC [103–109]. Some of these searches also considered different production modes, as well as other intermediate and final states, such as a ZZ/ZH resonance with fully leptonic or hadronic final states. As mentioned in section 2.3, this analysis is itself a continuation of a previous search by the CMS collaboration for a dibosonic resonance using data from 2016 [62].

In subsection 2.3.2 we discussed the expected event structure for the decay events of interest, in which the leptonic decay of the $W^{\pm}$ boson results in an $e\nu$ or $\mu\nu$ pair with large missing transverse momentum from the neutrino, the hadronic decay of the V/H boson results in a single, large-radius jet with substructure, and VBF processes produce forward-facing jets. The boosted topology is a result of the fact that the resonances considered have masses in the TeV range, which causes the $W^{\pm}$ and V/H bosons to have transverse

momenta on the order of several hundred GeV. This requires the use of specialized techniques to identify and reconstruct the individual boosted $W^\pm$ and V/H bosons based on information from the reconstructed lepton, missing transverse momentum of the neutrino, two-pronged substructure of the jet, and in the case of H jets, substructure of the resulting $b\bar{b}$ jets, such as secondary vertices. Additionally, the signal models used for the analysis assume that the resonance width is narrow, meaning that the decay width of the resonance in the WV/WH diboson mass spectrum is smaller than the experimental resolution.

The sources of SM background for this analysis include W+jets, SM diboson, $t\bar{t}$, single-t processes. One aspect of the previous analysis that this work inherits is a novel signal extraction method, in which the SM background contributions are estimated from the data using a two-dimensional (2D) maximum likelihood fit. Taking the correlations between variables into account, this process is performed in the plane formed by the mass of the jet from the V/H decay m_{jet}, and the invariant mass of the WV/WH diboson system $m_{WV/WH}$. To perform the background modeling, we group the SM background sources into two classes of backgrounds. The first is a background class that is resonant in the m_{jet} spectrum denoted by $W+V/t$, and the second consists of contributions that are non-resonant in m_{jet} that are referred to as $W + \mathrm{jets}$. The $W + V/t$ background includes SM diboson events, while the $W+\mathrm{jets}$ class consists of W+jets events, with $t\bar{t}$ and single-t events being shared across both classes of background depending on whether or not they are resonant in the m_{jet} spectrum. Figure 4.1 shows example Feynman diagrams for each of these two classes of background. One advantage of using a 2D fit is the ability to retain more events for modeling background in the sideband regions within the 2D $m_{WV/WH}$-m_{jet} plane, as opposed to a 1D search for a resonance in the $m_{WV/WH}$ spectrum. This also allows for conducting a simultaneous search of WW, WZ, and WH resonances, as opposed to performing separate analyses in pre-defined m_{jet} windows.

For this chapter, we examine the complete analysis process of the search for a dibosonic resonance produced in proton collisions at the LHC with center-of-mass energies of $\sqrt{s} =$
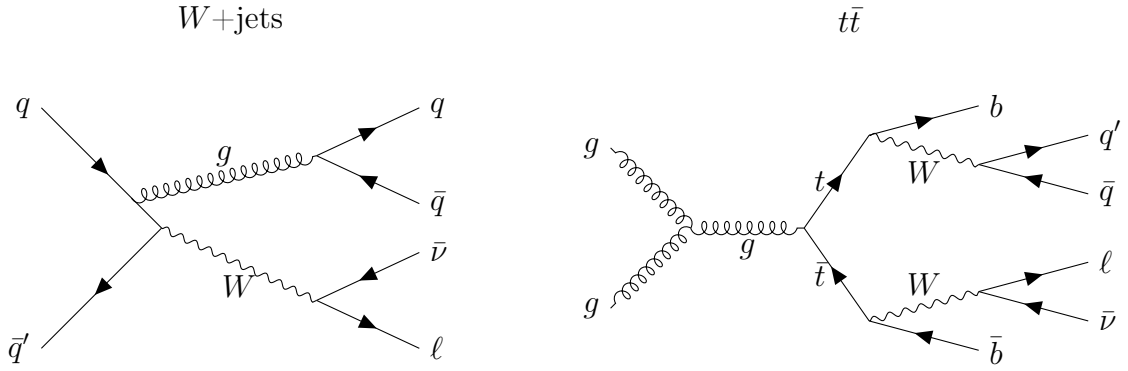
Figure 4.1: Example leading-order Feynman diagrams for the two classes of background considered for the search. Both cases produce a final state that is similar to the expected final state produced by the ggF, DY, and VBF processes for the benchmark signal models. The W+jets process (left) is a contribution from the non-resonant background class (denoted by $W+$jets), while the $t\bar{t}$ process (right) is grouped as part of the resonant background class (denoted by $W + V/t$).

13 TeV. The data used in this analysis were collected over Run 2 with integrated luminosities of 35.9 fb^{-1}, 41.5 fb^{-1}, and 59.7 fb^{-1} in 2016, 2017, and 2018, respectively. Section 4.2 provides an overview of the data and Monte Carlo (MC) simulation samples that were used for the analysis. In section 4.3, we discuss the selection cuts used to determine which events are used from the data and simulation samples, and we enumerate the event categories that are used in the analysis. For section 4.4, we check how well the variables used in our event selections and categorizations are modeled by comparing the data versus our MC samples in the control regions of the analysis. We then discuss the process of modeling the peak from the leptonically decaying $W^{\pm}$ using corrections to MC samples obtained from data in section 4.5. The two-dimensional signal extraction method is described in section 4.6, after which we go over the systematic uncertainties in section 4.7. Finally, the fit validation and bias testing procedures are described in section 4.8, which are followed by the results of the search in section 4.9.

4.2 Data and Simulation Samples

This search uses the proton collision data collected by the CMS detector during Run 2. The data are collected and stored for analysis after events generate trigger primitives in the detector subsystems and are selected by the L1 Trigger and HLT as described in chapter 3. We also list the MC signal samples used in the analysis that are based on the BSM models of subsection 2.3.1. Additionally, we list the MC samples that model SM background contributions to the search.

4.2.1 Data Samples

The data used for this work are based on three different sets over the three Run 2 years of 2016, 2017, and 2018. For each year of Run 2, documentation is available for the luminosity measurements [110–112]. The full dataset is divided into three sets per year, with contributions from the Single Muon, Single Electron, and MET[1] datasets. These sets are referred to as primary datasets, which are defined as a collection of events that have passed at least one of a set of HLT paths [113]. Such datasets may be overlapping in terms of which specific events are present, as they are constructed around grouping together events that have similar physics content in the final state of the event. For example, the Single Muon primary dataset contains events in which the HLT reconstructed a single muon originating from TPs that passed through the L1 trigger, as described in figure 3.13.

Data collected by CMS are certified by the Data Quality Management (DQM) group [114], which receives information from each subdetector group about the quality of data obtained over each data-taking period. The DQM then reviews the information from each subdetector group and certifies the data that is of sufficiently high quality, with relevant certification information released as golden data certificates.

---

[1]Here, MET denotes missing transverse energy ($E_\mathrm{T}^\mathrm{miss}$). However, this terminology is now deprecated and is instead replaced by missing transverse momentum ($p_\mathrm{T}^\mathrm{miss}$).

4.2.2 Simulated Samples

This analysis makes use of nine benchmark signal models to simulate the narrow resonances that are considered in the search. The models used are ggF/VBF $G_{\text{bulk}} \to WW \to \ell\nu q\bar{q}'$, ggF/VBF $\phi \to WW \to \ell\nu q\bar{q}'$, DY/VBF $W' \to WZ \to \ell\nu q\bar{q}$, DY $W' \to WH \to \ell\nu b\bar{b}$, and DY/VBF $Z' \to WW \to \ell\nu q\bar{q}'$. Additionally, we also use MC samples to simulate the background sources that this analysis takes into account as part of the search.

4.2.2.1 Signal Samples

The DY $W' \to WH$, DY $W' \to WZ$, and ggF $G_{\text{bulk}} \to WW$ samples are restricted to the semileptonic final state, while the other six samples also contain different final states that are not used in this analysis. Each signal has different samples with 50,000 events for each year of Run 2, for a total of three sets of samples per signal. Furthermore, each signal has separate samples with 50,000 events for the following resonance masses: 0.8, 1, 1.2, 1.4, 1.6, 1.8, 2.0, 2.5, 3.0, 3.5, 4.0, and 4.5 TeV. The 2016 VBF $Z' \to WW$ and 2016 VBF $W' \to WZ$ sets are the exception to this, lacking mass values below 1.2 TeV. Some samples also have masses that extend from 4.5 TeV to 8 TeV in increments of 0.5 TeV, though they are not used for this analysis. Figure 4.2 shows the cross sections multiplied by branching fractions for each benchmark signal model as a function of the resonance mass m_{X}. Each sample also has a resonance width that is set to 0.1% of the resonance mass to ensure that the narrow-width approximation is met. The samples for each benchmark signal were generated at leading-order (LO) in QCD with `MadGraph5_aMC@NLO` versions 2.2.2 and 2.4.2 [115].

The ggF/VBF $G_{\text{bulk}} \to WW$ model assumes a curvature of $\tilde{k} = 0.5$ to ensure that the natural width of the graviton is negligible with respect to the experimental resolution, and the cross sections for ggF $G_{\text{bulk}} \to WW$ are next-to-leading-order (NLO), while those of the VBF process are LO. For the ggF/VBF $\phi \to WW$ model, the samples are produced assuming $\Lambda_R = 3$ TeV and $k\pi r_c = 35$, with NLO cross sections used for the ggF process.

The VBF process does not have any theoretical cross sections available for the bulk scenario, but we use cross sections from a separate RS model.

The LO cross sections in the HVT model B are used for DY $Z' \to WW$, DY $W' \to WZ$, and DY $W' \to WH$, with coupling constants given by $g_V = 3$, $c_H = -0.98$, and $c_F = 1.02$. In this model, the resonances have large branching fractions to vector boson pairs, with fermionic couplings suppressed. Meanwhile, the VBF $Z' \to WW$ and DY $W' \to WZ$ samples use cross sections from the HVT model C, with $g_V \approx 1$, $c_H \approx 1$, and $c_F = 0$. For model C, the HVT resonances are only produced via VBF and decay to pairs of SM bosons because the fermionic couplings are zero.
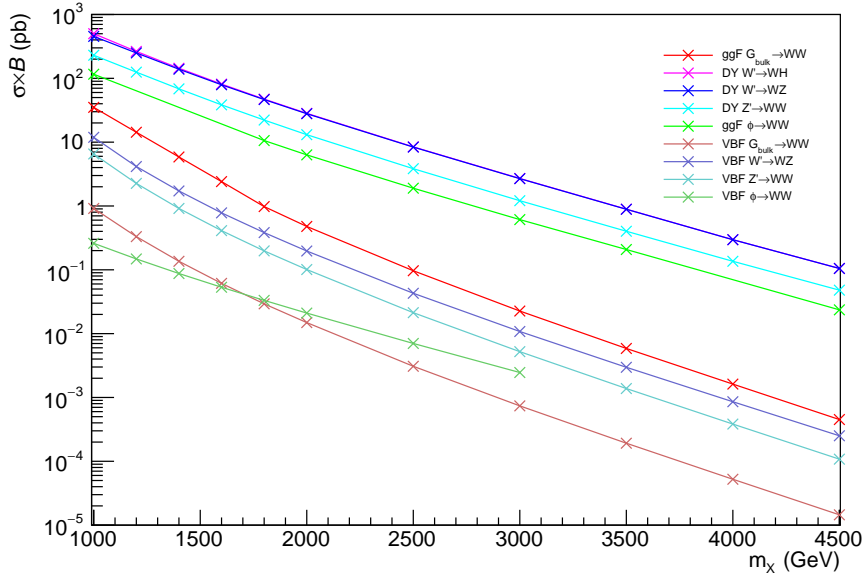
Figure 4.2: Cross sections multiplied by branching fractions for each of the benchmark signal MC samples as a function of the resonance mass m_X.

4.2.2.2   Background Samples

The MC samples used to simulate SM background contributions listed in table 4.1 along with their cross sections where available. These include the previously mentioned background

Category	Total cross section [pb]
W + jets	
DY +jets	
SM diboson	49.997
	43.53
	10.71
	3.28
$b\bar{b}$	0.1585
	0.1005
	0.0520
$t\bar{t}$	831.76
	87.31448
	380.094
	364.3508
Single-t	136.02
	80.95
	35.6
	35.6
QCD	

Table 4.1: Classes of background samples used for Run 2 with total cross sections for each sample used where available.

processes described in the introduction, consisting of W+jets, DY+jets, SM diboson, $b\bar{b}$, $t\bar{t}$, single-t, and QCD production samples. The W+jets process is produced to LO in QCD with `MadGraph5_aMC@NLO`. For the $t\bar{t}$ events, we use samples produced from `POWHEG` v2 [116–119], which are rescaled to the NNLO cross section value computed with `Top++` v2.0 [120]. The single-t events are generated in the t-channel and tW-channel at NLO with `POWHEG` [121,122]. Finally, the SM diboson processes are produced at NLO with `MadGraph5_aMC@NLO` using the merging scheme in reference [123] for WZ and ZZ, and with `POWHEG` for WW [124].

4.3   Event Selection and Categorization

In subsection 2.3.2, we described the expected event topology for the WV/WH dibosonic resonance that this work searches for. In particular, the semileptonic decay produces a highly energetic lepton (e or μ) and large p_T^{miss} from the neutrino from the $W \to \ell\nu$ decay, a large-radius jet from the hadronic $V \to q\bar{q}^{(\prime)}$ or $H \to b\bar{b}$ decay, and forward-facing VBF jets for VBF-produced resonances. To select for possible events that exhibit the expected final state structure, selection cuts must be made that capture the expected behavior and reduce

background. This section provides an overview of the cuts that were made in the analysis to optimize the search for the WV/WH dibosonic resonance.

4.3.1 Trigger

Multiple HLT trigger paths are used for recording the data that this analysis utilizes. Most of the data are collected from the Single Electron and Single Muon HLT paths, with the remainder coming from the MET, Single Photon, and E/Gamma[2] paths. The use of the Single Photon paths in conjunction with the Single Electron paths in 2017 and 2018 is to recover efficiency losses on the Single Electron path for high p_T electrons, which is necessary for electrons with $p_\mathrm{T} > 300$ GeV. For each year we use different HLT paths, which are listed in table 4.2.

Year	HLT Paths	Description
2016	Single Electron/	$p_\mathrm{T} > 27$ GeV, Tight WP for ele ID
	Single Photon	$p_\mathrm{T} > 45$ GeV, Loose WP for ele ID
		$p_\mathrm{T} > 115$ GeV
		$E_\mathrm{T} > 175$ GeV
	Single Muon	$p_\mathrm{T} > 50$ GeV
		tracker muon, $p_\mathrm{T} > 50$ GeV
	MET	$p_\mathrm{T}^\mathrm{miss} > 120$ GeV
2017	Single Electron/	$p_\mathrm{T} > 32$ GeV, Tight WP for ele ID
	Single Photon	$p_\mathrm{T} > 35$ GeV, Tight WP for ele ID
		$p_\mathrm{T} > 115$ GeV
		$E_\mathrm{T} > 200$ GeV
	Single Muon	$p_\mathrm{T} > 50$ GeV
		$p_\mathrm{T} > 100$ GeV
		tracker muon, $p_\mathrm{T} > 100$ GeV
	MET	$p_\mathrm{T}^\mathrm{miss} > 120$ GeV
2018	E/Gamma	$p_\mathrm{T} > 32$ GeV, Tight WP for ele ID
		$p_\mathrm{T} > 115$ GeV
	Single Muon	$p_\mathrm{T} > 50$ GeV
		$p_\mathrm{T} > 100$ GeV
		tracker muon, $p_\mathrm{T} > 100$ GeV
	MET	$p_\mathrm{T}^\mathrm{miss} > 120$ GeV

Table 4.2: HLT paths used in Run 2 data and MC. Here, "WP" and 'ID' refer to working point and identification, respectively.

The Single Electron p_T thresholds used are 27, 45, and 115 GeV for 2016, 32, 25, and 115 GeV for 2017, and 25 and 115 GeV for 2018. For Single Muon paths, the main thresh-

---

[2]This is specific to 2018 and denotes a combined Single Electron and Single Photon HLT path.

old is 50 GeV across all three years. These thresholds are chosen as part of compromises between energy thresholds and isolation tightness, as lower p_{T} thresholds result in a higher event rate and hence require tighter identification cuts, while higher p_{T} thresholds allow for looser working points. Lastly, the additional MET trigger path recovers some inefficiency in triggering on high p_{T} muons in the endcaps.

For both lepton triggers, the efficiencies for all Run 2 years are measured with respect to offline electron High Energy Electron Pairs (HEEP) requirements, and to muon high-p_{T} ID and isolation requirements, using a dataset enriched in boosted $W + \mathrm{jets}$ events. To correct for differences between modeling in simulation and data, we apply scale factors to account for various effects, which are obtained by taking the ratio of data to MC and applying these ratios to events as weights. The efficiencies and resulting data/MC scale factors for 2016 are shown in figures 4.3-4.5. We also separately measure the efficiencies of the lepton legs and of the MET legs by either triggering on MET and looking at Single Electron or Single Muon paths, or by triggering on one of the lepton paths and looking at the MET path. Large uncertainties in the data/MC scale factors for the lepton legs are observed at large p_{T} and η due to the low statistics in those regions. The muon channel for the MET efficiencies in figure 4.5 also does not have a turn-on curve since the chosen MET HLT path sees the whole $W^{\pm}$ as $p_{\mathrm{T}}^{\mathrm{miss}}$ in boosted $W \to \mu\nu$ events. The resulting event-level scale factor used in this analysis is defined as

$$S_{\mathrm{lep}} = \frac{\epsilon_{\mathrm{total}}(\mathrm{data})}{\epsilon_{\mathrm{total}}(\mathrm{MC})}, \tag{4.1}$$

where each efficiency ϵ is estimated as $\epsilon(\mathrm{lepton}) + \epsilon(\mathrm{MET}) - \epsilon(\mathrm{lepton})\epsilon(\mathrm{MET})$.

4.3.2 Pileup Reweighting

For a given collision event in the analysis, we are concerned with the hard-scatter event that takes place at the primary vertex (PV). However, additional proton interactions may take place in locations other than the PV along the beamline during a single bunch crossing.
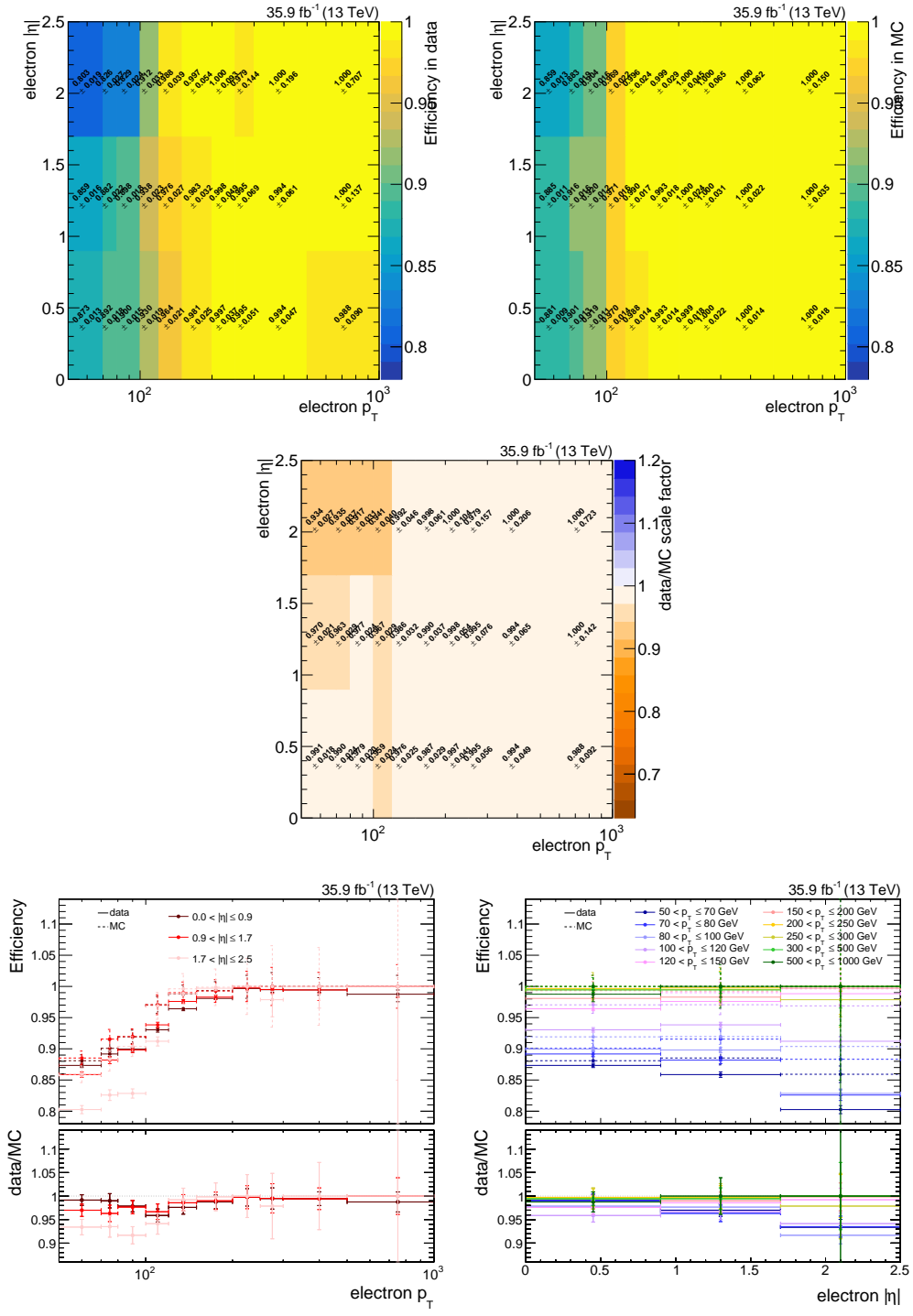
Figure 4.3: 2016 Single Electron trigger efficiencies versus offline electron p_T and η in data (top left) and MC (top right) and data/MC scale factors (middle), and efficiencies and scale factors versus p_T in bins of η (bottom left) and versus η in bins of p_T (bottom right).
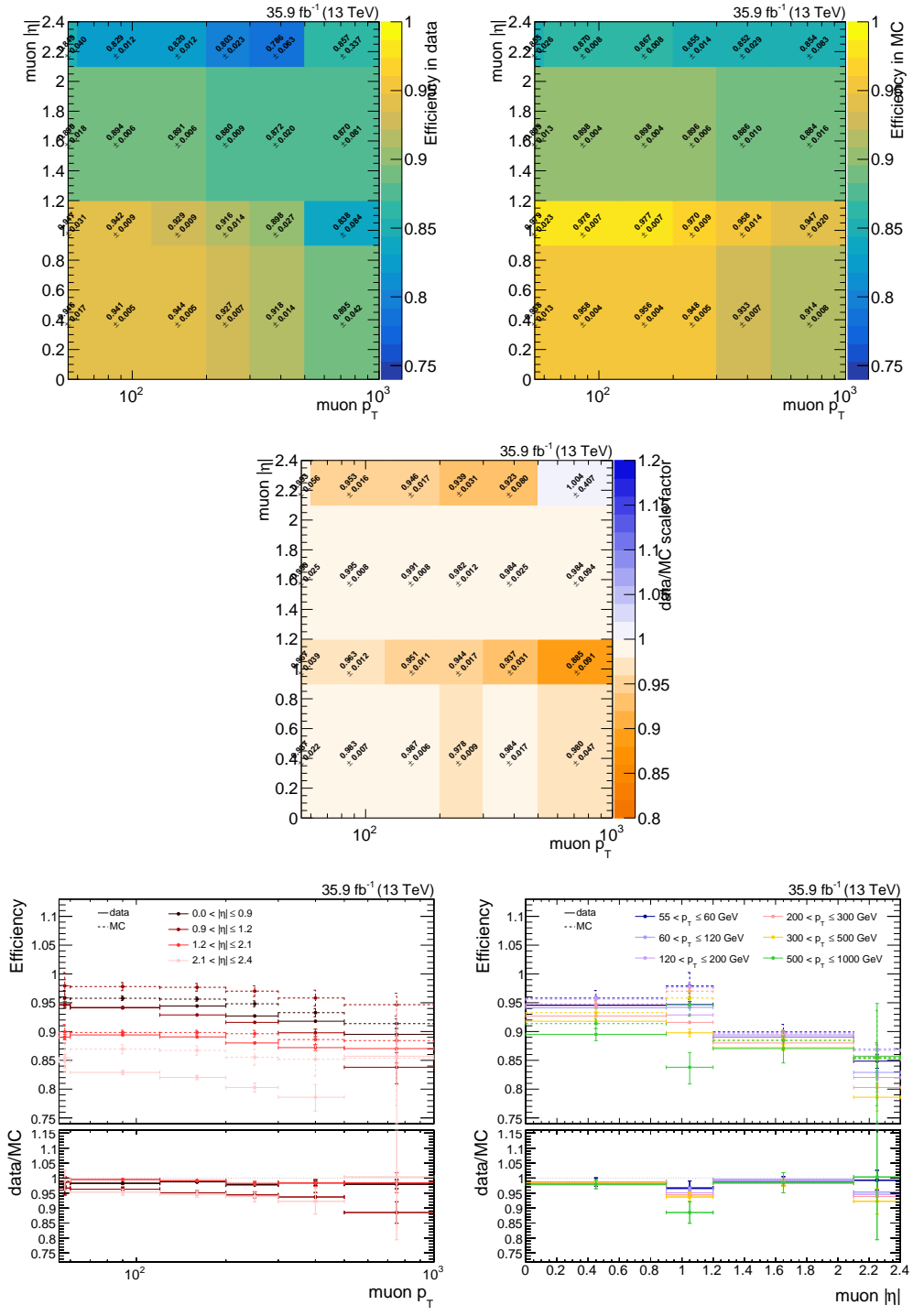
Figure 4.4: 2016 Single Muon trigger efficiencies versus offline muon p_{T} and η in data (top left) and MC (top right) and data/MC scale factors (middle), and efficiencies and scale factors versus p_{T} in bins of η (bottom left) and versus η in bins of p_{T} (bottom right).

65
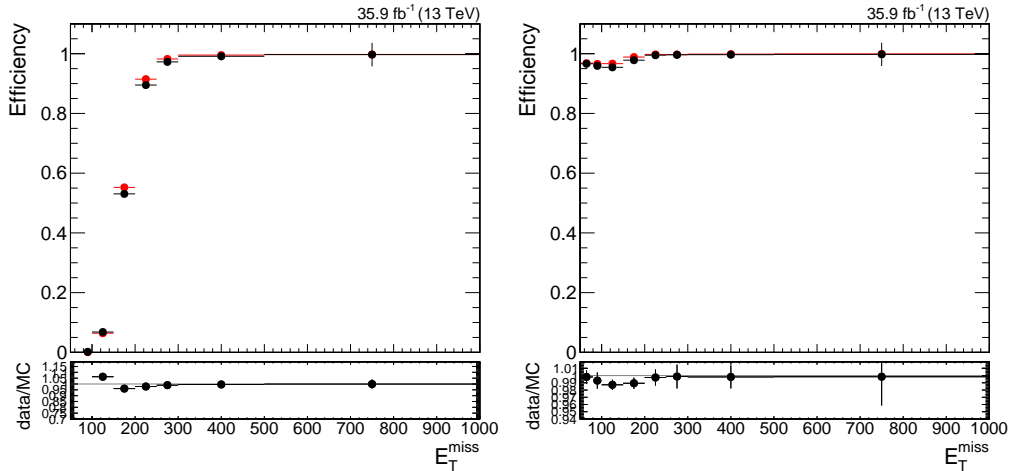
Figure 4.5: 2016 MET trigger efficiencies (top) for data (black) and simulation (red), in the electron (left) and muon (right) channels, with data/MC scale factors (bottom).

These interactions are referred to as pileup (PU) [125], and the presence of the additional PU energy requires corrective measures to be taken in order to accurately reconstruct jets in an event.

The data samples from all three Run 2 years have different pileup profiles than that of the simulation samples that were used for this analysis. In order to account for this, we compute and apply PU weights to our samples and compare distributions for the number of primary vertices, both with and without weights to the data. Figure 4.6 shows these distributions for Run 2. The weights are computed using the recommended minimum bias cross section of 69.2 mb.

4.3.3 Muon Selection

Muon reconstruction in CMS is a multi-stage process that involves creating muon objects from various trigger sources [91, 126]. This process starts with local reconstruction, in which detection hits in the muon chambers are reconstructed through the trigger system. The hits within the chambers are then matched to create track segments, known as track stubs.
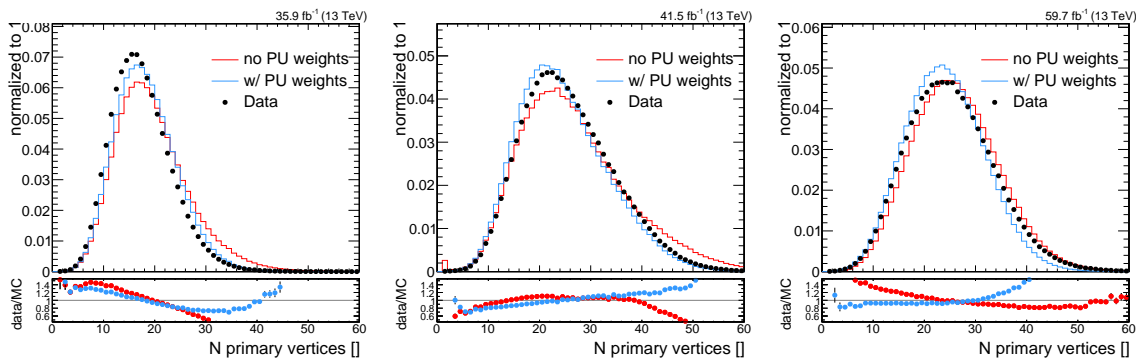
Figure 4.6: Distribution of the number of primary vertices reconstructed in simulation before and after pileup reweighting, with data present, for 2016 (left), 2017 (middle), and 2018 (right).

During offline reconstruction, the track stubs are used to create standalone muons, which are muon objects constructed by using the track stubs to estimate the muon transverse momentum using the Kalman filter technique. These objects are then used to create global muons, which are objects that combine standalone muon tracks with tracks from the inner tracking system, again using a Kalman filter.

When selecting muons for the analysis, they must pass the following high-p_T muon identification criteria [126].

- The muon is reconstructed as a global muon.

- At least one muon hit retained in the global track fit, including the hits of both tracker and standalone muons.

- Muon segments in at least two muon stations.

- The p_T relative error ($\sigma(p_T)/p_T$) of the muon best track is less than 30%.

- Its tracker track has transverse impact parameter $|d_{xy}| < 2$ mm with respect to the primary vertex.

- The longitudinal distance of the tracker with respect to the primary vertex is $|d_z| <$ 5 mm.

- The muon track has at least one pixel hit.

- The muon track has at least six tracker layer hits.

In addition to the high-p_T muon identification criteria, for this analysis we also require each muon to have $p_\mathrm{T} > 55$ GeV and to be confined to the region $|\eta| < 2.4$. Any additional muons in the event with $p_\mathrm{T} > 20$ GeV result in a veto for the event. We also apply an isolation requirement on the muons in order to further suppress background. This is done using the full relative Particle-Flow isolation using $\Delta\beta$ corrections, with the requirement that $I_\mathrm{rel} < 0.05$, with I_rel defined by [127]

$$I_\mathrm{rel} = \frac{\sum_{i\in\mathrm{PV}} p_{\mathrm{T},i} + \max\left(0, \sum_{j\in\mathrm{NH}} E_{\mathrm{T},j} + \sum_{k\in\mathrm{phot}} E_{\mathrm{T},k} - \Delta\beta \sum_{n\in\mathrm{PU}} p_{\mathrm{T},n}\right)}{p_{\mathrm{T},\mu}}, \qquad (4.2)$$

where PV denotes the set of charged hadrons from the primary vertex, NH is the set of neutral hadrons, phot is the set of photons, PU denotes the set of charged hadrons from pileup, and $p_{\mathrm{T},\mu}$ is the transverse momentum of the muon for which the isolation is being performed. The factor $\Delta\beta = 0.5$ corresponds approximately to the ratio of neutral particle to charged hadron production in inelastic proton collisions, which is estimated from simulation. Isolation is performed within a cone of size $\Delta R = 0.3$ centered around the $p_{\mathrm{T},\mu}$ axis, where $\Delta R \equiv \sqrt{\Delta\eta^2 + \Delta\phi^2}$.

Scale factors for muon identification are also applied to correct for the differences between muon identification in data and simulation [126]. These scale factors are defined as the ratio of data-to-simulation efficiency, given by

$$S_\mu = \frac{\epsilon_\mu(\mathrm{data})}{\epsilon_\mu(\mathrm{MC})}, \qquad (4.3)$$

where $\epsilon_\mu = \epsilon_{\mathrm{track}}\epsilon_{\mathrm{ID}}\epsilon_{\mathrm{reco}}\epsilon_{\mathrm{trig}}$ is the total muon efficiency, and $\epsilon_{\mathrm{track}}$, ϵ_{ID}, ϵ_{reco}, and ϵ_{trig} are the individual efficiencies for the track reconstruction, muon identification, muon reconstruction, and muon trigger, respectively. These scale factors are derived separately based on muon p_{T}, η region, and identification requirements, and are applied to the number of events as a weighting factor. To appropriately apply these scale factors as they vary by year to the full Run 2 dataset, we also weigh them by the fraction of integrated luminosity for each year. Furthermore, we also apply a scale factor for the isolation requirement, which is shown in figure 4.7. This scale factor was derived on top of muon high-p_{T} identification, in boosted Z and DY events over the full Run 2 period, which is found to be within 1% from unity and smaller than the systematic uncertainty for the muon trigger/reconstruction/identification of 5% used in signal extraction.
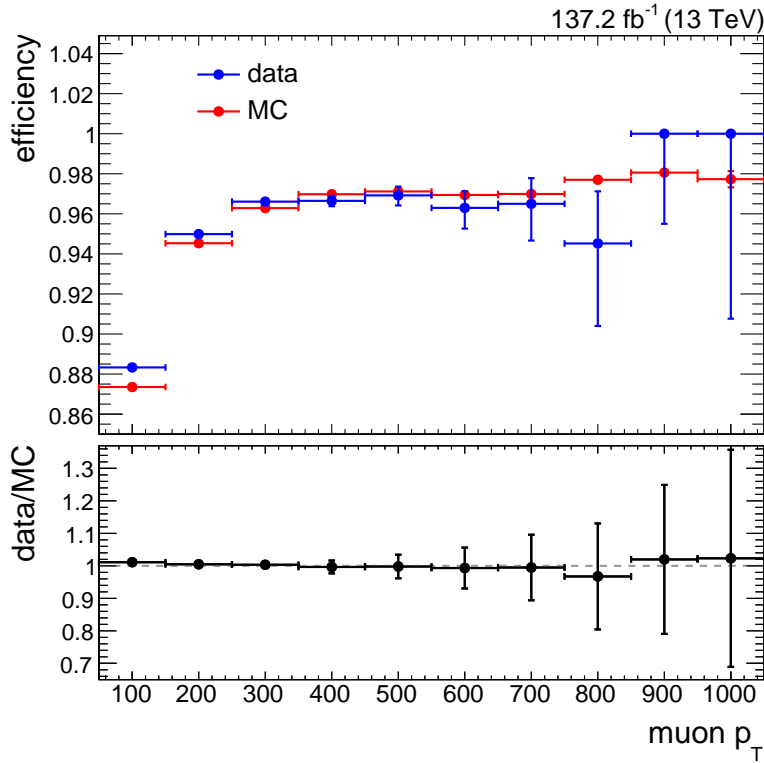
Figure 4.7: Efficiency in data and simulation (top) and data/MC scale factor (bottom) for muon isolation requirement.

4.3.4 Electron Selection

The electrons that are reconstructed from trigger primitives in the ECAL are required to pass identification requirements designed for energetic electrons. These requirements are chosen specifically to optimize the identification of high-energy electrons. The identification requirements ensure that the reconstructed electrons from the ECAL energy deposits are paired with a high quality track from the inner tracker and have a shape consistent with an electromagnetic shower in the calorimeter. These requirements are listed in table 4.3 in terms of identification variables. For our analysis, we also require the electrons to have $p_T > 55$ GeV and be within the pseudorapidity range $|\eta| < 2.5$, except for the region $[1.4442, 1.566]$. We also exclude events for which there are additional electrons with $p_T > 35$ GeV.

4.3.5 Jet Selection

As mentioned previously, there are two types of jets that are expected to be produced in the signal events of interest. The first is a large-radius jet that is produced via the V/H decay that exhibits two-pronged substructure, while the second type are regular-radius forward-facing jets only present in VBF production modes. This analysis therefore categorizes candidate jets into the two following types:

- "Large-radius" AK8 jets: V/H boson candidates that decay into $q\bar{q}^{(\prime)}$ or $b\bar{b}$, using the anti-k_T algorithm with distance parameter $R = 0.8$.

- "Standard" AK4 jets: VBF forward jet candidates and jets used to require or veto the presence of b-tagged jets in the event, using the anti-k_T algorithm with distance parameter $R = 0.4$.

For both types of jets, we use tight identification jets. These jets are required to pass identification requirements based on quantities such as the neutral hadron fraction, neutral EM fraction, number of constituents, and number of neutral particles [129]. We also apply jet

Variable	Barrel	Endcap
	Acceptance selections	
E_T	$E_\mathrm{T} > 35$ GeV	$E_\mathrm{T} > 35$ GeV
η	$|\eta_\mathrm{SC}| < 1.4442$	$1.566 < |\eta_\mathrm{SC}| < 2.5$
	Identification selections	
`isEcalDriven`	`true`	`true`
$\Delta\eta_\mathrm{in}^\mathrm{seed}$	$|\Delta\eta_\mathrm{in}^\mathrm{seed}| < 0.004$	$|\Delta\eta_\mathrm{in}^\mathrm{seed}| < 0.006$
$\Delta\phi_\mathrm{in}$	$|\Delta\phi_\mathrm{in}| < 0.06$	$|\Delta\phi_\mathrm{in}| < 0.06$
H/E	$H/E < 1/E + 0.05$	$H/E < 5/E + 0.05$
$\sigma_{i\eta i\eta}$	-	$\sigma_{i\eta i\eta} < 0.03$
$\frac{E_{1\times5}}{E_{5\times5}},\ \frac{E_{2\times5}}{E_{5\times5}}$	$\frac{E_{1\times5}}{E_{5\times5}} > 0.83$ or $\frac{E_{2\times5}}{E_{5\times5}} > 0.94$	-
Inner lost layer hits	lost hits ≤ 1	lost hits ≤ 1
Impact parameter, d_{xy}	$|d_{xy}| < 0.02$	$|d_{xy}| < 0.05$
	Isolation selections	
EM + had depth 1 isolation, I	$I < 2 + 0.03E_\mathrm{T} + 0.28\rho$	$I < 2.5 + 0.28\rho$ ($E_\mathrm{T} < 50$ GeV) else $I < 2.5 + 0.03(E_\mathrm{T} - 50$ GeV$) + 0.28\rho$
p_T isolation, I_{p_T}	$I_{p_\mathrm{T}} < 5$ GeV	$I_{p_\mathrm{T}} < 5$ GeV

Table 4.3: Definitions of HEEP identification V7.0 selections [128]. Here, the "SC" subscript denotes a supercluster, which corresponds to a collection of arrays of ECAL crystals. Quantities with an "in" subscript correspond to the point of closest approach to the beam spot, while the "seed" superscript denotes a quantity related to a seed crystal, which is the crystal containing the largest amount of energy from a deposit. H/E denotes the ratio of the sum of the HCAL tower energies to the supercluster energies within a cone of $\Delta R = 0.15$ around the electron. The shower-shape variable is denoted by $\sigma_{i\eta i\eta}$. Finally, the cluster energies $E_{n\times m}$ correspond to the energy deposited within an $n \times m$ grid of ECAL crystals.

energy corrections for data and MC prescribed by the Jet Energy Resolution and Corrections (JERC) subgroup [130].

The hadronic jet resulting from the V/H decay is selected by taking the jet with the highest p_T from the large-radius jets, with a minimum threshold of $p_T > 200$ GeV and a pseudorapidity range of $|\eta| < 2.5$. Any large-radius jets that have an electron or tight muon within $\Delta R < 1.0$ are discarded to suppress background events. For the standard jets, we require that $p_T > 30$ GeV, and we discard any jets within $\Delta R < 0.4$ of any selected electron or muon, or within $\Delta R < 0.8$ of any large-radius jet.

4.3.5.1 V-jet Tagging

A central component of the analysis is the ability to accurately identify and reconstruct the hadronically decaying V/H boson, which we shall refer to as V_{had}. Once the jets in the final state are identified, algorithms must be applied to determine the substructure of the jets. This analysis makes use of the Pileup Per Particle Identification (PUPPI) algorithm, which takes Particle-Flow object candidates and assigns weights to each particle based energy shape profiles [131]. The resulting reweighted candidates are put into substructure algorithms for further analysis.

The jets obtained from the PUPPI algorithm are groomed by using the "soft drop" algorithm [132], which removes soft wide-angle radiation from jets. The soft drop algorithm starts by using the Cambridge-Aachen algorithm [133, 134] to recluster the constituents of a given jet. For a jet with radius R with two constituents, the soft drop algorithm removes the softer constituent if it does not satisfy the condition

$$\frac{\min\left(p_{T,1}, p_{T,2}\right)}{p_{T,1} + p_{T,2}} > z\left(\frac{\Delta R_{12}}{R}\right)^{\beta}, \tag{4.4}$$

where the $p_{T,i}$ are the transverse momenta of the jet constituents, ΔR_{12} is the separation between the constituents in the y-ϕ plane, R is the characteristic radius, z is the soft drop

threshold, and β is the angular exponent. For this analysis, we use $z = 0.1$ based on theoretical considerations of the jet mass from QCD [135, 136]. We also use an angular exponent of $\beta = 0$ and a characteristic radius of $R = 0.8$. The soft drop mass is denoted by m_{jet}, and we apply recommended corrections [137].

To determine the degree to which the jet has substructure, we use the "N-subjettiness" as a measure of how many subjets are present in the jet [138, 139]. It is designed to identify boosted hadronic objects based on the angular distances of jet constituents relative to their nearest subjet axis. Figure 4.8 shows an example of a jet with two subjets defined by axes $\hat{\mathbf{n}}_1$ and $\hat{\mathbf{n}}_2$, which exhibits the two-pronged structure expected to be observed by the V_{had} boson decay. We proceed by reclustering the jets with the k_{T} algorithm until N jets remain, then compute the N-subjettiness defined by

$$\tau_N = \frac{1}{d_0} \sum_k p_{\mathrm{T},k} \min\left(\Delta R_{1,k}, \Delta R_{2,k}, \ldots, \Delta R_{N,k}\right), \tag{4.5}$$

where d_0 is a normalization factor given by

$$d_0 = \sum_k p_{\mathrm{T},k} R_0, \tag{4.6}$$

with R_0 as the clustering parameter of the original jet, $p_{\mathrm{T},k}$ is the transverse momentum of the k-th jet constituent, and $\Delta R_{n,k}$ is the distance to the n-th subjet in the η-ϕ plane.

In some cases it is advantageous to consider ratios of N-subjettiness. For example, in this analysis we consider the ratio τ_{21}, defined by

$$\tau_{21} \equiv \frac{\tau_2}{\tau_1} = \frac{\sum_k p_{\mathrm{T},k} \min\left(\Delta R_{1,k}, \Delta R_{2,k}\right)}{\sum_k p_{\mathrm{T},k} \Delta R_{1,k}}. \tag{4.7}$$

which is a measure of whether or not the jet exhibits the properties we would expect from a jet with two subjets versus a single jet with no substructure. The smaller τ_{21} is, the more likely the jet is two-pronged. This allows for separating jets originating from boosted vector bosons
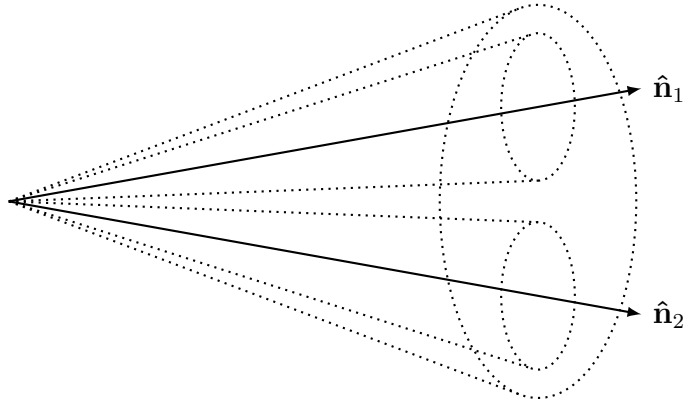
Figure 4.8: Illustration of jet substructure for a two-pronged jet with axes $\hat{\mathbf{n}}_1$ and $\hat{\mathbf{n}}_2$. The N-subjettiness τ_N is used as a measure of how many subjets are present within a jet.

versus jets that are produced from quarks and gluons, thereby allowing further background suppression. This analysis uses a modified version of the N-subjettiness ratio that reduces the dependency of τ_{21} on the jet mass, which is denoted by the designed decorrelated tagger (DDT) N-subjettiness τ_{21}^{DDT} [140]. It is defined by

$$\tau_{21}^{\mathrm{DDT}} = \tau_{21} - M \ln \left(\frac{m_{\mathrm{jet}}^2}{p_{\mathrm{T,jet}} \mu} \right), \tag{4.8}$$

where $M = -0.08$ is a coefficient obtained by taking the slope of a fit for the τ_{21} profile versus $\ln \left(m_{\mathrm{jet}}^2 / p_{\mathrm{T,jet}} \mu \right)$ in non-resonant $W + $ jets background events after applying the full analysis selection cuts, and μ is a constant chosen such that $\mu = 1$ GeV. Figure 4.9 shows a comparison of τ_{21} versus τ_{21}^{DDT} for signal and background MC events, with their distributions normalized to unity. The distributions for τ_{21}^{DDT} have peaks for signal and background that are more separated than the distributions for τ_{21}, resulting in better discrimination against background.

For this analysis, we only consider large-radius jets that satisfy $\tau_{21}^{\mathrm{DDT}} \leq 0.80$. We also later use τ_{21}^{DDT} for event categorization to split the analysis into high and low purity jet categories, as discussed in subsection 4.3.10.2.
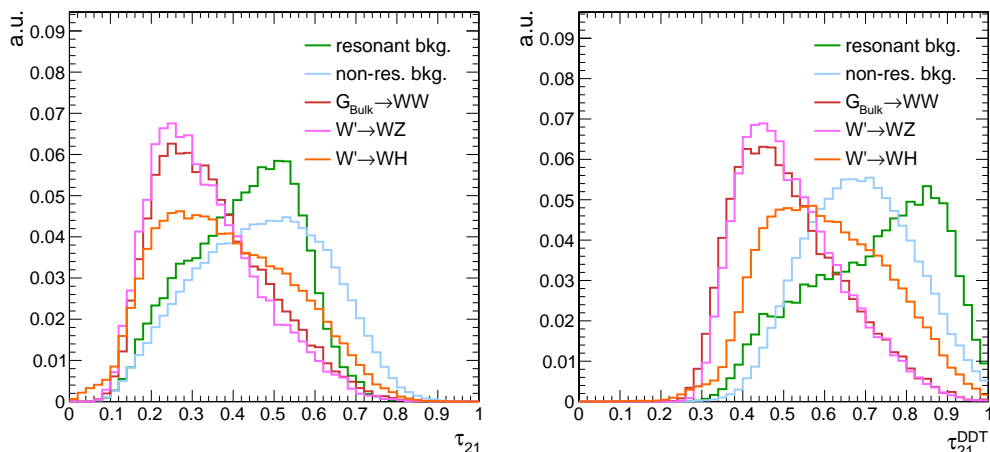
Figure 4.9: Comparison of the distributions for signal versus background for τ_{21} (left) and τ_{21}^{DDT} (right), with distributions normalized to unity. The signal distributions for τ_{21}^{DDT} exhibit larger separation from the background distributions compared to τ_{21}.

4.3.5.2   *b*-tagging

Jets produced from b quarks have unique characteristics that distinguish them from other hadronic decays. Because of the relatively long lifetime of hadrons that contain b quarks, the secondary vertices (SVs) corresponding to the location of the decay tend to have displacements on the order of a few millimeters away from the primary vertex. Another distinguishing property is that decays from b hadrons result in a boosted jet topology, as the products that b quarks decay into are much lighter. Finally, the heavy hadrons containing b quarks tend to favor semileptonic decays, resulting in soft leptons present in the jet. The techniques used to identify such jets are referred to as b-tagging.

For this analysis, we use b-tagging to suppress background contributions by removing events with at least one b-tagged standard jet, as these events are dominated by processes containing top quark decays, such as $t\bar{t}$ events. We also use b-tagged jets for defining the top-enriched control region, which is discussed in section 4.4. Jets in the region $|\eta| < 2.5$ are b-tagged if they pass the `medium` working point of the Combined Secondary Vertex (CSV)

or DeepCSV algorithms [141]. The `medium` working point for CSV is 0.8484 in 2016, and for DeepCSV the working points are 0.4941 and 0.4184 for 2017 and 2018, respectively. We also apply b-tagging scale factors and weights that depend on the jet p_T, η, and value of the b-tagging discriminant.

4.3.5.3 $b\bar{b}$-tagging

The V-tagging methods previously described account for identifying and grooming jets resulting from the V_had decay, but additional techniques are applied in this analysis to account for a large-radius $b\bar{b}$ jet. Such a jet signifies the decay $H \to b\bar{b}$ in the final state and hence a WH resonance, which allows for discriminating against background with light jet flavors. Furthermore, a unique feature of the topology of $b\bar{b}$ jets is the fact that the constituent b quarks have secondary vertices that are displaced from the PV of the jet. To identify such $b\bar{b}$ jets, we therefore use a b-tagging discriminator to identify Higgs boson jet candidates that uses information from displaced tracks and secondary vertices [142]. We also apply a cut on the M2 operating point of the "DoubleB tagger" [141] to categorize events in subsection 4.3.10.2, for which the threshold is 0.8 for Run 2.

Additionally, we apply data/MC efficiency scale factors to our signal sample normalizations, while the scale factors for the background are estimated from the data in the control regions. We use two sets of scale factors that depend on $p_\mathrm{T,jet}$. One is for $H \to b\bar{b}$ jets resulting from the $W' \to WH \to \ell\nu b\bar{b}$ signal model, and the other is for mistagging $W^\pm$ bosons resulting from $t\bar{t}$ events, which are applied to the $G_\mathrm{bulk} \to WW \to \ell\nu q\bar{q}'$ and $W' \to WZ \to \ell\nu q\bar{q}$ signal models. The weights are calculated by considering the probability

of a given configuration of jets in MC and data as

$$P(\text{MC}) = \prod_{i=\text{tagged}} \epsilon_{b\bar{b},i} \prod_{j=\text{not tagged}} (1 - \epsilon_{b\bar{b},j}), \tag{4.9}$$

$$P(\text{data}) = \prod_{i=\text{tagged}} S_i \epsilon_{b\bar{b},i} \prod_{j=\text{not tagged}} (1 - S_j \epsilon_{b\bar{b},j}), \tag{4.10}$$

where $\epsilon_{b\bar{b},i}$ is the b-tagging efficiency in MC, and the scale factors S_i and $\epsilon_{b\bar{b},i}$ are functions of the jet flavor, p_{T}, and η. The weight is then calculated as

$$w = \frac{P(\text{data})}{P(\text{MC})}. \tag{4.11}$$

For this analysis, first we measure the MC $b\bar{b}$-tagging efficiencies $\epsilon_{b\bar{b}}$, then apply the event weights for the $b\bar{b}$-tagged category as

$$w^{b\bar{b}}(p_{\text{T}}) = \frac{S(p_{\text{T}})\epsilon_{b\bar{b}}(p_{\text{T}})}{\epsilon_{b\bar{b}}(p_{\text{T}})} = S(p_{\text{T}}), \tag{4.12}$$

while for the $b\bar{b}$-untagged category, we instead use

$$w^{\text{non-}b\bar{b}}(p_{\text{T}}) = \frac{1 - S(p_{\text{T}})\epsilon_{b\bar{b}}(p_{\text{T}})}{1 - \epsilon_{b\bar{b}}(p_{\text{T}})}. \tag{4.13}$$

4.3.6 Missing Transverse Momentum

For this analysis, we use type-I corrected Particle-Flow missing transverse energy (PFMET) to account for the energy of the neutrino from the W_{lep} decay, where PFMET is defined as the magnitude of the negative vector sum of all transverse momenta from Particle-Flow objects [143]. The correction is a propagation of the jet energy corrections (JEC) to $p_{\text{T}}^{\text{miss}}$, which is given by

$$\left(p_{\text{T}}^{\text{miss}}\right)^{\text{Type}-\text{I}} = \left| -\sum_{\text{jet}} \mathbf{p}_{\text{T,jet}}^{\text{JEC}} - \sum_{i \in \text{uncl.}} \mathbf{p}_{\text{T},i} \right|, \tag{4.14}$$

where the first sum is over clustered jets and the second sum is over unclustered parti-
cles. We require $\left(p_{\mathrm{T}}^{\mathrm{miss}}\right)^{\mathrm{Type-I}} > 40$ GeV if the selected lepton in the event is a muon, and
$\left(p_{\mathrm{T}}^{\mathrm{miss}}\right)^{\mathrm{Type-I}} > 80$ GeV if it is an electron.

4.3.7 Leptonic $W^{\pm}$ and WV reconstruction

To reconstruct the leptonically decaying $W^{\pm}$ candidate W_{lep}, we select the highest p_{T} lepton
in the event and combine it with the $\left(p_{\mathrm{T}}^{\mathrm{miss}}\right)^{\mathrm{Type-I}}$ resulting from the neutrino. We also apply
a $W^{\pm}$ mass constraint to estimate the z-component of the missing momentum $p_{\nu,z}$. This is
done by solving a second order equation for $p_{\nu,z}$ given by

$$4(E_\ell^2 - p_{\ell,z}^2)p_{\nu,z}^2 - 4(m_W^2 + 2\mathbf{p}_{\ell,\mathrm{T}} \cdot \mathbf{p}_{\nu,\mathrm{T}})p_{\ell,z}p_{\nu,z} + 4E_\ell^2(p_{\mathrm{T}}^{\mathrm{miss}})^2 - (m_W^2 + 2\mathbf{p}_{\ell,\mathrm{T}} \cdot \mathbf{p}_{\nu,\mathrm{T}})^2 = 0, \quad (4.15)$$

where E_ℓ is the energy of the lepton, $\mathbf{p}_\ell$ is the momentum of the lepton, $\mathbf{p}_\nu$ is the momentum
of the neutrino, and m_W is the mass of the $W^{\pm}$ boson. When solving for $p_{\nu,z}$ we choose the
root with the smaller magnitude, and if the discriminant is imaginary then we select only
the real part of $p_{\nu,z}$. The resulting W_{lep} is then combined with the large-radius V_{had} jet to
form a diboson candidate, with mass denoted by $m_{WV/WH}$.

To select a diboson-like topology we apply angular selection criteria between the lepton,
V_{had}, W_{lep}, and $\left(p_{\mathrm{T}}^{\mathrm{miss}}\right)^{\mathrm{Type-I}}$ candidates. The first is that the angular distance in η-ϕ between
the V_{had} and lepton candidates is required to be $\Delta R > \pi/2$. For the second requirement,
the difference in the azimuthal angle between the V_{had} and $\left(p_{\mathrm{T}}^{\mathrm{miss}}\right)^{\mathrm{Type-I}}$ must be $|\Delta\phi| > 2$.
Finally, the third requirement is that the difference in the azimuthal angle between the V_{had}
and W_{lep} satisfies $|\Delta\phi| > 2$ as well.

4.3.8 VBF Forward Jets

The defining signature of the VBF production process is the presence of two boosted jets
in the forward regions of the detector, along with the decay products in the central region

resulting from the W_{lep} and V_{had} resonances. The analysis therefore exploits the specific event topology of VBF events to define a VBF-tagged category that is sensitive to VBF-produced resonances, as defined in subsection 4.3.10.2.

We select candidate VBF jets from the two highest p_{T} standard AK4 jets as defined in subsection 4.3.5. This requires that the VBF jets satisfy $p_{\text{T}} > 30$ GeV, and that they do not overlap with the selected lepton and large-radius jet. We then apply selection cuts to the two candidate VBF jets based on their separation in pseudorapidity $\Delta\eta_{\text{VBF}}$ and VBF invariant mass $m_{\text{jj}}^{\text{VBF}}$.

For the cut on $\Delta\eta_{\text{VBF}}$, we exploit the fact that the VBF jets are expected to be found in the high $|\eta|$ regions of the detector near the endcaps and be roughly anti-parallel to each other. Figure 4.10 (left) shows the relative shape differences in $\Delta\eta_{\text{VBF}}$ between the VBF $\phi \to WW$ signal MC sample and the background MC samples used in this analysis. To retain a signal efficiency of 40-50%, we choose a cut of $\Delta\eta_{\text{VBF}} > 4$.
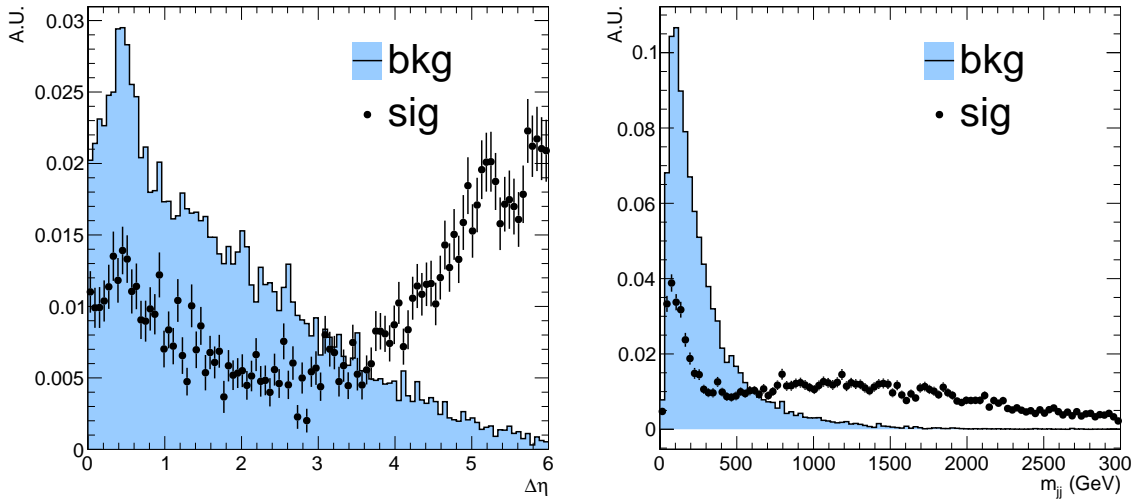
Figure 4.10: Shape comparison of a VBF $\phi \to WW$ signal sample and background MC samples, normalized to unity, for $\Delta\eta_{\text{VBF}}$ (left) and $m_{\text{jj}}^{\text{VBF}}$ (right). The shape discrepancy between the VBF signal and background distributions in $\Delta\eta_{\text{VBF}}$ and $m_{\text{jj}}^{\text{VBF}}$ allows for distinguishing signal from background.

The other kinematic cut applied to the VBF candidate jets is on the invariant mass of the sum of the VBF jet four-vectors, $m_{\text{jj}}^{\text{VBF}}$. For this cut, we consider the Punzi significance obtained for a VBF signal sample as a function of the thresholds of the cuts for $\Delta\eta_{\text{VBF}}$ and $m_{\text{jj}}^{\text{VBF}}$. The Punzi significance is defined by $\epsilon/(1.5 + \sqrt{B})$ [144], where ϵ is the number of signal events obtained by the cuts assuming an integrated luminosity of $\mathcal{L}_{\text{int}} = 1 \text{ pb}^{-1}$ and a cross section of $\sigma = 1$ pb, while the number of background events B is weighted with the total luminosity. We again require that the selection cut on $m_{\text{jj}}^{\text{VBF}}$ retains 40-50% signal efficiency, as we did for $\Delta\eta_{\text{VBF}}$. This leads to a cut of $m_{\text{jj}}^{\text{VBF}} > 500$ GeV.

4.3.9   Spin Polarization and Boson Rapidities

The VBF production process has another distinctive feature in which some kinematic variables are sensitive to the spin of the X resonance, thereby providing the ability to distinguish between signal models. This effect can be seen in the distributions for the separation in rapidity between the V_{had} and W_{lep} diboson system, which we denote by $\Delta y_{WV/WH}$. Figure 4.11 shows the shape discrepancies between the MC signals and backgrounds in $\Delta y_{WV/WH}$, separated by non-VBF and VBF-produced signals.

The signals produced via ggF or DY have minor shape differences between each other, and their distributions are consistently narrower and more concentrated in the low $\Delta y_{WV/WH}$ region compared to the background MC samples. This on its own suggests that categorizing the search based on $\Delta y_{WV/WH}$ would increase the search sensitivity.

For the VBF-produced signals, the shape differences between signals are much more apparent. The spin-1 VBF $W' \to WZ$ and $Z' \to WW$ signals both peak around $\Delta y_{WV/WH} = 1.4$ rather than plateauing like the background from $\Delta y_{WV/WH} = 0$ to 0.8. Meanwhile, the spin-2 VBF $G_{\text{bulk}} \to WW$ signal has two peaks, with a large and narrow peak occurring at $\Delta y_{WV/WH} = 0$, followed by a smaller peak around $\Delta y_{WV/WH} = 2.0$. Finally, the VBF $\phi \to WW$ signal exhibits no difference in its $\Delta y_{WV/WH}$ distribution compared to the ggF $\phi \to WW$ signal since it is a spin-0 resonance, but it still differs from the other VBF signals
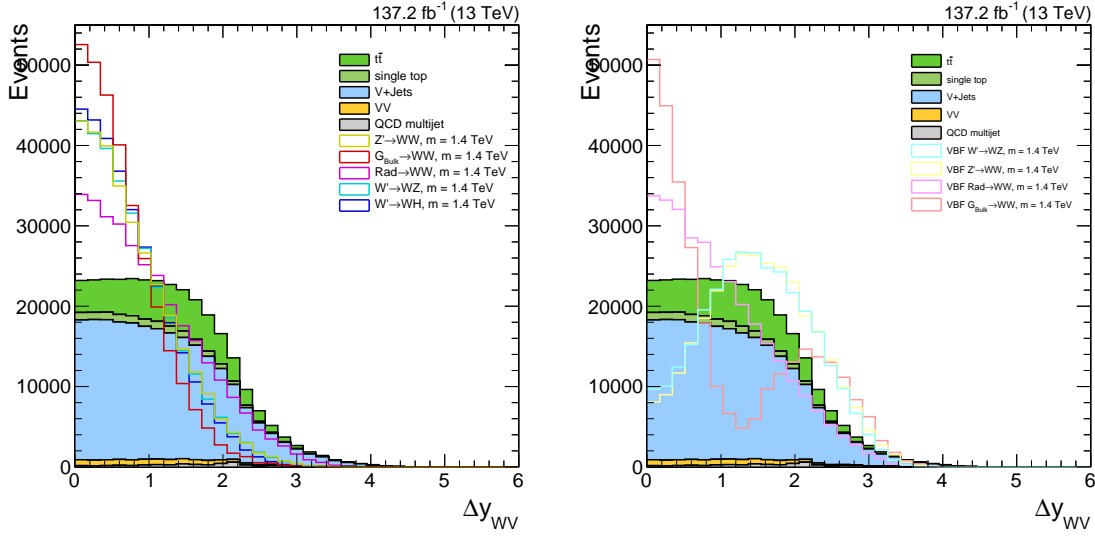
Figure 4.11: Shape comparison of the angular separation $\Delta y_{WV/WH}$ between the two re-constructed bosons for simulated background and signals, in the signal region. Background distributions are stacked and normalized to the expected luminosity for the full Run 2 set, while signal distributions are overlaid, all arbitrarily normalized to the same integral as the sum of backgrounds. Non-VBF (left) and VBF (right) signals are shown separately. The shape differences between signals are most apparent in the case of VBF production, allowing for distinguishing between spin-0, spin-1, and spin-2 signals. This defines a new layer of categorization for the analysis.

since it only has a peak at $\Delta y_{WV/WH} = 0$.

The shape differences between the VBF signals allow for not only enhancing the search sensitivity by using categories based on $\Delta y_{WV/WH}$, but by also allowing for distinguishing between spin-0 ($\phi \rightarrow WW$), spin-1 ($Z' \rightarrow WW$, $W' \rightarrow WZ$, $W' \rightarrow WH$), or spin-2 ($G_{\text{bulk}} \rightarrow WW$) VBF signal models. For this reason, we use two categories defined in subsection 4.3.10.2 based on rapidity: a low-$\Delta y_{WV/WH}$ category defined by the condition $\Delta y_{WV/WH} < 1.0$, and a high-$\Delta y_{WV/WH}$ category defined by $\Delta y_{WV/WH} \geq 1.0$. Originally a 3-category scheme was considered for the analysis, but it was found that this did not leave sufficient background MC statistics in all three categories in order to build robust 2D background templates.

4.3.10 Final Event Selection and Categorization

For this analysis, we make a final event selection in order to select events that exhibit the expected behavior of the final state described in subsection 2.3.2 and optimize the search potential for a semileptonically decaying heavy X resonance produced via ggF, DY, or VBF. We then divide the analysis into disjoint categories in order to enhance the search sensitivity.

4.3.10.1 Final Event Selection

The final event selection used in the analysis is defined by the following:

1. Exactly one charged lepton as defined in subsections 4.3.3 and 4.3.4.

2. Lepton veto: no additional loose electron ($p_{\text{T}} > 35$ GeV) or muon ($p_{\text{T}} > 20$ GeV) in the event.

3. Type-I corrected missing transverse momentum $\left(p_{\text{T}}^{\text{miss}}\right)^{\text{Type-I}}$: events are required to have $\left(p_{\text{T}}^{\text{miss}}\right)^{\text{Type-I}} > 80$ GeV for the electron channel and $\left(p_{\text{T}}^{\text{miss}}\right)^{\text{Type-I}} > 40$ GeV for the muon channel to suppress contributions from QCD multijet backgrounds.

4. Leptonic $W^{\pm}$ p_T: the p_T of the reconstructed W_lep must satisfy $p_\mathrm{T} > 200$ GeV in order to select a boosted $W^{\pm}$ topology.

5. Hadronic V/H p_T: the p_T of the reconstructed V_had must satisfy $p_\mathrm{T} > 200$ GeV in order to select a boosted V/H topology.

6. Diboson angular separation: the angular distance between the selected lepton and V_had is required to be $\Delta R > \pi/2$, the difference in the azimuthal angle between V_had and $\left(p_\mathrm{T}^\mathrm{miss}\right)^\mathrm{Type-I}$ is required to be $|\Delta\phi| > 2$, and the difference in the azimuthal angle between V_had and W_lep is required to be $|\Delta\phi| > 2$.

7. b-tag veto: the event is required to have no b-tagged standard jets.

8. ZH veto: to ensure that the selection is disjoint from the $X \to ZH \to \ell\ell b\bar{b}$ search [145], which uses different electron and muon identification selections, we explicitly veto events where a ZH candidate is selected with their criteria.

9. Search region: the search region is defined as $0.7 < m_{WV/WH} < 6.0$ TeV and $20 < m_\mathrm{jet} < 210$ GeV.

4.3.10.2 Final Event Categories

After considering the final event selection, we split the search region into 24 disjoint event categories. By doing so, the sensitivity of the search is enhanced since this allows for discriminating between different signal models based on their final state (WW, WZ, or WH), their production mechanism (ggF, DY, or VBF), or the spin of the resonance (0, 1, or 2). The categories are based on four successive criteria based on the lepton channel, V jet tagging, VBF/$b\bar{b}$/non-$b\bar{b}$ categories, and $\Delta y_{WV/WH}$ categories.

First, we split the event sample based on the lepton flavor of the reconstructed W_lep candidate, defining two channels:

- **Electron channel (e):** The selected lepton is an electron.

- **Muon channel (mu):** The selected lepton is a muon.

Second, we exploit the fact that the jets originating from V/H decays exhibit a two-pronged structure. The analysis is split based on V jet tagging via cuts on the value of the mass-decorrelated N-subjettiness ratio τ_{21}^{DDT} as described in subsection 4.3.5. This defines the following two categories:

- **High Purity (HP):** $\tau_{21}^{\mathrm{DDT}} \leq 0.50$.

- **Low Purity (LP):** $0.50 < \tau_{21}^{\mathrm{DDT}} \leq 0.80$.

Third, to enhance the sensitivity of resonances decaying to $WH \to \ell\nu b\bar{b}$, and to separate events consistent with VBF production, we split the sample three-way based on the value of the DoubleB tagger (as described in subsection 4.3.5) and the presence of VBF-compatible jet candidates described in subsection 4.3.8:

- **VBF-tagged (vbf):** Two candidate VBF jets, $\Delta\eta_{\mathrm{VBF}} > 4$, $m_{\mathrm{jj}}^{\mathrm{VBF}} > 500$ GeV.

- **$b\bar{b}$-tagged (bb):** DoubleB > 0.8, no VBF tag.

- **$b\bar{b}$-untagged (nobb):** DoubleB ≤ 0.8, no VBF tag.

Fourth, to further discriminate all signals against background and distinguish between VBF-produced signals of different spins, we split the sample using the diboson rapidity separation $\Delta y_{WV/WH}$ between the W_{lep} and V_{had} as discussed in subsection 4.3.9:

- **Low $\Delta y_{WV/WH}$ (LDy):** $\Delta y_{WV/WH} < 1.0$.

- **High $\Delta y_{WV/WH}$ (HDy):** $\Delta y_{WV/WH} \geq 1.0$.

This selection defines $2 \times 2 \times 3 \times 2 = 24$ search categories that are referred to with labels such as e-HP-bb-LDy, mu-LP-vbf-HDy, etc.

4.4 Comparison of Simulation to Data

A crucial check on the validity of our selection cuts and categorizations is to compare the MC samples to the data in regions where no signal is expected to be observed. In this section, we review the data to MC comparisons for relevant kinematic distributions by looking at control plots in non-signal regions. We define two control regions of the analysis as follows: a jet mass sideband and a top-enriched control region.

The jet mass sideband applies the final event selection cuts of subsection 4.3.10, but with the m_{jet} selection cuts $20 < m_{\mathrm{jet}} < 70$ GeV or $150 < m_{\mathrm{jet}} < 210$ GeV, so that the V_{had} large-radius jets present do not originate from a corresponding V/H decay in signal events. To correct modeling of fake V jets at low p_{T}, we also define a separate $W + $ jets dominated sideband of $30 < m_{\mathrm{jet}} < 50$ GeV that is used to derive rescaling factors for the $W + $ jets background yields. These rescaling factors are applied to $W + $ jets background yields for the analysis.

The top-enriched control region is used to calibrate the performance of the soft drop algorithm and jet substructure variables on merged bosons. We define this region to be enriched in $t\bar{t}$ and single-t events, where the selected large-radius jet results from an actual hadronically decaying $W^{\pm}$ boson. This is done by applying the selection cuts of subsection 4.3.10, but with an inverted b-tag veto to ensure the presence of at least one standard AK4 b-tagged jet in the event. The resulting event sample is therefore largely dominated by $t\bar{t}$ and single-t events.

4.4.1 Control Plots

The control plots presented here run over the full dataset from Run 2. These plots were produced using separate MC samples for each year that are combined and weighted by their individual luminosities.

4.4.1.1 Control Plots in the Jet Mass Sideband Region

Figure 4.12 shows kinematic variables related to the lepton candidate, such as the lepton p_{T}, lepton η, $p_{\mathrm{T}}^{\mathrm{miss}}$, p_{T} and transverse mass of the W_{lep} candidate, and diboson invariant mass $m_{WV/WH}$, for the muon channel. For figure 4.13, the distributions show V_{had} and VBF forward jet variables, with the jet p_{T}, jet η, m_{jet}, τ_{21}^{DDT}, DoubleB of the large-radius jet from the V_{had} candidate, $\Delta\eta_{\mathrm{VBF}}$, $m_{\mathrm{jj}}^{\mathrm{VBF}}$, N_{jets}, and $\Delta y_{WV/WH}$. The rescaling factors applied to the $W + $ jets background yields are 0.96, 0.86, and 0.79 for 2016, 2017, and 2018, respectively.
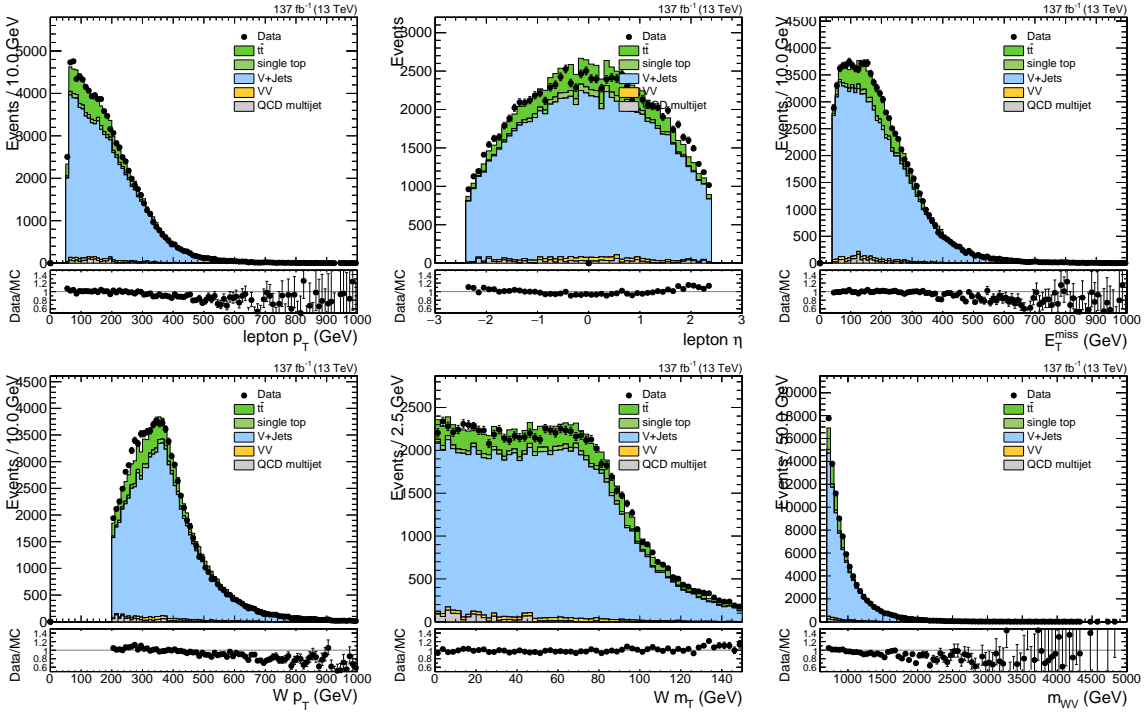
Figure 4.12: Comparison plots between data and MC from Run 2 for different W_{lep}-related observables, in the muon channel of the jet mass sideband. Top row: lepton p_{T}, lepton η, $p_{\mathrm{T}}^{\mathrm{miss}}$. Bottom row: p_{T} of the leptonic $W^{\pm}$, transverse mass of the leptonic $W^{\pm}$, diboson invariant mass.
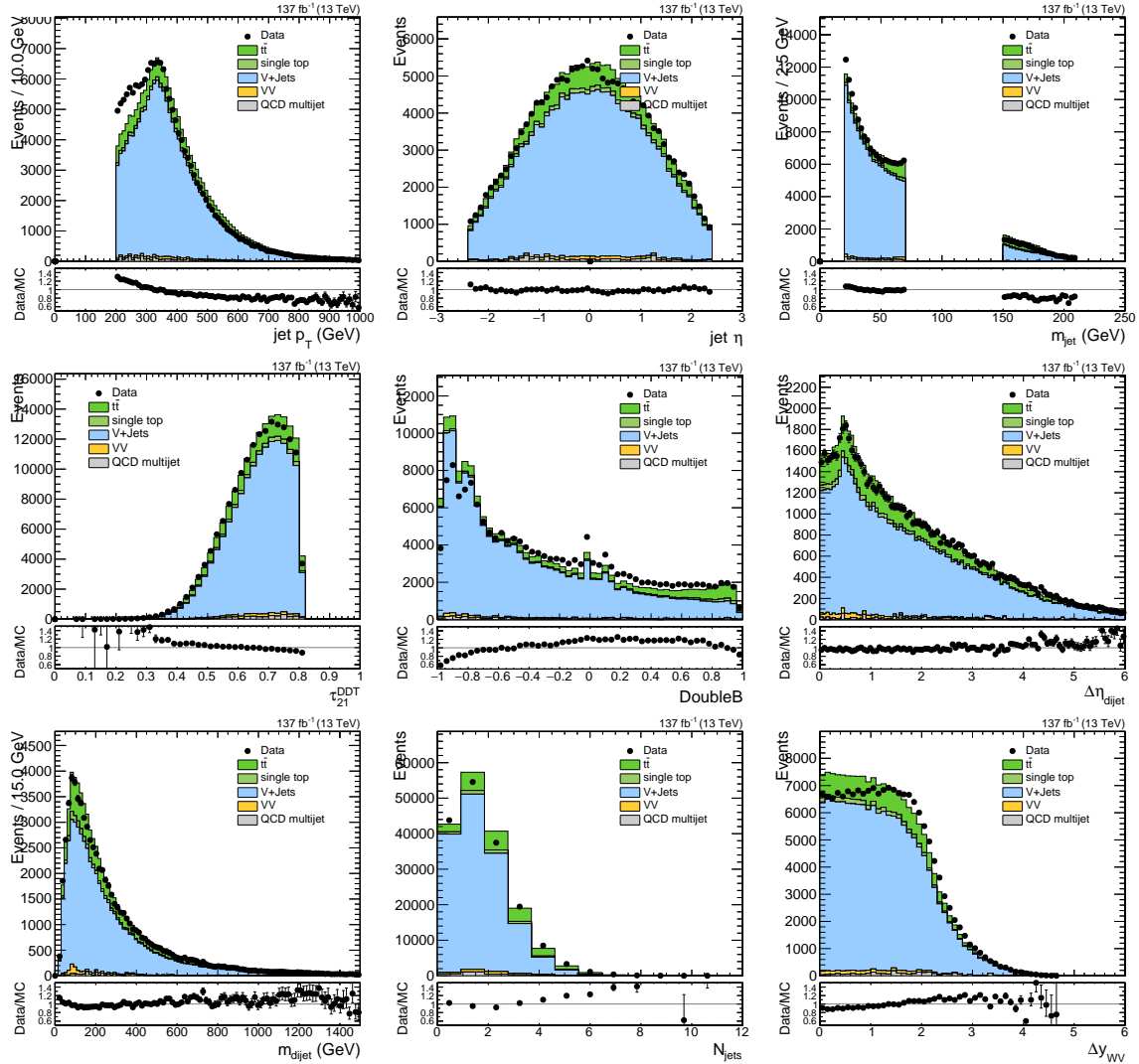
Figure 4.13: Comparison plots between data and MC from Run 2 for different V_{had} and VBF forward jet variables, in the jet mass sideband. Top row: jet p_{T}, jet η, m_{jet} (soft drop mass). Middle row: τ_{21}^{DDT}, DoubleB tagger of the selected V_{had} candidate, separation in η of the VBF forward jets. Bottom row: invariant mass of the VBF jets, number of selected standard jets, rapidity separation between the reconstructed bosons.

4.4.1.2 Control Plots in the Top-Enriched Control Region

Figure 4.14 shows control plots of lepton-related observables in the top-enriched control region, with the lepton p_T, lepton η, p_T^{miss}, p_T and transverse mass of the W_{lep} candidate, and diboson invariant mass $m_{WV/WH}$, for the muon channel. In figure 4.15, distributions of variables related to the V_{had} and VBF forward jets are shown, such as the jet p_T, jet η, m_{jet}, τ_{21}^{DDT}, DoubleB of the large-radius jet from the V_{had} candidate, $\Delta\eta_{\text{VBF}}$, $m_{\text{jj}}^{\text{VBF}}$, N_{jets}, and $\Delta y_{WV/WH}$.
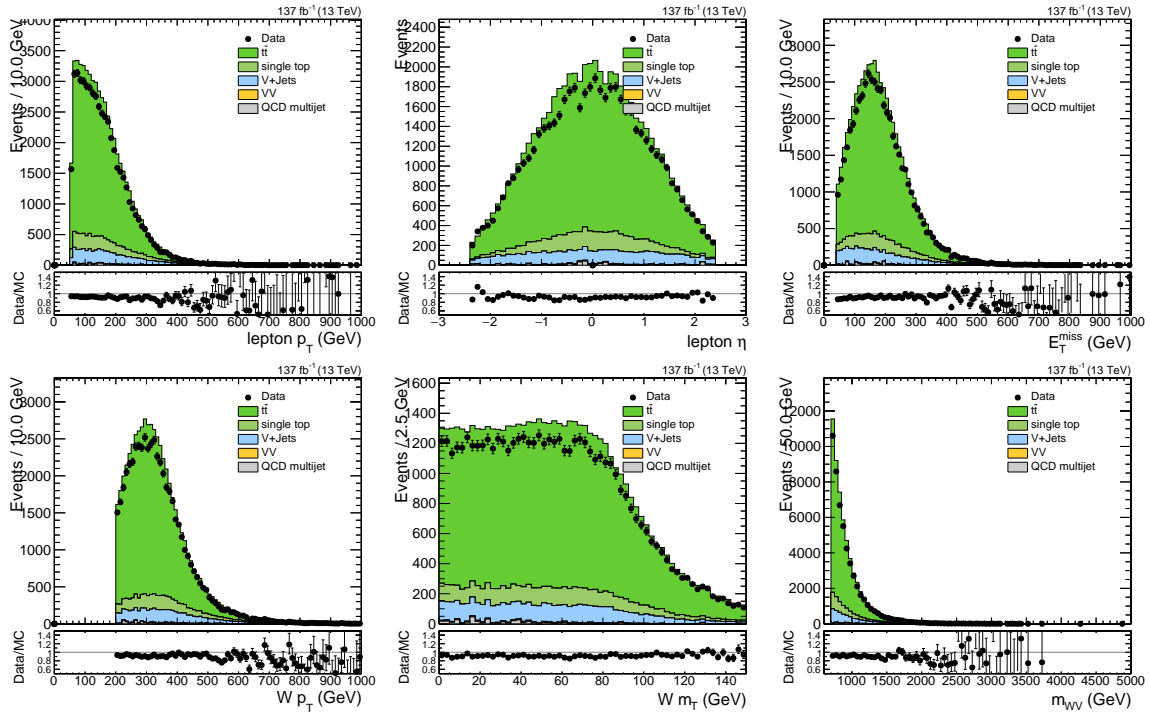
Figure 4.14: Comparison plots between data and MC from Run 2 for different W_{lep}-related observables, in the muon channel of the top-enriched control region. Top row: lepton p_T, lepton η, p_T^{miss}. Bottom row: p_T of the leptonic $W^{\pm}$, transverse mass of the leptonic $W^{\pm}$, diboson invariant mass.
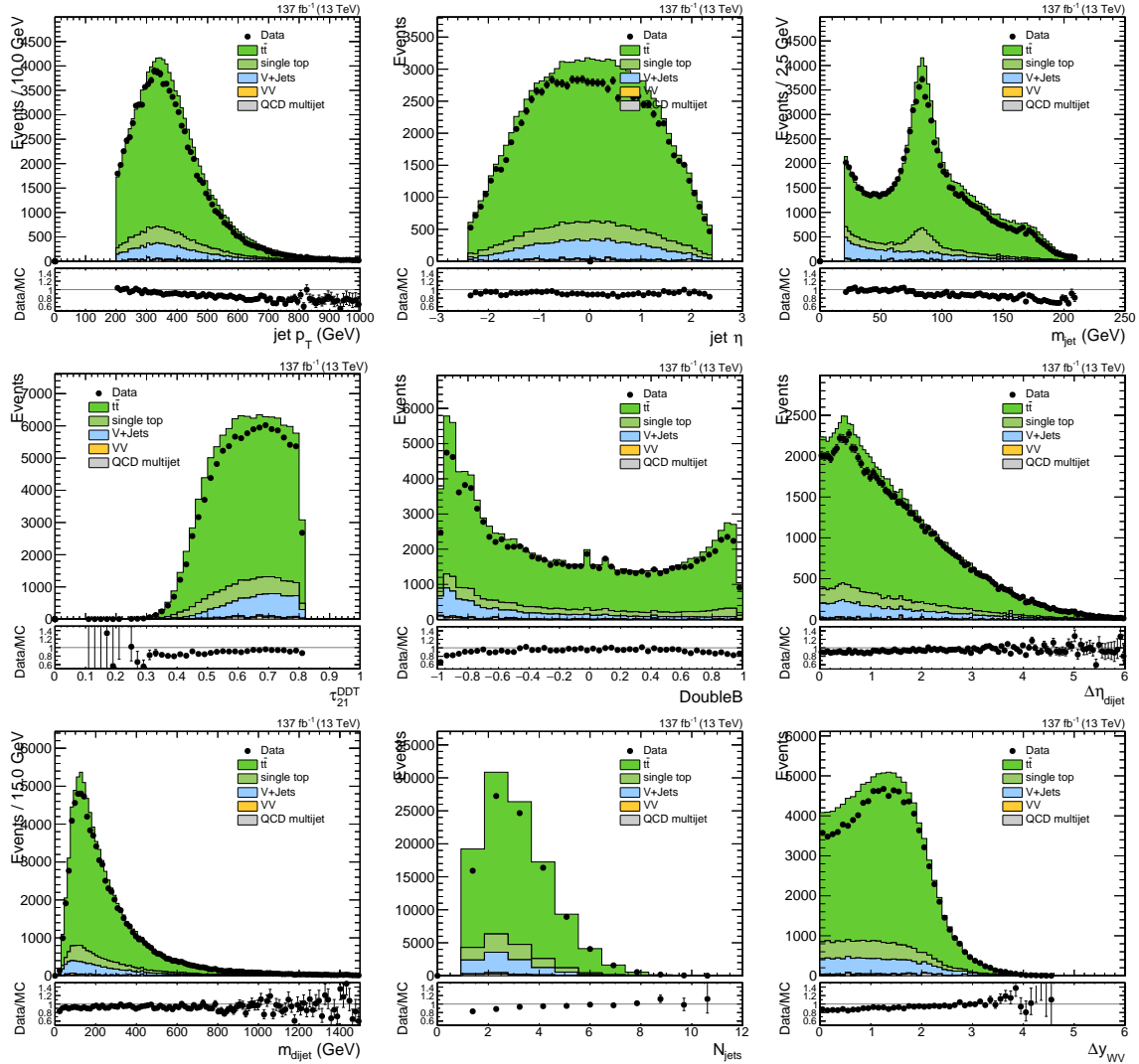
Figure 4.15: Comparison plots between data and MC from Run 2 for different V_{had} and VBF forward jet variables, in the top-enriched control region. Top row: jet p_{T}, jet η, m_{jet} (soft drop mass). Middle row: τ_{21}^{DDT}, DoubleB tagger of the selected V_{had} candidate, separation in η of the VBF forward jets. Bottom row: invariant mass of the VBF jets, number of selected standard jets, rapidity separation between the reconstructed bosons.

4.4.2 Mitigation of Non-operational HCAL Modules in Run 2

During Run 319077, the two HCAL towers HEM15 and HEM16 were non-operational, and the data obtained from the electron channel for the $W \rightarrow \ell\nu$ candidate in those regions results in an excess of events that can be seen in figure 4.16. To remedy this, we exclude events recorded after Run 319077 if the lepton candidate is an electron and falls within the region $-1.55 < \phi < -0.9$ and $-2.5 < \eta < -1.479$. Removing these events results in the correct behavior of the relevant kinematic variables for the electron candidate, and only discards 0.8% of events in the signal region.
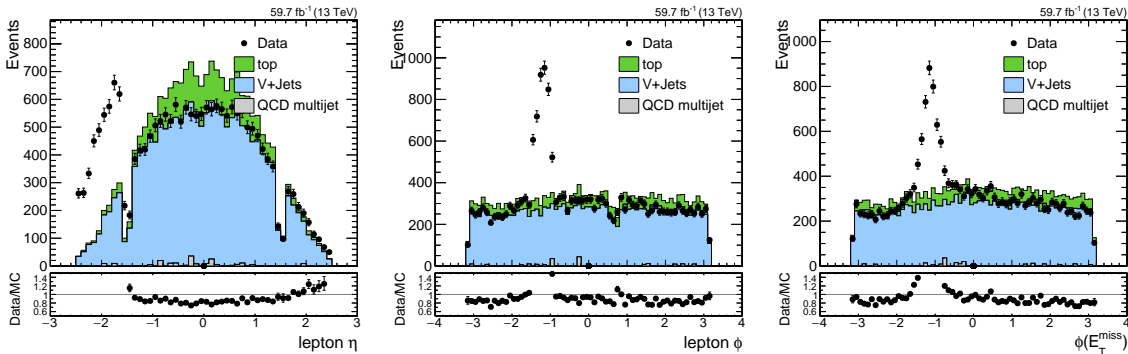
Figure 4.16: Comparison plots between 2018 data (including the HEM15 and HEM16 after Run 319077) and 2017 MC for the electron η, electron ϕ, and ϕ of the missing transverse momentum, in the jet mass sideband.

4.5 V-tagging Scale Factors

As mentioned previously, the top-enriched control region is obtained by inverting the b-tag veto, thereby requiring the presence of at least one b-tagged jet in the event. The region is used to calibrate the performance of the soft drop algorithm and jet substructure variables on merged bosons. In particular, the scale factors for the V-tagging selection in the HP and LP categories are derived in this region using a dedicated fit of the soft drop jet mass spectrum. We also include events with $\tau_{21}^{\mathrm{DDT}} > 0.80$ as a separate category denoted by NP

to avoid bias resulting from only selecting HP and LP events. This allows us to accurately model the $W^\pm$ peak for all categories used in the analysis.

4.5.1 Fit Model

Our fit model relies on two classes of events in the top-enriched region. The first corresponds to resonant $W^\pm$ events that are the result of a top decay, with the b jet outside of the AK8 jet. The second class consists of non-resonant events resulting from random combinations of a merged AK8 jet. To account for both of these types of events, we employ a fit model that uses a double crystal ball (DCB) for the $W^\pm$, another DCB for the partially reconstructed top quark, an exponential, and a uniform distribution. Once the fit is performed, we then merge the second DCB, exponential, and uniform distributions to form a single non-resonant shape.

The crystal ball function is a composite function consisting of a power-law stitched to a Gaussian core [146], defined by

$$f_{\mathrm{CB}}(x; \mu, \sigma, \alpha, n) = N \begin{cases} e^{-\frac{1}{2}\left(\frac{x-\mu}{\sigma}\right)^2}, & \frac{x-\mu}{\sigma} > -\alpha, \\ \left(\frac{n}{|\alpha|}\right)^n e^{-\frac{|\alpha|^2}{2}} \left(\frac{n}{|\alpha|} - |\alpha| - \frac{x-\mu}{\sigma}\right)^{-n} & \frac{x-\mu}{\sigma} \leq -\alpha, \end{cases} \tag{4.16}$$

where α is a parameter that determines the cutoff between the Gaussian core and the power-tail, n is the exponent of the powertail, and N is a normalization factor. The double crystal ball instead has powertails on both sides of the Gaussian core, and is given by

$$f_{\mathrm{DCB}}(x; \mu, \sigma, \alpha_1, \alpha_2, n_1, n_2) = N \begin{cases} \left(\frac{n_1}{|\alpha_1|}\right)^{n_1} e^{-\frac{|\alpha_1|^2}{2}} \left(\frac{n_1}{|\alpha_1|} - |\alpha_1| - \frac{x-\mu}{\sigma}\right)^{-n_1} & \frac{x-\mu}{\sigma} \leq -\alpha_1, \\ e^{-\frac{1}{2}\left(\frac{x-\mu}{\sigma}\right)^2}, & -\alpha_1 < \frac{x-\mu}{\sigma} < \alpha_2, \\ \left(\frac{n_2}{|\alpha_2|}\right)^{n_2} e^{-\frac{|\alpha_2|^2}{2}} \left(\frac{n_2}{|\alpha_2|} - |\alpha_2| - \frac{x-\mu}{\sigma}\right)^{-n_2} & \frac{x-\mu}{\sigma} \geq \alpha_2, \end{cases}$$

$$\tag{4.17}$$

where α_1 and n_1 are the powertail parameters for the left side of the tail, and α_2 and n_2 are

the powertail parameters for the right side of the tail.

The explicit form of the fit model f in each category (HP, LP, NP) is given by

$$f(\text{HP}) = r S^{\text{HP}} N_W^{\text{HP}} f_W^{\text{HP}} + N_{\text{NR}}^{\text{HP}} f_{\text{NR}}^{\text{HP}}, \tag{4.18}$$

$$f(\text{LP}) = r S^{\text{LP}} N_W^{\text{LP}} f_W^{\text{LP}} + N_{\text{NR}}^{\text{LP}} f_{\text{NR}}^{\text{LP}}, \tag{4.19}$$

$$f(\text{NP}) = r \left[N_{\text{Total}} - S^{\text{HP}} N_W^{\text{HP}} - S^{\text{LP}} N_W^{\text{LP}} \right] f_W^{\text{NP}} + N_{\text{NR}}^{\text{NP}} + f_{\text{NR}}^{\text{NP}}, \tag{4.20}$$

where f_W is the resonant distribution for the $W^\pm$ jet, f_{NR} is the non-resonant shape, r is a global scale factor accounting for lepton efficiency and luminosity, N_W^{HP}, N_W^{LP}, N_W^{NP}, and N_{Total} are the number of expected events in simulation for all three categories and the total number of events, and S^{HP} and S^{LP} are scale factors for the HP and LP categories, respectively. This normalization is chosen to account for migration between categories.

4.5.2 Fit Results

We perform the fit of equations 4.18-4.20 in a jet mass window of 20-145 GeV. The resulting post-fit distributions for all three years and the full Run 2 dataset and MC samples can be seen in figure 4.17. Table 4.4 shows the V-tagging scale factors in the HP and LP categories obtained by the fit for all years and the full Run 2 dataset, and table 4.5 shows the scale factors for the jet mass scale and resolution again for all years and for the full Run 2 dataset. For the analysis we use the Run 2 scale factors in the computation of the expected signal normalizations, and the Run 2 uncertainties are used as a flat systematic uncertainty for the signal normalizations. The scale factors for the jet mass scale and resolution are used as corrections to the signal shapes and $W^\pm$ peak for the resonant background templates.

92
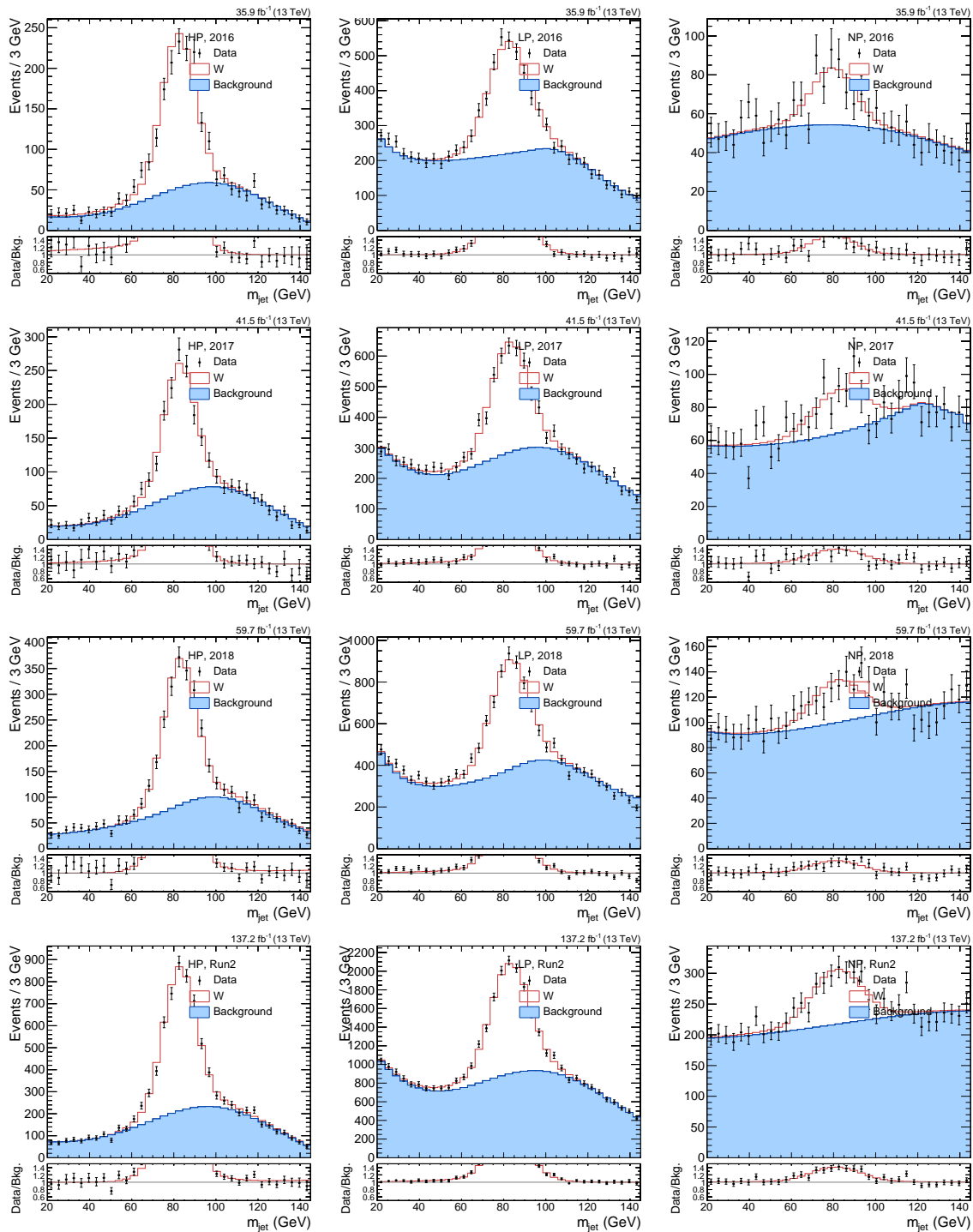
Figure 4.17: Post-fit distributions for the background MC and dataset for all three years and Run 2 (from top to bottom: 2016, 2017, 2018, Run 2), and for the three purity categories (from left to right: HP, LP, NP).

Year	HP	LP
2016	1.02 ± 0.04 (stat) ± 0.03 (syst)	0.98 ± 0.02 (stat) ± 0.03 (syst)
2017	0.83 ± 0.04 (stat) ± 0.03 (syst)	1.10 ± 0.02 (stat) ± 0.03 (syst)
2018	0.87 ± 0.03 (stat) ± 0.03 (syst)	1.08 ± 0.02 (stat) ± 0.03 (syst)
Run 2	0.88 ± 0.02 (stat) ± 0.03 (syst)	1.06 ± 0.02 (stat) ± 0.03 (syst)

Table 4.4: V-tagging scale factors for the HP and LP categories obtained from the fit process.

Year	Scale	Resolution
2016	0.991 ± 0.003 (stat) ± 0.002 (syst)	1.00 ± 0.03 (stat) ± 0.02 (syst)
2017	0.989 ± 0.003 (stat) ± 0.002 (syst)	1.07 ± 0.04 (stat) ± 0.02 (syst)
2018	0.987 ± 0.002 (stat) ± 0.002 (syst)	1.08 ± 0.03 (stat) ± 0.02 (syst)
Run 2	0.990 ± 0.002 (stat) ± 0.002 (syst)	1.08 ± 0.02 (stat) ± 0.02 (syst)

Table 4.5: Scale factors for the jet mass scale and resolution obtained from the fit process.

4.5.3 Momentum Dependence

We also conduct a study on the dependence of the V-tagging scale factors as a function of the diboson invariant mass $m_{WV/WH}$ to apply a systematic uncertainty on the V-tagging process. To do so, we measure the V-tagging scale factors for the full Run 2 dataset, but in three different binnings of $m_{WV/WH}$. We apply a low-mass binning of $[0.6, 0.8$ TeV], a mid-mass binning of $[0.8, 1.0$ TeV], and a high-mass binning of $[1.0, 1.5$ TeV]. The resulting post-fit distributions for all three binnings and for all purity categories may be see in figure 4.18.

The resulting scale factors, scale, and resolution as a function of $m_{WV/WH}$ are plotted in figure 4.19 (left). We observe no significant dependence for V-tagging as a function of $m_{WV/WH}$ for the three binnings used in this study. The V-tagging efficiency as a function of $m_{WV/WH}$ is also studied, which can be seen in figure 4.19 (right). This allows us to place an upper limit on the uncertainty of the p_{T} dependence. The fact that the scale factor is small and the simulation agrees with the data means that the scale factor will never be larger than the variations of the efficiency versus $m_{WV/WH}$. At high mass, we may therefore set an uncertainty equal to the difference of the signal efficiency at high mass versus low mass.
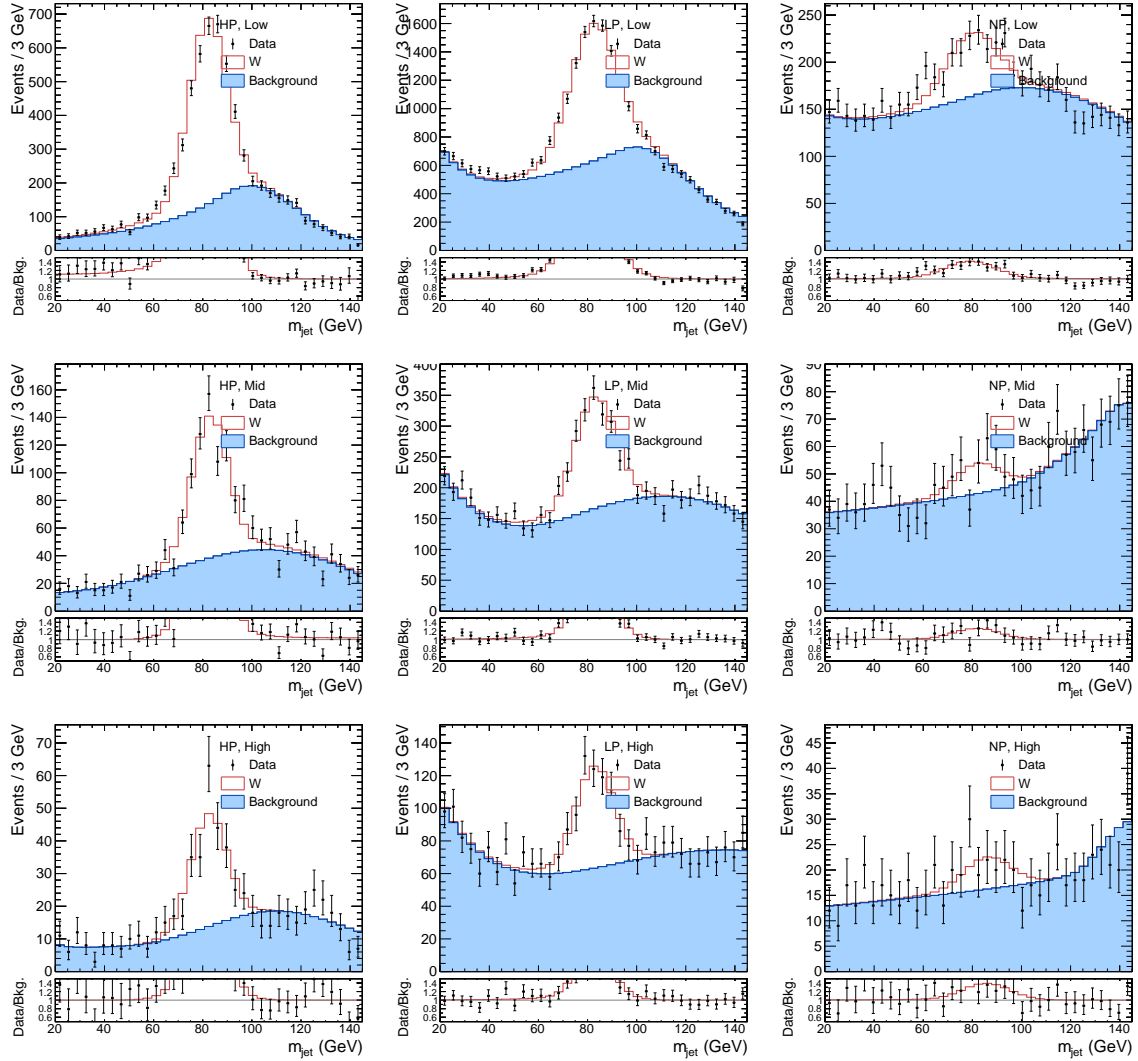
Figure 4.18: Post-fit distributions for three bins of the diboson invariant mass $m_{WV/WH}$ (from top to bottom: $[0.6, 0.8~\mathrm{TeV}]$, $[0.8, 1.0~\mathrm{TeV}]$, and $[1.0, 1.5~\mathrm{TeV}]$), in the three purity categories (from left to right: HP, LP, NP), for the full Run 2 dataset.
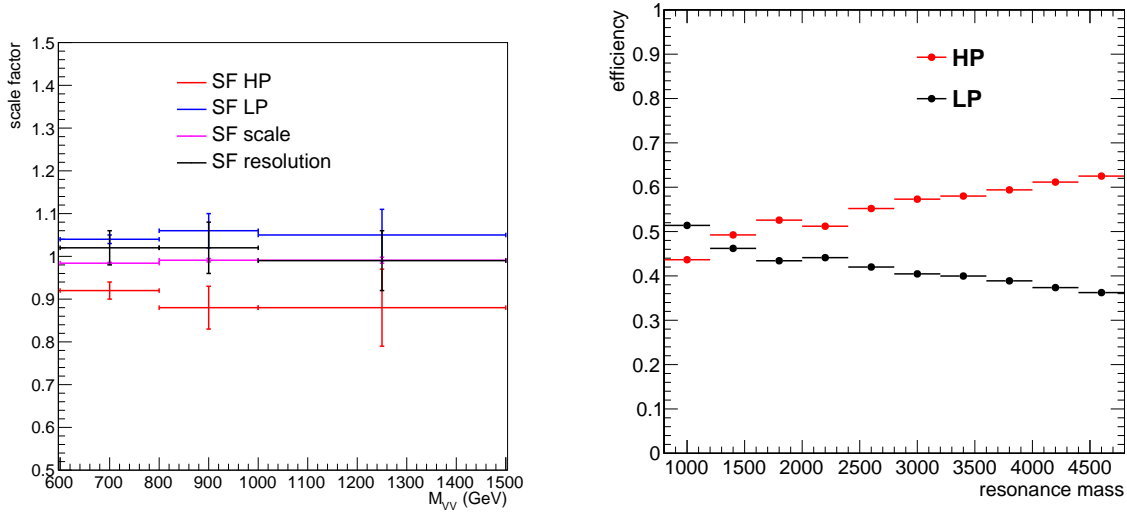
Figure 4.19: Left: Plot of all scale factors as a function of the diboson invariant mass $m_{WV/WH}$. Right: Plot of the V-tagging efficiency as a function of $m_{WV/WH}$.

4.6 Two-dimensional Fit Process

In a previous version of this analysis, the background estimation process relied upon the sideband of the groomed jet mass m_{jet} to estimate the background in the signal region. This method is known as the α ratio method, as described by references [106, 107]. It involves fitting the background contributions separately on the jet mass sidebands where no signal events are expected, then using a transfer function derived in simulation to extrapolate the background in the signal region. The transfer function α_{MC} is defined by

$$\alpha_{\text{MC}}(m_{WV/WH}) = \frac{F_{\text{MC,SR}}^{W+\text{jets}}(m_{WV/WH})}{F_{\text{MC,SB}}^{W+\text{jets}}(m_{WV/WH})}, \tag{4.21}$$

where $F(m_{WV/WH})$ is the probability density function used to model the $m_{WV/WH}$ spectrum in the signal and sideband regions. For both regions, the parameterization of the background takes the form $F(x) \propto e^{c_0 x + c_1/x}$. The $W+$jets background distribution in the signal region is then obtained by rescaling $F_{\text{Data,SB}}^{W+\text{jets}}(m_{WV/WH})$ by $\alpha_{\text{MC}}(m_{WV/WH})$. The resonant background

contributions from $W + V/t$ are added on top of the obtained $W + \text{jets}$ background in the signal region. We then associate an uncertainty to the background prediction and select it to be large so that it covers the known differences between data and simulation, while also leaving it floating in the fitting process. Such differences are related to modeling effects that affect the known dependence of jet mass and jet p_T, as the ungroomed jet mass m_j follows the relation $\langle m_j^2 \rangle \propto p_\text{T}^2 R^2$, with jet radius R [147].

For this analysis, we instead use a novel 2D modeling method that uses a combined fit for the resonance mass $m_{WV/WH}$ and the jet groomed mass m_jet, which captures the correlations in the fit during the likelihood minimization process. Figure 4.20 shows an illustration of the sideband region accessible to the 2D fit process versus the traditional jet mass sidebands used by the α method. The 2D fit method allows for a simultaneous fit of the jet mass and diboson resonance sidebands due to its access to the full 2D sidebands in the $m_{WV/WH}$-m_jet plane, whereas the α method is restricted to modeling background in the $m_{WV/WH}$ and m_jet spectra in separate steps. Since the search region as defined in section 4.3.10 is the same for all signal models and accounts for the different resonances they may produce, the 2D fit also allows for treating the signal models on equal footing.

Thus, the 2D fit has the following advantages compared to the traditional α method previously used:

1. The sideband as seen in figure 4.20 is two-dimensional, thereby allowing for a simultaneous fit of the jet mass and resonance sidebands. This better constrains the background, which allows for improved sensitivity of the search.

2. The ability to add nuisance parameters that affect jet mass and resonance mass simultaneously, which allows us to account for the mismodeling of the correlation between the variables.

3. Being able to use the full jet mass line-shape to extract the signal instead of using jet mass windows, providing better discrimination between $W^\pm$ and Z peaks.

97
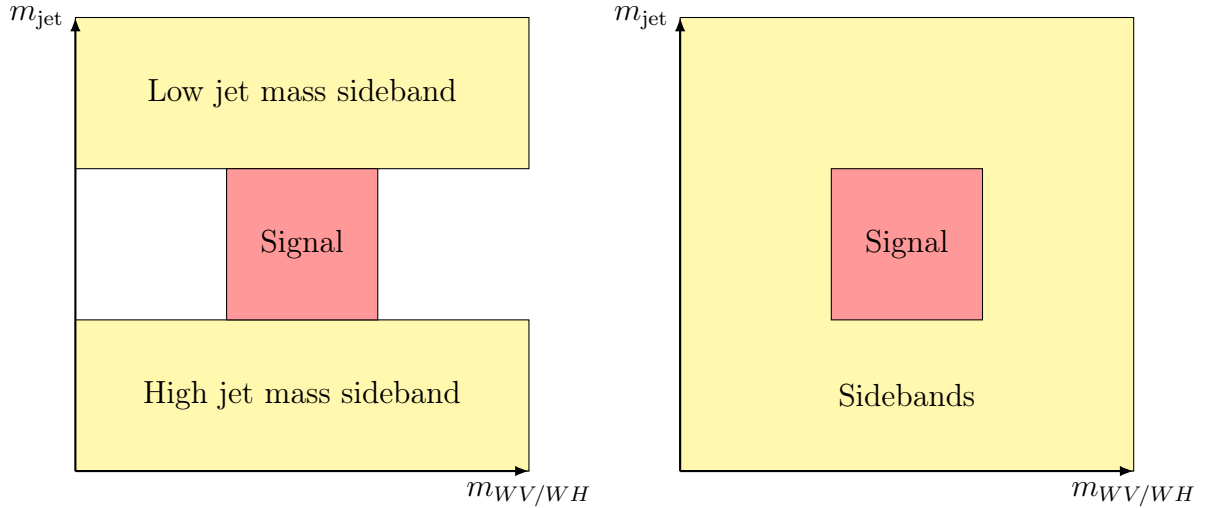
Figure 4.20: Sideband regions of the fit for traditional sideband background estimation methods (left) versus the sideband regions in the 2D fit approach (right). The 2D fit method performs a simultaneous fit in the 2D sideband region in the $m_{WV/WH}$-m_{jet} plane as opposed to modeling background in the $m_{WV/WH}$ and m_{jet} spectra in separate steps.

4. Simultaneous fitting of all WV/WH signals in the jet mass sideband, therefore allowing for easy implementation of exotic models such as Heavy Vector Triplets.

There are three types of shapes to consider for the 2D fit in the $m_{WV/WH}$-m_{jet} plane. The first is that of a signal process, for which we expect to see a resonance in both $m_{WV/WH}$ and m_{jet}. In this case, the correlations are related to the scale and resolution of the jet. For a background process in which there is a hadronically decaying $W^{\pm}$, Z, or top, we expect to observe a resonance in the m_{jet} dimension corresponding to the decay (i.e., peaks near the $W^{\pm}/Z$ masses and the top mass), but a falling spectrum in the $m_{WV/WH}$ dimension. Lastly, if we instead have a $W + \text{jets}$ process or QCD background, there will be broad background distributions in both $m_{WV/WH}$ and m_{jet}, for which the shapes are correlated.

As mentioned previously, two main classes of background are considered for this analysis, as classified based on resonant or non-resonant behavior in the m_{jet} spectrum:

- **Resonant ($W + V/t$):** Background events in which the jet mass shape is peaking as a $W^{\pm}$, Z, H, or t resonance in m_{jet} with a falling spectrum in $m_{WV/WH}$. The resonant peak in m_{jet} is due to partially or fully merged top jets and diboson events in which one boosted boson is reconstructed into a jet. This background class is therefore defined by requiring that both generated quarks from a hadronic V decay are located within $\Delta R = 0.8$ of the selected large-radius jet. The main contribution is $t\bar{t}$ events, along with SM diboson and single-t production events.

- **Non-resonant ($W + \text{jets}$):** Background events in which the jet is produced by the hadronization of one or more partons not originating from a vector boson. The dominant SM contribution is from $W + \text{jets}$ events, but additional contributions come from $t\bar{t}$ events in which the selected large-radius jet corresponds to a random combination of jets from the event rather than a $W^{\pm}$ or a top.

The templates are derived from MC samples for both signal and background as enumerated in section 4.2. These samples were created in successive campaigns over 2016, 2017, and 2018, and are separated by their production year. Previous versions of this analysis kept the templates separated by year, but for this iteration of the analysis we merge the samples for all three years and weight them by their respective luminosities to obtain combined Run 2 samples. This has the benefit of providing better modeling of templates in categories with low statistics.

4.6.1   Signal Modeling

Because the MC samples for the various signals used in this analysis only sample several points for the resonance mass m_{X}, we employ interpolation methods to model the signal for any arbitrary resonance mass m_{X} within the range 0.8-4.5 TeV. To do so, we derive each of the parameters for the signal shapes as functions of m_{X}, as well as the signal yield per pb of cross section as a function of m_{X}.

4.6.1.1 Signal Shapes

Each signal model takes the same functional form in the two-dimensional $m_{WV/WH}$-m_{jet} space. The signals are parameterized in 2D as the product of the two 1D $m_{WV/WH}$ and m_{jet} shapes for the jet mass and the resonance mass given by

$$P_{\mathrm{sig}}(m_{WV/WH}, m_{\mathrm{jet}}|m_{\mathrm{X}}) = P_{WV/WH}(m_{WV/WH}|m_{\mathrm{X}}, \boldsymbol{\theta}_1)P_{\mathrm{jet}}(m_{\mathrm{jet}}|m_{\mathrm{X}}, \boldsymbol{\theta}_2), \qquad (4.22)$$

where $\boldsymbol{\theta}_1$ and $\boldsymbol{\theta}_2$ are the nuisance parameters. In principle, the signal shape parameters depend on the resonance mass m_{X}. Both shapes are modeled separately based on the jet purity (HP/LP), rapidity (HDy/LDy), and bb/nobb/vbf categories. However, the e and mu categories are merged for the signal modeling process. To parameterize the shapes, we perform separate fits for the 1D shapes in the $m_{WV/WH}$ and m_{jet} spectra, then interpolate the parameters for each shape as a function of m_{X} to obtain $P_{\mathrm{sig}}(m_{WV/WH}, m_{\mathrm{jet}}|m_{\mathrm{X}})$ for arbitrary m_{X} between 1 and 4.5 TeV using uncorrelated polynomial functions. A DCB shape is used for $P_{WV/WH}(m_{WV/WH}|m_{\mathrm{X}}, \boldsymbol{\theta}_1)$ for all categories, while the jet resonance shape $P_{\mathrm{jet}}(m_{\mathrm{jet}}|m_{\mathrm{X}}, \boldsymbol{\theta}_2)$ uses a DCB for the HP categories, and the sum of a DCB and an exponential for the LP categories to properly capture the behavior of the low-mass tail of the distribution.

Figure 4.21 shows the DCB parameters (μ, σ, α_1, α_2) for the $m_{WV/WH}$ shapes in the 12 categories used to model the 2D signal shapes. The DCB parameters for the m_{jet} shapes are shown in figure 4.22.

In some categories there are not enough events present that result in a smooth fit for the parameters of $P_{WV/WH}(m_{WV/WH}|m_{\mathrm{X}}, \boldsymbol{\theta}_1)$ or $P_{\mathrm{jet}}(m_{\mathrm{jet}}|m_{\mathrm{X}}, \boldsymbol{\theta}_2)$. For example, signals that are VBF-produced will not have a sufficient number of events present for the bb/nobb categories. Because the signal parameters do not vary significantly between production modes, we allow for substituting non-VBF signal shapes with VBF shapes, and vice versa:

- DY $W' \to WZ$ shapes are used for VBF $W' \to WZ$ in the LP-bb-LDy (for m_{jet}) and

LP-nobb-HDy (for $m_{WV/WH}$) categories.

- VBF $W' \to WZ$ shapes are used for DY $W' \to WZ$ in the LP-vbf-HDy (for m_{jet}) and LP-bb-HDy (for $m_{WV/WH}$) categories.

- ggF $\phi \to WW$ shapes are used for VBF $\phi \to WW$ in the LP-bb categories.

- ggF $G_{\mathrm{bulk}} \to WW$ shapes are used for VBF $G_{\mathrm{bulk}} \to WW$ in the HP-bb-LDy and HP-vbf-LDy categories (for m_{jet}) and in the HP-nobb-HDy and HP-vbf-HDy (for $m_{WV/WH}$).

- ggF $G_{\mathrm{bulk}} \to WW$ shapes are used for DY $Z' \to WW$ in all categories.

- ggF $G_{\mathrm{bulk}} \to WW$ shapes are used for VBF $Z' \to WW$ in the bb-LDy categories.

For brevity, we show various signal parameters and shapes in the nobb category only. Figure 4.23 shows the $m_{WV/WH}$ signal shapes for non-VBF signals. For figure 4.24, we show the $m_{WV/WH}$ signal shapes for the VBF signals. In figure 4.25, the m_{jet} signal shapes are shown for the non-VBF signals. Finally, figure 4.26 shows the m_{jet} signal shapes for the VBF signals. We also perform a closure test by converting the $m_{WV/WH}$ and m_{jet} projections of the $m_{\mathrm{X}} = 2$ TeV version of the template of each signal model into 1D histograms, and compare them with the corresponding weighted MC distributions. An example of this is presented in figure 4.27 with the DY $G_{\mathrm{bulk}} \to WW$ signal.

4.6.1.2 Signal Yields

The process for parameterizing the signal yield as a function of m_{X} is similar to obtaining the parameters for the signal shapes. We compute the yield per pb of cross section for each mass point from our signal MC samples, then fit the result with a polynomial interpolation to obtain a function of m_{X}. Again, we only show figures for the nobb category. Figures 4.28 and 4.29 show the expected yields per pb of cross section for non-VBF and VBF signals, respectively.
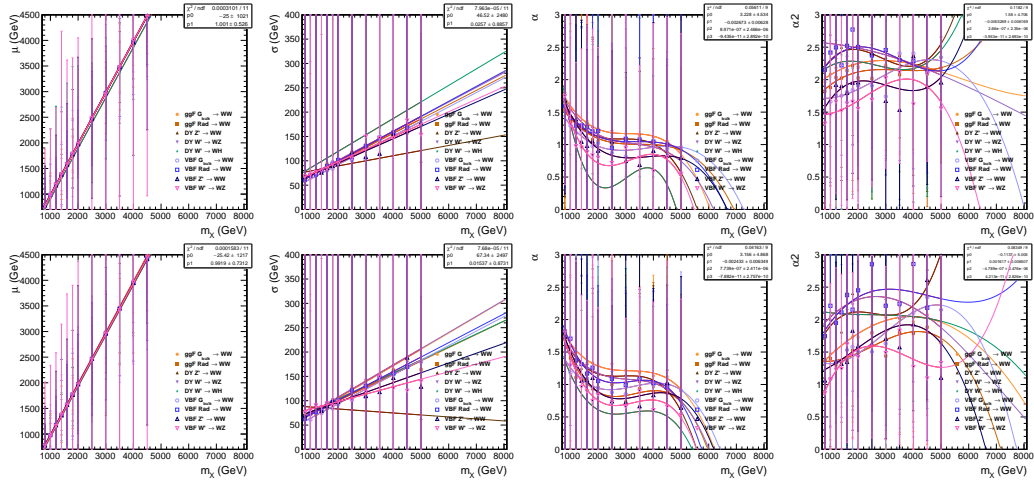
Figure 4.21: DCB parameters (from left to right: μ, σ, α_1, α_2) for the diboson reconstructed mass $m_{WV/WH}$ as a function of m_X. Top to bottom: HP-nobb-LDy, LP-nobb-LDy.
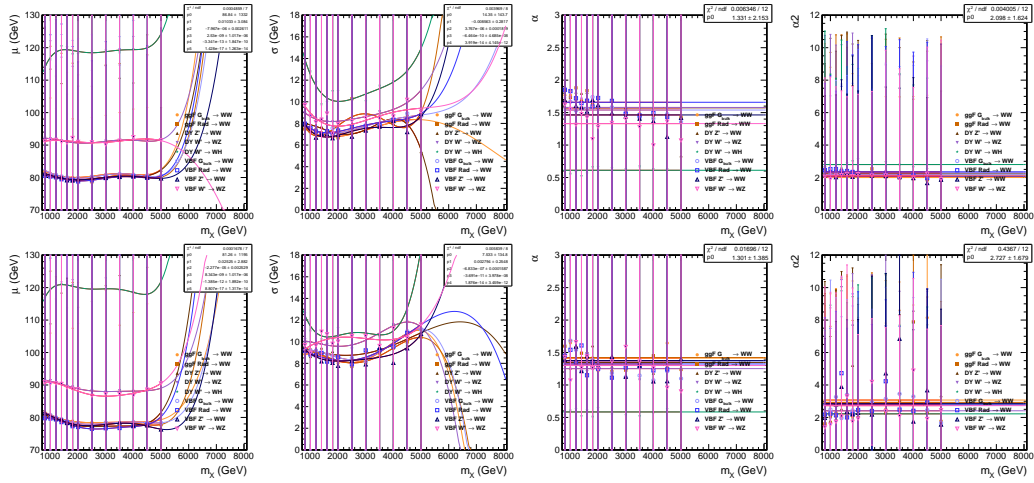
Figure 4.22: DCB parameters (from left to right: μ, σ, α_1, α_2) for the jet mass m_{jet} as a function of m_X. Top to bottom: HP-nobb-LDy, LP-nobb-LDy.
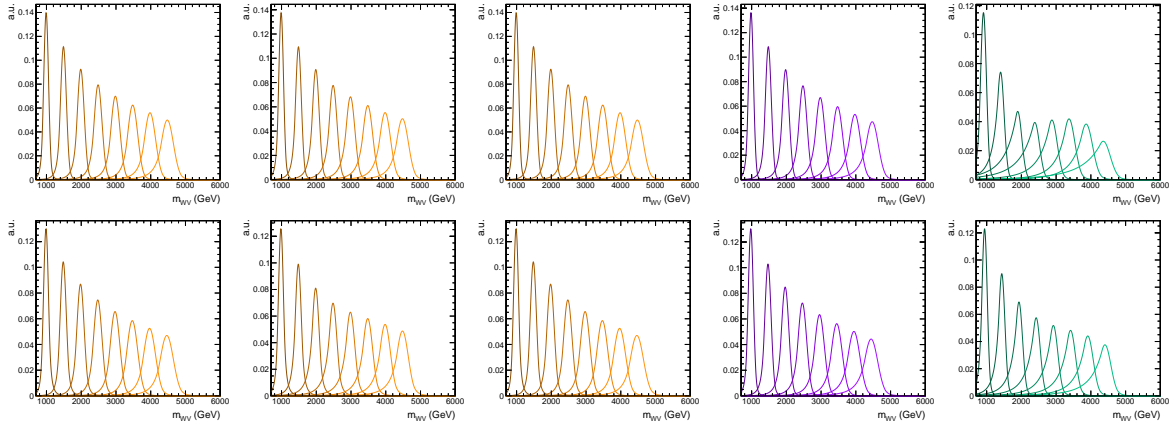
Figure 4.23: Signal shapes for the diboson reconstructed mass $m_{WV/WH}$ for ggF- and DY-produced signals, for 8 values of m_X. From left to right: $G_{\text{bulk}} \to WW$, $\phi \to WW$, $Z' \to WW$, $W' \to WZ$, $W' \to WH$. Top to bottom: HP-nobb-LDy, LP-nobb-LDy.
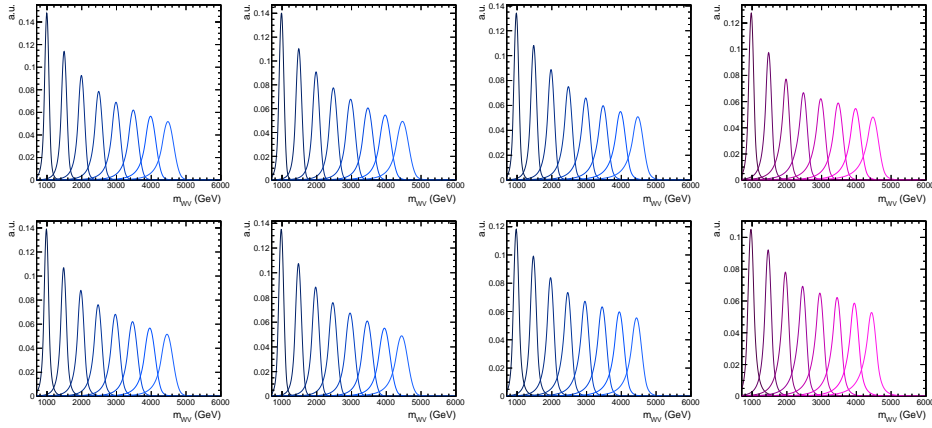
Figure 4.24: Signal shapes for the diboson reconstructed mass $m_{WV/WH}$ for VBF-produced signals, for 8 values of m_X. From left to right: $G_{\text{bulk}} \to WW$, $\phi \to WW$, $Z' \to WW$, $W' \to WZ$. Top to bottom: HP-nobb-LDy, LP-nobb-LDy.
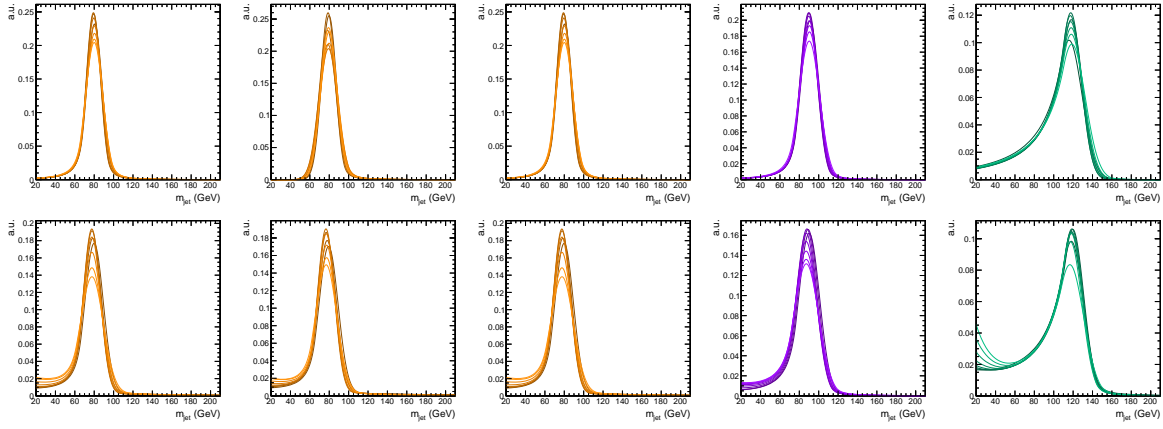
Figure 4.25: Signal shapes for the soft drop jet mass m_{jet} for ggF- and DY-produced signals, for 8 values of m_X. From left to right: $G_{\text{bulk}} \to WW$, $\phi \to WW$, $Z' \to WW$, $W' \to WZ$, $W' \to WH$. Top to bottom: HP-nobb-LDy, LP-nobb-LDy.
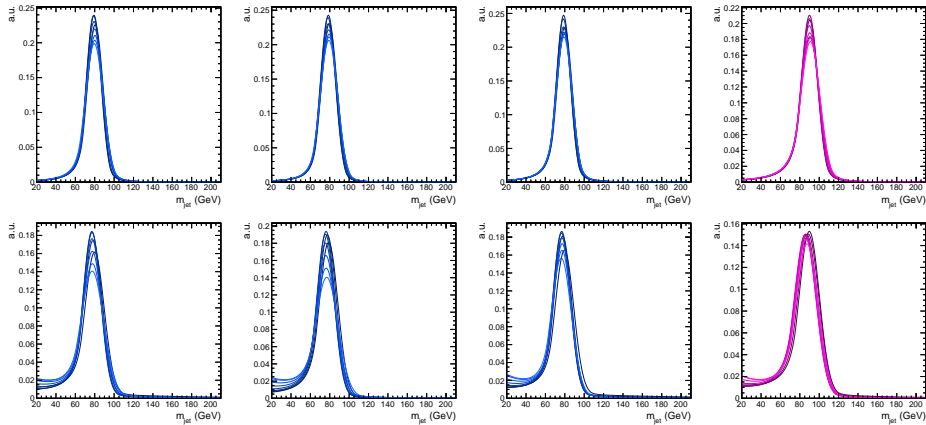
Figure 4.26: Signal shapes for the soft drop jet mass m_{jet} for VBF-produced signals, for 8 values of m_X. From left to right: $G_{\text{bulk}} \to WW$, $\phi \to WW$, $Z' \to WW$, $W' \to WZ$. Top to bottom: HP-nobb-LDy, LP-nobb-LDy.
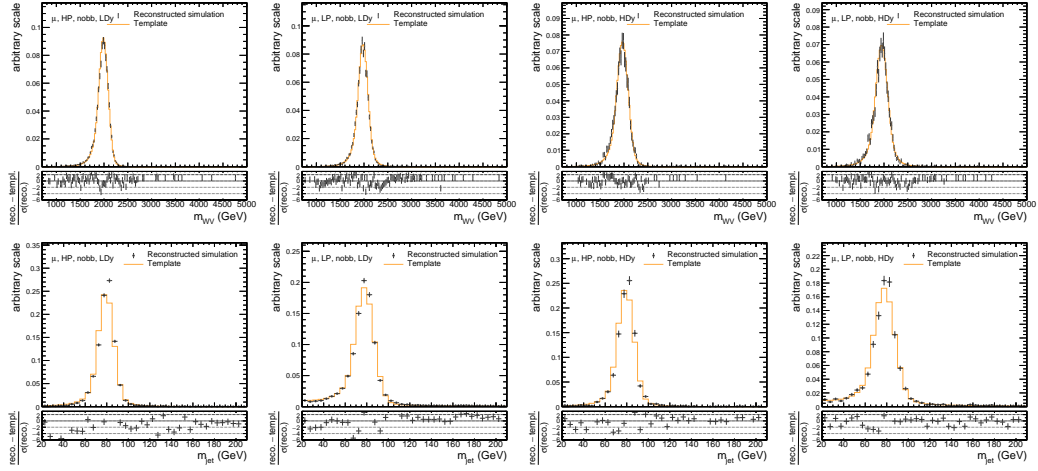
Figure 4.27: Comparison between the ggF $G_{\mathrm{bulk}} \to WW$ template for $m_{G_{\mathrm{bulk}}} = 2$ TeV (solid line) and the histogram from weighted simulated events (points) in the nobb muon event categories. Top to bottom: $m_{WV/WH}$ projections, m_{jet} projections.
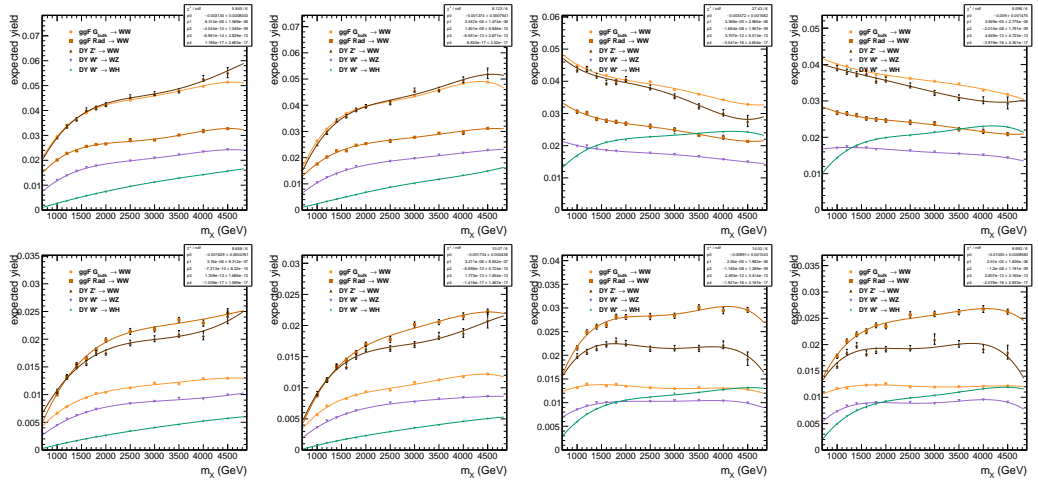
Figure 4.28: Parameterizations of the expected yields per pb of cross section for ggF- and DY-produced signals as a function of m_X. Left to right: mu-HP, e-HP, mu-LP, e-LP. Top to bottom: nobb-LDy, nobb-HDy.

105
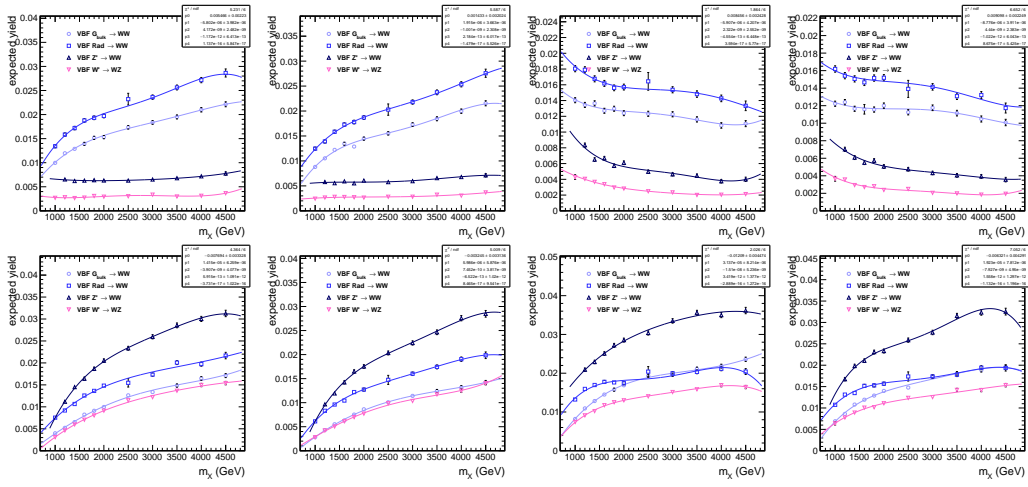
Figure 4.29: Parameterizations of the expected yields per pb of cross section for VBF-produced signals as a function of m_{X}. Left to right: mu-HP, e-HP, mu-LP, e-LP. Top to bottom: nobb-LDy, nobb-HDy.

106

4.6.2 Background Modeling

Unlike the signal shapes described in the previous section, both the resonant and non-resonant background modeling involve 2D histograms rather than analytical functions. This is in part due to the challenges encountered with the modeling process, which is a result of the low statistics for the background MC samples after applying the selection cuts.

4.6.2.1 Non-resonant Background Templates

The non-resonant background templates are modeled with conditional products, taking the form

$$P_{W+\text{jets}}(m_{WV/WH}, m_{\text{jet}}) = P_{WV/WH}(m_{WV/WH}|m_{\text{jet}}, \boldsymbol{\theta}_1)P_{\text{jet}}(m_{\text{jet}}|\boldsymbol{\theta}_2). \tag{4.23}$$

We derive a 1D template for the m_{jet} distribution $P_{\text{jet}}(m_{\text{jet}}|\boldsymbol{\theta}_2)$, which we then multiply with a 2D shape from $P_{WV/WH}(m_{WV/WH}|m_{\text{jet}}, \boldsymbol{\theta}_1)$ for the $m_{WV/WH}$ distribution.

For the 2D $m_{WV/WH}$ shape, we use a specialized Gaussian kernel method in order overcome the low statistics encountered for the background MC events. Standard Gaussian methods were found to be ineffective at capturing peaks in the 2D plane, as they would result in a smearing of the peaks from reconstructed simulation events. To remedy this, we employ a method in which we use a partially generated diboson invariant mass $m_{WV/WH}^{\text{part}}$, which is defined as the four-vector sum of the reconstructed W_{lep}, and a generated jet. The generated jet is made by clustering generated particle candidates with $\Delta R < 1.2$ around reconstructed jets using the anti-k_T algorithm, with a distance parameter of $R = 0.8$.

Because the generated jets are used in place of the reconstructed V_{had}, we must make use of a detector response function to accurately model reconstruction of the simulated jets. This is done in simulation by estimating the Gaussian mean and deviation of the resolution of $m_{WV/WH}/m_{WV/WH}^{\text{part}}$ in bins of the generated jet p_T, which can be seen in figure 4.30. We then begin generating the template by populating the m_{jet} spectrum using a coarse binning, with 16 bins used in m_{jet}. For each event in a slice of the m_{jet} spectrum, we add a 1D

Gaussian onto the partial mass with scale shifted by the detector response and width equal to the Gaussian resolution, as defined by

$$P_i(m_{WV/WH}) = \frac{w_i}{\sqrt{2\pi}\sigma} \exp\left[-\frac{1}{2}\left(\frac{m_{WV/WH} - s \cdot m_{WV/WH}^{\text{part}}}{\sigma}\right)^2\right], \qquad (4.24)$$

where w_i is the event weight, and s and σ are the scale and resolution parameters obtained from the detector response.
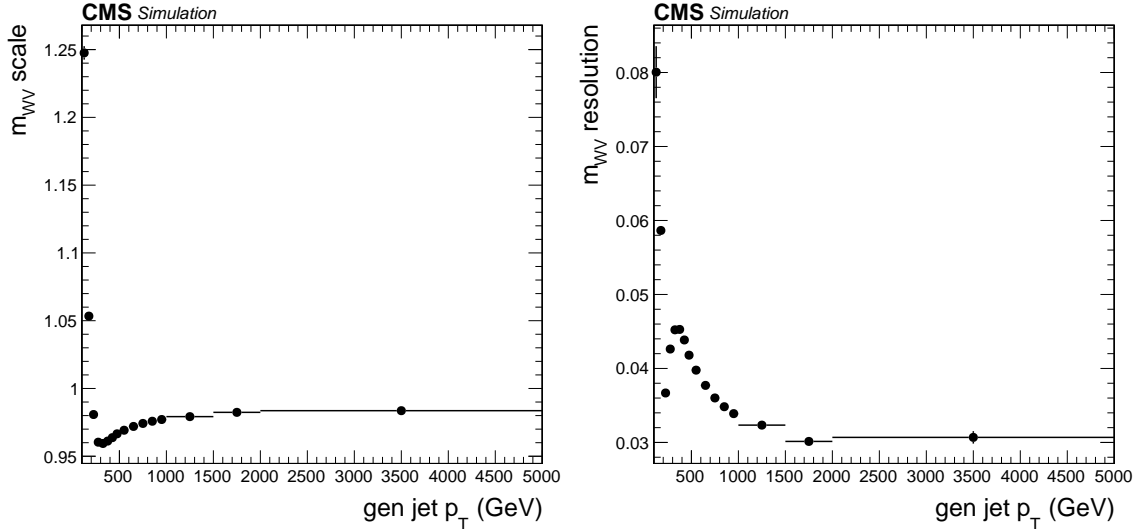
Figure 4.30: Scale (left) and resolution (right) of $m_{WV/WH}$ as a function of the generated jet p_{T}.

Another issue encountered with the low statistics of the MC samples is the lack of events at higher values of $m_{WV/WH}$. To address this, we perform a smoothing of the tails of the $m_{WV/WH}$ shape with a power-law function in each bin of m_{jet}. We then populate the 2D histogram with values from the $m_{WV/WH}$ shape in each m_{jet} bin, with the power-law functions sampled above thresholds of 1.1 TeV to 1.6 TeV depending on the category.

To ensure that the template is conditional with respect to m_{jet}, each histogram slice corresponding to one crude bin of m_{jet} is normalized. We then interpolate over the coarsely binned m_{jet} histogram for each $m_{WV/WH}$ bin using a spline, which is used to populate the 2D

histogram. As a final step, we normalize each m_{jet} slice again to ensure the conditionality of the template.

Ideally, this process of generating the 2D conditional templates would be done for all 24 categories as defined in subsection 4.3.10.2. However, this is met with more difficulties due to the low statistics provided by the MC samples. To resolve this issue, we merge categories together based on whether or not they exhibit similar behavior. We consider various metrics of behavior between categories, such as the correlation between $m_{WV/WH}$ and m_{jet}, as well as the average jet p_{T} as a function of the jet mass, which is shown in figure 4.31 between the four combinations of HP/LP and nobb/bb categories. The behavior is similar enough between the categories that they may be considered for merging. For this analysis, we merge the e/mu and bb/nobb/vbf categories while keeping the HP/LP and HDy/LDy categories separate, for a total of four 2D conditional non-resonant templates.
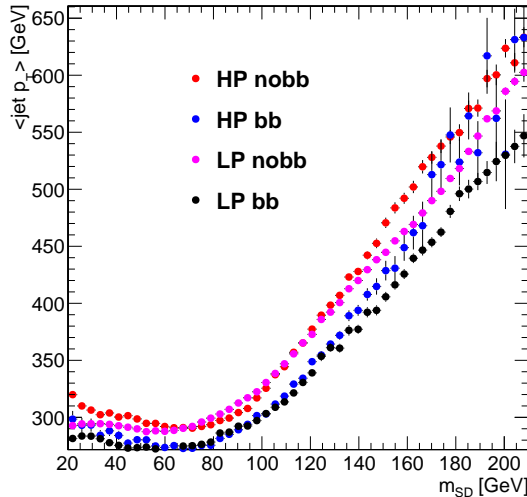
Figure 4.31: Average p_{T} of the jet as a function of the jet mass m_{jet} compared between the four combinations of HP/LP and nobb/bb categories for the non-resonant background MC samples.

Prior to creating the 2D conditional templates, a reweighting procedure is applied in the jet mass sideband region for the $m_{WV/WH}$ spectrum in order to ensure that the templates

accurately capture the behavior of the background events. We again merge the e and mu categories for this process due to their similar behavior, but for other categories such as nob-b/bb/vbf, we derive separate weighting functions for the $m_{WV/WH}$ spectrum. The categories are then merged to create the four conditional 2D templates after the weighting process. The reweighting function takes the form $f(m_{WV/WH}) = a + b/m_{WV/WH}$ to ensure that the weights behave as expected in the asymptotic limit, and the fit coefficients are derived by fitting the function to the ratio of data to MC. From this we obtain the weights w_i of equation 4.24. Figure 4.32 shows the $m_{WV/WH}$ distributions from which the weights are derived in the nobb category.

As a check on the closure of the 2D conditional template building process, we plot the projection of the templates on the $m_{WV/WH}$ spectrum versus the weighted MC distributions. Figure 4.33 shows the resulting comparison between the templates and the MC samples for each of the four merged categories, which show good agreement between each other.

The remaining step to complete the conditional product $P_{W+\text{jets}}(m_{WV/WH}, m_{\text{jet}})$ is to obtain the 1D template for $P_{\text{jet}}(m_{\text{jet}}|\boldsymbol{\theta}_2)$. Rather than using a kernel method as with the 2D conditional template, we instead use a coarsely binned histogram of weighted MC events for m_{jet}, and fit the result with a spline. The spline is then used to interpolate the $P_{\text{jet}}(m_{\text{jet}}|\boldsymbol{\theta}_2)$ template with the final m_{jet} binning. In this case, we also do not merge any of the 24 categories and keep the templates separate. Figure 4.34 shows the resulting 1D templates for the nobb category compared to the weighted MC distributions used to obtain them.

The final non-resonant templates are then obtained from the product of the 2D conditional template with the 1D jet mass shape. Figure 4.35 shows the 2D templates the nobb category. To better visualize the differences between each of the categories, figure 4.36 shows comparisons of the $m_{WV/WH}$ and m_{jet} projections of the templates.
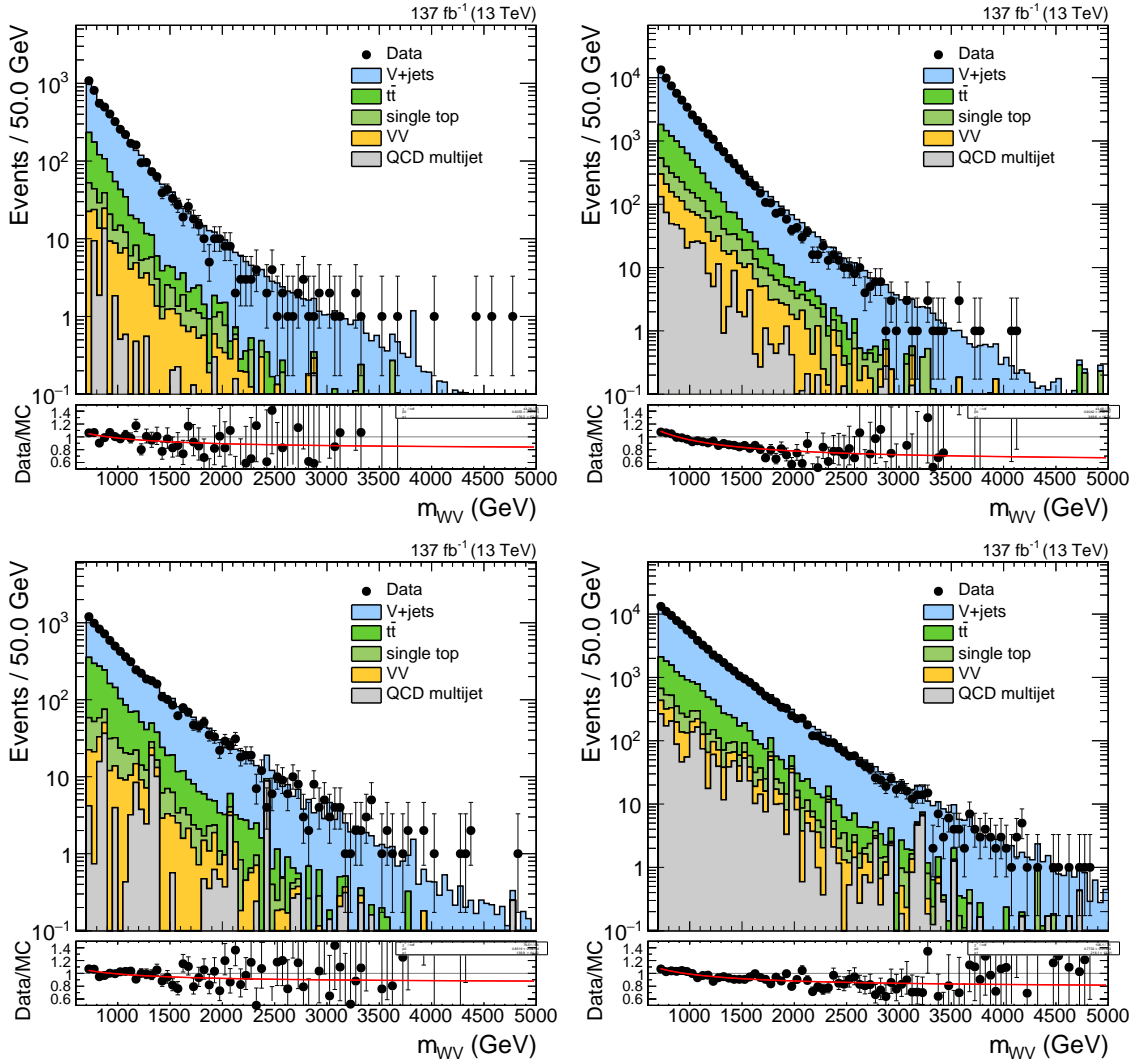
Figure 4.32: Plots of the $m_{WV/WH}$ spectra for the full Run 2 data and MC samples in the jet mass sideband for the nobb category, with the e and mu categories merged. After merging the e and mu categories, the remaining categories are kept separate and the ratio of data to MC is fitted with a function of the form $f(m_{WV/WH}) = a + b/m_{WV/WH}$. The resulting weights for each event w_i are then used in equation 4.24 when building the conditional 2D templates. Left to right: HP-LDy-nobb, LP-LDy-nobb, HP-HDy-nobb, LP-HDy-nobb.
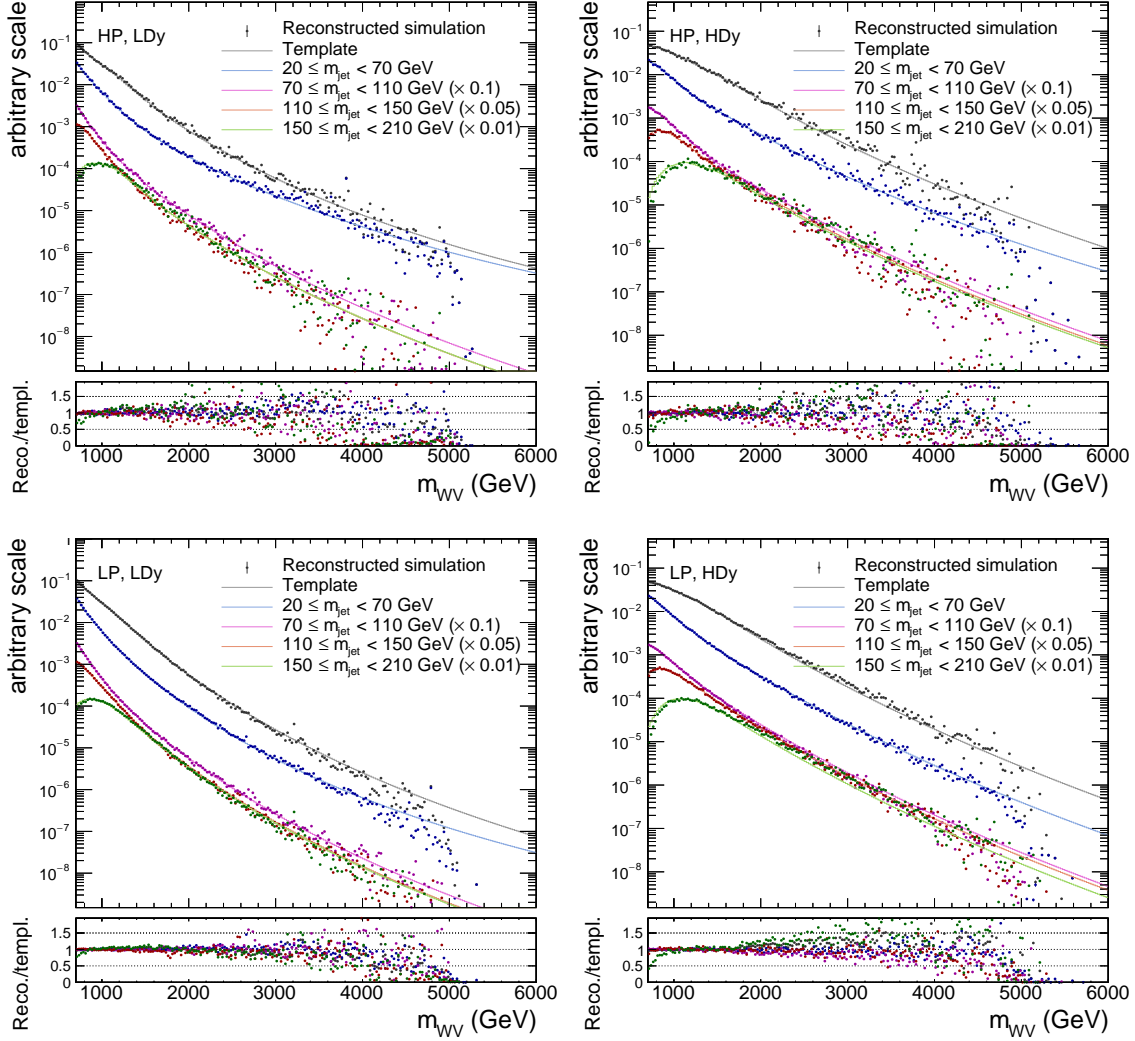
Figure 4.33: Comparison of the $m_{WV/WH}$ projection of the 2D conditional non-resonant background templates (solid lines) and the weighted MC events (points), for the HP-LDy (top left), HP-HDy (top right), LP-LDy (bottom left), and LP-HDy (bottom right) merged categories. Four separate m_{jet} ranges are plotted, with one corresponding to the full m_{jet} range, and three corresponding to the sub-ranges.

112
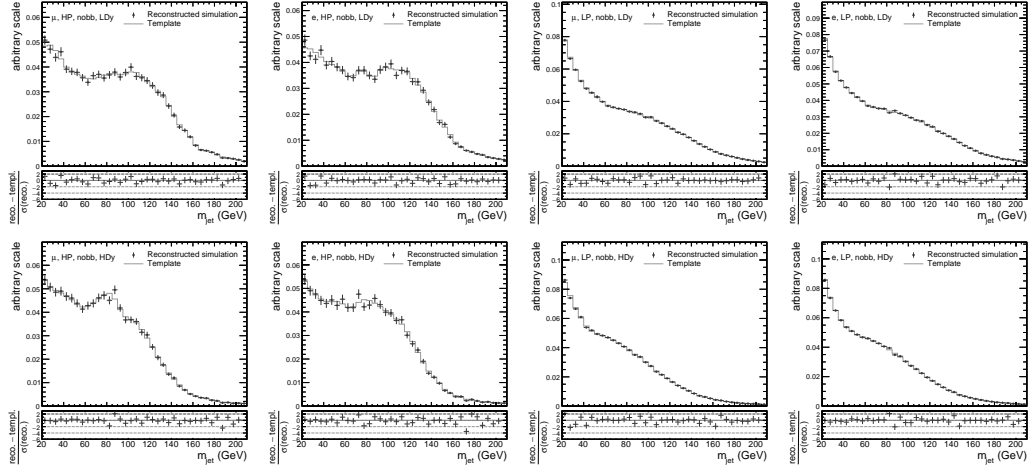
Figure 4.34: Comparison of the 1D m_{jet} templates for the non-resonant background (solid line) and the weighted MC distributions (points). Left to right: mu-HP, e-HP, mu-LP, e-LP. Top to bottom: nobb-LDy, nobb-HDy.
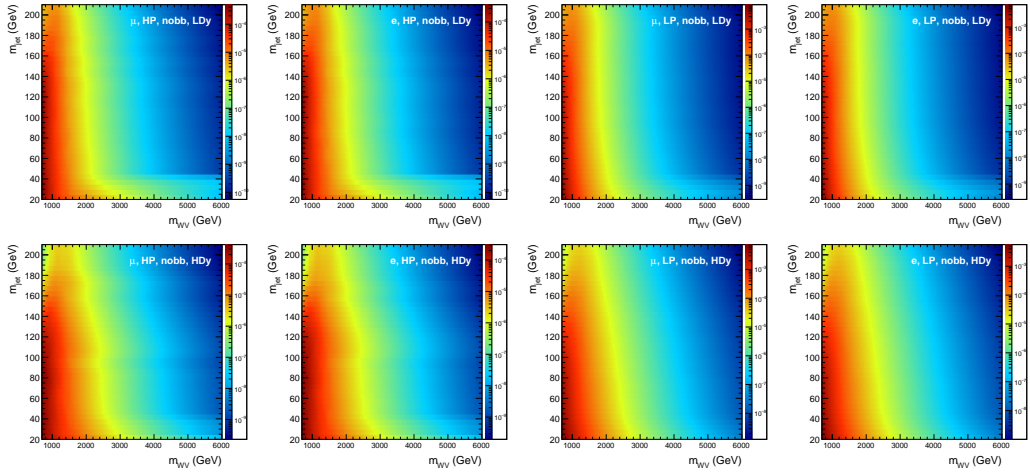
Figure 4.35: Final 2D non-resonant templates for the nobb category. Left to right: mu-HP, e-HP, mu-LP, e-LP. Top to bottom: nobb-LDy, nobb-HDy.
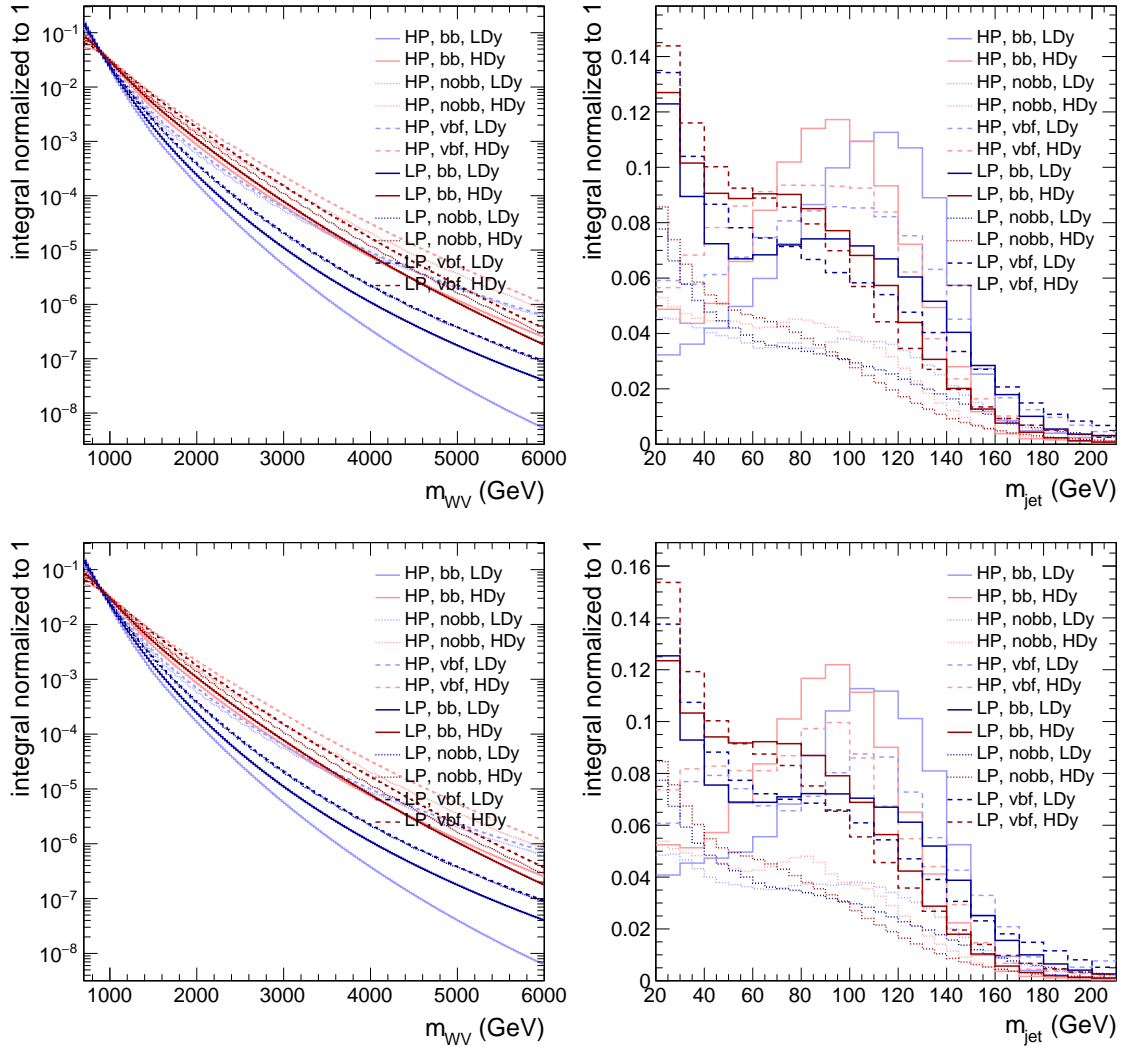
Figure 4.36: Comparisons of projections of the 2D non-resonant templates onto the $m_{WV/WH}$ (left) and m_{jet} (right) spectra, separated by e (top) and mu (bottom) contributions for each category.

4.6.2.2 Resonant Background Templates

The 2D templates in this case are very similar to the non-resonant templates, with a conditional product of the form

$$P_{W+V/t}(m_{WV/WH}, m_{\text{jet}}) = P_{WV/WH}(m_{WV/WH}|m_{\text{jet}}, \boldsymbol{\theta}_1)P_{\text{jet}}(m_{\text{jet}}|\boldsymbol{\theta}_2). \qquad (4.25)$$

As in the non-resonant case, we derive a 1D template for the m_{jet} distribution $P_{\text{jet}}(m_{\text{jet}}|\boldsymbol{\theta}_2)$ and multiply the result with a 2D shape from $P_{WV/WH}(m_{WV/WH}|m_{\text{jet}}, \boldsymbol{\theta}_1)$ for the $m_{WV/WH}$ distribution.

The 2D conditional template $P_{WV/WH}(m_{WV/WH}|m_{\text{jet}}, \boldsymbol{\theta}_1)$ is constructed in a slightly different manner compared to the non-resonant background. In this case, there is no reweighting of the $m_{WV/WH}$ spectrum as there was with the non-resonant templates. Additionally, while this method also makes use of the kernel method for populating the histograms of the templates, we do not use fine binning for m_{jet} because the $m_{WV/WH}$ spectrum for the resonant background templates only depends on whether or not we are in the $W^{\pm}$ peak or the top peak of the m_{jet} spectrum. Thus, we perform the resonant template fitting process in only two bins of m_{jet} for LP categories, and only one bin of m_{jet} for the HP categories. This allows us to overcome the issues that occur due to the low statistics of the top MC samples, and we build 12 templates for the resonant background by only merging the e and mu categories.

As with the non-resonant background, we smooth the high-$m_{WV/WH}$ tails by refitting the tail of the $m_{WV/WH}$ shape in each m_{jet} bin using a power-law function. The lower boundary for populating the histogram depends on the category due to the differences between the MC statistics and the turn-on regions. We use 1.1 TeV for the HP-vbf-LDy and LP-vbf-LDy categories, 1.2 TeV for the HP-bb-HDy, HP-bb-LDy, HP-vbf-HDy, and LP-bb-LDy categories, and 1.4 TeV for all other categories.

We perform a closure test similar to the one done on the non-resonant background templates, in which we compare the $m_{WV/WH}$ projection of the conditional templates against

the MC events used to derive them. Figure 4.37 shows the comparisons between the 2D resonant conditional templates for the nobb category (with e and mu separated) versus the MC samples. As in the non-resonant case, we find good agreement between the templates and the MC.
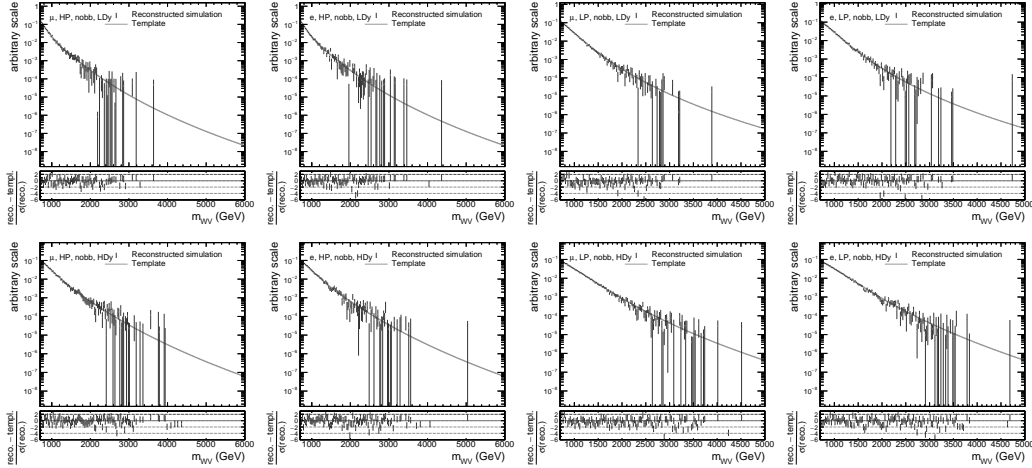
Figure 4.37: Comparison of the $m_{WV/WH}$ projection of the 2D conditional resonant background templates (solid lines) and the weighted MC events (points). Left to right: mu-HP, e-HP, mu-LP, e-LP. Top to bottom: nobb-LDy, nobb-HDy.

The 1D jet mass templates are constructed to capture the resonant behavior of the $W^\pm$ and top peaks in the m_{jet} spectrum. We use an analytic fit for the interpolation process for all 24 categories of the analysis, with the sum of two DCBs used for the HP categories, and the sum of two DCBs and an exponential for the LP categories. The fits obtained for the nobb category can be seen in figure 4.38. These fits are then used to populate the histograms for the 1D templates using the desired binning for m_{jet}. The comparisons between the 1D templates and the MC distributions are shown in figure 4.39.

The final resonant templates produced by the conditional product may be seen in figure 4.40. As was done with the non-resonant templates, figure 4.41 shows the comparisons of the $m_{WV/WH}$ and m_{jet} projections of the templates for each category.
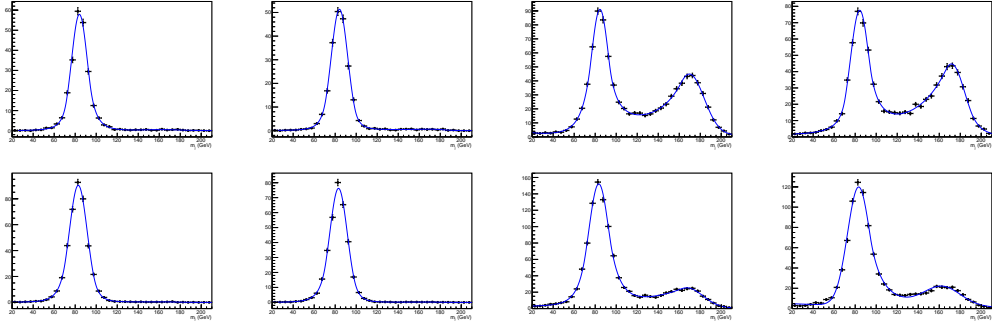
Figure 4.38: Fits for the 1D m_{jet} distributions of the resonant background for each of the 24 categories. Left to right: mu-HP, e-HP, mu-LP, e-LP. Top to bottom: nobb-LDy, nobb-HDy.
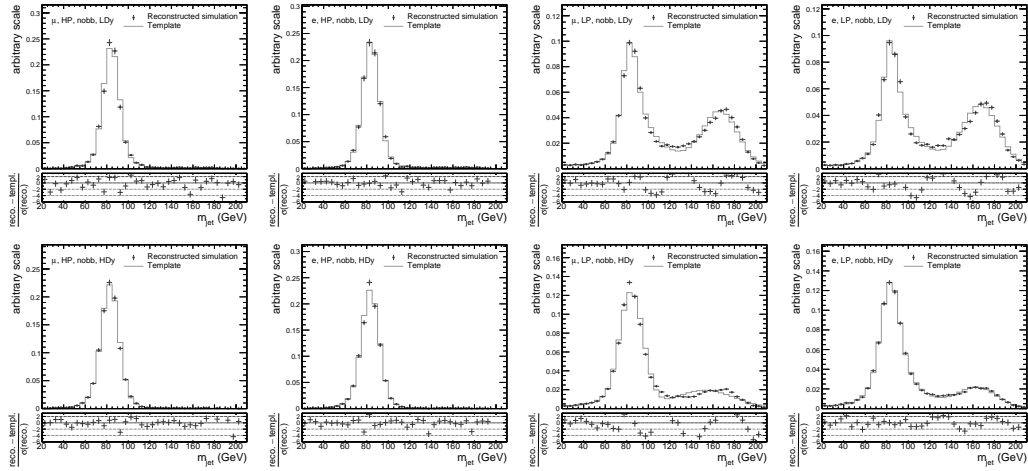
Figure 4.39: Comparison of the 1D m_{jet} templates for the resonant background (solid line) and the weighted MC distributions (points). Left to right: mu-HP, e-HP, mu-LP, e-LP. Top to bottom: nobb-LDy, nobb-HDy.
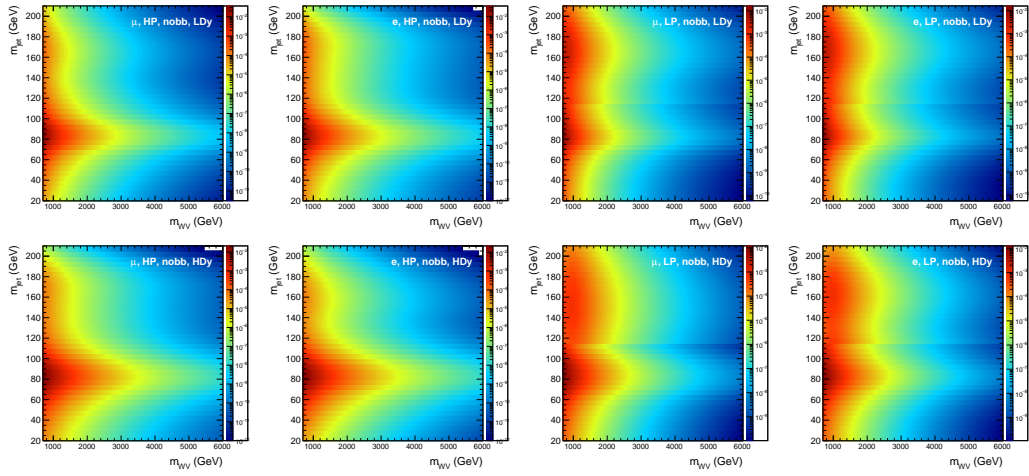
Figure 4.40: Final 2D resonant templates for the nobb category. Left to right: mu-HP, e-HP, mu-LP, e-LP. Top to bottom: nobb-LDy, nobb-HDy.
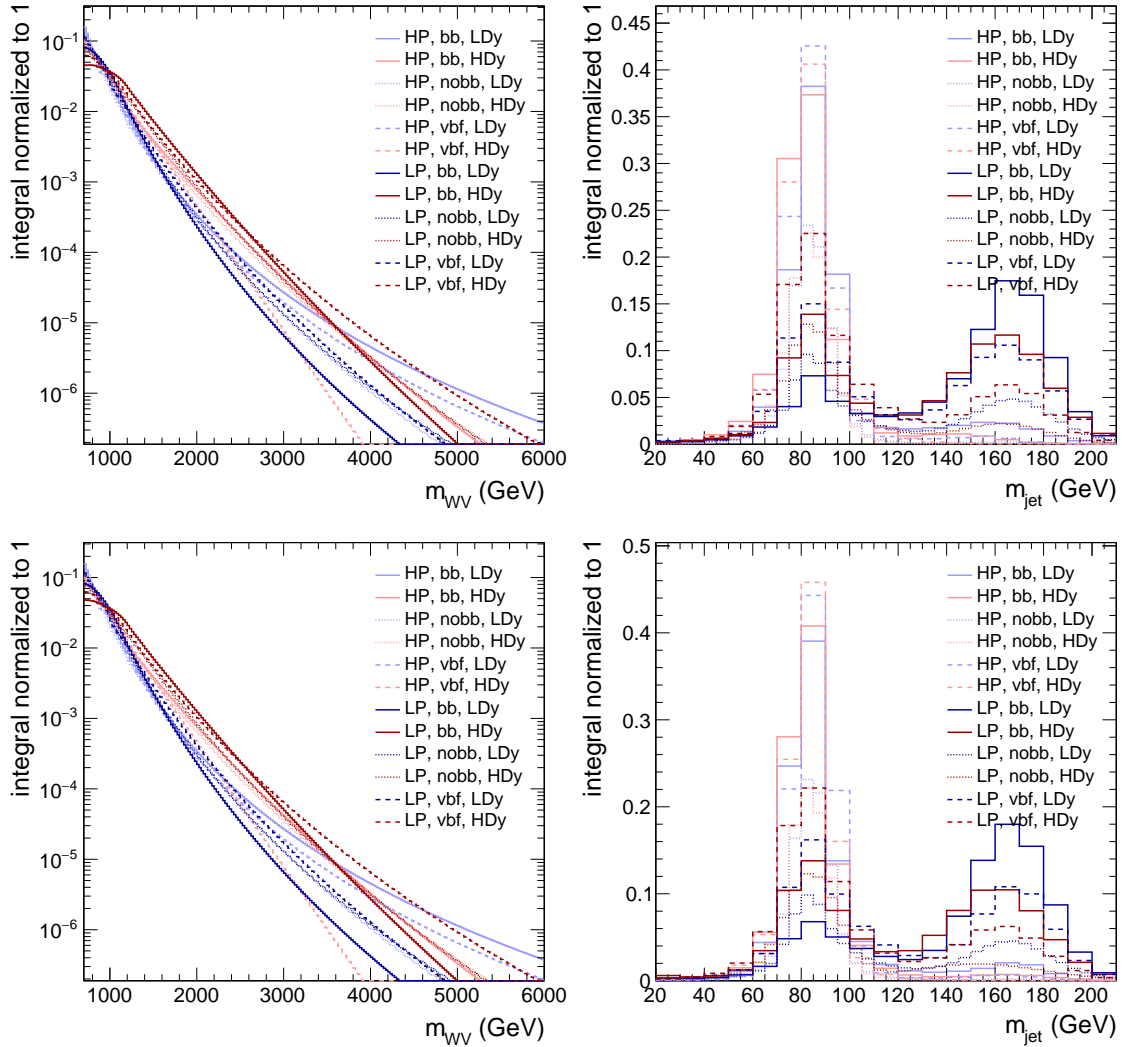
Figure 4.41: Comparisons of projections of the 2D resonant templates onto the $m_{WV/WH}$ (left) and m_{jet} (right) spectra, separated by e (top) and mu (bottom) contributions for each category.

4.7 Systematic Uncertainties

To implement systematic uncertainties in the analysis, we introduce nuisance parameters into the 2D fit that allow for changes to the shapes and normalizations for the signal and background models. In this section, we discuss the nuisance parameters that are applied to the signal and background processes, and how they are correlated between different categories.

4.7.1 Signal Normalization

The signal normalization uncertainties are 100% correlated between search categories unless otherwise stated.

- **Luminosity:** Normalization uncertainty of 1.8% [111, 112, 148].

- **Parton Distribution Function (PDF):** Normalization uncertainty of 1%. The scale uncertainties were evaluated as prescribed by references [149, 150]. For the PDF uncertainties, we follow the recommendations from the NNPDF 3.0 PDF set [151]. The uncertainties obtained in acceptance were found to be less than 0.1% for the scale variation, and 0.1-0.9% for the PDF evaluation.

- **Pileup reweighting:** Normalization uncertainty of 1.5%, estimated by shifting the minimum bias cross section by 4.6% and deriving alternative pileup weights.

- **Lepton identification and trigger efficiency:** Normalization uncertainty of 5% for the electron and muon channels separately. This is 100% correlated to a parameter for the resonant background, but uncorrelated with a similar parameter for the non-resonant background.

- **b-tag fake rate:** Normalization uncertainty of 2% accounting for modeling the no-b tag requirement.

- **V-tagging efficiency:** Normalization uncertainty for the scale factors S^{HP} and S^{LP} for the efficiency of the τ_{21}^{DDT} selection, with $\pm 4\%$ in HP and $\mp 4\%$ in LP[3].

- **Momentum dependence of the V-tagging efficiency:** Normalization uncertainty arising from the extrapolation of the V-tagging efficiency scale factors. We fit the m_{X} dependence of the V-tagging efficiency as seen in figure 4.19 (right) and subtract the efficiency at 650 GeV to obtain an m_{X}-dependent uncertainty for the HP and LP categories given by:

  - $\pm (4.95 \times 10^{-3})[(m_{\text{X}} - 650 \text{ GeV})/(1 \text{ GeV})]$ in the HP category.

  - $\mp (3.54 \times 10^{-3})[(m_{\text{X}} - 650 \text{ GeV})/(1 \text{ GeV})]$ in the LP category.

- **$b\bar{b}$-tagging efficiency:** Normalization uncertainty on the scale factors for the efficiency on the cut of the $b\bar{b}$-tagger obtained by shifting the scale factors up and down and propagating the results to the expected signal yields. This results in the following uncertainties:

  - $\pm 9\%$ (bb) / $\mp 0.4\%$ (nobb) for the WW signals.

  - $\pm 9\%$ (bb) / $\mp 1.5\%$ (nobb) for the WZ signals.

  - $\pm 6\%$ (bb) / $\mp 2.5\%$ (nobb) for the WH signal.

- **$\Delta y_{WV/WH}$ cut efficiency:** Normalization uncertainty for the efficiency of the cut at $\Delta y_{WV/WH} = 1.0$ separating the HDy and LDy categories. This is estimated by fitting a linear function to the data/MC ratio for the distribution of $\Delta y_{WV/WH}$ in the top-enriched control region, then linearly reweighing the signal distribution of $\Delta y_{WV/WH}$ for each signal model, using the slope obtained from the data/MC fit and using a y-intercept that keeps the total integral of the signal distribution constant. Taking the signal efficiency in HDy and LDy as the 1σ up uncertainty, we obtain the following:

---

[3]The uncertainties here and elsewhere have opposite signs due to the fact that they are anti-correlated

○ +4% (HDy) / −1.5% (LDy) for ggF $G_{\text{bulk}} \to WW$.

○ +4% (HDy) / −3.5% (LDy) for ggF and VBF $\phi \to WW$, and DY $Z' \to WW$.

○ +4% (HDY) / −2% (LDy) for DY $W' \to WZ$ and $W' \to WH$.

○ +6% (HDy) / −5% (LDy) for VBF $G_{\text{bulk}} \to WW$.

○ +2% (HDy) / −5.5% (LDy) for VBF $Z' \to WW$ and $W' \to WZ$.

4.7.2 Signal Shape

For the signal shapes, we implement nuisance parameters to the $m_{WV/WH}$ shape as relative scale factors on the mean μ and standard deviation σ of the DCB function. Each of the following $m_{WV/WH}$ shape parameters are 100% correlated across the categories in which they apply:

- **Jet energy scale and resolution:** 2% for the scale and 5% for the resolution.

- **Missing transverse momentum scale and resolution:** 2% for the scale and 1% for the resolution.

- **Electron and muon energy scale:** 0.5% for the electron channel and 0.3% for the muon channel.

The m_{jet} signal shape is affected by the uncertainty on the scale and resolution for the soft drop mass. To obtain these uncertainties, we correct the central values of the m_{jet} scale and resolution parameters with the factors of 0.990 and 1.08 obtained for Run 2 in table 4.5. The soft drop mass scale and resolution uncertainties obtained are the following:

- **Soft drop mass scale and resolution:** 1% for the scale and 8% for the resolution.

The resulting uncertainties are 100% correlated between the electron and muon channels, between the bb, nobb, and vbf categories, and between the HDy and LDy categories, but not the HP and LP categories.

4.7.3 Background Normalization

We use two sets of nuisance parameters for the background normalization:

- A 5% normalization uncertainty uncorrelated between the electron and muon channels, but 100% correlated between the resonant and non-resonant background, between the HP and LP categories, between the bb, nobb, and vbf categories, and between the HDy and LDy categories.

- A 25% normalization uncertainty uncorrelated between the resonant and non-resonant background, between the HP and LP categories, between the bb, nobb, and vbf categories, and between the HDy and LDy categories, but 100% correlated between the muon and electron channels.

The large uncertainties are assigned in order to account for the fact that the background normalization is largely estimated by the 2D fit, which captures differences between data and simulation in every category, and hence causes the nuisance parameters to be constrained by the data.

4.7.4 Non-resonant Background Shape

We define two shape variations for the conditional part of the likelihood for the 2D fitting process to account for the differences between data and simulation:

- **Jet p_T spectrum:** Derived by reweighting the jet p_T spectrum to be harder or softer. It affects only the $m_{WV/WH}$ dimension and is motivated by higher order corrections in the $W + $ jets production not modeled by the simulation.

- **Diagonal:** Modifies the correlation between the jet mass and the jet p_T. The variation changes the slope of the linear part of figure 4.31.

Both of these shape variations are left uncorrelated across categories due to the fact that they are sensitive to different regions of the PDFs. The projections of the nominal and $\pm 3\sigma$ alternative 2D shapes onto the $m_{WV/WH}$ dimension for the jet p_{T} spectrum and diagonal uncertainties for the nobb category are shown in figure 4.42.

Figure 4.42: Projections of the nominal and alternative shapes of the non-resonant background onto the $m_{WV/WH}$ dimension obtained from applying $\pm 3\sigma$ variations of the jet p_{T} spectrum uncertainties (top), and the diagonal uncertainties (bottom), for the electron channel in the nobb category. Left to right: HP-LDy, LP-LDy, HP-HDy, LP-HDy.

For the m_{jet} spectrum, we define two shape variations in order to account for hadronization-related effects:

- **Log weight:** A reweighting of events based on the difference in the hadronization behavior in data versus MC using the hadronization-sensitive variable $\ln(m_{\mathrm{jet}}^2/p_{\mathrm{T}})$. The weight is obtained by fitting the ratio of the data to MC in the $\ln(m_{\mathrm{jet}}^2/p_{\mathrm{T}})$ distribution seen in figure 4.43 in the region dominated by $W + \mathrm{jets}$. This region is fitted with a function consisting of a Gaussian plus a constant term, with the reweighting of the events based on the fitted function.

- **Soft drop mass scale:** Plain shift of the m_{jet} scale.

124

These nuisance parameters are also left uncorrelated across categories, with figure 4.44 showing the nominal and $\pm 3\sigma$ alternative shapes projected onto the m_{jet} dimension for the log weight and soft drop mass scale uncertainties for the nobb category in the electron channel.
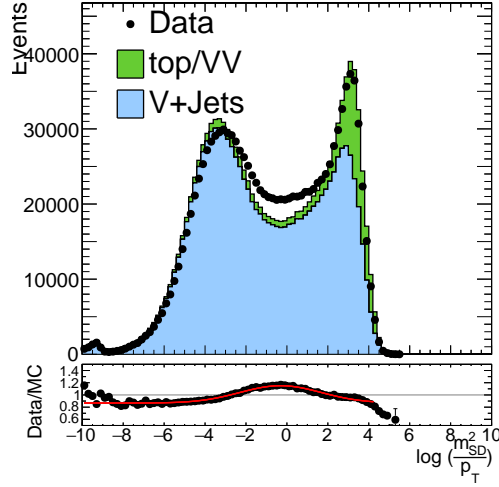
Figure 4.43: Comparison between the Run 2 data and MC distributions for $\ln(m_{\mathrm{jet}}^2/p_{\mathrm{T}})$ with all categories merged.

4.7.5 Resonant Background Shape

As with the non-resonant background shapes, we apply a jet p_{T} spectrum related uncertainty, but with two additional sets of nuisance parameters introduced for the LP categories corresponding to the two m_{jet} bins used to build the $m_{WV/WH}$ likelihood. The HP categories use only one m_{jet} bin, hence they only have one set of nuisance parameters. We also apply an uncertainty in the exponent of the power-law function used to populate the high-$m_{WV/WH}$ region of the template for each category. These nuisance parameters are also uncorrelated between categories and are uncorrelated between the resonant and non-resonant backgrounds. Figure 4.45 shows the nominal and $\pm 3\sigma$ alternative 2D shapes projected onto the $m_{WV/WH}$ dimension for the jet p_{T} spectrum uncertainties and the $m_{WV/WH}$ power-law exponent uncertainties in the nobb category for the electron channel.
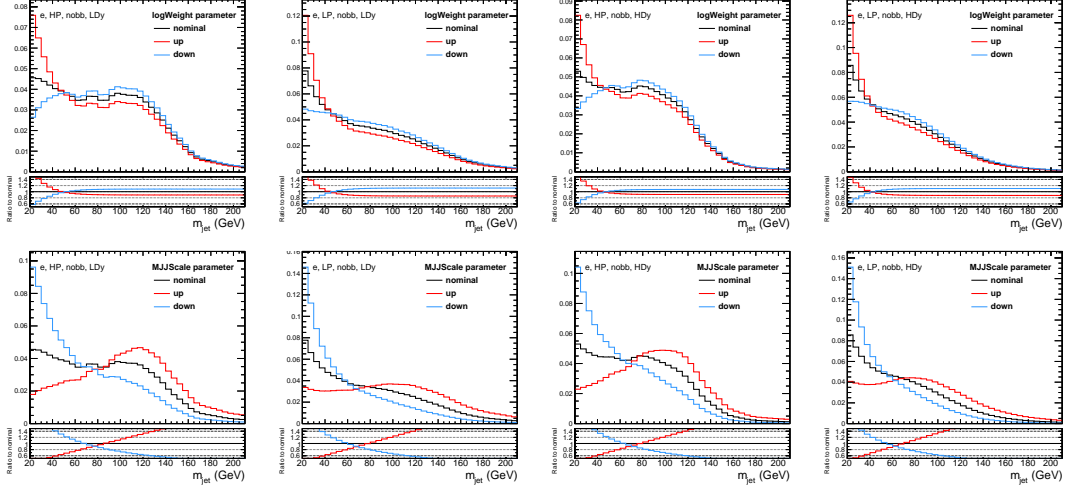
Figure 4.44: Projections of the nominal and alternative shapes of the non-resonant background onto the m_{jet} dimension obtained from applying $\pm 3\sigma$ variations of the log weight uncertainties (top), and the m_{jet} scale uncertainties (bottom), for the electron channel in the nobb category. Left to right: HP-LDy, LP-LDy, HP-HDy, LP-HDy.
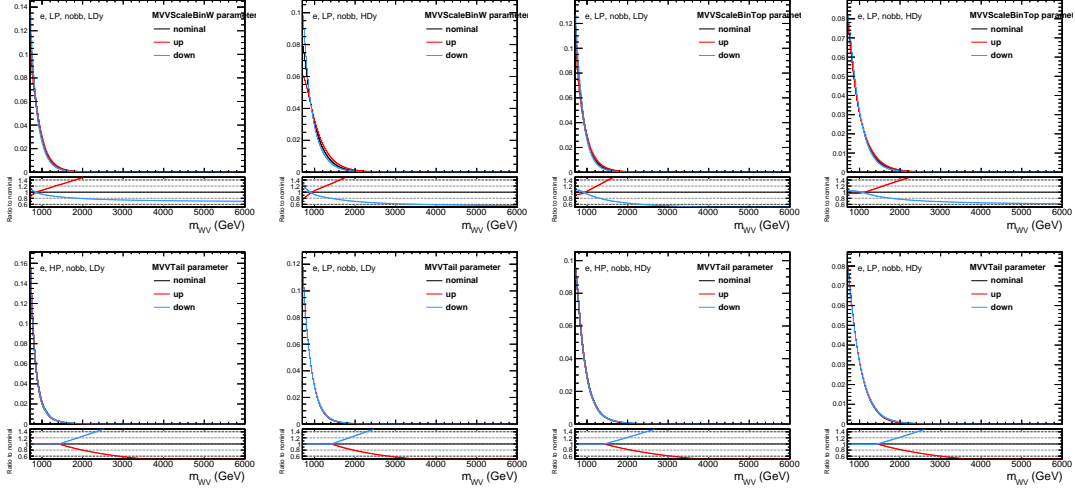
Figure 4.45: Projections of the nominal and alternative shapes of the resonant background onto the $m_{WV/WH}$ dimension obtained from applying $\pm 3\sigma$ variations of the jet p_{T} spectrum uncertainties (top), and the high-$m_{WV/WH}$ power-law tail uncertainties (bottom), for the electron channel in the nobb category. Left to right: HP-LDy, LP-LDy, HP-HDy, LP-HDy.

126

For the m_{jet} dimension of the resonant background, we consider three types of shape uncertainties. The first two are uncorrelated and modify the mean and width of the fitted DCB functions for the $W^{\pm}$ and top peaks, and they correspond to the nuisance parameters for the soft drop mass scale and resolution. Meanwhile, the last set of parameters determine the relative normalization of the $W^{\pm}$ and top peaks:

- **$W^{\pm}$ peak scale and resolution:** 1% for the scale and 8% for the resolution. We also correct the central values of the scale and resolution for the $W^{\pm}$ peak with factors of 0.990 and 1.08 using the Run 2 values of table 4.5. The nuisance parameters are uncorrelated between HP and LP categories, but 100% correlated between the electron and muon channels, the bb, nobb, and vbf categories, and the HDy and LDy categories. They are also 100% correlated to the m_{jet} scale and resolution parameters of the signal models.

- **Top peak scale and resolution:** 1% for the scale and 8% for the resolution. No corrections are made to the parameters of the top peak, and the nuisance parameters are uncorrelated between HP and LP categories, but 100% correlated between the electron and muon channels, the bb, nobb, and vbf categories, and the HDy and LDy categories.

- **$W^{\pm}$/top relative normalization:** Fraction of the $W^{\pm}$ peak normalization divided by the sum of the $W^{\pm}$ and top peaks defined such that $\pm 40\%$ corresponds to a $\pm 3\sigma$ shift. These parameters are uncorrelated between categories.

Figure 4.46 shows the nominal and $\pm 3\sigma$ alternative 2D shapes projected onto the m_{jet} dimension for the $W^{\pm}$ peak and scale uncertainties in the nobb category. Meanwhile, figure 4.47 shows the nominal and $\pm 3\sigma$ alternative 2D shapes projected onto the m_{jet} dimension for the top peak and scale uncertainties in the nobb category. Finally, figure 4.48 shows the nominal and $\pm 3\sigma$ alternative 2D shapes projected onto the m_{jet} dimension for the $W^{\pm}$ and top relative normalization uncertainty in the nobb category.
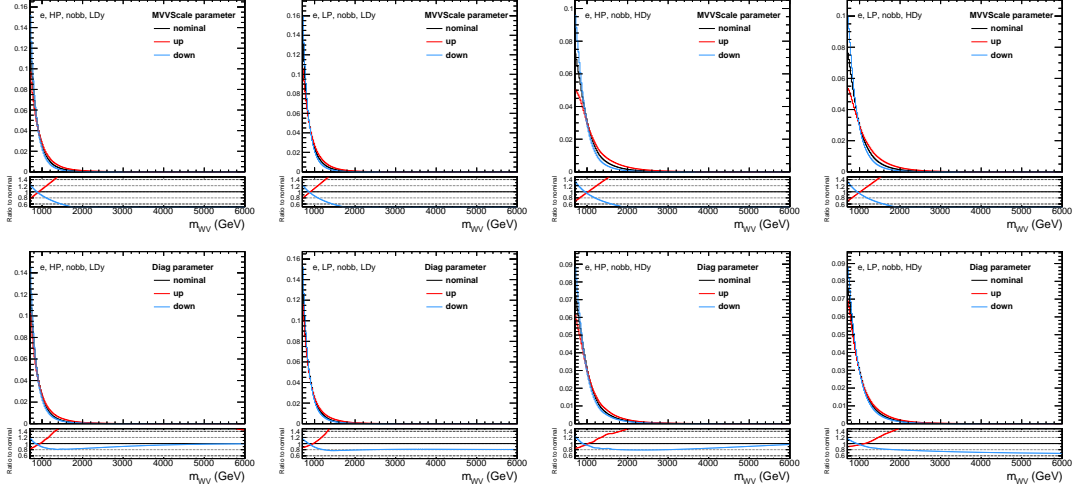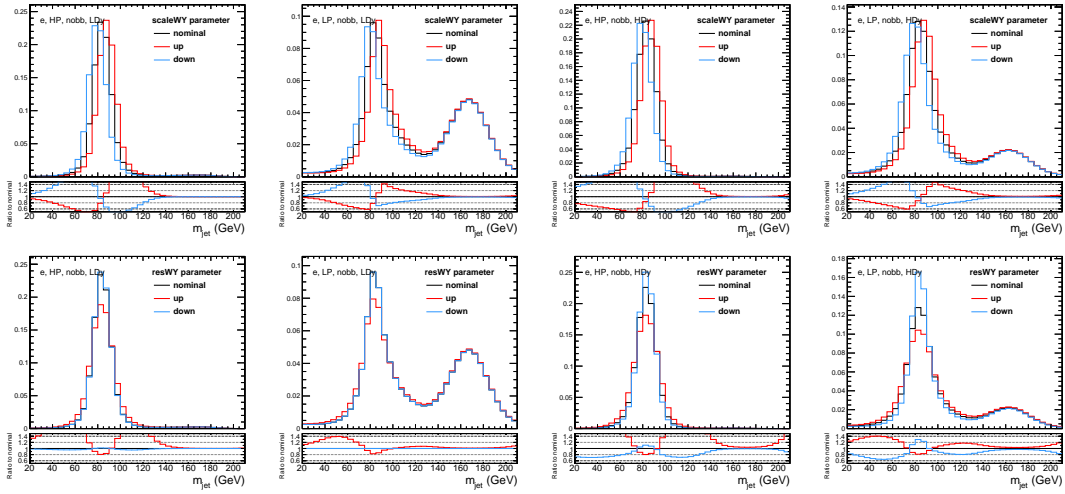
Figure 4.46: Projections of the nominal and alternative shapes of the resonant background onto the m_{jet} dimension obtained from applying $\pm 3\sigma$ variations of the $W^{\pm}$ peak scale (top) and resolution (bottom) uncertainties for the electron channel in the nobb category. Left to right: HP-LDy, LP-LDy, HP-HDy, LP-HDy.
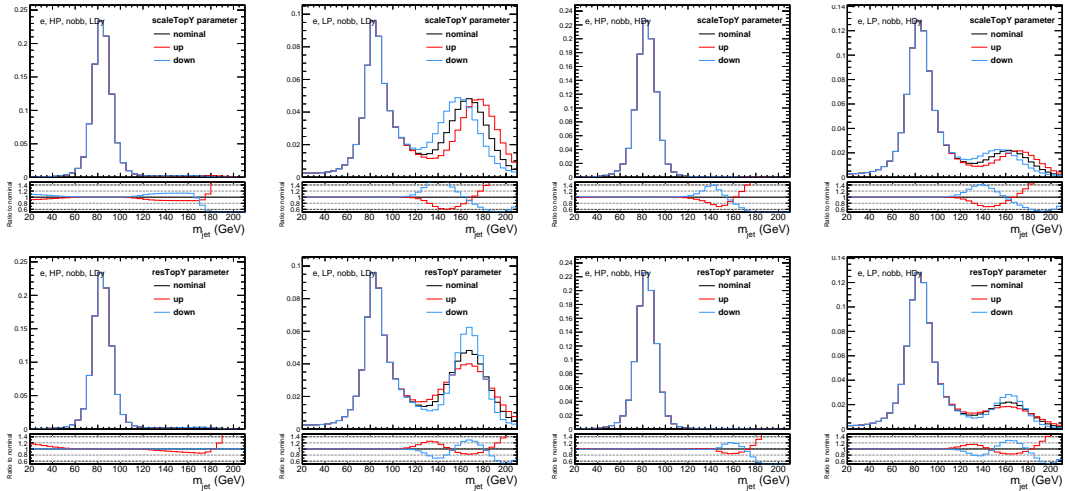
Figure 4.47: Projections of the nominal and alternative shapes of the resonant background onto the m_{jet} dimension obtained from applying $\pm 3\sigma$ variations of the top peak scale (top) and resolution (bottom) uncertainties for the electron channel in the nobb category. Left to right: HP-LDy, LP-LDy, HP-HDy, LP-HDy.
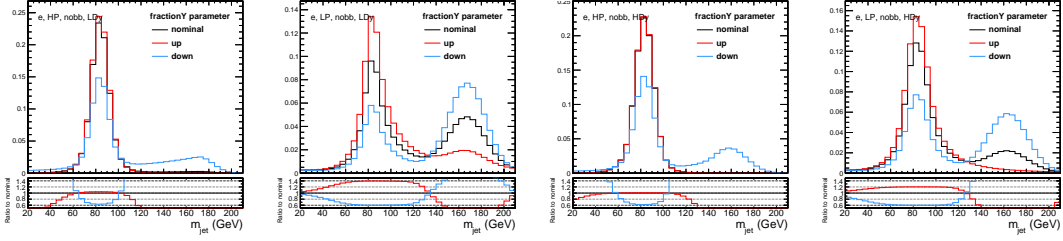
Figure 4.48: Projections of the nominal and alternative shapes of the resonant background onto the m_{jet} dimension obtained from applying $\pm 3\sigma$ variations of the $W^{\pm}$ and top relative normalizations for the electron channel in the nobb category. Left to right: HP-LDy, LP-LDy, HP-HDy, LP-HDy.

4.8 Fit Validation and Bias Testing

The nuisance parameters implemented as part of the 2D fitting process for each of the 24 categories result in various alternative shapes for the signal and background models. To check their performance, we apply fit validation and bias tests to evaluate the quality of the 2D fit, which includes the correctness of the shape uncertainties. We consider the post-fit pulls and impacts for each of the nuisance parameters described in section 4.7, post-fit distributions for a background-only fit in the signal region, a goodness-of-fit test using the saturated model algorithm, and a signal-injected bias test using a maximum likelihood fit.

4.8.1 Post-fit Pulls and Impacts

One of the tests performed examines the behavior of the nuisance parameters in a background-only fit and a signal+background fit for a given signal model and specified mass, with the signal cross section free to float, but without looking at its measured value prior to unblinding. We then compare the final post-fit values and uncertainties of the nuisance parameters to the pre-fit values and uncertainties, which can be seen in figure 4.49. Most post-fit nuisance parameters fall within the $\pm 1\sigma$ range of their pre-fit values, with some larger deviations in parameters related to the jet p_{T} spectrum.

129

We also consider the post-fit pull and impact of each parameter on the measured signal cross section for the $W' \to WH$ signal. The pulls are defined as the difference between the pre- and post-fit values divided by the pre-fit uncertainty for a given nuisance parameter, and the impacts are defined as the shift Δr of the measured signal cross section obtained by fixing the nuisance parameter to its $+1\sigma$ or -1σ post-fit values while all other parameters are profiled. Figure 4.50 shows the resulting post-fit pulls and impacts for the $W' \to WH$ signal. The resulting impacts are relatively small and range from 10^{-3} to 10^{-6}. We find that the parameters with the largest impacts are the shape parameters of the non-resonant background in the categories most sensitive to the considered signal. For example, the same pulls and impacts were considered for a VBF signal, and it was found that the parameters with the largest impacts were from vbf categories.

4.8.2 Post-fit Distributions

Another test performed to assess the fit quality involves performing a background-only fit and plotting post-fit distributions in the signal region. Figure 4.51 shows the post-fit distributions for all categories projected onto the m_{jet} dimension for all events in the full range of $m_{WV/WH}$, while figure 4.52 shows the post-fit distributions projected onto the $m_{WV/WH}$ dimension for all events in the full m_{jet} range. Good agreement between the data and post-fit templates is observed for all 24 categories.

4.8.3 Goodness-of-Fit Test

The goodness-of-fit (GOF) is estimated using the saturated model (Cousins-Baker) algorithm [152], in which 1,000 background toys are generated for the GOF estimator. The process is repeated for the data, which is compared to the GOF estimator distribution for the background toys in figure 4.53, with the red arrow corresponding to the location of the estimator for the data. We find that the GOF estimator for the data has good compatibility
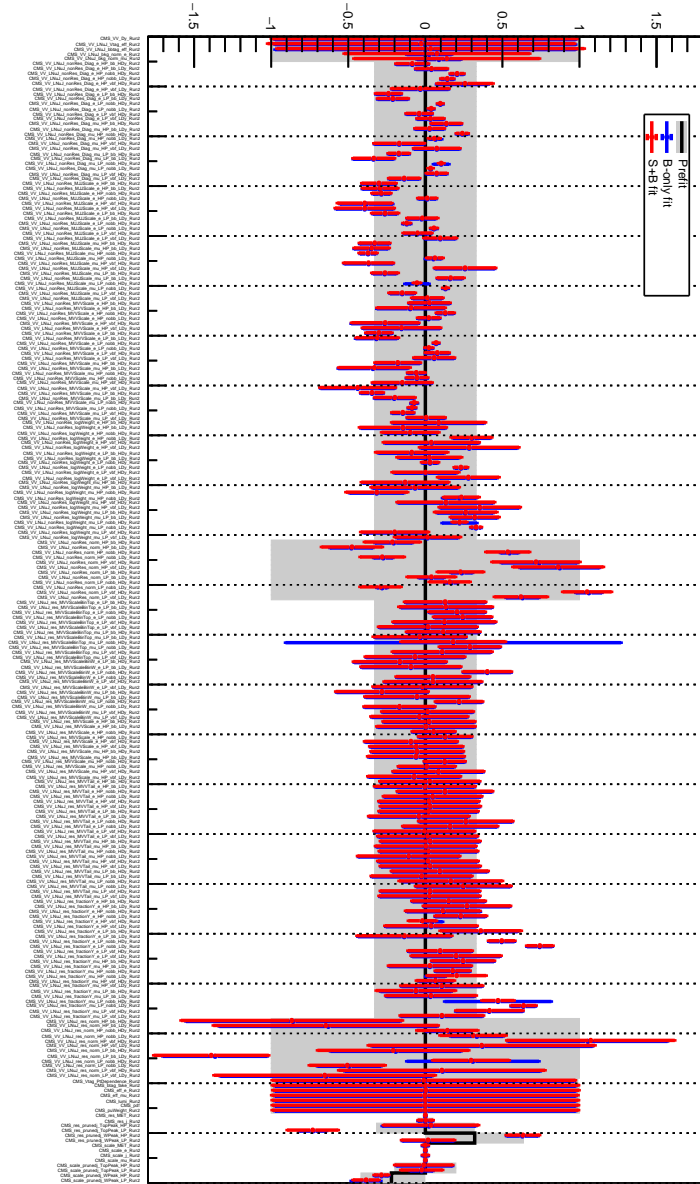
Figure 4.49: Comparison of the post-fit values and uncertainties for each nuisance parameter with respect to their pre-fit values and uncertainties for background-only and signal+background fits, using the DY $W' \rightarrow WH$ model with $m_{W'} = 1$ TeV. Gray bands and blue/red bars represent $\pm 1\sigma$ pre- and post-fit uncertainties, respectively.
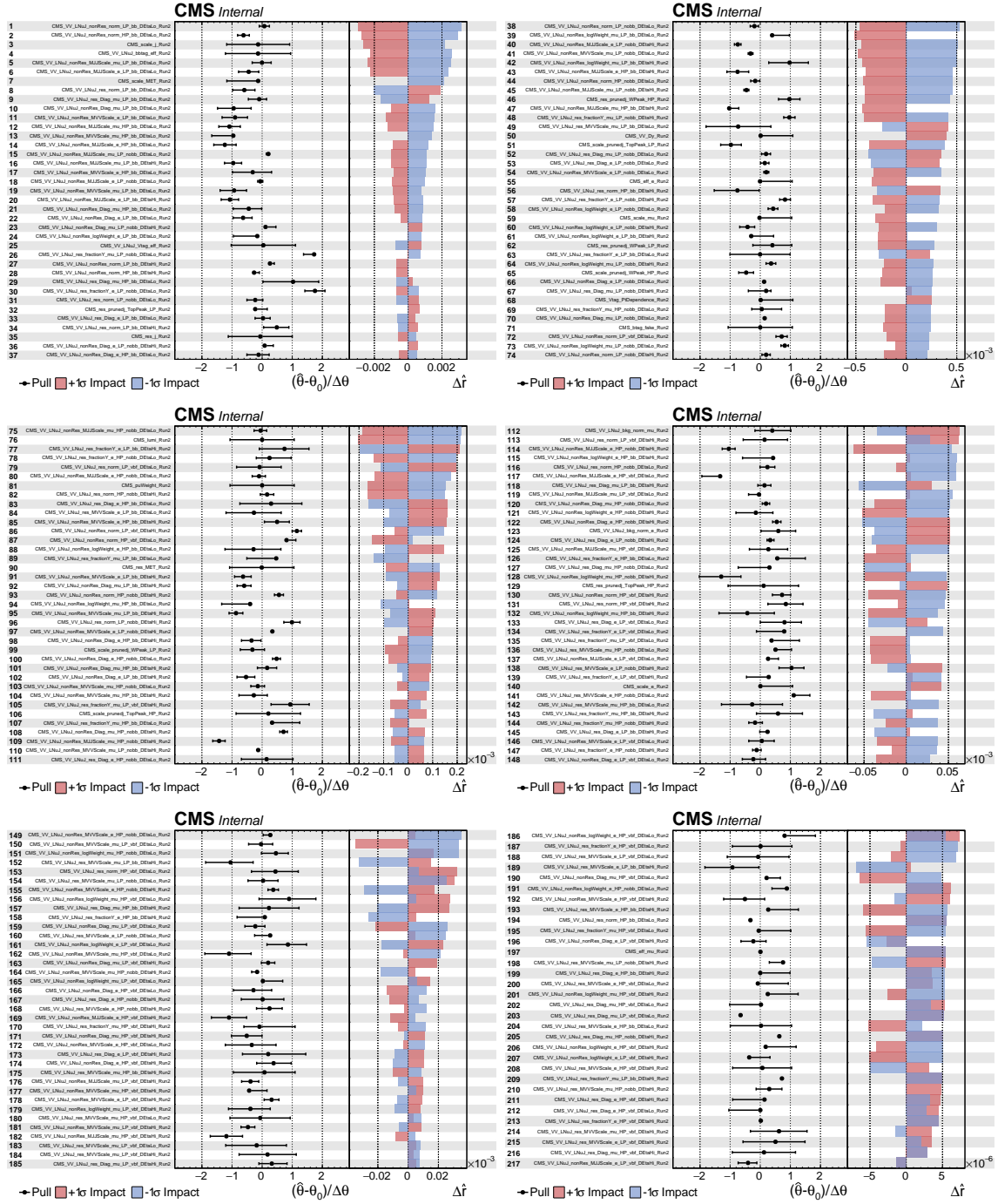
Figure 4.50: Pulls of the nuisance parameters, and impacts of a shift for each nuisance parameter on the measured signal cross section for the DY $W' \to WH$ model with $m_{W'} = 1$ TeV.
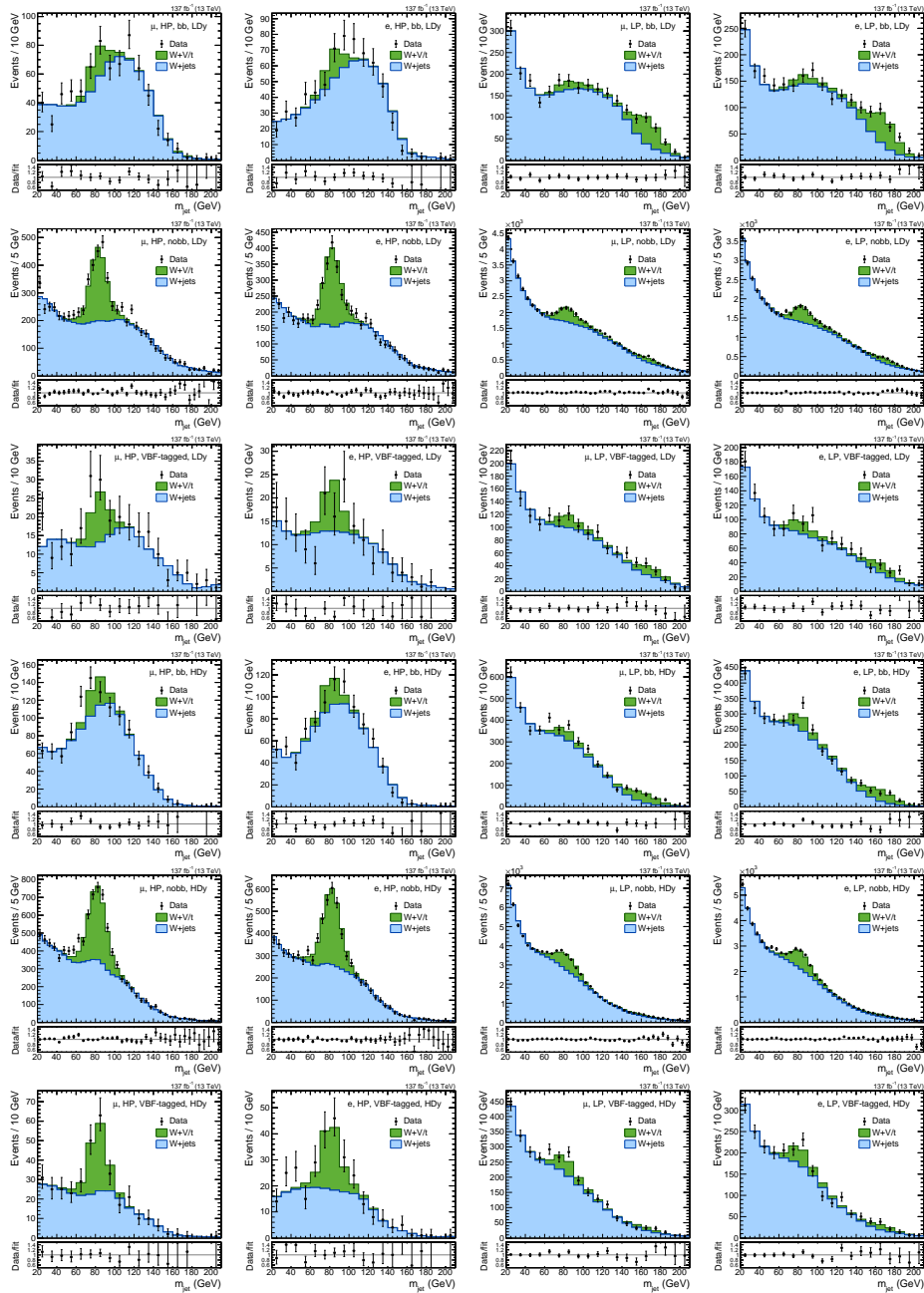
Figure 4.51: Post-fit distributions and data projected onto the m_{jet} dimension for the full range of $m_{WV/WH}$. Columns 1 to 4: mu-HP, e-HP, mu-LP, and e-LP. Rows 1 to 6: bb-LDy, nobb-LDy, vbf-LDy, bb-HDy, nobb-HDy, and vbf-HDy.

133
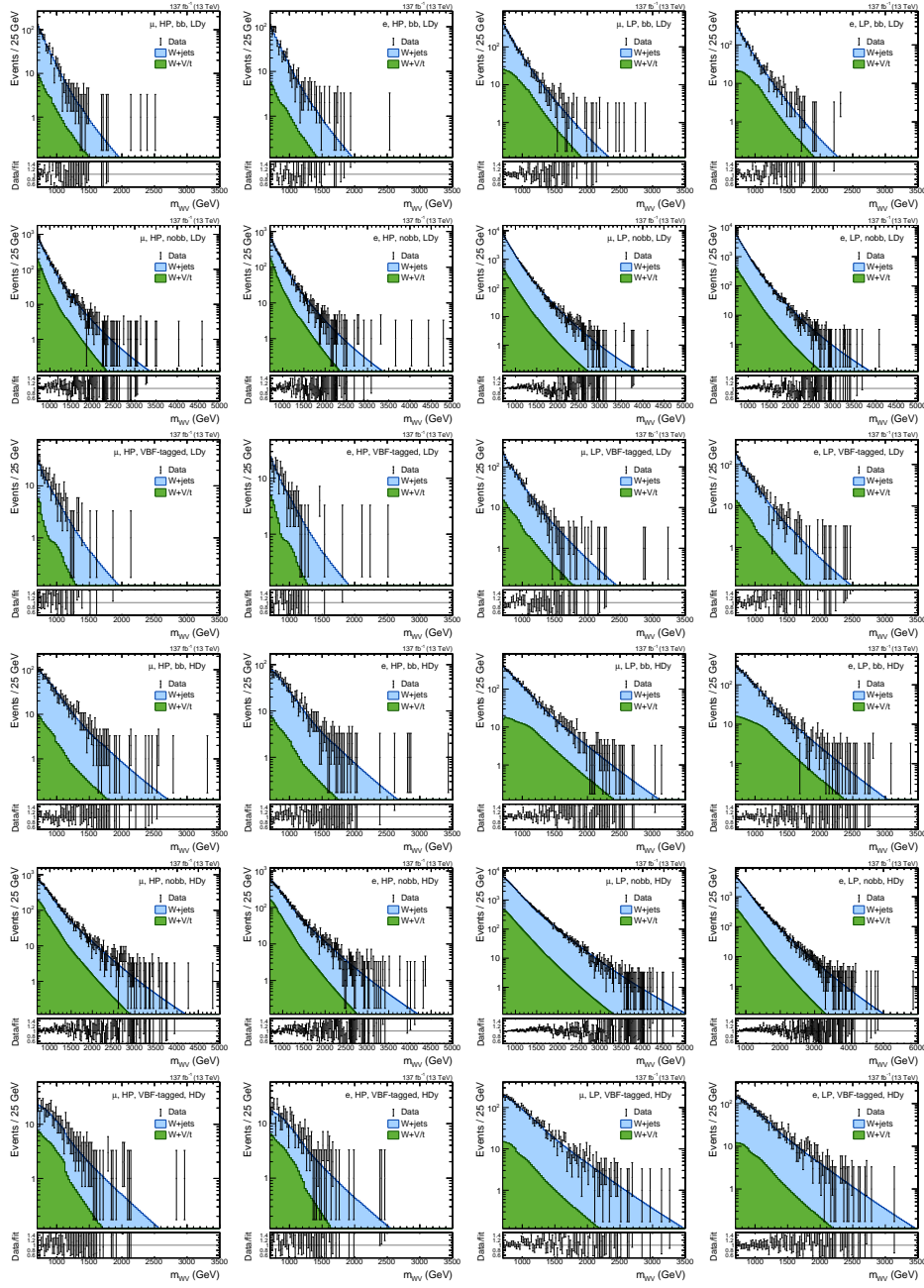
Figure 4.52: Post-fit distributions and data projected onto the $m_{WV/WH}$ dimension for the full range of m_{jet}. Columns 1 to 4: mu-HP, e-HP, mu-LP, and e-LP. Rows 1 to 6: bb-LDy, nobb-LDy, vbf-LDy, bb-HDy, nobb-HDy, and vbf-HDy.

134

with the background toys distribution.

The saturated model algorithm produces a quantity defined by a likelihood ratio that is similar to the χ^2 test statistic [153]. To illustrate the process, we shall consider the case of uncorrelated Gaussian distributed data, which has a likelihood given by

$$\mathcal{L} = \prod_i \frac{1}{\sqrt{2\pi\sigma_i^2}} \exp\left[-\frac{1}{2}\left(\frac{d_i - f_i}{\sigma_i}\right)^2\right],$$ (4.26)

where $d_i \pm \sigma_i$ is the ith measured data point with RMS deviation σ_i, and f_i is the value as predicted by the model. The saturated model for $\mathcal{L}$ is defined by setting $f_i = d_i$ for each data point i, which for the Gaussian case yields

$$\mathcal{L}_{\text{sat}} = \prod_i \frac{1}{\sqrt{2\pi\sigma_i^2}}.$$ (4.27)

This in turn gives the likelihood ratio

$$\lambda_{\text{sat}} = \frac{\mathcal{L}}{\mathcal{L}_{\text{sat}}} = \prod_i \exp\left[-\frac{1}{2}\left(\frac{d_i - f_i}{\sigma_i}\right)^2\right],$$ (4.28)

and hence the test statistic for the algorithm defined by $-2\ln\lambda$ gives us in this case the familiar χ^2 expression:

$$\chi^2 = -2\ln\lambda_{\text{sat}} = \sum_i \frac{(d_i - f_i)^2}{\sigma_i^2}.$$ (4.29)

Beyond this example, the saturated algorithm can compute a corresponding test statistic for an arbitrary combination of binned channels with constraints.

4.8.4 Signal-Injected Bias Tests

The last test performed to assess the 2D fit is a signal-injected bias test. We run a maximum likelihood fit on toy data samples generated from a signal+backgound model used in place of the data, then extract the measured cross section from the result. For the toy data
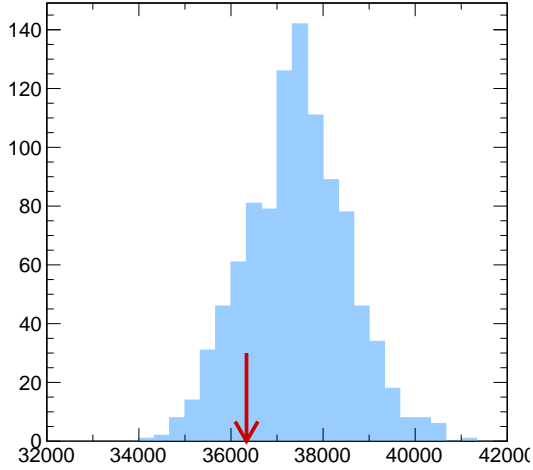
Figure 4.53: Distribution of the goodness-of-fit estimator for 1,000 background toys (blue) and the data (red arrow) using the saturated algorithm.

samples, we generate 1,000 toys for eight values of the resonance mass m_{X} (1 TeV to 4.5 TeV, in increments of 0.5 TeV) for each of the benchmark signal models and for two possible injected cross sections. We obtain an injected signal cross section for each value of m_{X} for each benchmark signal model for 2σ and 5σ local significance by scanning the cross section ranges at a given mass point m_{X} using a profile likelihood fit until the desired significance is obtained.

The cross section pull is defined by

$$P_r = \frac{r_{\mathrm{meas}} - r_{\mathrm{inject}}}{\sigma_r},\tag{4.30}$$

where r is the injected cross section times branching fraction, and σ_r is the measured cross section uncertainty. We define the bias as the median for the resulting cross section pull P_r, which is shown for each signal model as a function of m_{X} in figure 4.54. While the overall level of bias is very low, each benchmark signal model exhibits slight biases on the order of 0-10%, with some reaching as high as 20% at certain mass points. These biases have been

investigated, and are partly due to tail effects for the pull distributions at each mass point, with large pre-fit uncertainties causing some of the shapes to deviate far from the nominal ones in the toy datasets.

4.9   Results

The results of the search for a new heavy boson resonance are considered in terms of exclusion limits for the benchmark signal models described in this analysis. These limits are model-independent, and cover spin-0, spin-1, and spin-2 resonances decaying to WW, WZ, and WH.

4.9.1   Asymptotic Limits and Quantifying Excess

The exclusion limits obtained for the analysis are asymptotic frequentist limits for the production cross section times the branching fraction for each signal model. These limits are obtained by using an asymptotic approximation of the distributions for a test statistic $\tilde{q}_\mu$ that is based on a profile likelihood ratio under signal and background hypotheses with signal strength μ, where $\mu = 0$ is the background-only model and $\mu = 1$ is the nominal signal model [154, 155].

The test statistic used is

$$\tilde{q}_\mu = -2\ln\frac{\mathcal{L}(\text{data}|\mu, \hat{\boldsymbol{\theta}}_\mu)}{\mathcal{L}(\text{data}|\hat{\mu}, \hat{\boldsymbol{\theta}})}, \qquad 0 \le \hat{\mu} \le \mu, \tag{4.31}$$

where $\hat{\boldsymbol{\theta}}_\mu$ corresponds to the conditional maximum likelihood estimators of the nuisance parameters $\boldsymbol{\theta}$ for a specified signal strength μ and data, and $\hat{\mu}$ and $\hat{\boldsymbol{\theta}}$ are the estimators for the global maximum of the likelihood. After finding the observed test statistic $\tilde{q}_\mu^{\text{obs}}$, we obtain the values of the nuisance parameters $\hat{\boldsymbol{\theta}}_0^{\text{obs}}$ and $\hat{\boldsymbol{\theta}}_\mu^{\text{obs}}$ to describe the data for the background-only and signal+background hypotheses, respectively. We then generate toy
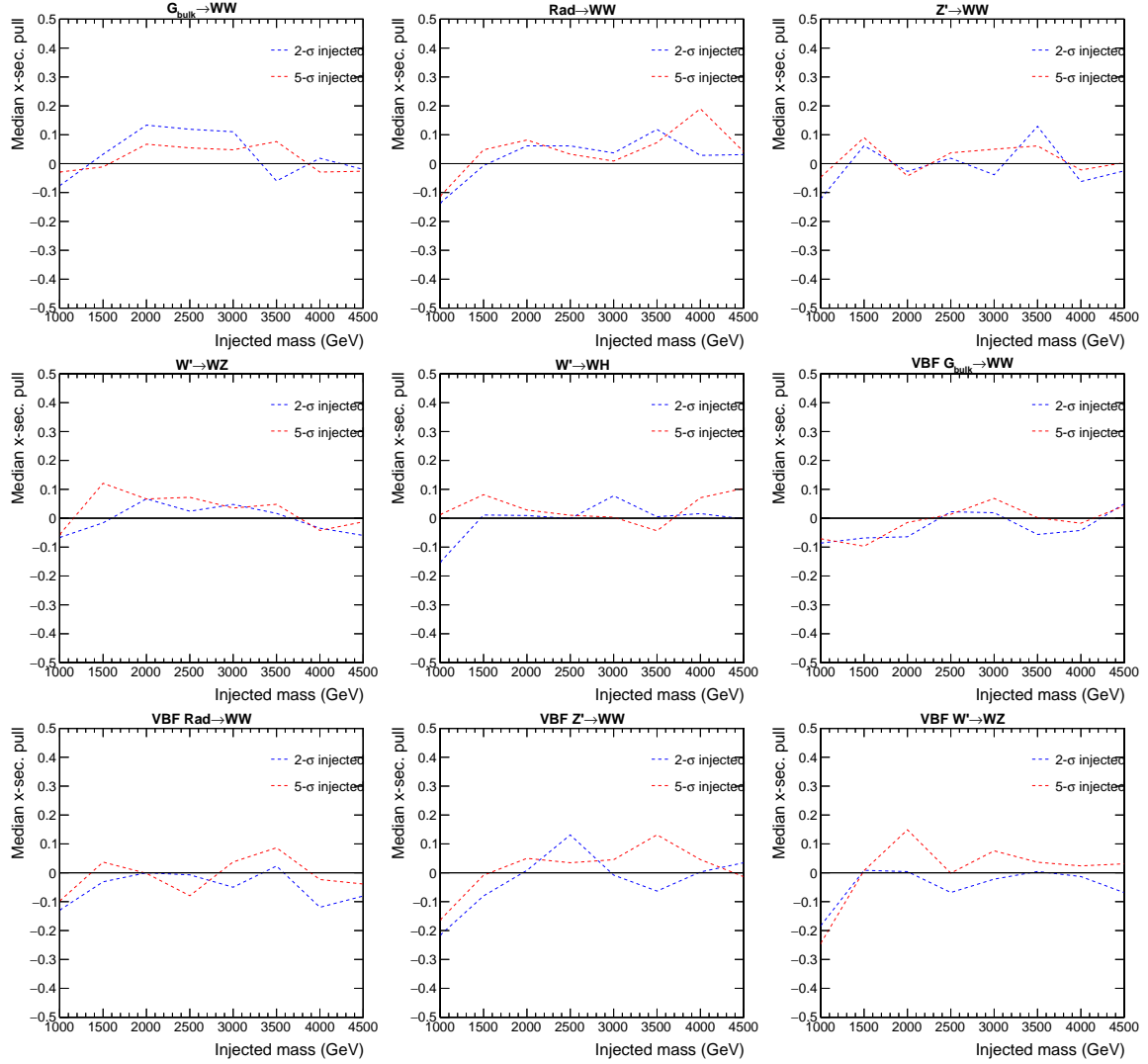
Figure 4.54: Difference in the median measured cross section and the injected signal cross section divided by the measured uncertainty as a function of the resonance mass hypothesis m_X, for both 2σ (blue) and 5σ (red) signal injection, plotted for the ggF $G_{\text{bulk}} \to WW$ (top left), ggF $\phi \to WW$ (top center), DY $Z' \to WW$ (top right), DY $W' \to WZ$ (middle left), DY $W' \to WH$ (middle center), VBF $G_{\text{bulk}} \to WW$ (middle right), VBF $\phi \to WW$ (bottom left), VBF $Z' \to WW$ (bottom center), and VBF $W' \to WZ$ (bottom right) benchmark signal models.

138

MCs to construct the corresponding pdfs, $f(\tilde{q}_\mu|0, \hat{\boldsymbol{\theta}}_0^{\mathrm{obs}})$ and $f(\tilde{q}_\mu|\mu, \hat{\boldsymbol{\theta}}_\mu^{\mathrm{obs}})$. These distributions are used to define two p-values associated with the background-only and signal+background hypotheses, which are denoted by p_b and p_μ, respectively. The p-values are given by

$$p_\mu = P(\tilde{q}_\mu \geq \tilde{q}_\mu^{\mathrm{obs}}|\mathrm{signal} + \mathrm{background}) = \int_{\tilde{q}_\mu^{\mathrm{obs}}}^{\infty} f(\tilde{q}_\mu|\mu, \hat{\boldsymbol{\theta}}_\mu^{\mathrm{obs}})\,\mathrm{d}\tilde{q}_\mu\,, \tag{4.32}$$

along with

$$1 - p_b = P(\tilde{q}_\mu \geq \tilde{q}_\mu^{\mathrm{obs}}|\mathrm{background\text{-}only}) = \int_{\tilde{q}_0^{\mathrm{obs}}}^{\infty} f(\tilde{q}_\mu|0, \hat{\boldsymbol{\theta}}_0^{\mathrm{obs}})\,\mathrm{d}\tilde{q}_\mu\,. \tag{4.33}$$

We then define the confidence-level (CL) upper limit CL_s as

$$CL_s = \frac{p_\mu}{1 - p_b}\,. \tag{4.34}$$

As an example, to obtain a 95% confidence-level (CL) upper limit, we adjust μ until we obtain a value of $CL_s = 0.05$.

4.9.2 Observed Limits

We derive 95% CL upper limits on the resonance production cross section times branching fraction to WW, WZ, or WH as a function of the mass hypothesis m_X for a narrow resonance, and compare them to expected cross sections from the benchmark models where available. The resulting limits are shown in figures 4.55-4.58 for the spin-0, spin-1, and spin-2 signal models. These limits are obtained for the combination of all 24 search categories, showing the observed and median expected limits with the 68% and 95% expected bands, along with the theoretical cross sections for each of the signal models. By comparing the observed limits to the theoretical cross sections, we may set mass exclusion limits for each of the resonance models.

For the observed limits, no significant excess in the m_X spectrum is observed anywhere

in the search region for any of the signal models. The largest deviations from the expected background occur for the VBF spin-1 signals, both for the neutral and charged signal models. These deviations occur at 1 TeV, with the largest p-value occurring in the VBF $W' \to WZ$ model with a local significance of 3.01σ. Comparing the observed limits to the theoretical cross sections, we find that for spin-0 resonances decaying to WW, ggF-produced Bulk Radions with masses below 3.1 TeV are excluded at the 95% CL. For spin-1 resonances of the HVT model B, DY-produced $Z' \to WW$ resonances lighter than 4.0 TeV, $W' \to WZ$ resonances lighter than 3.9 TeV, and $W' \to WH$ resonances lighter than 4.0 TeV are all excluded at the 95% CL. Finally, for spin-2 resonances decaying to WW, ggF-produced Bulk Gravitons with masses below 1.8 TeV are excluded at the 95% CL.
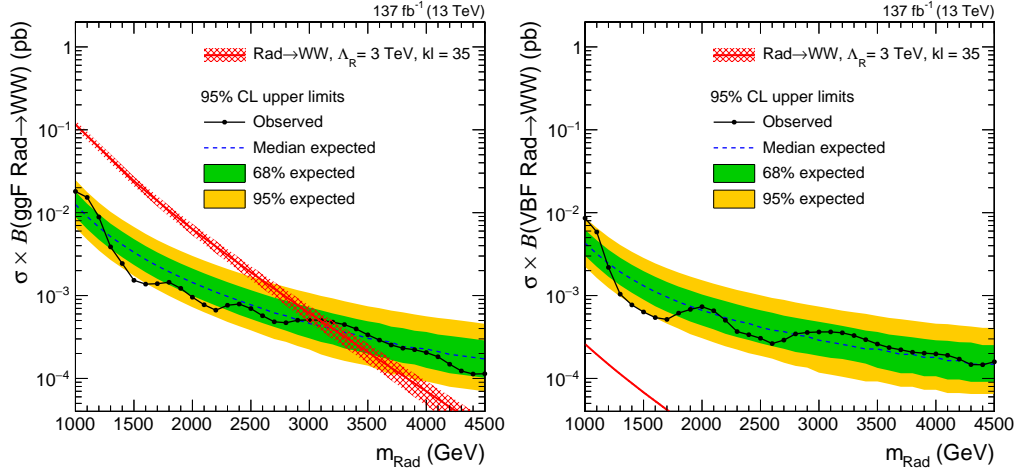
Figure 4.55: Exclusion limits for the production cross section times branching fraction for a new neutral spin-0 resonance produced via gluon-gluon fusion (left) or vector boson fusion (right) and decaying to WW, as a function of the resonance mass hypothesis m_X, compared with the predicted cross sections for a spin-0 Bulk Radion with $\Lambda_R = 3$ TeV and $kl = 35$. The signal cross section uncertainties are shown as red cross-hatched bands.
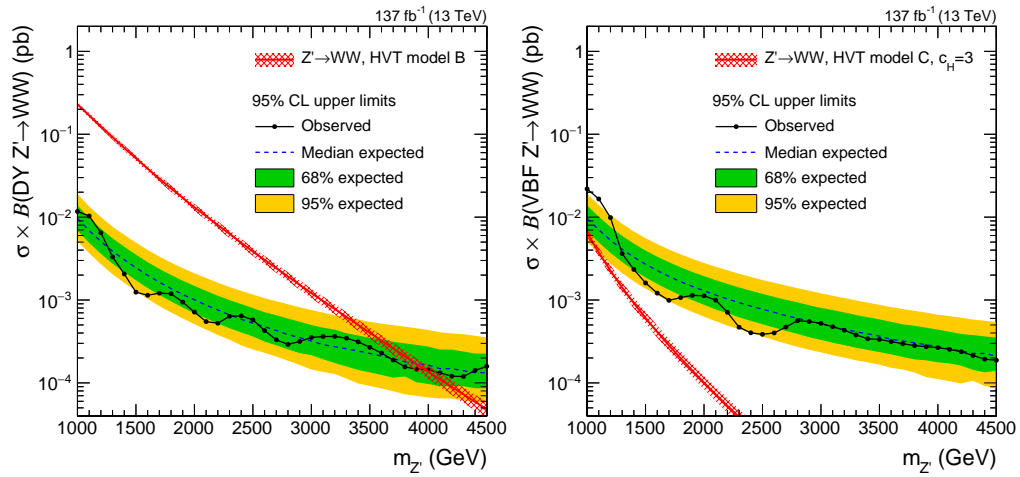
Figure 4.56: Exclusion limits for the production cross section times branching fraction for a new neutral spin-1 resonance produced via Drell-Yan (left) or vector boson fusion (right) and decaying to WW, as a function of the resonance mass hypothesis m_X, compared with the predicted cross sections for a Z' from HVT model B (for DY) or HVT model C with $c_H = 3$ (for VBF). The signal cross section uncertainties are shown as red cross-hatched bands.
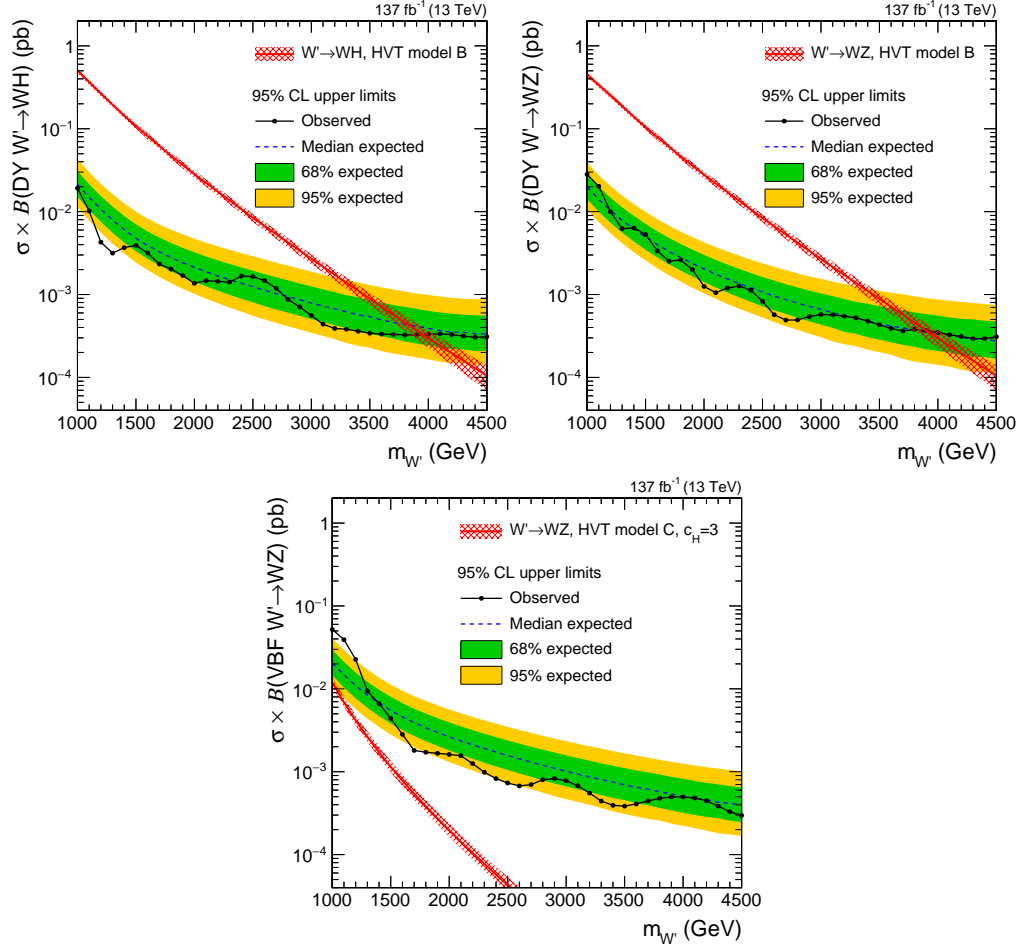
Figure 4.57: Exclusion limits for the production cross section times branching fraction for a new charged spin-1 resonance produced via Drell-Yan (top left) and decaying to WH, and for a new charged spin-1 resonance produced via Drell-Yan (top right) or vector boson fusion (bottom) and decaying to WZ, as a function of the resonance mass hypothesis m_X, compared with the predicted cross sections for a W' from HVT model B (for DY) or HVT model C with $c_H = 3$ (for VBF). The signal cross section uncertainties are shown as red cross-hatched bands.
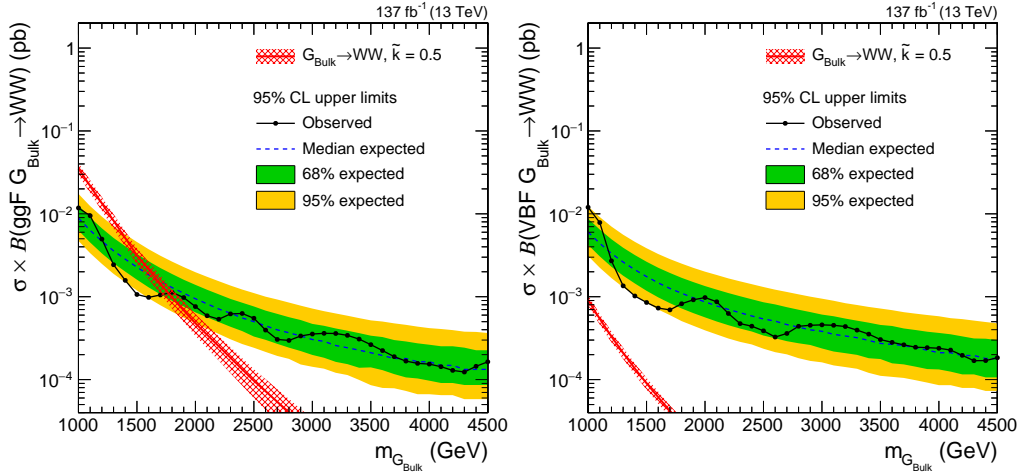
Figure 4.58: Exclusion limits for the production cross section times branching fraction for a new neutral spin-2 resonance produced via gluon-gluon fusion (left) or vector boson fusion (right) and decaying to WW, as a function of the resonance mass hypothesis m_X, compared with the predicted cross sections for a G_{bulk} with curvature $\tilde{k} = 0.5$. The signal cross section uncertainties are shown as red cross-hatched bands.

4.10   Conclusion

This chapter presents the search for a heavy dibosonic resonance decaying semileptonically to WW, WZ, and WH, with spin-0 and spin-2 resonances produced via ggF and VBF, and spin-1 resonances produced via DY and VBF. The data used were collected from 2016 to 2018 during Run 2 of the LHC, corresponding to center-of-mass energies of $\sqrt{s} = 13$ TeV, and a total integrated luminosity of 137.2 fb^{-1}. This analysis is performed with a novel 2D signal extraction technique that performs a simultaneous fit for the diboson invariant mass $m_{WV/WH}$ and soft drop jet mass m_{jet}, with several benchmark models used to model the hypothetical resonance. The results obtained are considered in terms of asymptotic limits for the production cross section times the branching fraction for each benchmark model, with no significant deviations from the median expected limits observed for any of the benchmark signal models. The observed limits establish exclusion limits on the resonances masses for

the DY- and ggF-produced signal models.

CHAPTER 5

Reconstructing Muons in Real Time at the High Luminosity Large Hadron Collider

5.1 Introduction

Chapter 3 explores the main characteristics of the CMS detector, and in particular, the various subsystems devoted to detecting muons that are produced in collision events. From its inception, it was recognized that the CMS detector would receive various upgrades over its operational lifetime, and to that end it has already had upgrades installed during its first Long Shutdown (LS1) period [156, 157]. At the time of this writing, the LHC is in its Long Shutdown 2 (LS2) phase that began on December 10, 2018, and is projected to resume taking data in 2022 [158].

In section 3.3.4 of chapter 3, a brief overview of the CMS trigger system was provided, and the basic architecture of the L1 Trigger was described. One component of the muon system in the L1 Trigger is the Barrel Muon Track Finder (BMTF), which sorts muon candidates and was commissioned in 2016 for data taking during Run 2 [159]. The architecture for the BMTF is based on custom processors mounted onto FPGAs, with the capability of calculating the transverse momenta of muons in the barrel region. It was conceived as a replacement for the legacy Drift Tube Track Finder (DTTF), which only received information from the DTs. The BMTF instead receives superprimitives made from a combination of DT and RPC primitives, which provides better resolution and trigger rates compared to the DTTF. However, as with other components of the CMS detector, the BMTF is slated to be replaced by newer hardware

that offers improvements in performance.

In this chapter, we present work towards the implementation of a novel algorithm for reconstructing muon tracks in real time at the LHC. In section 5.2, we discuss future upgrades to the CMS detector for Phase-2 that will allow for improvements in muon detection in conjunction with the high luminosity upgrades to the LHC. Later, in section 5.3, we introduce the Tracks Plus Stubs algorithm, which will allow for the reconstruction of muon tracks in real time at the L1 Trigger level.

5.2 Future Upgrades to CMS

The High-Luminosity Large Hadron Collider (HL-LHC) is scheduled to come online in 2027, with the Phase-1 period ending in 2024. During the Long Shutdown 3 (LS3) period in 2025, the CMS detector will undergo major upgrades to its L1 Trigger system [160]. Such upgrades are necessary in order to take advantage of the large number of collision events that the HL-LHC will offer, as it will aim for a peak luminosity of 7.5×10^{34} cm^{-2}s^{-1}. This will result in up to 200 simultaneous proton collisions per bunch crossing, which the existing L1 Trigger system is unequipped to handle. The new L1 Trigger system will have its latency extended from 3.2 µs to 12.5 µs, and it will also have its maximum output bandwidth increased from 100 kHz to 750 kHz. A unique aspect of these upgrades is that the L1 Trigger system will also take information from the inner tracker as input in addition to the muon and calorimeter systems. This will allow for using the new track finder to provide the initial information about particle transverse momentum p_T, angular position ϕ, pseudorapidity η, and charge q. Figure 5.1 shows the new architecture of the L1 Trigger that includes the track finder.

The prospect of more interactions per bunch crossing is also met with the demand for improvements to muon track reconstruction and resolution. New algorithms are being developed in order to take advantage of the higher maximum bandwidth and the new track finder in the L1 Trigger. Some make use of techniques such as Kalman Filters, with an
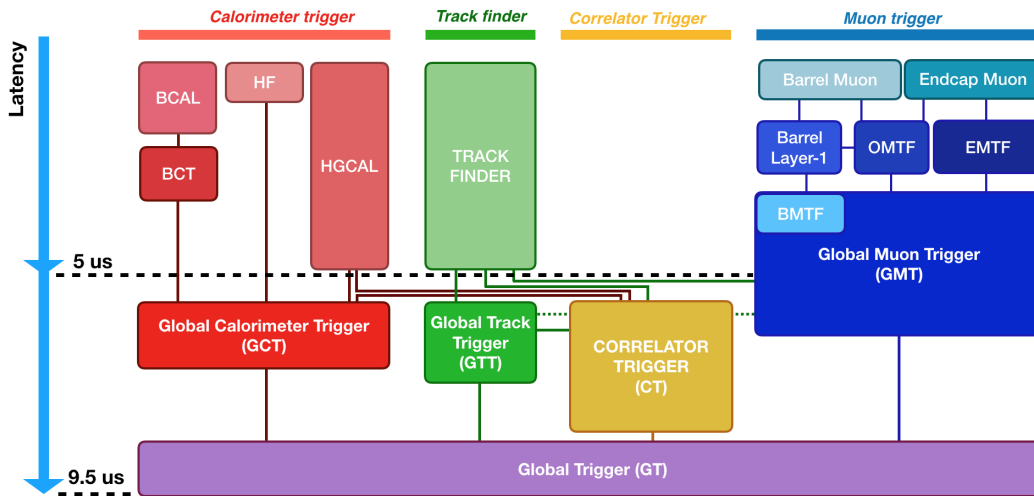
Figure 5.1: Architecture of the new L1 Trigger. In addition to taking inputs from the calorimeter and muon triggers, the Phase-2 upgrades will include a track finder in the L1 Trigger that takes input from the inner tracker.

algorithm that can be implemented onto FPGAs for the track trigger [161], or another for the muon trigger known as the Kalman Barrel Muon Track Finder (KBMTF) [162]. The work presented in this chapter instead relies on a novel approach for reconstructing muon tracks that uses both the track finder and the muon trigger.

5.3   The Tracks Plus Stubs Algorithm

As muons produced in collision events move through the detector, they create detection stubs in the DTs, RPCs, and CSCs, which are L1 Trigger primitives that contain information about the angular position ϕ and the bending angle[1] ϕ_b in the chamber for which the stub was created. Figure 5.2 shows a slice of the CMS detector in the r-ϕ plane, with an example of a process in which a muon passes through the DT chambers. The Tracks Plus Stubs (TPS) algorithm combines the information from the track trigger and the detection stubs in

---

[1]The bending angle ϕ_b is only measured in the DTs.

the chambers to create a candidate track that will later be reconstructed as a muon in the detector. By using the initial information from the track trigger, the algorithm propagates the initial muon track to the outer layers of the detector. The propagated values for the angular variables ϕ and ϕ_b are then compared to those as recorded by the stub measurements. From this, the algorithm can construct a candidate muon track, which is a combined object consisting of a track from the track trigger, and a collection of stubs associated to the track.
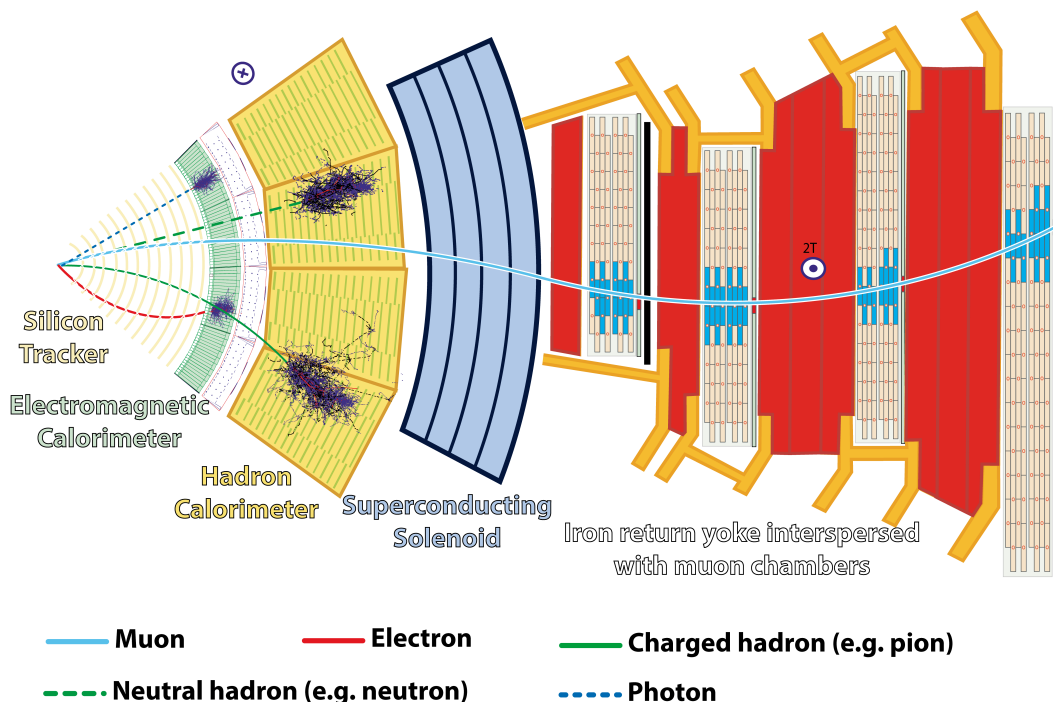
Figure 5.2: Slice of the CMS detector for a process in which a muon is produced [163]. As the muon passes through the silicon tracker and the muon chambers, the electronics obtain measurements of the muon's transverse momentum p_T, angular position ϕ, pseudorapidity η, and charge q. Such information is used by the L1 Trigger to decide whether or not to save an event for analysis.

5.3.1 Muon Track Propagation

One of the defining characteristics of the CMS detector is the 3.8 T solenoidal magnetic field that is aligned with the beam axis. In a uniform magnetic field B, a charged particle of charge q with momentum transverse to the magnetic field p_T will experience an induced centripetal force due to the Lorentz force that the magnetic field exerts on the charge. This in turn defines a radius of orbit R for the charge, which is related to the transverse momentum p_T by the relation $p_\mathrm{T} = qBR$. It is typical in particle physics to convert the units of the elementary charge so that in terms of B and R, we have

$$p_\mathrm{T} = 0.3BR \text{ GeV}/c. \tag{5.1}$$

However, it is too computationally expensive to use the exact formula for a circular arc in the L1 Trigger hardware in order to model the trajectory that a charged particle takes through the detector. Moreover, the transverse momenta for muons that result in a typical collision event of interest are such that a parabolic approximation is accurate enough to describe the track of the particle.

Assuming that the track starts in the center of the beamline as in figure 5.3, we may approximate the circular arc that the charged particle follows through the detector by

$$y(x) = \frac{x^2}{2R} + bx, \tag{5.2}$$

where R is the radius of curvature as in equation 5.1, and b is a constant to be determined. First, observe that at the origin, the tangent of the initial angle ϕ_0 corresponds to the first derivative of equation 5.2 evaluated at $x = 0$. Therefore,

$$\left.\frac{\mathrm{d}y}{\mathrm{d}x}\right|_{x=0} = \tan\phi_0 = b, \tag{5.3}$$

149

and hence

$$y(x) = \frac{x^2}{2R} + x \tan \phi_0. \tag{5.4}$$

At the position of the charge q, we also have that the tangent of the position angle ϕ is given by

$$\tan \phi = \frac{y(x_{\text{stub}})}{x_{\text{stub}}} = \frac{x_{\text{stub}}}{2R} + \tan \phi_0, \tag{5.5}$$

which we may rearrange to obtain

$$\tan \phi - \tan \phi_0 = \frac{x_{\text{stub}}}{2R}. \tag{5.6}$$

Since the p_{T} of a muon that passes through the threshold of the detector is high enough such that the radius R is large, $\Delta\phi \equiv \phi - \phi_0$ is small, and hence we may make the approximation that $\tan \phi - \tan \phi_0 \approx \phi - \phi_0$. Thus, the propagated position angle is

$$\phi_{\text{prop}} = \frac{x_{\text{stub}}}{2R} + \phi_0 = Ck + \phi_0, \tag{5.7}$$

where we have used the fact that $k = 1/R$ and C is a constant to be determined based on the position of the stub. Furthermore, in figure 5.3, we can see that due to the symmetry of the circular arc traced by the track of the particle, the bending angle ϕ_b must be equal to the change in the position angle $\Delta\phi$, from which we immediately obtain

$$\phi_{b,\text{prop}} = Ck. \tag{5.8}$$

With equations 5.7 and 5.8 in hand, we may now propagate the tracks based on the initial information about the curvature k and angle ϕ_0. The CMS detector consists of multiple layers of detection chambers, and each chamber requires its own propagation constant C. The relevant variables to consider for C based on the geometry of the detector are the pseudorapidity of the track η and the station depth d. Thus, the propagation constants $C(\eta, d)$
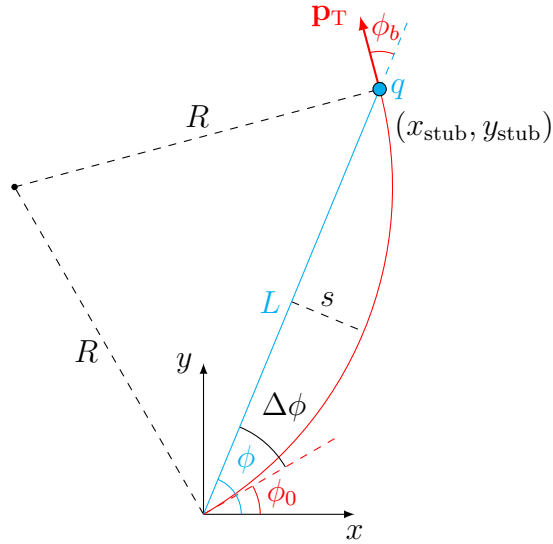
Figure 5.3: Illustration of the circular trajectory taken by a particle with charge q positioned at $(x_{\mathrm{stub}}, y_{\mathrm{stub}})$ in a uniform magnetic field, with orbit radius R. The track starts at the origin with an initial angle ϕ_0 tangent to the track of the particle, and ends with a final angle of ϕ for a total change in angle $\Delta\phi \equiv \phi - \phi_0$. The charged particle covers a radial distance L with respect to the origin of the track, and the perpendicular distance between the mid-point of the track and the radial line L is denoted by the sagitta s. The vector corresponding to the p_{T} of the charge is labeled, with the bending angle ϕ_b drawn with respect to L.

are functions of these two variables. Rather than obtaining these constants analytically, they are obtained by using simulation data.

To do this, we divide the detector into separate η regions and depths, as seen in figure 5.4, and treat each section as a separate detector with its own propagation constant $C(\eta, d)$. We then look at two-dimensional histograms of $\Delta\phi$ and ϕ_b from simulated detection stubs as functions of k for each section of the detector based on simulated detection stubs. An example of this can be seen in figure 5.5. For every bin in curvature k, the distribution of $\Delta\phi$ or ϕ_b is roughly Gaussian, and hence we fit Gaussians to the vertical slices of these histograms. We then consider the mean of these Gaussians and make linear fits for $\Delta\phi$ and ϕ_b in accordance with equations 5.7 and 5.8. These then define the propagation constants $C(\eta, d)$ for each detector, thereby allowing us to predict where a muon produced at the beamline during a collision event will end up in the detection chambers.
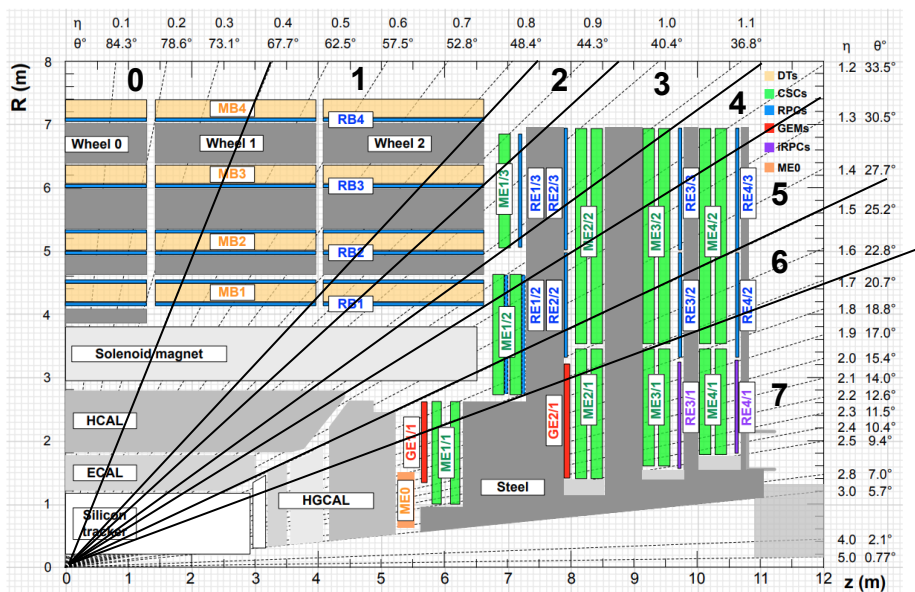
Figure 5.4: Cross section of the CMS detector in the r-z plane illustrating how the detector is separated into different η regions. Each η region and depth is treated as a separate detector for the TPS algorithm.
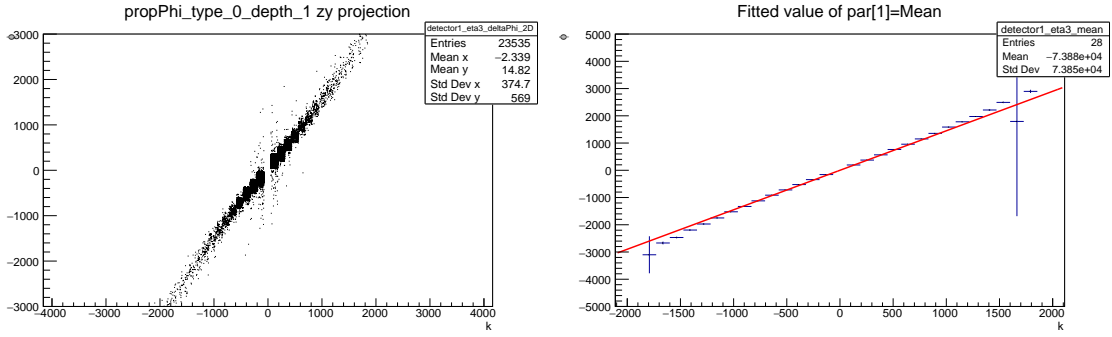
Figure 5.5: Two-dimensional distribution of $\Delta\phi$ from simulated detection stubs as a function of curvature k (left), and linear fit for the mean values of Gaussians fitted to the vertical slices of the two-dimensional histogram (right). Propagation constants $C(\eta, d)$ for $\Delta\phi$ and ϕ_b for each section of the detector are obtained through these linear fits, in accordance with equations 5.7 and 5.8.

5.3.2 Pull Distributions and Stub Matching

Once the propagation constants are obtained, the information for a candidate muon obtained from the track trigger can be used to predict where the muon detection stubs will be found based on the initial information about the curvature of the track k and the initial angle ϕ_0. One of the main considerations in matching a track to detection stubs is the position resolution for the stub measurements. The standard deviation of the Gaussian fits for $\Delta\phi$ and ϕ_b as described in the previous subsection corresponds to the position resolution of the measurements, and has a quadratic form

$$\sigma = \sqrt{\alpha k^2 + \beta}, \tag{5.9}$$

where α is a multiple scattering term that dominates for high curvature tracks (i.e., low p_T tracks), and β is a constant term corresponding to the position uncertainty of the detector [42].

However, this form for σ, as with the analytic forms for the propagated ϕ and ϕ_b values,

is too computationally expensive to implement into the hardware. Instead, we approximate the position resolution using

$$\sigma \approx a|k| + b, \tag{5.10}$$

where a and b are constants analogous to α and β. Figure 5.6 shows an example of the position resolution from one of the Gaussian fits for $\Delta\phi$ and the fit obtained for equation 5.10. As with the propagation coefficients $C(\eta, d)$, the position resolution constants $a(\eta, d)$ and $b(\eta, d)$ are also specific to each detector based on the η region and depth.
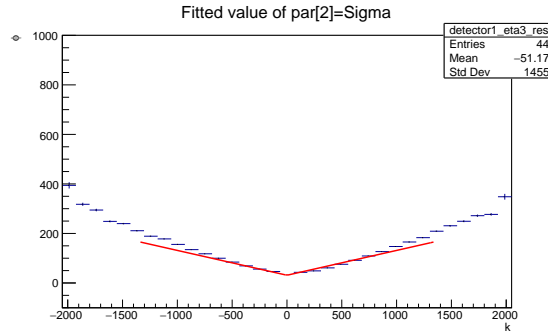
Figure 5.6: Plot of the resolution for the stub measurements based on the Gaussian fits obtained from the two-dimensional distributions of $\Delta\phi$. The resolution is fitted using the linear approximation of equation 5.10.

With the means to propagate the tracks from the track trigger and determine the resolution of the stub measurements, we may now proceed with determining whether or not a stub is suitable for being matched with a candidate muon. To do this, we consider the pull distributions for each stub with respect to a track. For each track, we check the pull values of every stub that may get matched with the track, which are given by

$$P_\phi = \frac{\phi_{\text{prop}} - \phi_{\text{stub}}}{\sigma} = \frac{\phi_{\text{prop}} - \phi_{\text{stub}}}{a|k| + b}. \tag{5.11}$$

The distributions made by sampling these pull values from simulation are Gaussian distributed, and an example may be seen in figure 5.7. We then match stubs to tracks by

considering the absolute value of the pulls for each stub. If $|P_\phi|$ for a stub is below a certain threshold for a track, then the stub will be matched to the track. Stubs that exceed the threshold for $|P_\phi|$ will instead be discarded.
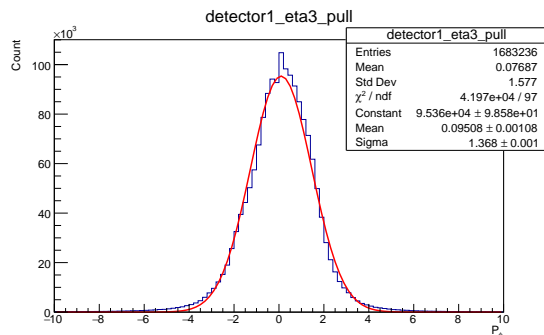
Figure 5.7: Example of a pull distribution for a single section of the detector based on the depth and η region. The histogram is made by sampling the pull values of all tracks in simulation based on equation 5.11. By construction, the pull distribution is a Gaussian with a mean of 0 and a standard deviation of 1.

5.3.3 Track Cleaning and Isolation

One issue that arises in the course of matching stubs to tracks is the possibility of having more than one detection stub shared between tracks. As a stub can only come from a single muon track, the algorithm requires a process by which tracks are discarded if they share one or more stubs. To deal with this, the TPS algorithm cleans tracks by checking if there are stubs shared between tracks after all the candidate tracks are obtained.

There are two cases that are considered during the cleaning process. The first is case 1 in figure 5.8, in which two or more tracks share one or more detection stubs. In this case, the track with the most detection stubs is retained and all others are discarded. For case 2, if two tracks have the same number of stubs, we instead consider the difference in the propagated values of ϕ versus the values as measured by the detection stubs. We check the

sum of the difference in these values by evaluating

$$\Delta\phi_{\text{prop,sum}} = \sum_i |\phi_{\text{prop},i} - \phi_{\text{stub},i}|, \tag{5.12}$$

where i denotes the depth in the detector, for each candidate track. The track with the smallest sum $\Delta\phi_{\text{prop,sum}}$ of the deviation in ϕ between the propagated and stub measured values is retained, while all others are discarded.

Figure 5.8: Illustration of the two different cases that are considered when cleaning candidate tracks that share detection stubs. In case 1 there are two tracks that share stubs but one track has more stubs than the other. In case 2, the tracks share the same number of stubs, but one track has a smaller sum of the deviation in the propagated ϕ values as given in equation 5.12.

The TPS algorithm also allows for track isolation when considering muon candidates in order to reduce heavy flavor contributions from QCD processes, which allows for reducing background. For each candidate track, the algorithm checks to see if there are any additional tracks whose origin is within $|d_z| < 0.2$ cm along the beamline of the candidate track's origin, and if these tracks are within a cone of radius ΔR centered around the candidate track, as seen in figure 5.9. The algorithm then evaluates the sum of the individual transverse momenta $p_{\text{T},i}$ given by

$$p_{\text{T,cone}} = \sum_{i \in \text{cone}} p_{\text{T},i}, \tag{5.13}$$

where we exclude the candidate track for which the cone is centered upon. If $p_{\text{T,cone}}$ exceeds

the threshold set for the algorithm, then the candidate track being evaluated is discarded.
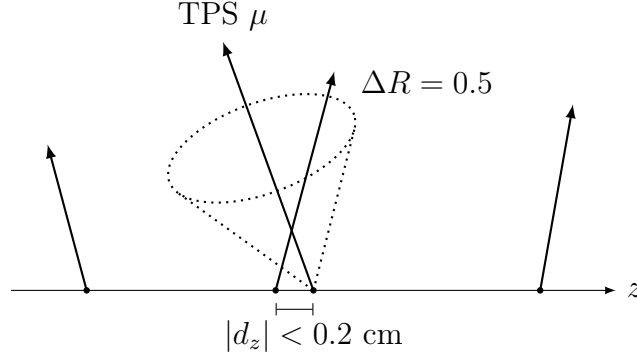
Figure 5.9: Illustration of the track isolation process used by the algorithm. A cone is defined about the origin of the candidate track TPS μ, and the algorithm checks if there are any adjacent tracks whose origin is within $|d_z|$ of the TPS μ origin, and if the track is within a cone of radius ΔR centered about TPS μ. Tracks for which $p_{\text{T,cone}}$ as defined by equation 5.13 exceeds the threshold set for the algorithm are discarded.

5.3.4 Trigger Efficiencies and Rates

To assess the effectiveness of the algorithm, efficiency studies were performed to see how well the algorithm matches stubs to real muon tracks in simulation. For a given event, the efficiency is defined by

$$\epsilon = \frac{N_{\text{TPS}}}{N_{\text{gen}}}, \tag{5.14}$$

where N_{TPS} is the number of TPS tracks obtained by the algorithm, and N_{gen} is the number of real muons generated in the simulation event. Figure 5.10 shows the results obtained when evaluating the efficiency for all events in a simulation sample of muons passing through the detector as a function of muon η and p_{T}. The performance of the TPS algorithm is compared to the existing KBMTF, and to an algorithm which matches tracks to KBMTF muons referred to as Track+KBMTF. For these efficiency studies, we required that a TPS track has at least two stubs. A notable feature of the TPS algorithm is its performance in

the gap region of $|\eta| \in [0.15, 0.35]$ between wheels 1 and -1. While other algorithms suffer significant losses in efficiency in the gap region, the TPS algorithm performs especially well by comparison in this region.
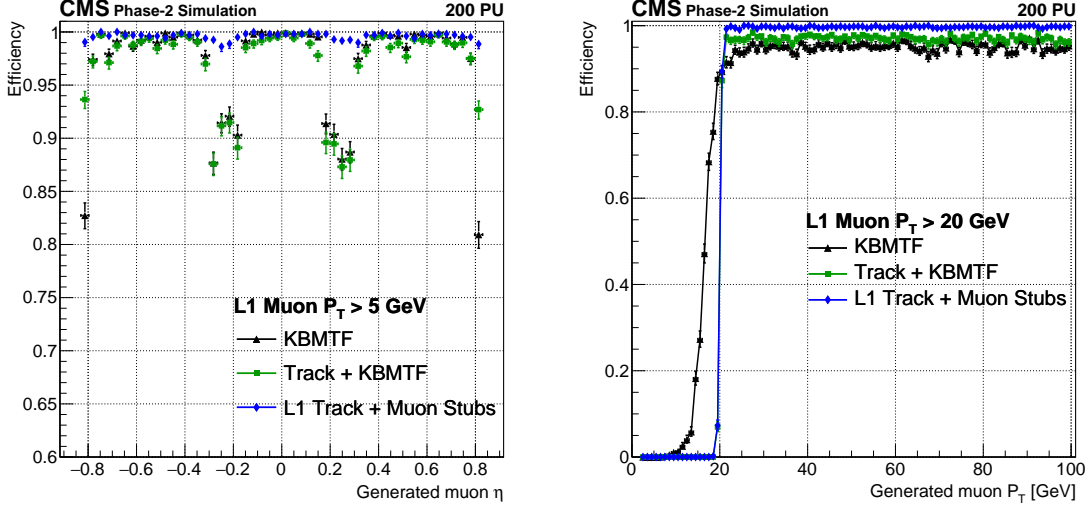
Figure 5.10: Comparison of the efficiencies defined by equation 5.14 for simulated muon η (left) and p_{T} (right). The TPS algorithm (denoted by L1 Track+Muon Stubs) is required to have two or more stubs associated to muon tracks, and is compared to the existing KBMTF, and to an algorithm that combines tracks with KBMTF muons (denoted by Track+KBMTF). The TPS algorithm offers better overall efficiency in comparison to the other algorithms.

One of the main upgrades to the L1 Trigger will be the ability to record events at 750 kHz. The bandwidth needed to record events is a precious resource, and as such it is desirable for a muon tracking algorithm to devote as much of it as possible to recording signal events. This problem is further exacerbated by pileup, as the HL-LHC could see up to 100-200 collision events at a time along the beam line. To study the effect of pileup on the trigger rate, we used a simulated background-only sample in which there are no muons present to test how often the TPS algorithm will trigger on false tracks. The trigger rates R_{trig} are computed using the fraction of events in simulation for which there is at least one TPS muon over a

specified transverse momentum threshold $p_{\mathrm{T,thresh}}$, according to

$$R_{\mathrm{trig}}(p_{\mathrm{T,thresh}}) = \frac{f_{\mathrm{orbit}} N_{\mathrm{bunch}}}{N_{\mathrm{event}}} \int_{p_{\mathrm{T,thresh}}}^{\infty} f(p_{\mathrm{T,max}}) \, \mathrm{d}p_{\mathrm{T,max}} \,, \tag{5.15}$$

where $f_{\mathrm{orbit}} = 11.2456$ kHz is the LHC revolution frequency, $N_{\mathrm{bunch}} = 2760$ is the number of proton bunches crossing the interaction point, N_{event} is the number of events in simulation, and $f(p_{\mathrm{T,max}})$ is a pdf populated with the maximum p_{T} of the matched tracks in a given event, which is populated over the full number of simulation events.

A comparison of the trigger rate at different trigger thresholds can be see in figure 5.11. The TPS algorithm performance is similar to the Track+KBMTF algorithm (~ 3 kHz at 20 GeV). Moreover, allowing for track isolation with a maximum $p_{\mathrm{T,cone}}$ of 5 GeV and a minimum $p_{\mathrm{T,i}}$ of 2 GeV results in a decrease in the rate by a factor of 2 at 20 GeV, thereby demonstrating the effectiveness of using track isolation to suppress background. These results also show that the TPS algorithm is well-suited for handling background noise while also efficiently matching detection stubs to real muon tracks.

5.4   Future Implementation

While initially tested as software, the TPS algorithm will eventually be implemented into the CMS detector through hardware to allow for fast processing. As of this writing, the UCLA CMS research group is currently in the process of testing a custom OCEAN Blade board with an FPGA that will allow for the TPS algorithm to be implemented as firmware. Figure 5.12 shows a picture of an assembled OCEAN Blade board being used for testing.

5.5   Conclusion

Work towards the TPS algorithm is presented, which is a novel muon tracking algorithm that takes advantage of the new track finder that will be implemented in the L1 Trigger
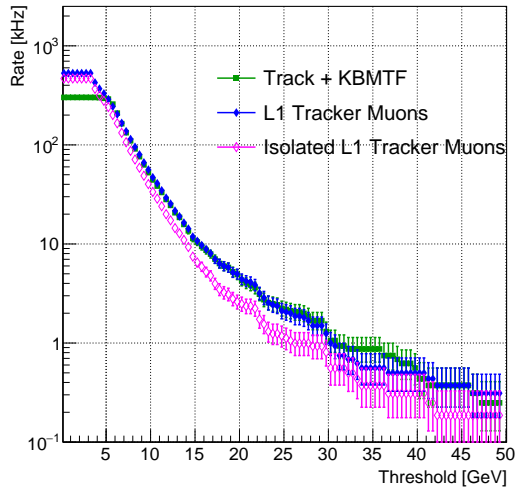
Figure 5.11: Comparison of the trigger rates at different p_T thresholds for the TPS (with and without track isolation) and Track+KBMTF algorithms when running on a background-only simulation sample in which there are no muons present. The TPS algorithm with isolation results in lower overall trigger rates compared to the Track+KBMTF algorithm.

during the LS3 upgrades. The algorithm matches tracks from the track finder to detection stubs from the muon trigger, while offering high efficiency and low trigger rates compared to competing algorithms. The TPS algorithm will be implemented via firmware onto an FPGA on the OCEAN Blade board.
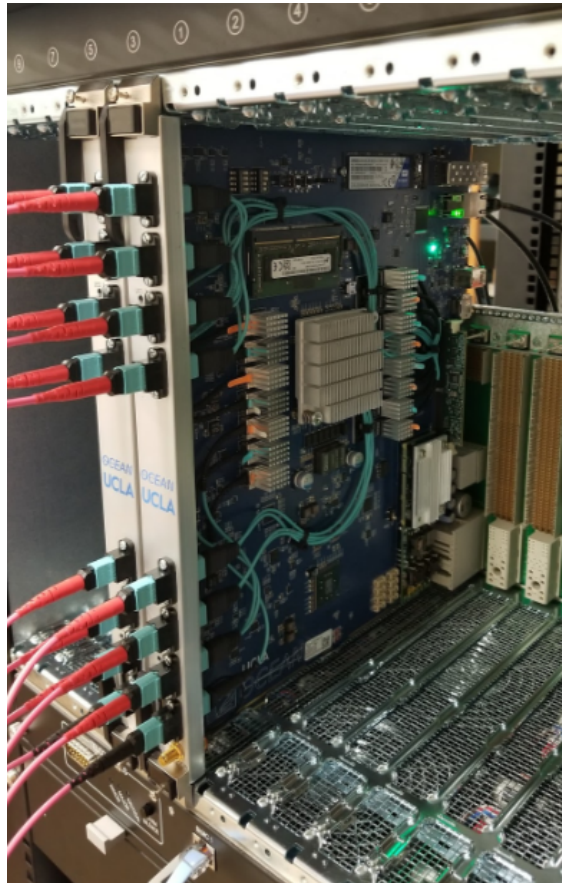
Figure 5.12: Picture of the assembled OCEAN Blade board that will be implemented into the CMS detector hardware. The onboard FPGA will allow for the TPS algorithm to be implemented directly as firmware into the muon trigger in the detector.

REFERENCES

[1] Charles Singer. *A Short History of Science to the Nineteenth Century*. Streeter Press, 1941.

[2] Sarojakanta Choudhury. *Educational Philosophy of Dr. Sarvepalli Radhakrishnan*. Deep & Deep Publications, 2006.

[3] J. J. Thomson and M. A. F. R .S. XL. cathode rays. *The London, Edinburgh, and Dublin Philosophical Magazine and Journal of Science*, 44(269):293–316, 1897. URL: `https://doi.org/10.1080/14786449708621070`, `arXiv:https://doi.org/10.1080/14786449708621070`.

[4] Vernon D. Barger and Roger J.N. Phillips. *Collider Physics*. Westview Press, 1991.

[5] S. Weinberg. *The Discovery of Subatomic Particles Revised Edition*. Cambridge University Press, 2003.

[6] D.V. Schroeder. *An Introduction to Thermal Physics*. Always learning. Pearson Education, 2013.

[7] A. Einstein. Über einen die erzeugung und verwandlung des lichtes betreffenden heuristischen gesichtspunkt. *Annalen der Physik*, 322(6):132–148, 1905. URL: `https://onlinelibrary.wiley.com/doi/abs/10.1002/andp.19053220607`, `arXiv:https://onlinelibrary.wiley.com/doi/pdf/10.1002/andp.19053220607`.

[8] Nobel Foundation. The Nobel Prize in Physics, 1921. URL: `https://www.nobelprize.org/prizes/physics/1921/summary/`.

[9] C. M. G. Lattes et al. Processes involving charged mesons. *Nature*, 159, 1947. URL: `https://doi.org/10.1038/159694a0`.

[10] C. D. Anderson. Early work on the positron and muon. *American Journal of Physics*, 29(12):825–830, 1961. URL: `https://doi.org/10.1119/1.1937627`, `arXiv:https://doi.org/10.1119/1.1937627`.

[11] Los Alamos Science. The Reines-Cowan experiments, 1997. URL: `https://library.lanl.gov/cgi-bin/getfile?00326606.pdf`.

[12] Leon M. Lederman. Resource letter neu-1 history of the neutrino. *American Journal of Physics*, 38(2):129–136, 1970. URL: `https://doi.org/10.1119/1.1976245`, `arXiv:https://doi.org/10.1119/1.1976245`.

[13] Yataro Sekido and Harry Elliot. *Early History of Cosmic Ray Studies*. Springfield Netherlands, 1985.

[14] A. Pevsner, R. Kraemer, M. Nussbaum, C. Richardson, P. Schlein, R. Strand, T. Toohig, M. Block, A. Engler, R. Gessaroli, and C. Meltzer. Evidence for a three-pion resonance near 550 MeV. *Phys. Rev. Lett.*, 7:421–423, Dec 1961. URL: `https://link.aps.org/doi/10.1103/PhysRevLett.7.421`.

[15] M. Gell-Mann. A schematic model of baryons and mesons. *Physics Letters*, 8(3):214–215, 1964. URL: `http://www.sciencedirect.com/science/article/pii/S0031916364920013`, `doi:https://doi.org/10.1016/S0031-9163(64)92001-3`.

[16] G. Zweig. *An SU(3) model for strong interaction symmetry and its breaking. Version 2*, pages 22–101. 2 1964.

[17] E. D. Bloom et al. High-energy inelastic $e-p$ scattering at 6° and 10°. *Phys. Rev. Lett.*, 23:930–934, Oct 1969. URL: `https://link.aps.org/doi/10.1103/PhysRevLett.23.930`.

[18] F.E. Close. Quarks and partons. Dec 1976. URL: `http://inis.iaea.org/search/search.aspx?orig_q=RN:09393746`.

[19] J. E. Augustin et al. Discovery of a narrow resonance in e^+e^- annihilation. *Phys. Rev. Lett.*, 33:1406–1408, Dec 1974. URL: `https://link.aps.org/doi/10.1103/PhysRevLett.33.1406`.

[20] J. J. Aubert et al. Experimental observation of a heavy particle *J. Phys. Rev. Lett.*, 33:1404–1406, Dec 1974. URL: `https://link.aps.org/doi/10.1103/PhysRevLett.33.1404`.

[21] Martin L. Perl et al. Properties of anomalous $e\mu$ events produced in e^+e^- annihilation. *Phys. Lett. B*, 63:466, 1976. `doi:10.1016/0370-2693(76)90399-3`.

[22] S. W. Herb et al. Observation of a dimuon resonance at 9.5 GeV in 400-GeV proton-nucleus collisions. *Phys. Rev. Lett.*, 39(5):252–255, Aug 1977. Provided by the SAO/NASA Astrophysics Data System. URL: `https://ui.adsabs.harvard.edu/abs/1977PhRvL..39..252H`, `doi:10.1103/PhysRevLett.39.252`.

[23] F. Abe et al. Observation of top quark production in $\overline{p}p$ collisions with the collider detector at fermilab. *Phys. Rev. Lett.*, 74:2626–2631, Apr 1995. URL: `https://link.aps.org/doi/10.1103/PhysRevLett.74.2626`.

[24] Steven Weinberg. A model of leptons. *Phys. Rev. Lett.*, 19:1264–1266, Nov 1967. URL: `https://link.aps.org/doi/10.1103/PhysRevLett.19.1264`.

[25] Nobel Foundation. The Nobel Prize in Physics, 1979. URL: `https://www.nobelprize.org/prizes/physics/1979/summary/`.

[26] G. Arnison et al. Experimental observation of isolated large transverse energy electrons with associated missing energy at $\sqrt{s} = 540$ GeV. *Physics Letters B*, 122(1):103–116, 1983. URL: `http://www.sciencedirect.com/science/article/pii/0370269383911772`, `doi:https://doi.org/10.1016/0370-2693(83)91177-2`.

[27] G. Arnison et al. Experimental observation of lepton pairs of invariant mass around 95 GeV/c^2 at the CERN SPS collider. *Physics Letters B*, 126(5):398–410, 1983. URL: `http://www.sciencedirect.com/science/article/pii/0370269383901880`, `doi:https://doi.org/10.1016/0370-2693(83)90188-0`.

[28] Peter W. Higgs. Broken symmetries and the masses of gauge bosons. *Phys. Rev. Lett.*, 13:508–509, Oct 1964. URL: `https://link.aps.org/doi/10.1103/PhysRevLett.13.508`.

[29] ATLAS Collaboration. Observation of a new particle in the search for the standard model Higgs boson with the ATLAS detector at the LHC. *Physics Letters B*, 716(1):1–29, 2012. URL: `http://www.sciencedirect.com/science/article/pii/S037026931200857X`, `doi:https://doi.org/10.1016/j.physletb.2012.08.020`.

[30] CMS Collaboration. Observation of a new boson at a mass of 125 GeV with the CMS experiment at the LHC. *Physics Letters B*, 716(1):30–61, 2012. URL: `http://www.sciencedirect.com/science/article/pii/S0370269312008581`, `doi:https://doi.org/10.1016/j.physletb.2012.08.021`.

[31] Alfredo Macías and Abel Camacho. On the incompatibility between quantum theory and general relativity. *Physics Letters B*, 663(1):99–102, 2008. URL: `http://www.sciencedirect.com/science/article/pii/S0370269308003936`, `doi:https://doi.org/10.1016/j.physletb.2008.03.052`.

[32] P. A. R. Ade, N. Aghanim, M. I. R. Alves, C. Armitage-Caplan, M. Arnaud, M. Ashdown, F. Atrio-Barandela, J. Aumont, H. Aussel, et al. Planck 2013 results. i. overview of products and scientific results. *Astronomy & Astrophysics*, 571:A1, Oct 2014. URL: `http://dx.doi.org/10.1051/0004-6361/201321529`.

[33] Utpal Sarkar. *Particle and Astroparticle Physics*. CRC Press, 2008.

[34] Shaaban Khalil. Search for supersymmetry at LHC. *Contemporary Physics*, 44(3):193–201, 2003. URL: `https://doi.org/10.1080/0010751031000077378`, `arXiv:https://doi.org/10.1080/0010751031000077378`.

[35] P. Kanti. Black holes at the large hadron collider. *Lecture Notes in Physics*, pages 387–423, 2009. URL: `http://dx.doi.org/10.1007/978-3-540-88460-6_10`.

[36] Nobel Foundation. The Nobel Prize in Physics, 1965. URL: `https://www.nobelprize.org/prizes/physics/1965/summary/`.

[37] Tatsumi Aoyama, Masashi Hayakawa, Toichiro Kinoshita, and Makiko Nio. Tenth-order electron anomalous magnetic moment: Contribution of diagrams without closed lepton loops. *Physical Review D*, 91(3), Feb 2015. URL: `http://dx.doi.org/10.1103/PhysRevD.91.033006`.

[38] C. N. Yang and R. L. Mills. Conservation of isotopic spin and isotopic gauge invariance. *Physical Review*, 96(1):191–195, Oct 1954. Provided by the SAO/NASA Astrophysics Data System. URL: `https://ui.adsabs.harvard.edu/abs/1954PhRv...96..191Y`, `doi:10.1103/PhysRev.96.191`.

[39] Tian Yu Cao. *Conceptual Developments of 20th Century Field Theories*. Cambridge University Press, 1997. `doi:10.1017/CBO9780511563997`.

[40] Sven Krippendorf, Fernando Quevedo, and Oliver Schlotterer. Cambridge lectures on supersymmetry and extra dimensions, 2010. `arXiv:1011.1491`.

[41] Michael E Peskin and Daniel V Schroeder. *An Introduction to Quantum Field Theory*. Westview, 1995. URL: `https://cds.cern.ch/record/257493`.

[42] P. A. Zyla et al. Review of particle physics. *Phys. Rev. D*, 2020.

[43] T. Muta. *Foundations of Quantum Chromodynamics: An Introduction to Perturbative Methods in Gauge Theories*. World Scientific lecture notes in physics. World Scientific, 2010. URL: `https://books.google.com/books?id=Rq5q0l5XRVkC`.

[44] Mark Srednicki. *Quantum Field Theory*. Cambridge Univ. Press, Cambridge, 2007. URL: `https://cds.cern.ch/record/1019751`.

[45] Robert D. Klauber. *Student Friendly Quantum Field Theory: Basic Principles and Quantum Electrodynamics*. Sandtrove Press, Fairfield, Iowa, 2013.

[46] Ta-Pei Cheng and Ling-Fong Li. *Gauge Theory of Elementary Particle Physics*. Oxford science publications. Clarendon Press, 1984. URL: `https://books.google.com/books?id=lk8GEzVNb10C`.

[47] David J. Griffiths. *Introduction to Elementary Particles*. Pearson Educational International, 2008.

[48] Jeffrey Goldstone, Abdus Salam, and Steven Weinberg. Broken symmetries. *Phys. Rev.*, 127:965–970, Aug 1962. URL: `https://link.aps.org/doi/10.1103/PhysRev.127.965`.

[49] Peter W. Higgs. Broken symmetries, massless particles and gauge fields. *Phys. Lett.*, 12:132–133, Sep 1964. `doi:10.1016/0031-9163(64)91136-9`.

[50] Joseph D. Lykken. Beyond the standard model. *arXiv e-prints*, page arXiv:1005.1676, May 2010. Provided by the SAO/NASA Astrophysics Data System. URL: `https://ui.adsabs.harvard.edu/abs/2010arXiv1005.1676L`, arXiv:1005.1676.

[51] A. Zee. *Quantum Field Theory in a Nutshell*. Princeton University Press, 2010.

[52] Stephen P. Martin. A supersymmetry primer. *Advanced Series on Directions in High Energy Physics*, pages 1–98, Jul 1998. URL: `http://dx.doi.org/10.1142/9789812839657_0001`.

[53] J. Wess and B. Zumino. A lagrangian model invariant under supergauge transformations. *Physics Letters B*, 49(1):52–54, 1974. URL: `http://www.sciencedirect.com/science/article/pii/0370269374905784`, doi:`https://doi.org/10.1016/0370-2693(74)90578-4`.

[54] Michael Dine. *Supersymmetry and String Theory: Beyond the Standard Model*. Cambridge University Press, 2007. `doi:10.1017/CBO9780511618482`.

[55] Howard Georgi and S. L. Glashow. Unity of all elementary-particle forces. *Phys. Rev. Lett.*, 32:438–441, Feb 1974. URL: `https://link.aps.org/doi/10.1103/PhysRevLett.32.438`.

[56] Bastian Diaz, Martin Schmaltz, and Yi-Ming Zhong. The leptoquark hunter's guide: pair production. *Journal of High Energy Physics*, 2017(10), Oct 2017. URL: `http://dx.doi.org/10.1007/JHEP10(2017)097`.

[57] M. Shiozawa et al. Search for proton decay via $p \rightarrow e^+\pi^0$ in a large water cherenkov detector. *Phys. Rev. Lett.*, 81:3319–3323, Oct 1998. URL: `https://link.aps.org/doi/10.1103/PhysRevLett.81.3319`.

[58] JoAnne L. Hewett and Thomas G. Rizzo. Low-energy phenomenology of superstring-inspired E_6 models. *Physics Reports*, 183(5):193–381, 1989. URL: `http://www.sciencedirect.com/science/article/pii/0370157389900719`, doi:`https://doi.org/10.1016/0370-1573(89)90071-9`.

[59] Mirjam Cvetič and Stephen Godfrey. Discovery and identification of extra gauge bosons. *Electroweak Symmetry Breaking and New Physics at the TeV Scale*, pages 383–415, May 1997. URL: `http://dx.doi.org/10.1142/9789812830265_0007`.

[60] Theodor Kaluza. Zum unitätsproblem der physik. *Sitzungsberichte der Königlich Preußischen Akademie der Wissenschaften (Berlin)*, pages 966–972, Jan 1921. Provided by the SAO/NASA Astrophysics Data System. URL: `https://ui.adsabs.harvard.edu/abs/1921SPAW.......966K`.

[61] Lisa Randall and Raman Sundrum. An alternative to compactification. *Phys. Rev. Lett.*, 83:4690–4693, Dec 1999. URL: `https://link.aps.org/doi/10.1103/PhysRevLett.83.4690`.

[62] A. M. Sirunyan, A. Tumasyan, W. Adam, F. Ambrogi, E. Asilar, T. Bergauer, J. Brandstetter, E. Brondolin, M. Dragicevic, et al. Search for a heavy resonance decaying to a pair of vector bosons in the lepton plus merged jet final state at $\sqrt{s}$ = 13 TeV. *Journal of High Energy Physics*, 2018(5), May 2018. URL: `http://dx.doi.org/10.1007/JHEP05(2018)088`.

[63] Walter D. Goldberger and Mark B. Wise. Modulus stabilization with bulk fields. *Physical Review Letters*, 83(24):4922–4925, Dec 1999. URL: `http://dx.doi.org/10.1103/PhysRevLett.83.4922`.

[64] Walter D. Goldberger and Mark B. Wise. Phenomenology of a stabilized modulus. *Physics Letters B*, 475(3-4):275–279, Mar 2000. URL: `http://dx.doi.org/10.1016/S0370-2693(00)00099-X`.

[65] Duccio Pappadopulo, Andrea Thamm, Riccardo Torre, and Andrea Wulzer. Heavy vector triplets: bridging theory and data. *Journal of High Energy Physics*, 2014(9), Sep 2014. URL: `http://dx.doi.org/10.1007/JHEP09(2014)060`.

[66] Liam Fitzpatrick, Jared Kaplan, Lisa Randall, and Lian-Tao Wang. Searching for the Kaluza-Klein graviton in bulk RS models. *Journal of High Energy Physics*, 2007(09):013–013, Sep 2007. URL: `https://doi.org/10.1088%2F1126-6708%2F2007%2F09%2F013`.

[67] Kaustubh Agashe, Hooman Davoudiasl, Gilad Perez, and Amarjit Soni. Warped gravitons at the CERN LHC and beyond. *Phys. Rev. D*, 76:036006, Aug 2007. URL: `https://link.aps.org/doi/10.1103/PhysRevD.76.036006`.

[68] Alexandra Carvalho. Gravity particles from warped extra dimensions, predictions for LHC, 2018. `arXiv:1404.0102`.

[69] Michael Rauch. Vector-boson fusion and vector-boson scattering, 2016. `arXiv:1610.08420`.

[70] R. Abbasi, M. Ackermann, J. Adams, M. Ahlers, J. Ahrens, K. Andeen, J. Auffenberg, X. Bai, M. Baker, S.W. Barwick, et al. The IceCube data acquisition system: Signal capture, digitization, and timestamping. *Nuclear Instruments and Methods in Physics Research Section A: Accelerators, Spectrometers, Detectors and Associated Equipment*, 601(3):294–316, Apr 2009. URL: `http://dx.doi.org/10.1016/j.nima.2009.01.001`.

[71] Maxim Perelstein. Introduction to collider physics. *Physics of the Large and the Small*, Mar 2011. URL: `http://dx.doi.org/10.1142/9789814327183_0008`.

[72] B.R. Martin and G. Shaw. *Particle Physics*. Manchester Physics Series. Wiley, 2008. URL: `https://books.google.com/books?id=whIbrWJdEJQC`.

[73] Werner Herr and B Muratori. Concept of luminosity. 2006. URL: `https://cds.cern.ch/record/941318`, `doi:10.5170/CERN-2006-002.361`.

[74] M. Bicer, H. Duran Yildiz, I. Yildiz, G. Coignet, M. Delmastro, T. Alexopoulos, C Grojean, S. Antusch, T. Sen, et al. First look at the physics case of TLEP. *Journal of High Energy Physics*, 2014(1), Jan 2014. URL: `http://dx.doi.org/10.1007/JHEP01(2014)164`.

[75] Wolfgang K. H. Panofsky. The evolution of particle accelerators & colliders, 1997. URL: `https://www.slac.stanford.edu/pubs/beamline/27/1/27-1-panofsky.pdf`.

[76] Lyndon R Evans and Philip Bryant. LHC machine. *JINST*, 3:S08001. 164 p, 2008. This report is an abridged version of the LHC Design Report (CERN-2004-003). URL: `https://cds.cern.ch/record/1129806`, `doi:10.1088/1748-0221/3/08/S08001`.

[77] S Chatrchyan et al. The CMS experiment at the CERN LHC. *JINST*, 3:S08004. 361 p, 2008. Also published by CERN Geneva in 2010. URL: `https://cds.cern.ch/record/1129810`, `doi:10.1088/1748-0221/3/08/S08004`.

[78] Lucas Taylor. Detector overview: CMS experiment, Nov 2011. URL: `http://cms.web.cern.ch/news/detector-overview`.

[79] Esma Mobs. The CERN accelerator complex - august 2018. complexe des accélérateurs du CERN - août 2018. Aug 2018. General Photo. URL: `https://cds.cern.ch/record/2636343`.

[80] CERN. LHC performance reaches new highs, 2016. URL: `https://home.cern/news/news/accelerators/lhc-performance-reaches-new-highs`.

[81] CMS Collaboration. CMS luminosity - public results, 2018. URL: `https://twiki.cern.ch/twiki/bin/view/CMSPublic/LumiPublicResults`.

[82] Michael E. Peskin. *Concepts of Elementary Particle Physics*. Oxford Master Series in Particle Physics, Astrophysics, and Cosmology - 26. Oxford University Press, USA, April 2, 2019.

[83] Tai Sakuma. Cutaway diagrams of CMS detector. May 2019. URL: `https://cds.cern.ch/record/2665537`.

[84] CMS Collaboration. Commissioning and performance of the CMS pixel tracker with cosmic ray muons. *Journal of Instrumentation*, 5(03):T03007–T03007, Mar 2010. URL: `http://dx.doi.org/10.1088/1748-0221/5/03/T03007`.

[85] Serguei Chatrchyan et al. Description and performance of track and primary-vertex reconstruction with the CMS tracker. *JINST*, 9:P10009, 2014. `arXiv:1405.6569`, `doi:10.1088/1748-0221/9/10/P10009`.

[86] The CMS Phase-1 pixel detector upgrade. *JINST*, 16:P02027, 2021. `arXiv:2012.14304`, `doi:10.1088/1748-0221/16/02/P02027`.

[87] S Chatrchyan et al. Alignment of the CMS silicon tracker during commissioning with cosmic rays. *JINST*, 5(arXiv:0910.2505):T03009. 39 p, Oct 2009. URL: `https://cds.cern.ch/record/1211825`, `doi:10.1088/1748-0221/5/03/T03009`.

[88] Tai Sakuma and Thomas McCauley. Detector and event visualization with SketchUp at the CMS experiment. *Journal of Physics: Conference Series*, 513(2):022032, Jun 2014. URL: `http://dx.doi.org/10.1088/1742-6596/513/2/022032`.

[89] CMS Collaboration. Performance of the CMS hadron calorimeter with cosmic ray muons and LHC beam data. *Journal of Instrumentation*, 5(03):T03012–T03012, Mar 2010. URL: `http://dx.doi.org/10.1088/1748-0221/5/03/T03012`.

[90] James S. Gainer, Kunal Kumar, Ian Low, and Roberto Vega-Morales. Improving the sensitivity of Higgs boson searches in the golden channel. *Journal of High Energy Physics*, 2011(11), Nov 2011. URL: `http://dx.doi.org/10.1007/JHEP11(2011)027`.

[91] A. M. Sirunyan et al. Performance of the CMS muon detector and muon reconstruction with proton-proton collisions at $\sqrt{s} = 13$ TeV. *Journal of Instrumentation*, 13(06):P06015–P06015, Jun 2018. URL: `https://doi.org/10.1088%2F1748-0221%2F13%2F06%2Fp06015`.

[92] G. Abbiendi, J. Alcaraz Maestre, A. Álvarez Fernández, B. Álvarez González, N. Amapane, I. Bachiller, J.M. Barcala, L. Barcellan, C. Battilana, M. Bellato, et al. Study of the effects of radiation on the CMS drift tubes muon detector for the HL-LHC. *Journal of Instrumentation*, 14(12):C12010–C12010, Dec 2019. URL: `http://dx.doi.org/10.1088/1748-0221/14/12/C12010`.

[93] The CMS collaboration. The performance of the CMS muon detector in proton-proton collisions at $\sqrt{s} = 7$ TeV at the LHC. *Journal of Instrumentation*, 8(11):P11002–P11002, Nov 2013. URL: `https://doi.org/10.1088%2F1748-0221%2F8%2F11%2Fp11002`.

[94] Priyanka Kumari. Improved-RPC for the CMS muon system upgrade for the HL-LHC, 2020. `arXiv:2005.11396`.

[95] V. Khachatryan, A.M. Sirunyan, A. Tumasyan, W. Adam, E. Asilar, T. Bergauer, J. Brandstetter, E. Brondolin, M. Dragicevic, J. Erö, et al. The CMS trigger system. *Journal of Instrumentation*, 12(01):P01020–P01020, Jan 2017. URL: `http://dx.doi.org/10.1088/1748-0221/12/01/P01020`.

[96] CMS Collaboration. Performance of the CMS level-1 trigger in proton-proton collisions at $\sqrt{s} = 13$ TeV, 2020. `arXiv:2006.10165`.

[97] Daniele Trocino. The CMS high level trigger. *Journal of Physics: Conference Series*, 513(1):012036, Jun 2014. URL: `https://doi.org/10.1088%2F1742-6596%2F513%2F1%2F012036`.

[98] Sergio Cittolin, Attila Rácz, and Paris Sphicas. *CMS The TriDAS Project: Technical Design Report, Volume 2: Data Acquisition and High-Level Trigger. CMS trigger and data-acquisition project.* Technical Design Report CMS. CERN, Geneva, 2002. URL: `http://cds.cern.ch/record/578006`.

[99] Particle-flow event reconstruction in CMS and performance for jets, taus, and MET. Technical Report CMS-PAS-PFT-09-001, CERN, Geneva, Apr 2009. URL: `http://cds.cern.ch/record/1194487`.

[100] Commissioning of the particle-flow event reconstruction with the first LHC collisions recorded in the CMS detector. Technical Report CMS-PAS-PFT-10-001, 2010. URL: `http://cds.cern.ch/record/1247373`.

[101] Matteo Cacciari, Gavin P Salam, and Gregory Soyez. The anti-k_t jet clustering algorithm. *Journal of High Energy Physics*, 2008(04):063–063, Apr 2008. URL: `http://dx.doi.org/10.1088/1126-6708/2008/04/063`.

[102] Simone Marzani, Gregory Soyez, and Michael Spannowsky. Looking inside jets. *Lecture Notes in Physics*, 2019. URL: `http://dx.doi.org/10.1007/978-3-030-15709-8`.

[103] M. Aaboud, G. Aad, B. Abbott, O. Abdinov, B. Abeloos, S. H. Abidi, O. S. Abouzeid, N. L. Abraham, H. Abramowicz, et al. Search for WW/WZ resonance production in $\ell\nu qq$ final states in pp collisions at $\sqrt{s} = 13$ TeV with the ATLAS detector. *Journal of High Energy Physics*, 2018(3), Mar 2018. URL: `http://dx.doi.org/10.1007/JHEP03(2018)042`.

[104] M. Aaboud, G. Aad, B. Abbott, O. Abdinov, B. Abeloos, S.H. Abidi, O.S. Abouzeid, N.L. Abraham, H. Abramowicz, H. Abreu, et al. Search for diboson resonances with boson-tagged jets in pp collisions at $\sqrt{s} = 13$ TeV with the ATLAS detector. *Physics Letters B*, 777:91–113, Feb 2018. URL: `http://dx.doi.org/10.1016/j.physletb.2017.12.011`.

[105] G. Aad, B. Abbott, J. Abdallah, S. Abdel Khalek, O. Abdinov, R. Aben, B. Abi, M. Abolins, O. S. AbouZeid, et al. Search for production of WW/WZ resonances decaying to a lepton, neutrino and jets in pp collisions at $\sqrt{s} = 8$ TeV with the ATLAS detector. *The European Physical Journal C*, 75(5), May 2015. URL: `http://dx.doi.org/10.1140/epjc/s10052-015-3425-6`.

[106] V. Khachatryan, A. M. Sirunyan, A. Tumasyan, W. Adam, T. Bergauer, M. Dragicevic, J. Erö, C. Fabjan, M. Friedl, et al. Search for massive resonances decaying into pairs of boosted bosons in semi-leptonic final states at $\sqrt{s} = 8$ TeV. *Journal of High Energy Physics*, 2014(8), Aug 2014. URL: http://dx.doi.org/10.1007/JHEP08(2014)174.

[107] A. M. Sirunyan, A. Tumasyan, W. Adam, E. Asilar, T. Bergauer, J. Brandstetter, E. Brondolin, M. Dragicevic, J. Erö, et al. Search for massive resonances decaying into WW, WZ or ZZ bosons in proton-proton collisions at $\sqrt{s} = 13$ TeV. *Journal of High Energy Physics*, 2017(3), Mar 2017. URL: http://dx.doi.org/10.1007/JHEP03(2017)162.

[108] A.M. Sirunyan, A. Tumasyan, W. Adam, E. Asilar, T. Bergauer, J. Brandstetter, E. Brondolin, M. Dragicevic, J. Erö, M. Flechl, et al. Combination of searches for heavy resonances decaying to WW, WZ, ZZ, WH, and ZH boson pairs in proton-proton collisions at $\sqrt{s} = 8$ and 13 TeV. *Physics Letters B*, 774:533–558, Nov 2017. URL: http://dx.doi.org/10.1016/j.physletb.2017.09.083.

[109] Georges Aad et al. Search for heavy diboson resonances in semileptonic final states in pp collisions at $\sqrt{s} = 13$ TeV with the ATLAS detector. *Eur. Phys. J. C*, 80(12):1165, 2020. arXiv:2004.14636, doi:10.1140/epjc/s10052-020-08554-y.

[110] CMS luminosity measurements for the 2016 data taking period. Technical Report CMS-PAS-LUM-17-001, CERN, Geneva, 2017. URL: https://cds.cern.ch/record/2257069.

[111] CMS luminosity measurement for the 2017 data-taking period at $\sqrt{s} = 13$ TeV. Technical Report CMS-PAS-LUM-17-004, CERN, Geneva, 2018. URL: http://cds.cern.ch/record/2621960.

[112] CMS luminosity measurement for the 2018 data-taking period at $\sqrt{s} = 13$ TeV. Technical Report CMS-PAS-LUM-18-002, CERN, Geneva, 2019. URL: http://cds.cern.ch/record/2676164.

[113] Giovanni Franzoni. Dataset definition for CMS operations and physics analyses. *Nuclear and Particle Physics Proceedings*, 273-275:929–933, 2016. 37th International Conference on High Energy Physics (ICHEP). URL: https://www.sciencedirect.com/science/article/pii/S2405601415006331.

[114] CMS Data Quality Management Group. Public CMS data quality information, 2020. URL: https://twiki.cern.ch/twiki/bin/view/CMSPublic/DataQuality#Run_1_Data_Quality_Information.

[115] J. Alwall, R. Frederix, S. Frixione, V. Hirschi, F. Maltoni, O. Mattelaer, H.-S. Shao, T. Stelzer, P. Torrielli, and M. Zaro. The automated computation of tree-level and next-to-leading order differential cross sections, and their matching to parton shower

simulations. *Journal of High Energy Physics*, 2014(7), Jul 2014. URL: `http://dx.doi.org/10.1007/JHEP07(2014)079`.

[116] Paolo Nason. A new method for combining NLO QCD with shower monte carlo algorithms. *Journal of High Energy Physics*, 2004(11):040–040, Nov 2004. URL: `http://dx.doi.org/10.1088/1126-6708/2004/11/040`.

[117] Stefano Frixione, Paolo Nason, and Carlo Oleari. Matching NLO QCD computations with parton shower simulations: the POWHEG method. *Journal of High Energy Physics*, 2007(11):070–070, Nov 2007. URL: `http://dx.doi.org/10.1088/1126-6708/2007/11/070`.

[118] Simone Alioli, Paolo Nason, Carlo Oleari, and Emanuele Re. A general framework for implementing NLO calculations in shower monte carlo programs: the POWHEG BOX. *Journal of High Energy Physics*, 2010(6), Jun 2010. URL: `http://dx.doi.org/10.1007/JHEP06(2010)043`.

[119] Simone Alioli, Sven-Olaf Moch, and Peter Uwer. Hadronic top-quark pair-production with one jet and parton showering. *Journal of High Energy Physics*, 2012(1), Jan 2012. URL: `http://dx.doi.org/10.1007/JHEP01(2012)137`.

[120] Michał Czakon and Alexander Mitov. Top++: A program for the calculation of the top-pair cross-section at hadron colliders. *Computer Physics Communications*, 185(11):2930–2938, Nov 2014. URL: `http://dx.doi.org/10.1016/j.cpc.2014.06.021`.

[121] Simone Alioli, Paolo Nason, Carlo Oleari, and Emanuele Re. NLO single-top production matched with shower in POWHEG: *s*- and *t*-channel contributions. *Journal of High Energy Physics*, 2009(09):111–111, Sep 2009. URL: `https://doi.org/10.1088/1126-6708/2009/09/111`.

[122] Emanuele Re. Single-top Wt-channel production matched with parton showers using the POWHEG method. *The European Physical Journal C*, 71(2), Feb 2011. URL: `http://dx.doi.org/10.1140/epjc/s10052-011-1547-z`.

[123] Rikkert Frederix and Stefano Frixione. Merging meets matching in MC@NLO. *Journal of High Energy Physics*, 2012(12), Dec 2012. URL: `http://dx.doi.org/10.1007/JHEP12(2012)061`.

[124] Paolo Nason and Giulia Zanderighi. w^+w^-, wz and zz production in the POWHEG-BOX-V2. *The European Physical Journal C*, 74(1), Jan 2014. URL: `http://dx.doi.org/10.1140/epjc/s10052-013-2702-5`.

[125] A. Perloff and CMS Collaboration. Pileup measurement and mitigation techniques in CMS. *Journal of Physics: Conference Series*, 404:012045, Dec 2012. URL: `https://doi.org/10.1088/1742-6596/404/1/012045`.

[126] A.M. Sirunyan et al. Performance of the reconstruction and identification of high-momentum muons in proton-proton collisions at $\sqrt{s} = 13$ TeV. *Journal of Instrumentation*, 15(02):P02027–P02027, Feb 2020. URL: `https://doi.org/10.1088/1748-0221/15/02/p02027`.

[127] A.M. Sirunyan, A. Tumasyan, W. Adam, E. Asilar, T. Bergauer, J. Brandstetter, E. Brondolin, M. Dragicevic, J. Erö, M. Flechl, et al. Particle-flow reconstruction and global event description with the CMS detector. *Journal of Instrumentation*, 12(10):P10003–P10003, Oct 2017. URL: `http://dx.doi.org/10.1088/1748-0221/12/10/P10003`.

[128] CMS Collaboration. Electron and photon reconstruction and identification with the CMS experiment at the CERN LHC, 2020. `arXiv:2012.06888`.

[129] Jet algorithms performance in 13 TeV data. Technical report, CERN, Geneva, 2017. URL: `https://cds.cern.ch/record/2256875`.

[130] Vardan Khachatryan et al. Jet energy scale and resolution in the CMS experiment in pp collisions at 8 TeV. *JINST*, 12:P02014, 2017. `arXiv:1607.03663`, `doi:10.1088/1748-0221/12/02/P02014`.

[131] Daniele Bertolini, Philip Harris, Matthew Low, and Nhan Tran. Pileup per particle identification. *Journal of High Energy Physics*, 2014(10), Oct 2014. URL: `http://dx.doi.org/10.1007/JHEP10(2014)059`.

[132] Andrew J. Larkoski, Simone Marzani, Gregory Soyez, and Jesse Thaler. Soft drop. *Journal of High Energy Physics*, 2014(5), May 2014. URL: `http://dx.doi.org/10.1007/JHEP05(2014)146`.

[133] Yu.L Dokshitzer, G.D Leder, S Moretti, and B.R Webber. Better jet clustering algorithms. *Journal of High Energy Physics*, 1997(08):001–001, Aug 1997. URL: `http://dx.doi.org/10.1088/1126-6708/1997/08/001`.

[134] M Wobisch and T Wengler. Hadronization corrections to jet cross sections in deep-inelastic scattering. (hep-ph/9907280. PITHA-99-16):10 p, Jul 1999. URL: `https://cds.cern.ch/record/393035`.

[135] Mrinal Dasgupta, Alessandro Fregoso, Simone Marzani, and Alexander Powling. Jet substructure with analytical methods. *The European Physical Journal C*, 73(11), Nov 2013. URL: `http://dx.doi.org/10.1140/epjc/s10052-013-2623-3`.

[136] Mrinal Dasgupta, Alessandro Fregoso, Simone Marzani, and Gavin P. Salam. Towards an understanding of jet substructure. *Journal of High Energy Physics*, 2013(9), Sep 2013. URL: `http://dx.doi.org/10.1007/JHEP09(2013)029`.

[137] Jonathan M. Butterworth, Adam R. Davison, Mathieu Rubin, and Gavin P. Salam. Jet substructure as a new Higgs search channel at the LHC. *Phys. Rev. Lett.*, 100:242001, 2008. `arXiv:0802.2470`, `doi:10.1103/PhysRevLett.100.242001`.

[138] Jesse Thaler and Ken Van Tilburg. Identifying boosted objects with N-subjettiness. *Journal of High Energy Physics*, 2011(3), Mar 2011. URL: `http://dx.doi.org/10.1007/JHEP03(2011)015`.

[139] Jesse Thaler and Ken Van Tilburg. Maximizing boosted top identification by minimizing N-subjettiness. *Journal of High Energy Physics*, 2012(2), Feb 2012. URL: `http://dx.doi.org/10.1007/JHEP02(2012)093`.

[140] James Dolen, Philip Harris, Simone Marzani, Salvatore Rappoccio, and Nhan Tran. Thinking outside the ROCs: Designing decorrelated taggers (DDT) for jet substructure. *Journal of High Energy Physics*, 2016(5), May 2016. URL: `http://dx.doi.org/10.1007/JHEP05(2016)156`.

[141] A.M. Sirunyan, A. Tumasyan, W. Adam, F. Ambrogi, E. Asilar, T. Bergauer, J. Brandstetter, E. Brondolin, M. Dragicevic, J. Erö, et al. Identification of heavy-flavour jets with the CMS detector in pp collisions at 13 TeV. *Journal of Instrumentation*, 13(05):P05011–P05011, May 2018. URL: `http://dx.doi.org/10.1088/1748-0221/13/05/P05011`.

[142] Identification of double-b quark jets in boosted event topologies. Technical Report CMS-PAS-BTV-15-002, CERN, Geneva, 2016. URL: `https://cds.cern.ch/record/2195743`.

[143] Albert M Sirunyan et al. Performance of missing transverse momentum reconstruction in proton-proton collisions at $\sqrt{s} = 13\,\text{TeV}$ using the CMS detector. *JINST*, 14:P07004, 2019. `arXiv:1903.06078`, `doi:10.1088/1748-0221/14/07/P07004`.

[144] Giovanni Punzi. Sensitivity of searches for new signals and its optimization. *eConf*, C030908:MODT002, 2003. `arXiv:physics/0308063`.

[145] Search for a spin-1 heavy resonance that decays to a z boson and higgs boson in the semileptonic final states with run-2 data. Technical Report CMS-PAS-B2G-19-006, CERN, Geneva, 2020. URL: `http://cds.cern.ch/record/2725672`.

[146] Jia-Hua Cheng, Zhe Wang, Logan Lebanowski, Guey-Lin Lin, and Shaomin Chen. Determination of the total absorption peak in an electromagnetic calorimeter. *Nuclear Instruments and Methods in Physics Research Section A: Accelerators, Spectrometers, Detectors and Associated Equipment*, 827:165–170, Aug 2016. URL: `http://dx.doi.org/10.1016/j.nima.2016.05.010`.

[147] Jessie Shelton. TASI lectures on jet substructure, 2013. `arXiv:1302.0260`.

[148] Precision luminosity measurement in proton-proton collisions at $\sqrt{s} = 13$ TeV in 2015 and 2016 at CMS, 2021. Submitted to *Eur. Phys. J. C.* `arXiv:2104.01927`.

[149] M Cacciari, S Frixione, M.L Mangano, P Nason, and G Ridolfi. The $t\bar{t}$ cross-section at 1.8 and 1.96 TeV: a study of the systematics due to parton densities and scale dependence. *Journal of High Energy Physics*, 2004(04):068–068, Apr 2004. URL: `https://doi.org/10.1088%2F1126-6708%2F2004%2F04%2F068`.

[150] Stefano Catani, Daniel de Florian, Massimiliano Grazzini, and Paolo Nason. Soft-gluon resummation for Higgs boson production at hadron colliders. *Journal of High Energy Physics*, 2003(07):028–028, Jul 2003. URL: `https://doi.org/10.1088%2F1126-6708%2F2003%2F07%2F028`.

[151] Richard D. Ball, Valerio Bertone, Francesco Cerutti, Luigi Del Debbio, Stefano Forte, Alberto Guffanti, José I. Latorre, Juan Rojo, and Maria Ubiali. Impact of heavy quark masses on parton distributions and LHC phenomenology. *Nuclear Physics B*, 849(2):296–363, 2011. URL: `http://www.sciencedirect.com/science/article/pii/S0550321311001842`, `doi:https://doi.org/10.1016/j.nuclphysb.2011.03.021`.

[152] Steve Baker and Robert D. Cousins. Clarification of the use of chi-square and likelihood functions in fits to histograms. *Nuclear Instruments and Methods in Physics Research*, 221(2):437–442, 1984. URL: `http://www.sciencedirect.com/science/article/pii/0167508784900164`, `doi:https://doi.org/10.1016/0167-5087(84)90016-4`.

[153] Robert D. Cousins. Generalization of chisquare goodness-of-fit test for binned data using saturated models, with applications to histograms. 2013. URL: `http://www.physics.ucla.edu/~cousins/stats/cousins_saturated.pdf`.

[154] Glen Cowan, Kyle Cranmer, Eilam Gross, and Ofer Vitells. Asymptotic formulae for likelihood-based tests of new physics. *The European Physical Journal C*, 71(2), Feb 2011. URL: `http://dx.doi.org/10.1140/epjc/s10052-011-1554-0`.

[155] Procedure for the LHC higgs boson search combination in summer 2011. Technical Report CMS-NOTE-2011-005. ATL-PHYS-PUB-2011-11, CERN, Geneva, Aug 2011. URL: `https://cds.cern.ch/record/1379837`.

[156] Carlo Battilana. The CMS muon system: status and upgrades for LHC Run-2 and performance of muon reconstruction with 13 TeV data. *JINST*, 12(01):C01048, 2017. `doi:10.1088/1748-0221/12/01/C01048`.

[157] B. Kreis et al. Run 2 upgrades to the CMS level-1 calorimeter trigger. *JINST*, 11(FERMILAB-CONF-15-503-CMS. 01):C01051. 10 p, Oct 2015. 10 pages, 7 figures. URL: `https://cds.cern.ch/record/2103853`, `doi:10.1088/1748-0221/11/01/C01051`.

[158] CERN. Longer term LHC schedule, 2019. URL: `https://lhc-commissioning.web.cern.ch/schedule/LHC-long-term.htm`.

[159] Janos Ero, Ioannis Evangelou, G Flouris, Costas Foudas, Luigi Guiducci, Nikitas Loukas, Nikolaos Manthos, Ioannis Papadopoulos, Evangelos Paradas, S Sotiropoulos, D Sphicas, Andrea Triossi, and Claudia Wulz. The CMS Level-1 trigger barrel track finder. Technical Report CMS-CR-2015-304. 03, CERN, Geneva, Nov 2015. URL: `https://cds.cern.ch/record/2102885`, `doi:10.1088/1748-0221/11/03/C03038`.

[160] The Phase-2 upgrade of the CMS level-1 trigger. Technical Report CERN-LHCC-2020-004. CMS-TDR-021, CERN, Geneva, Apr 2020. Final version. URL: `http://cds.cern.ch/record/2714892`.

[161] Christian Amstutz et al. An FPGA based track finder at L1 for CMS at the high luminosity LHC. Technical Report CMS-CR-2016-112, CERN, Geneva, May 2016. URL: `https://cds.cern.ch/record/2194514`, `doi:10.1109/RTC.2016.7543102`.

[162] Michail Bachtis. Upgrade of the CMS barrel muon track finder for HL-LHC featuring a Kalman filter algorithm and an ATCA host processor with Ultrascale+ FPGAs. Technical Report CMS-CR-2018-294, CERN, Geneva, Oct 2018. URL: `https://cds.cern.ch/record/2648953`, `doi:10.22323/1.343.0139`.

[163] David Barney. CMS detector slice, Jan 2016. CMS Collection. URL: `http://cds.cern.ch/record/2120661`.